Modelling and Evaluation of the Performance of Building-Integrated Open Loop Air-based Photovoltaic/Thermal Systems

Luis Miguel Candanedo Ibarra

A Thesis

In the Department

of

Building, Civil and Environmental Engineering

Presented in Partial Fulfillment of the Requirements

for the Degree of Doctor of Philosophy (Building Studies) at

Concordia University

Montreal, Quebec, Canada

August 2010

©Luis Miguel Candanedo Ibarra, 2010

Library and Archives Canada

Published Heritage Branch

395 Wellington Street
Ottawa ON K1A 0N4
Canada

Bibliothèque et Archives Canada

Direction du Patrimoine de l'édition

395, rue Wellington
Ottawa ON K1A 0N4
Canada

Your file Votre référence
ISBN: 978-0-494-71143-9
Our file Notre référence
ISBN: 978-0-494-71143-9

NOTICE:

The author has granted a non-exclusive license allowing Library and Archives Canada to reproduce, publish, archive, preserve, conserve, communicate to the public by telecommunication or on the Internet, loan, distribute and sell theses worldwide, for commercial or non-commercial purposes, in microform, paper, electronic and/or any other formats.

The author retains copyright ownership and moral rights in this thesis. Neither the thesis nor substantial extracts from it may be printed or otherwise reproduced without the author's permission.

AVIS:

L'auteur a accordé une licence non exclusive permettant à la Bibliothèque et Archives Canada de reproduire, publier, archiver, sauvegarder, conserver, transmettre au public par télécommunication ou par l'Internet, prêter, distribuer et vendre des thèses partout dans le monde, à des fins commerciales ou autres, sur support microforme, papier, électronique et/ou autres formats.

L'auteur conserve la propriété du droit d'auteur et des droits moraux qui protège cette thèse. Ni la thèse ni des extraits substantiels de celle-ci ne doivent être imprimés ou autrement reproduits sans son autorisation.

In compliance with the Canadian Privacy Act some supporting forms may have been removed from this thesis.

While these forms may be included in the document page count, their removal does not represent any loss of content from the thesis.

Conformément à la loi canadienne sur la protection de la vie privée, quelques formulaires secondaires ont été enlevés de cette thèse.

Bien que ces formulaires aient inclus dans la pagination, il n'y aura aucun contenu manquant.

Canada

ABSTRACT

Building-Integrated Photovoltaic/Thermal Systems (BIPV/T) systems are photovoltaic installations incorporated as the exterior layer of the building envelope with the additional function of recovering thermal energy, which can then be used for space heating, domestic water heating and possibly for cooling. Some advantages of a BIPV/T system over an autonomous PV array include lower installation costs due to the replacement of cladding material, elimination of extra support structures and reduced electrical transmission losses. In addition, recovering the heat from the photovoltaic panels cools them and thus improves their electrical efficiency. Due to the novelty of BIPV/T systems, there is a need for the measurement of convective heat transfer coefficients and development of correlations for their prediction. The development of an integrated energy model, including correlations for the prediction of convective heat transfer coefficients in BIPV/T systems was one of the main objectives of this thesis.

Accurate measurements of convective heat transfer coefficients have been carried out for two open loop BIPV/T configurations: smooth and ribbed. The BIPV/T systems were tested at 30°-45° tilt angles and had a length/hydraulic diameter ratio of 38 which is representative of roof applications. It was found that for the BIPV/T ribbed case, the calculated Nusselt numbers are on average 2.6 times higher than the Nusselt numbers predicted by the Dittus-Boelter correlation.

Pressure drop measurements were performed for the two configurations and the results are presented in terms of the Darcy friction factors and compared to the Blasius equation. For both cases, the friction factors are higher compared to the ones predicted by the Blasius equation.

Previous existing electrical photovoltaic models have been used to couple their features to the lumped parameter thermal network modelling approach used in this thesis. Two thermal network models, steady state and transient, have been developed in this work and validated against experimental data. The steady state model is useful for a quick evaluation of the thermal/electrical performance, while the transient model gives a more accurate representation of the system by considering the thermal storage capacity of the materials. Finally, conclusions and general recommendations and guidelines for the design and construction of BIVP/T systems are provided.

Acknowledgments

I would like to thank my thesis supervisor Dr. Andreas Athienitis for his expert guidance. His dedication in research and his expertise in the building energy field has been a source of motivation during the course of this work. I want also to thank him for giving me the opportunity to work in such a relevant and current field.

I want to thank the Canadian Solar Buildings Research Network, a strategic NSERC research network and NRCan-CanmetENERGY (Varennes) for funding this project. I would also like to acknowledge the technical and other support of Dr. Yves Poissant and Josef Ayoub. The technical assistance of Joseph Hrib and Kwang Wook Park in the set up of the experiment is gratefully acknowledged. The technical assistance of Luc Demers and Jacques Payer are also acknowledged.

I would like to thank all the current and past members of the Solar Energy and Lighting Laboratory at Concordia University. I have benefited from their constant support, assistance in setting up experiments, and from the group discussions about different topics ranging from energy conservation, sustainable buildings and physics in general. Thank you very much guys. I also want to thank all the friends that have helped me during this time.

I would like to thank especially my parents for their constant support and encouragement, my brother Jose and my sister in-law Stephanie for all the help and support during this time. Finally, my special thanks to Erika for her continuous love, support and understanding in this period when I was working very hard.

Table of Contents

Table of Contents vi

List of Figures ix

List of Tables xii

Nomenclature xiii

1. Introduction 1

1.1 Background 1

1.2 Energy Balance of a BIVP/T System 4

1.3 Electrical Considerations of PV 7

1.3.1 Electrical characterization and modelling of photovoltaic modules 9

1.4 Solar Geometry and Availability 12

1.5 Building Envelope 12

1.6 Motivation 13

1.7 Problem Statement 18

1.8 Objectives and Scope 19

1.9 Thesis Overview 21

2. Literature Review of BIPV/T Systems 23

2.1 Air-Based PV/T Systems 23

2.1.1 Solar air collectors 23

2.1.2 BIPV/T systems 36

2.1.3 Transpired solar air collectors 44

2.2 Water-Based Solar Collectors and Liquid PV/T Systems 49

2.3 Demonstration Projects 51

3. Convective Heat Transfer Coefficients in a Building-Integrated Photovoltaic/Thermal System 54

3.1 Introduction 54

3.3 Convective Heat Transfer Coefficients 56

3.3.1 Correlations employed in BIPV/T models 57

3.3.2 Correlations employed in air hybrid photovoltaic/thermal (PV/T) collector models 59

3.3.3 Context of the heat transfer correlations 60

3.3.4 Limitations of the correlations that have been used in BIPV/T modelling 61

3.3.5 Mixed convection studies 62

3.3.6 Friction factor correlations 66

3.4 Experimental Setup 69
3.4.1 Transient response 73
3.4.2 Computation of convective heat transfer coefficients 76

3.5 Results and Discussion 77
3.5.1 Local effects 77
3.5.2 Average Nusselt numbers 79
3.5.3 Comparison of the new correlation with previous results 83
3.5.4 Local Nusselt numbers for the top surface 85
3.5.5 Grashof and Rayleigh numbers 85
3.5.6 Nusselt numbers for the laminar convection regime (Re<2300) 87
3.5.7 Comparison with Wu, Xu and Jackson correlation 89

3.6 Framing Effects on Nusselt Number 91
3.6.1 Local Nusselt numbers for the top surface 95

3.7 Pressure Drop in the BIPV/T systems 96
3.7.1 Friction factors 97

4. Comparison of Electrical Models for the Tested Photovoltaic Modules .. 101

4.1. Single-Diode Model 101

4.2. Photovoltaic Array Performance Model (Sandia) 107

4.3 Model Performance Comparison at STC 108

4.4 Model Performance Comparison at Different Temperatures 110

4.5 Model Performance Comparison at Field Conditions 112

5. Transient and Steady State Models for Open-Loop Air-Based BIPV/T Systems 118

5.1 Introduction 118

5.2 Existing Numerical Models 119

5.3 Common Modelling Approaches 120
5.3.1 Steady state vs transient solution. 120
5.3.2. Air temperature variation within the control volume. 121
5.3.3. Radiative heat transfer. 121
5.3.4. Effect of view factors. 121
5.3.5. Convective interior heat transfer correlations. 122
5.3.6. Convective and radiative exterior heat transfer coefficients. 122
5.3.7. Incidence angle adjustments. 123
5.3.8. Effect of moisture content. 123
5.3.9. Inlet air temperature effects. 123
5.3.10. Electrical efficiency modelling. 123
5.3.11 Equations solving method. 124
5.3.12 Pressure drop. 124

5.4 Experimental Facility 124

5.5 Proposed Models: Steady State and Transient 127
5.5.1 Steady state (SS) model 128
5.5.2 Transient (TR) Model 132
5.6 Results - Model Performance 134
5.7 Demonstration Project: EcoTerra House 138
5.8 Heat Removal Factor and Thermal Efficiency 140
5.9 Numerical Sensitivity Study of Bottom Heat Transfer Coefficient 142
5.10 Numerical Sensitivity Study of Insulation Level 144
6. Conclusion 146
6.2 Research Contributions 150
6.3 Design Guidelines and Recommendations 152
6.4 Recommendations for Future Work 154
References 156
Appendix A. Solar Geometry and Availability 171
Appendix B. Measurement Uncertainty 176
Appendix C. Mathcad Single-Diode Model 180
Appendix D. Mathcad PV Performance Sandia Model 193
Appendix E. MATLAB PV Performance Sandia Model 196
Appendix F. Steady State Model 199
Appendix G. Transient Model 206

List of Figures

Figure 1.1. Schematic of a typical air-based open-loop BIPV/T system, subdivided into five sections for thermal network modelling (Candanedo, L.M. *et al.*, 2010) 5
Figure 1.2. Basic lumped parameter thermal network for a section of the BIPV/T roof installation. 6
Figure 1.3. Single-diode circuit (DGS, 2005) 10
Figure 1.4. Left: Current-Voltage (I-V) curve of a solar cell. Right: I-V curve for a module, and the effect of temperature on the maximum power point at same irradiation level (DGS, 2005). 11
Figure 1.5. I-V curve of a solar cell and the corresponding fill factor (DGS, 2005). 12
Figure 2.1. A: Basic unglazed hybrid solar air collector. B: Glazed hybrid solar air collector. 23
Figure 2.2. The three PV/T air configurations tested at Patras University (Tripanagnostopoulos, Y. et al., 2000b). 30
Figure 2.3. Schematic of the PV façade structure simplification studied by Yang et al. (2000). 30
Figure 2.4. Thermal network representation of the BIPV/T simplified model by Bazilian and Prasad (2002) 37
Figure 2.5. Façade heat transfer parameters after Mei et al. (2002). 38
Figure 2.6. Thermal efficiencies for four types of hybrid PV/T systems. The filled symbols correspond to the PV/T collectors with reflectors (Tripanagnostopoulos, Y. et al., 2002). 39
Figure 2.7. Schematic of the desiccant cooling system and process representation in a psychrometric chart. Adapted from (Mei, L. et al., 2006). 41
Figure 2.8. Configurations studied numerically and experimentally by Charron and Athienitis (2006a). 42
Figure 2.9. Left: Sketch of the heat fluxes for the corrugated plate. Right: Boundary layer development for the corrugated transpired solar air collector (Gawlik, K. & Kutscher, C., 2002) 46
Figure 2.10. PV SolarWall results for 900 W/m^2 solar radiation, 1 m/s wind speed and a flow rate of 7 CFM/ft^2 (Hollick, J., 2005). 47
Figure 2.11. The test set-up at CANMET (Hollick, J., 2005) 48
Figure 2.12. Typical closed loop liquid-cooled PV/T system (Bosanac, M. et al., 2003). 50
Figure 3.1. BIPV/T thermal network model showing the interior convective heat transfer coefficients h_{ct} and h_{cb} (Candanedo, L.M. et al., 2010) (the configuration shown corresponds to an experimental prototype studied in this thesis). 56
Figure 3.2. Photograph of the BIPV/T roof in the EcoTerra™ House. The amorphous PV modules are attached to a metal roof skin on vertical and horizontal wood framing that also creates the flow channel. (The roof has a length of 5.8 m in the flow direction shown by the arrows). 69
Figure 3.3. (a) Experimental BIPV/T setup replicating 1 strip of the BIPV/T system of the EcoTerra house with and without amorphous PV modules attached; (b) schematic of the setup; (c) cross section details of BIPV/T. 70

Figure 3.4. Transient response of the bulk air temperature for constant volumetric flow rate $0.021 m^3/s$ and incident total solar radiation 815 W/m^2 (the arrow shows increasing time)..... 74
Figure 3.5. Bulk air temperature for different Reynolds numbers compared with exponential correlation fits (points show experimental measurements and solid lines the exponential fit)..... 75
Figure 3.6. Local Nusselt number for the top surface versus non-dimensional distance from the entrance..... 78
Figure 3.7. Nusselt numbers for the top surface versus Reynolds number. The data is compared with the correlation given by equation 3.25. The uncertainties of each of the data points are shown by the vertical line segments..... 81
Figure 3.8. Nusselt numbers for the bottom surface versus Reynolds number. The data is compared with the correlation equation 3.26. The uncertainties of each of the data points are shown by the vertical bars..... 82
Figure 3.9. Nusselt numbers for the top surface versus Reynolds number comparison for 45° and 30° tilt angles..... 82
Figure 3.10. Comparison of the top channel surface Nusselt number correlation (eq. 3.25) with Dittus-Boelter, Gnielinski, Martinelli, Malik and Mercer correlations..... 84
Figure 3.11. Comparison of Equations 3.1 and 3.2 with the experimental data (Pr=0.71). All the experimental points are above the limits established by the equations..... 86
Figure 3.12. a) Experimental Re and $Ra(D_h/L)$ data. b) Metais and Eckert (1964) map for vertical tubes..... 87
Figure 3.13. a) Experimental data of measured Nusselt number to the addition of the Dittus-Boelter and natural convection components for 30° and 45° tilt angle (n=1 in equation 3.29). b) Experimental data comparison of Nusselt numbers to equation 3.29 (for n = 1 for Re< 2300 and n = 0.638 for Re>2300)..... 88
Figure 3.14. Experimental data comparison to Equations 3.31 and 3.33..... 90
Figure 3.15. a) Photo of the wood framing structure employed to support the PV modules in the BIPV/T system of Northern Light Canadian Solar Decathlon 2005 house (Pasini, M. & Athienitis, A.K., 2006) b) Photo of the wood framing elements employed to support the PV modules in the BIPV/T system of the EcoTerra demonstration house (Chen, Y. et al., 2007a)..... 91
Figure 3.16. Sketch of the wood framing effect test in the BIPV/T channel..... 92
Figure 3.17. Nusselt numbers for the top surface versus Reynolds number. The data is compared with the correlation given by equation 3.34 . The uncertainties of each of the data points are shown by the vertical and horizontal line segments..... 92
Figure 3.18. Pitch of ribs and rib height in the BIPV/T channel..... 94
Figure 3.19. Local Nusselt number for the top surface for the framing test versus non dimensional distance from the entrance..... 95
Figure 3.20. Pressure drop as a function of the flow rate in the channel in L/s..... 96
Figure 3.21. Measured friction factors in the two BIPV/T systems as a function of Re number..... 98
Figure 3.22. Friction factors ratio in the two BIPV/T systems as a function of Re number. 99
Figure 3.23. Measured friction factors in the two BIPV/T systems in the laminar region.. 99
Figure 3.24. Friction factors ratio in the two BIPV/T systems in the laminar region..... 100
Figure 4.1. Single-diode circuit (De Soto, W. et al., 2006)..... 102

Figure 4.2. Current-Voltage (I-V) curve simulated with the five parameter model and Sandia Model. 110
Figure 4.3. Current-Voltage (I-V) curves simulated with the five parameter model and Sandia Model for 1000 W/m^2 radiation and different cell temperatures. 111
Figure 4.4. Normalized Performance at STC for 13 a-Si modules by (King, D.L. et al., 2000a) 113
Figure 4.5. Degradation curve for amorphous silicon module by Delahoy, A.E. *et al.* (2002) 114
Figure 4.6. Fill factor curve for amorphous silicon modules at 250 and 1000 W/m^2 by Ruther, R. et al. (2008). 114
Figure 4.7. Models comparison to I-V measurements for November 28th, 2009. 115
Figure 4.8. Models comparison to I-V measurements for March 5th, 2010. 115
Figure 5.1. Open and closed loop configurations for solar collectors (the heat exchanger may be eliminated in the open loop configuration). 118
Figure 5.2. Models studied: Model SS (steady state) and Model TR (transient). 128
Figure 5.3. Air temperature profiles within the channel as predicted by CFD simulations. 132
Figure 5.4. (a) Measured average air speed in the channel, and estimated interior heat transfer coefficients; (b) Wind speed and exterior heat transfer coefficient. 136
Figure 5.5. (a) Average temperature of the top of the BIPV/T channel (measurements, Model SS), (b) Average temperature of the top of the BIPV/T channel (measurements, Model TR) Solar radiation incident on collector (G) and exterior air temperatures (T_o) are also shown. 136
Figure 5.6. Outlet air temperatures (measurements, Model SS and Model TR). 137
Figure 5.7. Left: BIPV/T module of the roof under construction in the factory (before installing metal layer and PV modules) Right: BIPV/T module completed (with PV modules installed). 138
Figure 5.8. EcoTerra™ solar house photograph. 139
Figure 5.9. Temperature profiles for the EcoTerra house on March 17th, 2008 (measurement and Model TR). 139
Figure 5.10. Temperature profiles for the EcoTerra house on March 17th, 2008 (measurement and Model TR using framing correlation). 140
Figure 5.11. Heat removal factor and thermal efficiency of the BIPV/T channel. 141
Figure 5.12. The figure shows the effect of increasing the insulation value and its effect to the outlet air temperature. 144
Figure 5.13. The percentage relative deviation from the outlet air temperature at 50 RSI versus the insulation level. 145
Figure A.1. Equations of time E as function of day of the year. 173
Figure A.2. a) Solar geometry angles for a tilted surface (zenith, slope, surface azimuth, solar b) Plan view showing solar azimuth angle (Duffie, J.A. & Beckman, W.A., 2006). 174

List of Tables

Table 1-1. Concordia University BIPV/T studies and facilities. 15
Table 2-1. Companies producing hybrid PV/T systems 48
Table 2-2. BIPV/T demonstration projects around the world. 49
Table 2-3. Main BIPV/T research groups listed by country. 53
Table 3-1. Nusselt number correlations for flow in a cavity or duct 67
Table 4-1. Reference parameters at STC conditions for Uni-Solar PVL-68 manufacturer's data 109
Table 4-2. Sandia Model Parameters at STC for Uni-Solar PVL-68 109
Table 4-3. Maximum power at different cell temperatures for 1000 W/m^2 radiation obtained with five parameter model and Sandia model for Uni-Solar PV-68. 111
Table 4-4. Models comparisons for November 28th, 2009 (AST = 12.4hr) 116
Table 4-5. Models comparisons for March 5th, 2009 (AST = 11.4hr). 116
Table 5-1. Material Parameters. 126

Nomenclature

Symbols

A	Area, m^2
A_c	Exposed area of the BIPV/T collector, m^2
A_{cv}	Area of the control volume, m^2
F_{PV}	View factor between the surfaces
C_{pv}	Thermal capacitance per unit area, $J/(kg \cdot K \cdot m^2)$
c_p	Specific heat of the air, $J/(kg \cdot K)$
E	Equation of time, min
E_p	Electrical power, W
F_R	Heat removal factor
f	Darcy friction factor
f_B	Darcy friction factor from Blasius relationship
G_t	Total incident solar radiation on the plane of the collector per unit area, W/m^2
h	Hour angle, °
h_o	Exterior convective heat transfer coefficient or wind coefficient per unit area, $W/(m^2K)$
h_r	Cavity radiative heat transfer coefficient per unit area, $W/(m^2K)$

h_{ct}	Convective heat transfer coefficient for the top surface per unit area, $W/(m^2K)$
h_{cb}	Convective heat transfer coefficient for the bottom surface per unit area, $W/(m^2K)$
i	Sub-index, time step counter
I_{PH}	Photocurrent, A
I_p	Current through the parallel resistor, A
I	Solar cell terminal current, A
I_o	Diode reverse saturation current, A
I_L	Light current or photocurrent, A
I_{mp}	Current at maximum power point, A
k	Thermal conductivity, W/mK
L_{st}	Local standard meridian, °
L_{Loc}	Longitude of the considered location, °
La	Latitude of the location (North+), °
m	Mass flow rate, kg/s
n	Day of the year, e.g. January 1st = n = 1
P	Power, W
P_{elect}	Electrical power per unit area, W/m^2

q_{sky}	Radiative heat loss to the sky per unit area, W/m^2
q_{rec}	Heat recovered in the control volume per unit area, W/m^2
Q_u	Total heat recovered in the BIPV/T collector, W
Q	Heat transfer rate, W
R_P	Parallel resistance, Ω
R_{SH}	Shunt resistance, Ω
R_S	Series resistance, Ω
R_{PV}	Thermal resistance of the PV module, m^2K/W
R_{ins}	Combined thermal resistance of the insulation and plywood layer, m^2K/W
T	Temperature, K or °C
T_L	Thermal energy loss from the top part of the module (radiation+convection), W
T_{ma}	Average air temperature, °C
T_a	Ambient air temperature, K
T_c	Temperature of the cell, °C
T_{dp}	Dew point temperature, °C
T_o	Ambient air temperature, °C
$T_{PV_{TOP}}$	PV exterior surface temperature, °C
$T_{PV_{MID}}$	PV temperature at the middle of module, °C

$T_{PV_{BOT}}$	PV interior surface temperature, °C
T_b	Interior insulation temperature, °C
t	Time from midnight, hr
U_L	Heat loss coefficient, W/(m^{2}K)
V_{wind}	Wind speed, m/s
V_{ch}	Air speed in the channel, m/s
V	Solar cell terminal voltage, V
V_{mp}	Voltage at maximum power, V
V_D	Diode voltage, V
W	Width of the control volume, m

Abbreviations and Acronyms

BIPV	Building Integrated Photovoltaic
BIPV/T	Building Integrated Photovoltaic/Thermal
CFD	Computational Fluid Dynamics
DST	Daylight saving time
ESP-r	Energy systems performance-research program
EVA	Ethylene vinyl acetate
HVAC	Heating, Ventilating and Air Conditioning
MPP	Maximum power point
PV	Photovoltaics
PV/T	Photovoltaic/Thermal
SS	Steady state
ST	Solar time
TRNSYS	TRaNsient SYstems Simulation program
TMY2	Typical meteorological year weather file, v.2
TR	Transient

Greek letters

α	Solar absorptance
α_s	Solar altitude angle, °
β	Tilt angle, °, temperature coefficient, %/°C
Δ	Change in a variable
δ	Declination angle, °
γ	Surface azimuth angle, °
γ_s	Solar azimuth angle, °
Δx	Length of control volume, m
η_n	Nominal electrical efficiency of the PV module
η_{STC}	Electrical efficiency at standard test conditions
η_{mp}	Maximum power electrical efficiency of the PV module
ε	Surface long-wave emissivity
θ	Incidence angle, °
θ_z	Zenith angle, °

1. Introduction

1.1 Background

No matter how abundant they may seem, fossil energy sources are finite. Moreover, they have the serious drawback that their exploitation has detrimental environmental consequences, in both the short and long terms. Fossil fuel reserves are concentrated in a few countries in the world, with important geopolitical implications. Finally, these fossil resources must be transported at considerable financial and energy expenditure. As a result of the reasons expressed above, it is vital to invest in the research, development and applications of renewable energy sources.

Alone among renewable energy sources, solar energy is available to everyone, worldwide, in virtually every climate. It is environmentally clean, extremely abundant and infinite on the human scale. Unlike hydro power and wind generation, solar energy use has practically no effect on the landscape. Often, its use does not require complicated or expensive systems. It can be applied to a broad range of scales - from powering solar watches and calculators to supplying electricity to neighborhoods and cities. Quiet and often unobtrusive, systems that recover, transform or control solar energy are ideal for integration as functional elements of buildings.

Building-Integrated Photovoltaic (BIPV) systems consist of photovoltaic arrays that are integrated as components of the building envelope of residential homes or commercial buildings. Apart from providing electricity, they serve an architectural purpose as the cladding material of façades or roofs. As with any other element of the building envelope, their integration has to be done carefully in order to avoid problems with rain penetration,

wind loads and thermal expansion. Fire and electrical hazard protection must also be considered in their design. BIPVs offer lower installation costs than stand-alone PV systems by replacing shingles, bricks or the external layer of curtain walls and by obviating the need for extra framing systems. BIPVs optimize the use of space, which is especially important in densely populated areas. Another advantage is that, since the electricity is generated on site where it is needed, electrical transmission losses are reduced.

A BIPV/Thermal (BIPV/T) system is a special type of BIPV technology in which part of the solar energy received by the PV panels is collected as heat. This heat is usually removed by circulating a fluid, which can be either a liquid or air, beneath the panels. The heat removed can then be used for purposes such as fresh air and domestic water heating, space heating and clothes drying (Chen, Y. *et al.*, 2007a). It can even be used for cooling (e.g., with a desiccant cooling device). This arrangement also lowers the temperature of the PV panels, thus increasing their electricity generation efficiency as described below in section 1.3. This PhD thesis will focus on one of the most common and useful configurations of BIPV/Ts: open loop air-based systems. In this type of system, outdoor air is drawn under the BIPV with a fan, getting heated as it flows. It is then brought to the mechanical room or energy system of the house for use as heated fresh air or as a source of useful heat for a heat exchanger or a heat pump.

Efforts of researchers towards understanding and modelling the energy balance of air-based BIPV/T systems still have not led to an accurate model of the heat transfer in typical full-scale installations. The heat transfer is usually modelled using a thermal network approach. This method requires convective and radiative heat transfer coefficients in order

to write the conservation energy equations, and thus to find the PV and bulk air temperatures.

Previous studies (Bazilian, M.D. & Prasad, D., 2002; Eicker, U., 2003; Charron, R. & Athienitis, A.K., 2006b; Charron, R. & Athienitis, A.K., 2006a) have employed heat transfer correlations developed for similar geometries such as pipes and channels. This implicitly assumes a number of ideal conditions including developed flow conditions, symmetric heating, and either uniform wall temperatures or uniform heat flux rates, among others. However, this approach is not accurate because of the complexity of BIPV/T channels, which include heating asymmetry, high aspect ratios, non-uniform heat fluxes, non-uniform wall temperatures, non-developed flow conditions, mixed flows (air and water vapour), and non-uniform cross sections due to framing and different PV geometries. A major objective of the research presented here is to contribute to accurate modelling of heat transfer and fluid flow phenomena in BIPV/T systems for design, optimisation, operation control and evaluation of their performance. The temperature of the PV panels is also needed to accurately determine their electrical output.

After this background discussion, this chapter continues with a description of the energy balance existing in a BIPV/T system. Following this, a brief description of electrical considerations of photovoltaic systems is presented and the influence of temperature on their power output is discussed. A brief description of solar geometry is presented. Next, a summary of the main motivations of the research is presented. Finally, the problem statement is presented and discussed.

1.2 Energy Balance of a BIVP/T System

Photovoltaic modules either absorb or reflect the electromagnetic radiation that comes from the sun (including a small portion that is reflected from neighboring surfaces such as the ground). The fraction of energy that is absorbed will depend on the optical properties of the PV module and on the incidence angle of the solar radiation, which is a function of time of day, month of the year and tilt angle of the PV module. Photovoltaic modules are usually covered with a layer of tempered glass or another encapsulant that often has an antireflective coating. The portion of the reflected solar radiation is on the order of 5-8% for normal incidence angles (Parretta, A. *et al.*, 1999).

The fraction of incident solar radiation within the spectrum region for which the solar cells are sensitive (band gap) (DGS, 2005) can be converted into electricity. The efficiency of a photovoltaic module is the fraction of the total incident energy that is converted into electricity and is typically 8 to 18% for commercially available modules. The rest of the absorbed solar radiation is converted into heat. This heat will be released to the exterior of the building and to the back of the PV panel through convective and longwave radiation heat transfer. Radiation heat transfer is often modelled using the PV temperature and a reference sky temperature in the Stefan-Boltzmann equation. The heat released by convection to the exterior air will depend on the speed of the wind impinging on the PV panel. In the back surface of the panel, heat is also transferred by convection to the air passing through the channel. The rest of the energy is exchanged by radiation between the surfaces in the PV channel. Figure 1.1 depicts the energy exchanges taking place in a typical BIPV/T roof installation.

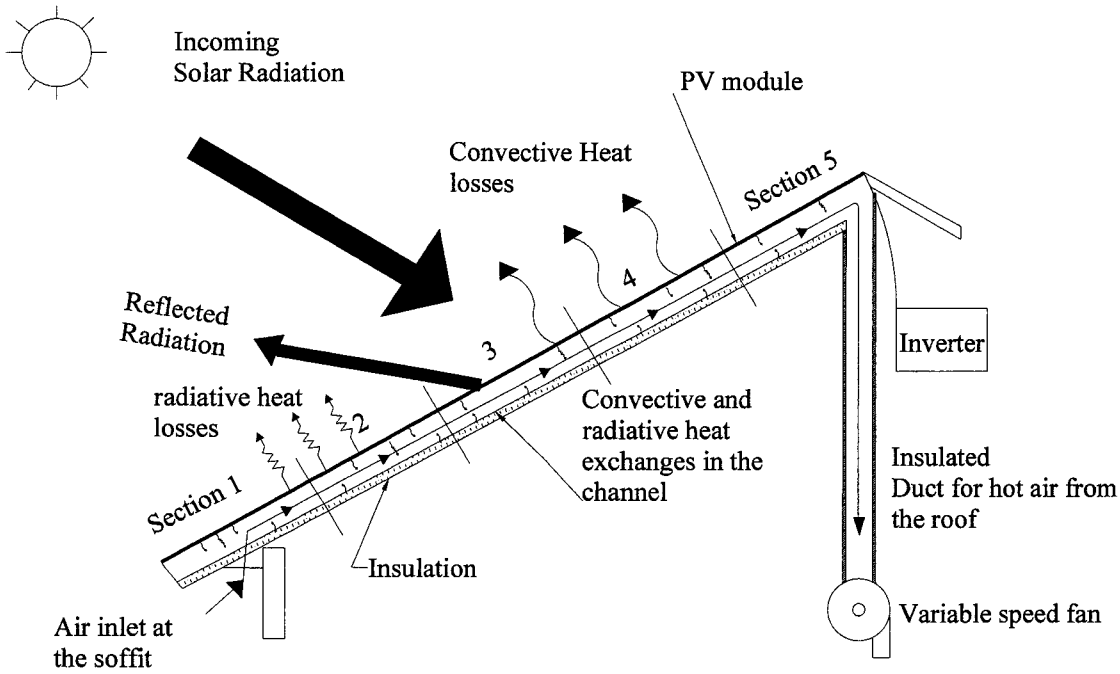

Figure 1.1. Schematic of a typical air-based open-loop BIPV/T system, subdivided into five sections for thermal network modelling (Candanedo, L.M. *et al.*, 2010).

The BIPV/T system shown in Figure 1.1 (typically 6-10m long) has been discretized into five sections for thermal network modelling. Simple and relatively accurate representations can be created with lumped parameter models. A single control volume representing the whole BIPV/T channel can be used; however, several control volumes (as depicted in Figure 1.1), increase the accuracy and spatial resolution of the results. The thermal network for a section of the system is presented in Figure 1.2. This thermal network assumes a negligible thermal capacitance and resistance for the PV module.

The energy balance for the PV module can be expressed as:

$$\alpha \cdot A_m \cdot G_t = E_p + T_L + Q_c + Q_r \qquad 1.1$$

where $\alpha \cdot A_m \cdot G$ is the absorbed solar radiation, E_p is the electrical power produced by the photovoltaic module, T_L is the thermal heat transfer rate loss from the top part of the

module to the exterior (convective + radiative to the sky), Q_c is the convective loss from the module to the channel air stream and Q_r is the radiative heat transfer to the back plate.

Convective heat transfer between the heated air and the BIPV/T roof surfaces is a complex phenomenon, heavily dependent on the geometry of the installation. Many researchers have traditionally employed Nusselt number correlations developed for fully-developed flow in smooth pipes and channels. These correlations usually do not represent the actual conditions found in an open-loop BIPV/T system such as non-uniform cross sections and non-uniform heat fluxes and non-develop flow conditions.

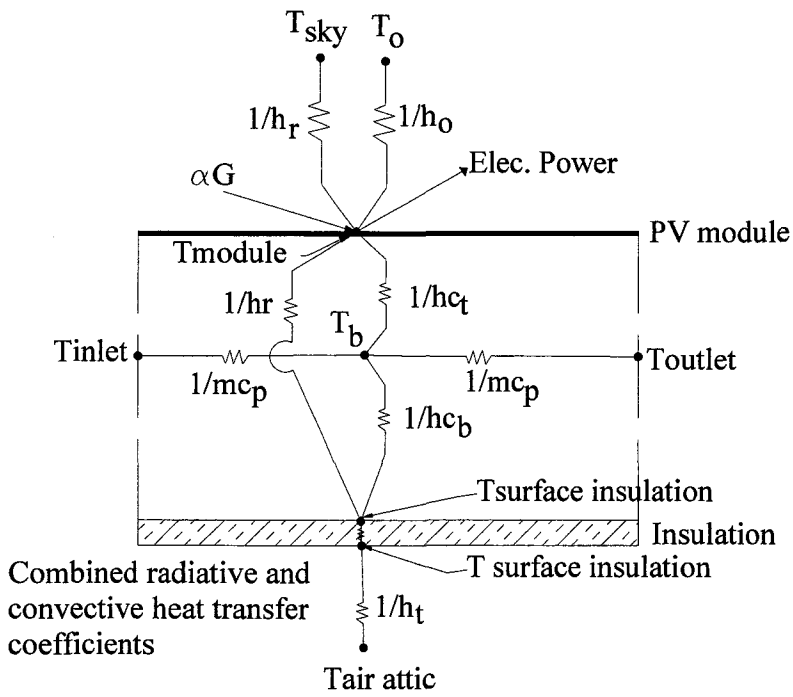

Figure 1.2. Basic lumped parameter thermal network for a section of the BIPV/T roof installation.

1.3 Electrical Considerations of PV

As their temperature increases, silicon cells commonly used in PV modules suffer a reduction in their electrical conversion efficiency. Temperature coefficients are employed to calculate the influence of temperature on different parameters such as: voltage, current and maximum power. The maximum power temperature coefficient is the most commonly used temperature coefficient (Duffie, J.A. & Beckman, W.A., 2006).

Temperature increase can thus have an important effect on the performance of a PV system. It has been reported that unventilated PV installations on façades can deliver 9% less energy than delivered by stand-alone systems; for unventilated systems installed on roofs, the reduction in energy delivery is of the order of 5.5% (DGS, 2005). This effect is likely due to higher temperatures.

Standard test conditions (STC) have been defined in order to be able to compare different cells and modules and to determine their electrical characteristics. These standard test conditions, are described in the IEC standard IEC 60904-1 (2006) as follows:

- Normal irradiance of 1000 W/m^2;
- Cell temperature of 25°C with a tolerance of ± 2°C;
- Defined light spectrum (spectral distribution of the solar reference irradiance according to IEC 60904-3) with an air mass AM = 1.5.

The nominal efficiency of solar modules, η_n, is measured under standard test conditions (STC).

It is defined as:

$$\eta_{mp} = \frac{P_{MPP(STC)}}{A \cdot 1000 \frac{W}{m^2}} \qquad 1.2$$

where $P_{MPP(STC)}$ is the power produced at the maximum power point[1] under standard test conditions and A is the area of the module. The effective efficiency is taken as (Duffie, J.A. & Beckman, W.A., 2006)

$$\eta_{mp} = \eta_{mp,ref} + \Delta\eta \qquad 1.3$$

The change of efficiency is given by:

$$\Delta\eta = \mu_{mp} \times (T_c - T_{c,ref}) \qquad 1.4$$

where T_c is the temperature of the cell and μ_{mp} is the temperature coefficient for the maximum power. (The temperature coefficient μ_{mp} is also often indicated with the Greek letter β). The reference temperature, $T_{c,ref}$ is usually 25°C. Typically μ_{mp} is negative.

The temperature coefficient μ_{mp} can be calculated from equation 1.2 as follows:

$$\mu_{mp} = \frac{d\eta_{mp}}{dT} = \left(I_{mp} \frac{dV_{mp}}{dT} + V_{mp} \frac{dI_{mp}}{dT} \right) \frac{1}{AG_t} \qquad 1.5$$

where G_t is the total solar irradiance on the module or cell, and A is the area of the PV module.

Commercially available monocrystalline and polycrystalline modules typically have maximum power efficiency temperature coefficients between -0.04 to -0.08 % per °C (Sandia National Laboratories, 2006).

[1] As discussed in the next section, the maximum power point is the point in the current-voltage curve where maximum power is produced.

Amorphous PV technology is less affected by temperature increase (King, D.L. & Kratochvil, J.A., 1997; DGS, 2005). For low irradiance levels (below 500 W/m^2), they may even have positive temperature coefficients (i.e., their performance improves with temperature), but on average their coefficients are negative. The power temperature coefficients for amorphous PV modules are between -0.01 to -0.026 % °C (Sandia National Laboratories, 2006) .

Since PV modules perform better at lower temperatures, two objectives can be achieved by reducing their temperature in a BIPV/T application: to increase electrical performance and to collect useful thermal energy.

1.3.1 Electrical characterization and modelling of photovoltaic modules

The basic unit of a PV module is a solar cell. A solar cell can be modelled as a current source in parallel with a diode. A diode is a two-terminal device that allows electrical current to flow in only one direction. The standard model of a solar cell is called a single-diode model (DGS, 2005) and includes a parallel resistance (accounting for leakage losses) and a series resistance (accounting for voltage losses) between the semiconductor and the electrical contacts of the module.

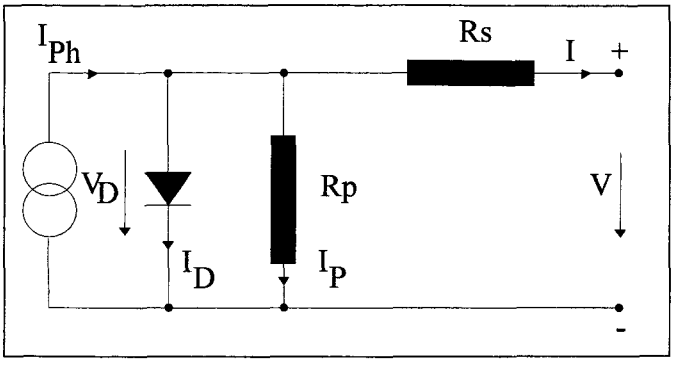

Figure 1.3. Single-diode circuit (DGS, 2005).

In Figure 1.3, V is the solar cell terminal voltage, V_D is the diode voltage, I_{PH} is the so-called photocurrent (the ideal current produced by the panel), I_D is the diode (or dark) current, I_P is the parallel resistor current, I is the solar cell terminal current, R_P is the parallel resistance, and R_S is the series resistance.

The characteristic equation of the circuit is given by

$$I = I_{PH} - I_0\left(e^{\frac{V+IR_S}{a}} - 1\right) - \frac{V + IR_S}{R_P} \qquad 1.6$$

where the first term corresponds to the photocurrent, the second term represents the current through the diode, and the third term represents the current through the parallel resistor. The parameters I_0, V_T, R_S and R_P in equation 1.6 depend on the photovoltaic technology employed, as well as on the construction of each cell. The physical parameter "*a*" depends on the temperature of the panel.

Equation 1.6 can be used to trace the IV curve of a solar cell. Solar modules, which consist of many cells, have similar characteristic curves. Since the IV curve depends on both solar radiation and temperature, different curves will be found under different conditions.

The operating voltage will depend on the characteristics of the load connected. For example, a battery has nearly constant voltage, and it would suffice to replace V in equation 1.6 with the battery voltage. The IV characteristic of a resistor is a straight line. To find the operating conditions, equation 1.6 must be solved simultaneously with the line equation corresponding to this load ($V = IR_L$), which is equivalent to finding the intersection of the straight line and the characteristic curve (a typical characteristic curve is shown in Figure 1.4).

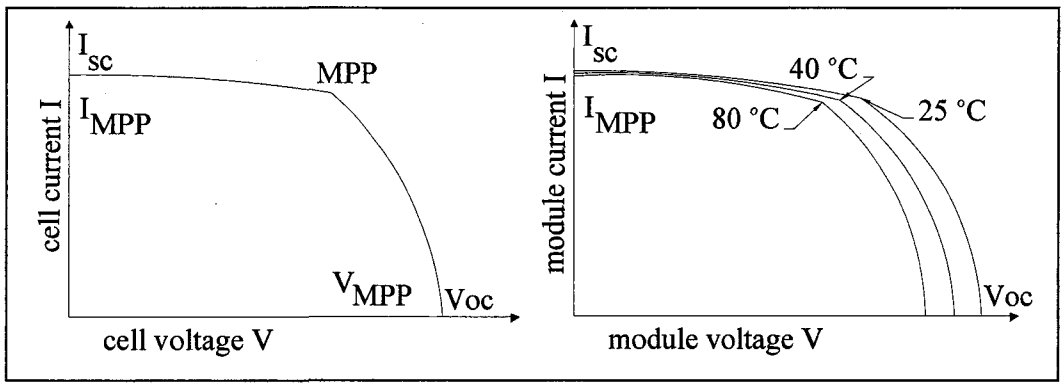

Figure 1.4. Left: Current-Voltage (I-V) curve of a solar cell. Right: I-V curve for a module, and the effect of temperature on the maximum power point at same irradiation level (DGS, 2005).

Solar cells and PV modules may produce energy at a maximum power point (MPP), where the product I x V is maximal. The position of the MPP changes depending on the solar radiation and temperature of the panel (Figure 1.4). For instance, in the case of constant solar radiation, higher temperatures will reduce the voltage of the maximum power point, thus reducing the power output of the module. Maximum power point tracking algorithms are used by charge controllers and inverters to ensure that the MPP is tracked.

A common variable used to compare solar cells is the **fill factor**, which represents the ratio of the actual maximum power obtained to the power that could be obtained if the cell

operated at open circuit voltage and short circuit current. Figure 1.5 shows the representative areas for I_{sc} & V_{oc}, and I_{mp} with V_{mpp}.

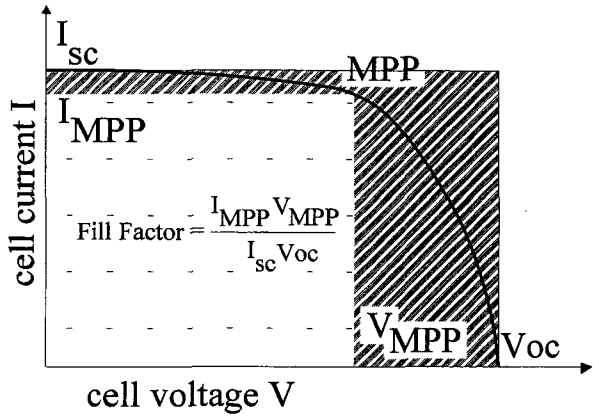

Figure 1.5. I-V curve of a solar cell and the corresponding fill factor (DGS, 2005).

1.4 Solar Geometry and Availability

In order to be able to predict the total incident radiation on a surface, it is necessary to describe the sun's position in the sky. The total incoming solar radiation can be described by three main components: beam solar radiation, diffuse sky solar radiation and diffuse radiation reflected from the ground. Appendix A summarizes the main solar angles employed to describe the sun position in the sky and the equations used to calculate the solar incidence angle to any surface as a function of time.

1.5 Building Envelope

In order to successfully integrate the PV modules into the building envelope, it is necessary to incorporate architectural/structural considerations and to take measures to prevent rain penetration and reduce snow accumulation. It is also advisable that the system

be applied seamlessly so that the system is not "architecturally disturbing" (Prasad, D. & Snow, M., 2005). For this, roof tile dimensions and color of the project must be considered.

In roof installations, the PV modules can be overlapped like shingles so that the system is waterproof (Eiffert, P. & Kiss, G.J., 2000). There are special profiles on the market for the integration of PV modules into the roof that are watertight. Usually these elements are made of aluminum (Prasad, D. & Snow, M., 2005). Thin film PV roof systems are usually attached with adhesive on a metal roof and they are nailed or screwed on the top part of the PV module and then covered by the roof ridge to avoid any water infiltration.

1.6 Motivation

The photovoltaic industry is growing rapidly. It has been reported that during the 1980s and 90s PV panel production grew between 18 to 20% per year (Lin, G.H. & Carlson, D.E., 2000). According to these authors, PV electricity production could reach 65 GW per year by the year 2025, and the application of PV would be mainly for building-integrated systems due to the aforementioned lower installation costs. In a report by the European Photovoltaic Industry Association (2010) it is stated the world installed capacity by the end of 2009 was 22.8 GW.

Residential buildings in Canada consume a considerable amount of energy, mainly due to the heating needs during the winter months (about 17% of the secondary energy consumption (Natural Resources Canada, 2009; Statistics Canada, 2009)). Space and water heating accounted for 80% of the energy consumed in residential buildings between 1997 and 2007 according to statistics from the Natural Resources of Canada and Statistics Canada

(2009; 2009). Passive solar design guidelines help to reduce the heating loads. Measures such as using large windows oriented to the south, efficient use of distributed thermal mass and high insulation values in walls help to reduce heating loads considerably. However, these measures do not eliminate all the heating loads. This is an important argument in favor of the use of BIPV/T systems.

The BIPV/T system is an application that is particularly well-suited to Canadian weather conditions: the coldest days during the winter, when heat is needed the most, are often clear, sunny days. Therefore, it is expected that BIPV/T systems will become more common and it is important to find optimum integration guidelines that can be used by engineers and PV installing companies, in order to improve the overall utilization of the available solar energy.

Table 1-1 presents a list of the facilities and concepts, along with demonstration projects studied at Concordia University over the past five years.

Table 1-1. Concordia University BIPV/T studies and facilities.

Project / Facility	Concepts under study
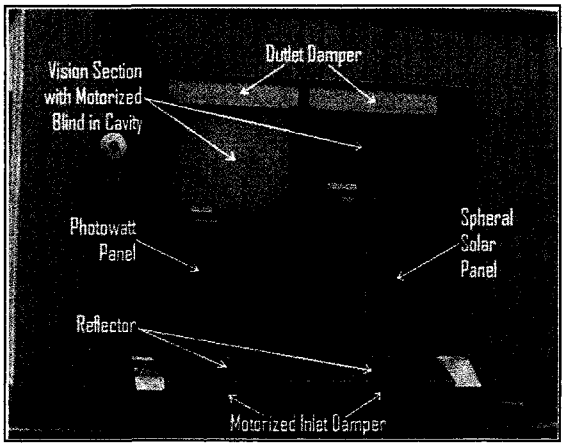	BIPV/T in a **multifunctional façade** (roof of the BE Bldg). The facility has been used for the determination of heat convective transfer coefficients, as well as of the thermal and electrical performance of the system (Charron, R. & Athienitis, A.K., 2006a; Liao, L. *et al.*, 2007). It incorporates a ventilated window section to allow daylight into the facility. On the left, the PV modules are exposed to the exterior, while on the right the PV is inserted in the interior of the cavity. The electrical production is higher in the installation on the left but the thermal energy delivered is lower compared to that delivered by the panels inserted in the gap.
	The Northern Light was the first Canadian house participating in the U.S. Department of Energy's Solar Decathlon competition in 2005. It employed the concept of BIPV/T. A prize for integration of the solar panels onto the roof was granted by BP Solar. The tilt angle of the PV installation was optimized for Washington, DC, where the competition was held.

	The **EcoTerra Alouette solar house** located in Eastman, Québec, was one of the winners of the EQuilibrium competition organized by the CMHC (Chen, Y. et al., 2007a). It incorporates several concepts in passive solar energy design as well as an active BIPV/T system and a geothermal heat pump. The house employs amorphous PV modules installed on the roof of the second storey. The system has an installed capacity of 2.8 kW. The air is heated as is taken from under the soffit and blown through the cavity formed by the modules and the roofing. The hot air is then used to heat up a hollow core slab in the basement and to preheat DHW. EcoTerra produces about 2,500 kWh of electricity a year. The roof thermal efficiency is about 9.4% and the PV efficiency is about 5.1%.
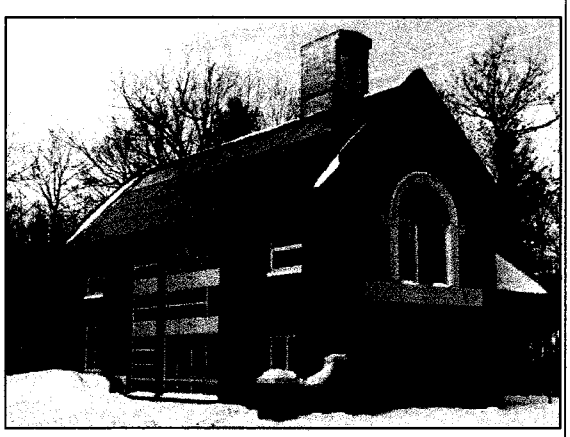	The **Alstonvale Net Zero House** is another winner of the EQuilibrium competition (Candanedo, J.A. *et al.*, 2007). Polycrystalline modules will be used and placed close to the air inlet. After passing under the PV section, the air will flow under a glazing section, using low-emissivity glass to increase the thermal energy collected and to boost the temperature with the purpose of increasing its usefulness. A highly-insulated duct brings the air to a heat exchanger where the air can be used directly or as the source of two heat pumps.[2]

[2] The house was damaged in a recent fire and the company (Sevag Pogharian Design –SPD-) has plans to rebuild it.

	This picture displays a **new test facility** at Concordia University. A BIPV/T system has been incorporated onto the roof of the facility and its performance is being evaluated. On the façade, the concept of a perforated (transpired) solar air collector is tested together with PV modules. The air removes the heat from the PV modules making them more efficient and the pre-heated air can be employed as make-up air in HVAC commercial systems.
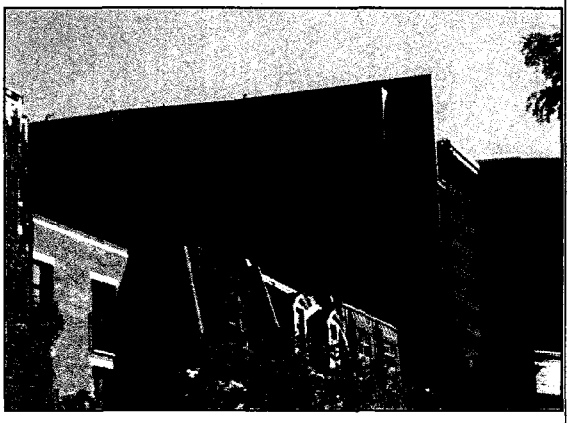	The new **John Molson School of Business** has 24.5 kWp of photovoltaic panels installed on its near south-facing façade. The modules, which have been custom-made, are incorporated on top of transpired solar air collectors. They are narrower than conventional modules and are placed horizontally.

1.7 Problem Statement

As shown in the previous sections, the electrical power production of PV modules is affected considerably by temperature. It has been reported that high operating temperatures (greater than about 75-80 °C) can cause deterioration of the modules and shorten their life expectancy (Zondag, H.A. & van Helden, W.G.J., 2002). Therefore, when designing such systems, it is important to keep the PV panels as cool as possible. When water (or other liquid) is used as the heat transfer fluid in solar thermal systems, closed loop systems are employed, in which the fluid is continuously circulated through the solar absorber.

Optimal design of open-loop BIPV/T systems has not been studied in detail. Convective heat transfer coefficients or pressure drops have not been quantified under different conditions, such as channel aspect ratios or flow rates. This situation has forced engineers and researchers to estimate the values of the heat transfer coefficients with correlations developed for either pipes or ducts which give an approximate idea of the performance, but only provide rough estimates of the surface and air temperatures and cannot fully represent the thermal interchange taking place in the BIPV/T system. It is also important to take into account factors such as heating asymmetry, mixed flows, non-developed flow conditions, non-uniform cross section, and so on, making this a very complex problem. Optimal design can only be achieved through detailed and complementary experimental and numerical thermofluid studies.

When the appropriate values of convective heat transfer inside the channel formed by the PV and the roofing are known, it is possible to accurately estimate the energy that can be extracted from the system, as well as the achievable outlet air temperatures. Consequently, other parts of the HVAC mechanical system in solar homes and buildings, such as heat

pumps and thermal storage tanks, can be selected correctly. It is also necessary to be able to estimate the static pressure loss in the air stream due to friction across the roofs or façades in order to select the appropriate fan and to develop appropriate control strategies.

If the temperature distribution across the PV modules in the cladding of the building can be estimated, modules that will work at the same voltage level due to their temperature can be appropriately wired, ensuring maximum electrical power production. Research will be focused on the integration of the PV on roof surfaces.

1.8 Objectives and Scope

This thesis focuses on thermal and fluid modelling of typical BIPV/T installations in order to accurately predict their electrical and thermal energy output.

The specific objectives of this work are:

- To develop a general methodology for the integrated energy analysis of open loop air-based BIPV/T systems.
- To measure local and average convective heat transfer coefficients and to develop correlations for the most commonly used BIPV/T configurations. These heat transfer correlations may be used as inputs for simple lumped parameter thermal models (as presented in this work). They may also be used in whole building simulation software packages such as ESP-r, EnergyPlus and TRNSYS, to allow other researchers and engineers to evaluate the energy outputs of customized BIPV/T systems.

- To determine the pressure drop and calculate friction factors in typical BIPV/T systems and to compare them to typical friction factor correlations. This information is especially important for the selection of the fan driving the air flow.

- To develop guidelines for the selection of simple electrical models and to compare their results to field conditions and identify their advantages and limitations.

- To develop and validate lumped parameter steady state and transient BIPV/T numerical models for performance evaluation.

This work does not intend to model and assess the integration of BIPV/T systems in buildings. There are a number of advanced and validated software tools for building energy simulations, such as ESP-r, EnergyPlus and TRNSYS that can be used to obtain the energy loads profiles for buildings at different environmental conditions. For example, depending on the available solar radiation level at a specific time, it may or not justify turning on the fan of the BIPV/T system. An example of an investigation of control strategies considering a BIPV/T system was carried out by Candanedo, J.A. & Athienitis, A.K. (2010). In their work, weather forecasts were used in combination with real-time model based predictions of the building response in order to manage collection, storage and delivery of thermal energy from a BIPV/T system.

1.9 Thesis Overview

Chapter 1 starts by describing the motivation of this work and establishing the problem statement in BIPV/T systems. The basic energy balance for BIPV/T system is presented and the main research objectives are presented.

Chapter 2 presents a literature review. Research on air-based PV/T systems (not necessarily building-integrated) is included and special focus is placed on solar air collectors and transpired solar air collectors because they share many attributes and features with BIPV/T systems. The importance of the accurate determination of pressure drop and actual heat transfer coefficients is identified in this chapter. Much of the previous experimental work on heat transfer in solar air collectors has been done using "flow straithteners". A typical BIPV/T system would not use such installations. Common numerical modelling approaches have been identified and have been taken into account in the thesis. For example, it was determined that thermal capacitive effects must be taken into consideration when modelling PV/T systems in order to account for sudden changes in solar radiation levels and wind gusts. The chapter also identifies typical values of Nusselt numbers.

Chapter 3 presents a detailed experimental study on convective heat transfer coefficients for BIPV/T systems. The chapter starts with a summary of the correlations that have been employed to date to estimate convective heat transfer rates in BIPV/T systems. An extensive literature review is presented discussing the experimental procedures used to develop these correlations, and how these conditions compare with typical BIPV/T installations. The chapter presents the developed Nusselt number correlations for BIPV/T systems. Finally, the chapter presents typical pressure drops in the studied BIPV/T channels.

In order to obtain ratios of the effective pressure drop, the Darcy friction coefficients are calculated and compared to the Blasius correlation, using the data from the measurements.

Chapter 4 compares two existing electrical models employed in this research to evaluate electrical performance of PV modules. The models can predict the power curve (I-V), including the effect of temperature. The models are used in Chapter 5 where lumped parameter numerical models are presented.

Chapter 5 presents transient and steady state models developed for air-based open-loop BIPV/T systems. First, a short review of current models is given. From them, common modelling approaches are identified and suggestions to improve them are presented. The energy balance equations are written for a set of nodes and solved using computer codes written in MATLAB. Although not measured, a group of two exterior convective heat transfer correlations are selected because of their good agreement with experimental data. Finally, the model is compared to a demonstration project (EcoTerra House).

Chapter 6 summarizes the main conclusions, presents some design guidelines for BIPV/T systems and proposes future work.

2. Literature Review of BIPV/T Systems

Air based PV/T systems are covered, first subdividing them into solar air collectors, which are considered here because of their many similarities to PV/T systems, then into BIPV/T systems, and finally into transpired solar air collectors. A short review of water-based solar collectors and liquid PV/T systems is then presented.

2.1 Air-Based PV/T Systems

A hybrid solar air collector is a module in which the Photovoltaic Panel (PV) is employed as a solar absorber and produces electricity and heat by heating up the circulating air (Zondag, H.A., 2008a). See Figure 2.1. Hybrid solar air collectors come in different configurations, including one in which the PV panel is exposed directly to the exterior and another in which the PV is covered with an extra glass panel. The extra glazing acts to reduce the effect of wind on the exterior heat losses.

2.1.1 Solar air collectors

There is a considerable amount of public documentation on solar air collectors and they have very similar configurations to hybrid solar air collectors, the main difference being the absence of PV modules, these are included as part of the literature review.

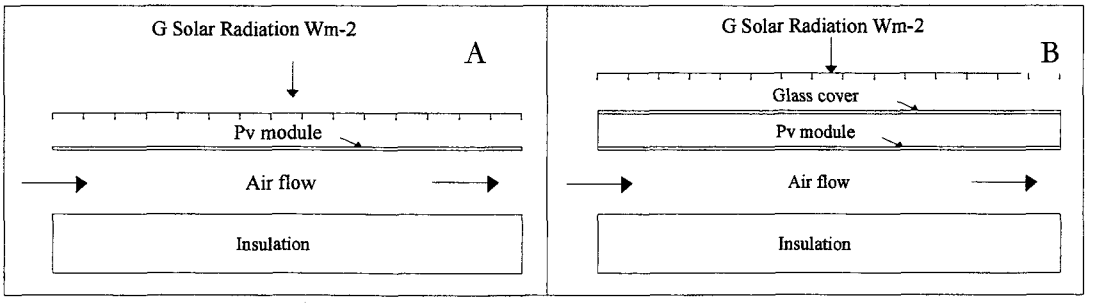

Figure 2.1. A: Basic unglazed hybrid solar air collector. B: Glazed hybrid solar air collector.

Early in the 1960's solar energy research was carried out on the performance of solar air heaters (Whillier, A., 1964). A model was presented and a discussion was presented on the effect of adding either a metallic or plastic wire screen into the air stream, which would increase the heat gains due to the reduction of the radiation resistance between the absorber and the air flow.

One of the first studies on duct design optimization for solar air heaters was done in Australia (Charters, W.W.S., 1971). The study focused on the developed flow region of the duct. It was recognized that further work on relationships of pressure drop and heat transfer in the non developed region was necessary. The report concluded that there was no easy method to optimize the design of the duct based on technical approach, and that any optimization must also include the materials' costs.

Related work on hybrid solar air collectors was carried out at different institutions, (Smith, D.R. *et al.*, 1978; Hendrie, S.D., 1982; Zondag, H.A., 2008a). Hendrie (1982) studied the performance of early designs of flat plate hybrid collectors. The electrical and thermal efficiencies were below the expected. New designs were made, but testing was not carried out due to budget cuts.

At Waterloo University, optimization studies on the passage geometry of air solar collectors was carried out (Hollands, K.G.T. & Shewen, E.C., 1981). The main conclusion was that when the length of the air flow passage is made less than 1 m, the heat transfer coefficient increases dramatically. This is not a surprising result, since the heat transfer coefficients are higher for the entrance regions for pipes and ducts (Oosthuizen, P.H. & Naylor, D., 1999; Incropera, F.P. & De Witt, D.P., 2002; Kays, W. *et al.*, 2005). However, the maximum heat transfer augmentation happened when adding a V-shaped corrugated

absorber plate as the top surface, in which case the heat transfer is increased between 47 to 300%. There were gains in efficiency on the order of 7 to 12%. Gains of 3.3% in the efficiency were reported when changing the emissivity of the inner surface of the flow passage from 0.2 corresponding to bare metal to 0.9 for painted black metal. It is important to mention that the geometry for the V-shaped corrugated plate absorber does not resemble the one found in typical hybrid PV-T collectors, which prevents the extension of the results to these systems.

Research on heat transfer enhancement in solar air heaters using transversal wires placed on the bottom plate was done in the turbulent flow regime. The results were summarized in Nusselt number correlations for Reynolds numbers in the range of 3,000 to 18,000 (Gupta, D. *et al.*, 1993).

Work related to BIPVs was also done at the University of Wales (Cross, B.M., 1994). Even though it did not include BIPV/T systems, it is interesting to mention that temperatures of 80 °C were measured for the modules close to the ridge of the roof. The experiment was carried out in a Solar Simulator, where special light bulbs reproduce the effect of the solar radiation.

A comparison of numerical studies and experimental results was presented in the work of Ong (1995a) for different types of solar air collectors. Nusselt number correlations for the laminar, transitional, turbulent and natural regimes that are available in the public literature were employed for the models. According to the author, the models seemed to yield accurate results using those correlations. The research was done for rectangular channels, which are not representative of a BIPV/T system.

Work concerning optimization of the flow channel depth for flat plate solar air heaters was carried out by Hegazy (1996). The examination was done in a purely theoretical fashion. An expression was developed, but it relies on the determination of the friction factor and the skin friction coefficient.

An analytical solution for a hybrid air solar heater was developed by Sopian et al. (1996). The analysis considered two design options, one in which the air flow was limited to one side of the PV, and another in which the air will flow around both sides of the PV. The numerical results show a better thermal performance for the double-pass design. This is a very similar configuration to the one displayed in the testing facility at Concordia University as the first item of Table 1-1.

Vandaele et al. (1996) examined different issues concerning the installation of hybrid PV/T air liquid systems into buildings and pointed out different objectives for research, including thermal and electrical performance of the system, and ventilation performance for natural and mechanical ventilation.

A naturally ventilated PV façade was constructed and tested indoors at the Hong Kong Polytechnic University and a numerical model versus a CFD model were compared for a BIPV/T application (Yang, H.X. *et al.*, 1996). It was not mentioned, however, which type of turbulence model was employed for the CFD analysis. Temperature reductions of the PV modules between 15 to 20 °C and a power increase yield of 8% were reported.

The building simulation software ESP-r has been used to evaluate PV/T air systems (Clarke, J.A. *et al.*, 1997). A model was used to compute the electrical power produced by the PV modules using an algorithm to find the maximum power production. The model is

compared with experimental results: however, the agreement is only qualified as reasonable, and no measure of the error between simulated and measured performance is mentioned.

Similar research on performance evaluation of hybrid PV/T solar air collectors was carried out at the Indian Institute of Technology (Garg, H.P. & Adhikari, R.S., 1997). Their model uses analytical solutions for the differential equations in the energy balance. The main assumptions of the model are steady state analysis, constant heat flux across the boundary, no air leakage through the system, the temperature of the elements only change along the direction of the air flow, and negligible side losses.

Evaluation of four different configurations of hybrid solar air heaters was carried out by Mohamad (1997). The study focused on use of a glazing layer on top of the PV to minimize the convection losses due to wind that would exist if the PV was in direct contact with the exterior.

Results from the PV façade integration at the Mataro public library in Spain and from a testing rig in Stuttgart were simulated and reported by Eicker (1999). The results show that exit air temperatures of the façade easily reach 50 °C during the summer. The researchers recommended to extent the length of the façade and reduce the mass flow rate to achieve temperatures high enough to regenerate a desiccant-based cooling system.

The performance evaluation of an air BIPV/T system in North Carolina was discussed by Fitzpatrick (1999). It is important to note that PV electrical power output was reduced between 17 to 25% when the fan that drew the air in the system was stopped.

Experimental and numerical work was carried out in Germany for different configuration of solar air heaters (Pottler, K. *et al.*, 1999). The results indicated that for smooth surfaces, the optimum air gap depth for maximum heat extraction was between 7 and 8 mm. The heat

extraction was increased with the same mass flow rate in a channel with a wider gap using continuous aluminum fins attached to the absorber and it proved to be 33% more effective at removing heat from the absorber.

It has been pointed out that conditions for the roof usually fall in the developing region of pipes and ducts (Brinkworth, B.J., 2000). The developing regions are where the temperatures and velocities are continuously changing. Different correlations are employed on the model depending on its nature, laminar or turbulent, based on the Reynolds number.

In another study, Brinkworth et al. (2000), developed a model for naturally ventilated PV. The model is presented and validated against experimental data taken at an indoor test rig. The model includes the effect of wind and buoyancy. However, it is not clear how the simulated external wind conditions were reproduced in an indoor test.

Eicker and Fux (2000) reported an air temperature increase of 35°C for a ventilated PV façade when the radiation exceeds 700 W/m^2 (Mataro library, Barcelona). It was explained that for summer time, the temperature of the air is high enough to be used for an adsorption cooling system. The measurement of the heat extracted from the PV façade indicates that the system can provide 20% of the heat required for an adsorption cooling system.

In Egypt, a study of four different PV/T configurations was performed (Hegazy, A.A., 2000a). The designs were all the glazed solar hybrid air heaters type. One of the main conclusions of the study is that due to the high temperatures in these configurations, low emissivity coatings in the glass are not adequate because of the subsequent electrical power reduction caused by high temperatures. It is possible that the glass contained large portions of iron that could diminish the transmittance of this transparent layer, which could explain the power reduction in the system.

In another study on optimal geometry for solar air heaters it was found that the depth to length ratio should be 2.5×10^{-3} (Hegazy, A.A., 2000b). The results were obtained with the following main assumptions: 1) the flow in the channel is hydraulically smooth, 2) there was no air leakage, and 3) the heat capacity of the materials is negligible and that the temperature of the top and bottom plates only changes in the x-direction.

In Greece, a study of a hybrid PV/T air system was carried out and it was found that introducing a flat black metal plate, similar to that in Figure 2.2, helped to increase the exit air temperature of the system. The temperature of the inner most layer was also lower with this plate (Tripanagnostopoulos, Y. *et al.*, 2000a). The author stresses the affordability of this modification.

The same group in Greece tested different configurations of PV/T air systems and compared them to water systems (Tripanagnostopoulos, Y. *et al.*, 2000b). The study concluded that adding fins to the surface opposite to the PV increases heat transfer to the air, subsequently reducing the temperature of the surface that belongs to the exterior of the building. It also reduces the temperature of the PV panel by around 2 to 3 °C and increases the air output temperature by between 1 and 2 °C (see Figure 2.2). Regarding the performance of the water system, the report concluded that removed more heat from the PV panel during the summer, but pointed out that the system is also more costly.

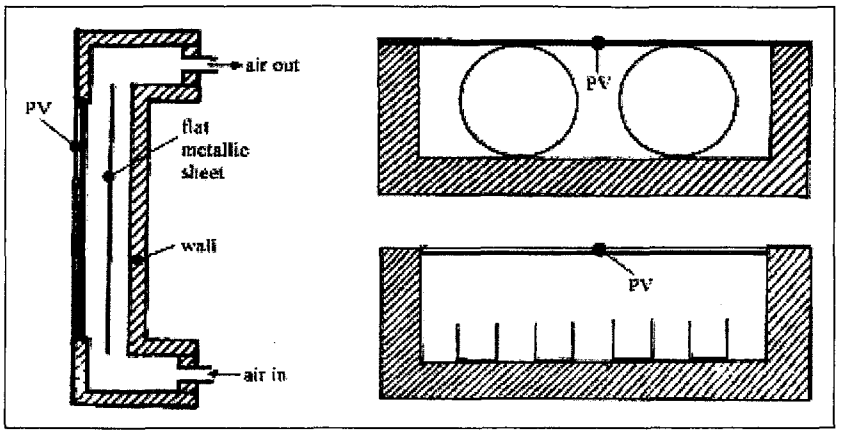

Figure 2.2. The three PV/T air configurations tested at Patras University (Tripanagnostopoulos, Y. et al., 2000b).

According to simulation work by Yang et al. (2000), adding PV to the façade of buildings contributes to reduce the cooling load by removing a fraction of the solar heat impinging the building by the ventilated façade. The study carried out relies on simulation; the performance evaluation for the cities of Beijing, Shanghai and Hong Kong were done using its respective weather data. The concept is supported by the idea that the heat transfer coefficients for the front of the exterior wall of the building are lower due to the presence of the air cavity formed by the PV and the brick cladding. It is concluded that reductions of up to 50% of the cooling load can be achieved for the city with the highest solar radiation, in this study Beijing. The study was done for conditions of natural convection of the air (see Figure 2.3).

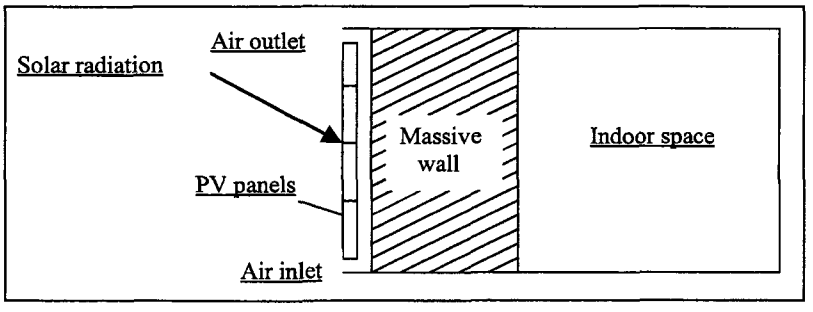

Figure 2.3. Schematic of the PV façade structure simplification studied by Yang et al. (2000).

A study carried out by the National Institute of Standards and Technology of the United States (NIST), on prediction of the building integrated cell temperatures, describes the development of a one-dimensional transient heat model (Davis, M.W. *et al.*, 2001). Although the model does not include the effect of having a ventilated PV cavity on the exterior of the building, it is interesting to note that very accurate results were obtained with the transient model. It was stated that accounting for the heat storage by the PV panel eliminates unrealistic temperature swings due to quick changes in the impinging solar radiation.

A thermal study using CFD for a BIPV system in an atrium found that changing the position of the air inlet improved the cooling effect of the PV panels that were installed on the roof of the structure (Gan, G. & Riffat, S.B., 2001). The simulations were done with constant heat fluxes through the roof. These were in the range of 25 to 400W/m^2, which represent a third of the energy incident on the roof (solar radiation between 75 to 1200W/m^2). The work concluded that the ventilation of the roof would have to be mechanical for acceptable thermal comfort levels.

In another publication, the response of the PV module temperature to changes in solar radiation was studied (Jones, A.D. & Underwood, C.P., 2001). It was found that a time constant of 7 min exists for a PV module composed of three layers of materials. The time constant is defined as the time taken by the module temperature to reach 63% of the total change in temperature resulting from significant change in radiation. Because of this, the authors developed a one-dimensional transient model to study the thermal behavior of the PV module. The array was exposed on both sides to the exterior temperature. The analysis distinguished between the forced convection effect and the natural convection effect. From the experimental data, the researchers estimated the exterior forced convection heat transfer

coefficients to be in the range of 2 W/m^2K for periods where the wind speed is 2 to 4 m/s, and 4 W/m^2K for wind speeds over 4 m/s.

A study on the viability of hybrid PV/T systems was carried out in Denmark and included an extensive literature review on PV/T systems (Bosanac, M. *et al.*, 2003). The PV-Hyphen project stands out among the literature surveyed. The project consisted of experimental and numerical work for different European cities, employing the ESP-r software program. The results concluded that the systems in northern European cities perform better in buildings with high demand of fresh air where up to 10% of the annual heating demand can be saved.

Two numerical models were compared to experimental data at the National Institute of Standards and Technology in the United States (Davis, M.W. *et al.*, 2003). One of which was developed by Sandia National Laboratories and the other by researchers at the NIST. The model from SNL needs more detailed information about the PV panels. The calculated energy output agreed within 7% of the measured energy output. The models under-predict the power production for high incidence angles of the solar radiation impinging on the panel.

Modelling of convective heat transfer in air collectors has been performed in detail and suggests which Nusselt number correlations can be employed for the different cases of convection (Eicker, U., 2003). It is stated that for developed laminar flow, the Nusselt number is around 5.4. The use of the Petukhov equation is recommended for the case of turbulent flow. Considerations when designing the air duct system and choosing the appropriate fan to drive the air flow are reviewed.

Experimental determination of natural convection film coefficients for curtain walls was carried out at Concordia University by researchers at the Center for Building Studies (Ge, H. & Fazio, P., 2003). The test consisted of the determination of the maximum air velocity beside the glass or the framing section of the curtain wall, in order to measure the inner region of the boundary layer where conduction effects dominate. By measuring the thermal gradient and knowing the conductivity of air, the heat flux in this region is determined using Fourier's equation. Then, since the heat flux is known, the computation of the convective film coefficient is easily done. The results of this research can be used to simulate PV installed in a curtain wall, employing the heat transfer coefficients as boundary conditions in a CFD model.

Comparisons between numerical models versus experimental results are presented for a naturally ventilated roof and façades by Infield, D.G. *et al.* (2003). The temperature difference between the model and the experiment is usually around 4 °C. The difference can be larger or smaller depending on the solar radiation level and the wind speed. It is also recognized that the main problem for modelling natural convection flows is the determination of the accurate flow rate inside the ventilated façade. It is important to note that the model employed the ambient air temperature as inlet temperature. Experimental data taken at Concordia suggest that this is not a correct assumption. The temperature at the inlet can differ from the exterior temperature by up to 5 °C.

Experimental work on heat transfer augmentation in solar air heaters by the use of a wire mesh was carried out in India (Thakur, N.S. *et al.*, 2003). The correlations for pressure drop and heat transfer were summarized using the Colburn j factor and are supposed to be valid for Reynolds numbers from 182 to 1168. The experiment employed flow straighteners in

front of the entrance of the test sections. The straightener sections had a length of 0.9 m, which represents 19 times the hydraulic diameter of the test. An average heat transfer coefficient was determined based on the experimental data. No information about local heat transfer coefficients was presented.

Zondag, H.A. & van Helden, W.G.J. (2003) from the Energy Research Center of the Netherlands examined numerically the results of different PV/T systems, water and air, open and closed systems. The paper recommends the use of PV/T water system based on the fact it can perform better thermally. However, the conclusion does not include the increased cost of PV/T water systems compared to air systems.

The importance of different aspects in PV/T module design and manufacturing in order to enhance the heat transfer in PV/T systems is discussed by van Helden, W.G.J. *et al.* (2004). The study states that careful selection of spectrally selective coatings can increase the system performance by absorbing a larger portion of the incoming solar radiation. The absorption for the reflective metallic wiring connecting the PV cells in the modules should be increased by lowering their reflection through the use of coatings or by simply reducing the area they cover.

Determination of buoyancy-driven flows for ducts was examined in detail experimentally in a test rig and compared to the theory by Brinkworth, B.J. & Sandberg, M. (2005). The effects of using different rigs, or transversal elements attached to one of the sides, were examined experimentally and then compared to the theoretical estimation; a satisfactory agreement was apparently obtained.

Strategies to increase the solar absorption of the PV module in the long-wave region are discussed by Santbergen and van Zolingen (2005). The study explains in detail the

composition of a typical PV panel, which consists of a glass over, a top grid, and anti-reflection coating, a semiconductor and a back contact. The study relies on the assumption that the absorption in the semiconductor only takes place for the band gap energy, the rest of the long-wave irradiance is not absorbed. It is recommended that semitransparent solar cells be used; these will absorb the short-wave radiation but allow the passage of the long-wave radiation to be absorbed in the back contact. It is important to note that in the article, long-wave radiation is considered as that with a wavelength longer than 1.1 μm. Solar irradiance lies mostly in the region below 3 μm. Typically long-wave radiation is defined as having a wavelength longer than 3 μm (Duffie, J.A. & Beckman, W.A., 2006).

The feasibility of maintaining the outlet temperature of a glazed solar air collector was studied in Japan (Ito, S. *et al.*, 2006). The results were encouraging, suggesting that the control system based on the air flow rate manages to maintain the exit air temperature. The control employed a simple digital controller that regulated the speed of the fan according to the temperature at the exit. For sudden changes in irradiation, the thermal mass of the collector will keep the outlet temperature within the tolerance margin. However, when there are continuous changes in wind velocity, solar radiation and mass flow rate in the system, it is necessary to account for the thermal mass. In the cases of estimation of yearly performance of solar air collectors, steady state analysis seems to yield adequate results.

Researchers from the Indian Institute of Technology performed several experiments for a ribbed solar air heater and developed correlations for Nusselt number and friction factors (Jaurker, A.R. *et al.*, 2006). The heat flux was controlled by means of electrical resistances and the data reduction was for an averaged h coefficient instead of a local one. The researchers

estimated that the effect of the ribbed surfaces increased the Nusselt number on the order of twice that of a smooth surface.

Researchers from the Center of Energy studies from the Indian Institute of Technology carried out studies of a hybrid PV/T air system for the climate of New Delhi (Tiwari, A. *et al.*, 2006). The researchers claim good agreement between the experiment and the numerical analysis; however, it is not clear how the convective heat transfer values were obtained from the experiments in the channel.

Experimental work was carried out in solar air heaters to increase the overall efficiency by the use of baffles inside the channel (Romdhane, B.S., 2007). For the experiment, the baffles were pasted onto the absorber. No relationships for the convective heat transfer coefficients were provided, but the different designs showed significant improvements in efficiency.

An extensive literature review on correlations for different types of solar air collector was carried out by researchers in India (Varun *et al.*, 2007). The correlations examine the use of different shapes of fins and ribs and provide an averaged value of heat transfer coefficients and friction factors. These can be employed for numerical comparisons for different geometries.

2.1.2 BIPV/T systems

Hybrid solar air collectors were first used in the roof and façade of the Solar One house of the University of Delaware built in 1973/1974 (Böer, K.W. & Tamm, G., 2003).

Studies of a BIPV/T installation have been done using a thermographic camera (Bazilian, M.D. *et al.*, 2002). The study states that infrared cameras are useful tools for qualitatively evaluating BIPV/T installations in terms of temperature gradient and are efficient in

detecting air leakage in the system. The effect of the emissivity of the surfaces is also detected by the infrared camera. For the BIPV/T installation section, when there is no forced heat removal with air in the cavity, the temperature can be 10 °C higher than the surrounding metallic shingles used in the house.

The same research group developed a numerical model for performance evaluation of BIPV/T systems (Bazilian, M.D. & Prasad, D., 2002). It employed the Engineering Equation Solver from the University of Madison, ESS, to solve the equations of the model. See Figure 2.4 for a representation of the thermal network. The model was also used to evaluate yearly performance using TMY2 weather data files.

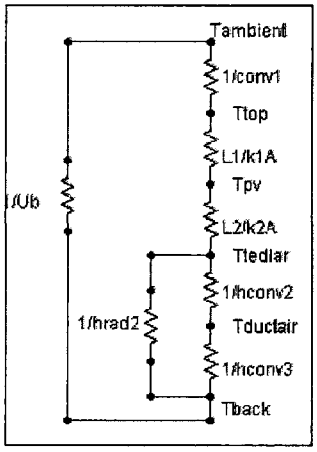

Figure 2.4. Thermal network representation of the BIPV/T simplified model by Bazilian and Prasad (2002).

Another numerical model for PV cooling was developed at Cardiff University (Brinkworth, B.J., 2002). The model focused on the thermal interaction by radiation and convection between the two smooth grey surfaces, where the back surface was assumed to be adiabatic. It was also mentioned that information about turbulence intensity was scarce for CFD input and validation.

A neural network approach was employed to determine the total heat transfer coefficient (Mei, L. *et al.*, 2002). Four main parameters were identified to represent the thermal behavior of the façade (Figure 2.5).

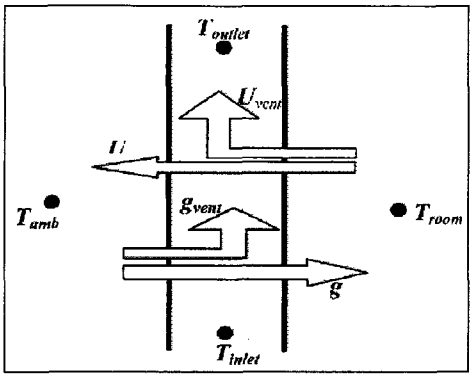

Figure 2.5. Façade heat transfer parameters after Mei et al. (2002).

A study presented by Tripanagnostopoulos et al. (2002) states that for PV building application in locations with low solar radiation and low exterior temperatures, such as Canada, where space heating is required for most of the year, PV cooling using air can be more useful and cost-effective than using a liquid system. The authors estimated that a liquid hybrid PV solar heater costs around 10% more than a simple PV installation compared with 5% more for a hybrid air-based system. The investigation also compares glazed and unglazed collectors. Reflectors are used to increase the incident radiation on the panel and its effect on the efficiency is studied. Figure 2.6 illustrates the efficiency increase by the use of reflectors.

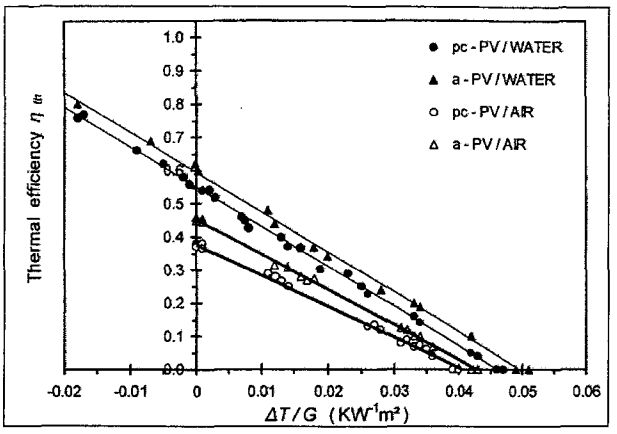

Figure 2.6. Thermal efficiencies for four types of hybrid PV/T systems. The filled symbols correspond to the PV/T collectors with reflectors (Tripanagnostopoulos, Y. et al., 2002).

A review on building-integrated PV products was done at the University of Southampton and different types of special PV tiles and popular frames were detailed (Bahaj, A.S., 2003). The paper lists requirements for the satisfaction of the users of BIPV systems. These include easy incorporation into any housing design, capacity to eliminate a portion of the roof to diminish costs, satisfaction of building regulations, installation by a traditional roofer, and finally ease of maintenance. For roof installations the systems generally are made of aluminum.

Investigation of a double skin façade with integrated photovoltaic panels was carried out in Montréal at Concordia University by Athienitis, A.K. *et al.* (2004). The report describes the outdoor experimental setup and the development of a numerical model. In one test, the PV modules were exposed to the exterior; in another, the module was mounted in the middle of the cavity. The test in which the PV was mounted in the middle of the cavity resulted in significantly higher thermal efficiencies.

A two-dimensional model using the control volume finite difference method was developed for a ventilated PV façade at Concordia University (Dehra, H., 2004). The results showed general good agreement with experimental measurements. For the PV module, the model over-predicted the temperature of the panel by 4°C. The model under-predicted the measured temperature of the air by 2 °C.

An experimental and numerical study of a hybrid PV façade was done in Italy at the joint Research Centre of the European Commission, in the Renewable Energies section at Ispra (Bloem, J.J., 2004). The model under-predicted the temperature of the exit air and over-predicted the temperature of the surfaces, which led to the conclusion that the convective heat exchange between the surfaces and the air was underestimated. A three-dimensional model of the test was created using FLUENT (FLUENT Inc., 2006), and it was concluded that the convective heat exchange is non-linear. According to the authors, the relative location of the inlet and outlet affect turbulence, which in turn increases the heat transfer coefficient. After the simulations in FLUENT, the new film coefficients were incorporated into the numerical model and helped to obtain more accurate results. However, there is no mention of the value of the heat transfer coefficients estimated with FLUENT.

Experimental studies suggest that wind has a strong impact on the performance of ventilated façades (Infield, D. *et al.*, 2004). The largest contribution of the wind to the air ventilation rate in the Mataro Library occurs when the wind is perpendicular to the façade.

The heat extracted from the ventilated PV façade in Mataro is used also to provide cooling to the building during the summer months (Mei, L. *et al.*, 2006). The system is also connected to a solar air collector to boost the temperature incoming from the ventilated PV façade. It is then connected to a desiccant wheel system in order to regenerate it (dry it) for

use in dehumidification of the intake air intended for cooling of the building (see Figure 2.7). When comparing the simulated values with those measured in the system, there was a disagreement in the incoming air from the BIPV/T system and solar air heaters of 7.8 °C. The incoming measured air was 61.7 °C versus 69.5 °C simulated.

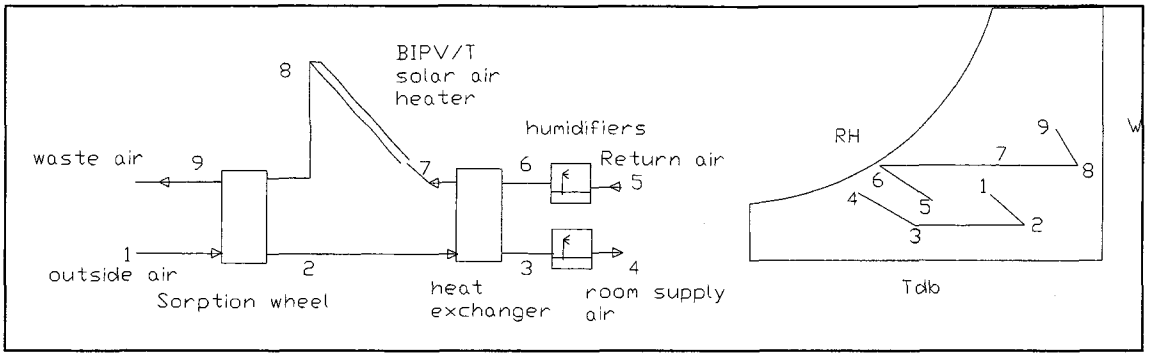

Figure 2.7. Schematic of the desiccant cooling system and process representation in a psychrometric chart. Adapted from (Mei, L. et al., 2006).

A theoretical study on the optimal channel depth was done theoretically assuming a constant heat flux (Brinkworth, B.J., 2006). In order to obtain a recommended value of channel depth, the criteria of minimization of the temperature rise on the PV side were employed. For such situations, the theoretical analysis gives a ratio of length of the channel to hydraulic diameter (L/D_h) of around 20 for ducts, and a ratio of 40 for very wide ducts. It is assumed that the heat fluxes across the boundary and the value of the convective heat transfer coefficient are constant.

A one-dimensional numerical model is employed to estimate the heat removal increase from PV panels using fins attached to them in a double façade set-up (Charron, R. & Athienitis, A.K., 2006a). The use of the fins is recommended for the case when the PV is placed in the middle of a cavity of a double façade. Figure 2.8 shows the set-up. In this case, the PV panel tends to have a higher temperature, thus lowering the electrical efficiency. However, the thermal efficiency is higher than when only the PV is exposed to the exterior.

An algorithm was embedded in the numerical model to choose which correlation for convection film coefficient to use, based on Reynolds and Grashof numbers.

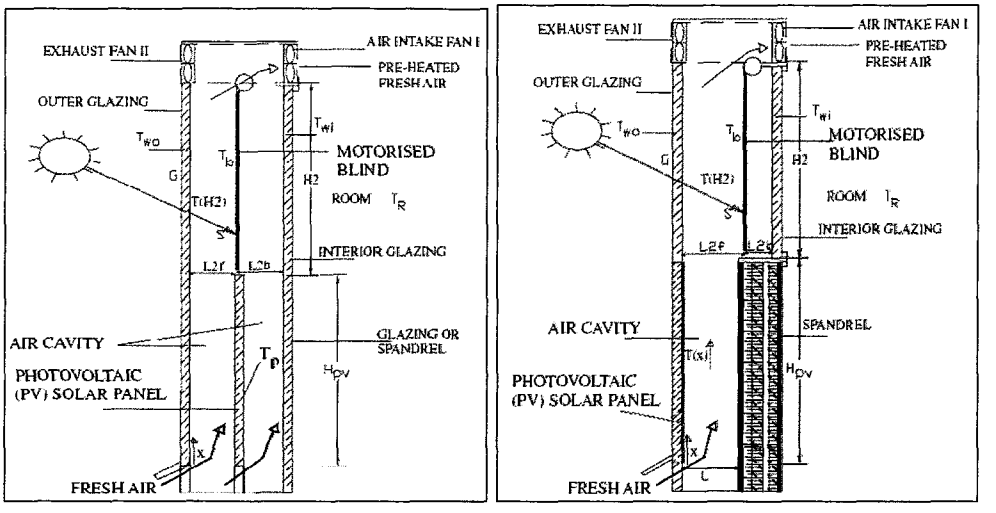

Figure 2.8. Configurations studied numerically and experimentally by Charron and Athienitis (2006a).

The 1D model developed by Charron and Athienitis was later improved using a 2D model that accounted for the PV temperature variation along the vertical direction of the set-up (Charron, R. & Athienitis, A.K., 2006b). The study concluded that discrepancies between the model and experimental results were caused by the lower values of convective heat transfer coefficients in correlations than the ones found experimentally and numerically.

A group of researchers from Australia and Ireland compared different configurations of a hybrid BIPV/T using a Life Cycle Energy Analysis (Crawford, R.H. *et al.*, 2006). The comparisons used, among other things, the concept of the embodied energy of the materials for the construction of the BIPV/T system. The system that yielded the shortest energy payback period, 4.3 years, was the one that used amorphous PV material. The study states that the location of the system will have an impact on the period of energy payback for the system.

Computational Fluid Dynamics and experimental work was carried out by researchers from Concordia University, Waterloo University and the CANMET Energy Technology Center (Liao, L. *et al.*, 2007). The work focused on the determination of convective heat transfer coefficients for a PV/T façade. The results were also reported using the Nusselt number correlation for the PV façade and for the insulation side. The model found a higher convective heat transfer coefficient for the insulation side compared to the PV side. The numerical model was two-dimensional and represented a simple smooth channel. However, the strength of the work resides in the use of actual measured data for the boundary conditions. The simulated channel had a length of 1 m, which has the limitation that the Nusselt number correlation may not be valid for other lengths. The convective heat transfer coefficient was evaluated at a reference temperature: taken as the inlet air temperature of the façade. However, in order to adhere to a more standard definition of heat transfer coefficient, the bulk temperature should have been used to determine the film coefficients.

Simulations were performed of the integration of a BIPV/T system for one of the participating houses for the CMHC EQuilibrium Housing competition, the Alstonvale Net Zero house (Candanedo, J.A. *et al.*, 2007). The simulations employed TMY2 weather data for the city of Montréal. For turbulent flow, the simulations employed the Gnielinski correlation to determine the convective heat transfer coefficient inside the BIPV/T system. In order to ensure high temperatures at the outlet even for low irradiation levels and high wind speed, a glazed section following the BIPV/T is included. The air duct system is later connected to a heat exchanger or to a heat pump. The final use of the air will depend on the exit temperature; if this air temperature is high enough, the air will be used to heat water in a thermal storage tank, otherwise it will be used as the source of a heat pump. It is recognized

by the author that the highest uncertainty in the simulation resides in the appropriate values for the convective heat transfer coefficient.

Experimental work was done on a hybrid PV/T collector in Greece in order to quantify the heat transfer enhancement achieved with the use of fins and a metallic sheet inserted in the middle of the air cavity (Tonui, J.K. & Tripanagnostopoulos, Y., 2007; Tonui, J.K. & Tripanagnostopoulos, Y., 2008). It is not mentioned how the airflow inside the channel was determined. The results however, do show that the efficiency is increased to 30% with the use of the fins compared to 25% efficiency for a simple design. Work in the same area was continued in another publication by one of the authors (Tripanagnostopoulos, Y., 2007) in which the heat impinging the PV/T surface was increased using reflectors. The study does not mention any value for the convective heat transfer coefficients.

Another experimental facility of BIPV/T in a vertical surface was tested in Italy (Bloem, J.J., 2008). The experiment stated that thermal efficiencies of up to 42% can be achieved for a simple case that consists of a smooth cavity. The study also includes computational fluid dynamics analysis and utilizes the thermal boundaries conditions. It is stated that the convective heat transfer coefficients are higher than expected because of the short length of the channel. However, the values of the film coefficients for each velocity are not quoted.

2.1.3 Transpired solar air collectors

A transpired solar air collector is another type of solar heat exchanger in which the absorber plate or cladding is perforated. Air is then taken in all around the structure. It is one of the most efficient systems but has the disadvantage of typically having not very high outlet air temperatures. It is usually preferred for make-up air for HVAC systems in commercial buildings.

Studies focusing on the airflow characteristics for perforated unglazed solar air collector were carried out in Waterloo (Gunnewiek, L.H. *et al.*, 1996). It has been recognized that this type of air heater is efficient because the convective heat loss to the air in front of the perforated plate is later recuperated when the thermal boundary layer is taken into the plenum. The study was a two-dimensional CFD model of the perforated solar air heater that employed a k-ε turbulence model. It also focused on the effects of buoyancy on the velocity profiles and performance of the collector.

A CFD study was carried out for the transpired solar air collector (Arulanandam, S.J. *et al.*, 1999). This work considered the exterior temperature conditions but assumed no wind conditions. The numerical study also only considered one perforated entry out of the multiple entries present; repeatability was assumed for the rest of the domain. Nusselt number correlations were reported.

Studies on exterior convective heat transfer coefficients for transpired solar air collectors were carried out at the National Renewable Energy Laboratory (NREL) (Gawlik, K. & Kutscher, C., 2002). The study was done using experimental data and numerical simulations. See Figure 2.9 for a schematic of the energy balance. FLUENT 4.25 was employed as the CFD software for such task. The study determined that the maximum heat loss ocurred at the crest points of the corrugated solar air collector. The difference between the numerical and the experimental results for heat transfer was less than 3%. It was determined that when the velocity of the air is high enough, there is a separation that increases the heat loss to the exterior. An alternative to reduce separation is to increase the suction velocity.

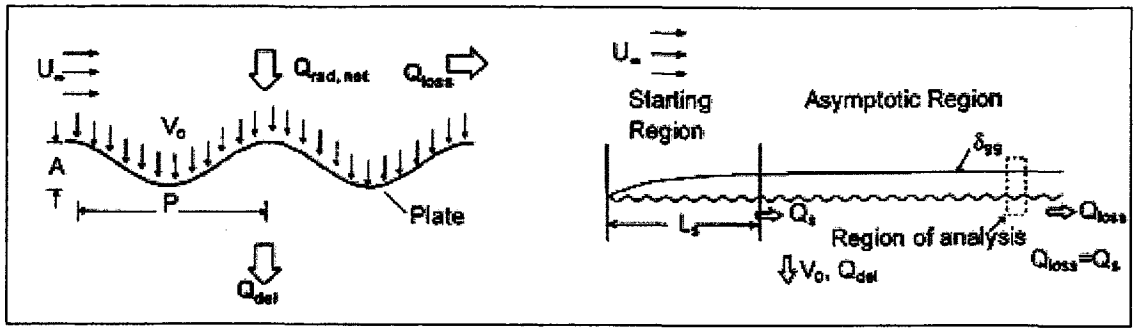

Figure 2.9. Left: Sketch of the heat fluxes for the corrugated plate. Right: Boundary layer development for the corrugated transpired solar air collector (Gawlik, K. & Kutscher, C., 2002).

An experimental study of a transpired collector was carried out at the National Renewable Energy Laboratory of the United States in a controlled test environment (Gawlik, K. *et al.*, 2005). The study focused on the impact of the thermal conductivity of the transpired solar collector materials on heat transfer. Transpired solar collectors made of aluminum, styrene and polyethylene were compared. Significant performance decreases were not found using a material having a lower thermal conductivity, although the maximum efficiency was found with aluminum solar collector. The results were corroborated by the researchers with CFD simulations. The study concluded stating that collectors can be made of flexible sheets which can be easily dismounted after their use. The results appear to be consistent since the effectiveness of a transpired solar collector depends on the intake of the thermal boundary layer forming directly in front of the collector.

The SolarWall product with a PV attached to it was tested at the CANMET's National Solar Test Facility and promising results were obtained regarding the cooling effect of the PV and electrical efficiency improvement (Hollick, J., 2005). Figure 2.10 illustrates the effect of the forced ventilation on the temperature of the PV modules. In the study the orientation

of the groove was vertical as shown in Figure 2.11. The importance of the portion of the PV covering the solar wall and its impact on overall efficiency were not studied.

Table 2-1 and Table 2-2 summarize the companies that produce hybrid PV/T products and the demonstration projects utilizing BIPV/T throughout the world.

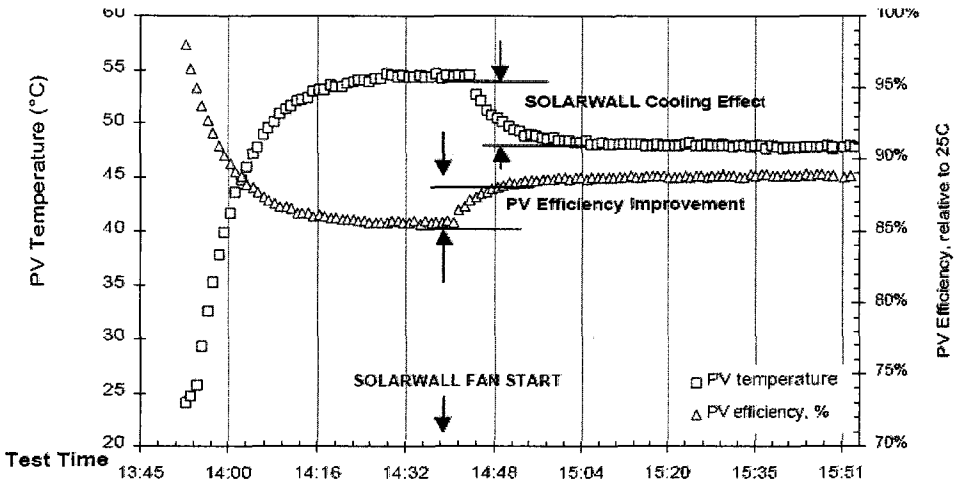

Figure 2.10. PV SolarWall results for 900 W/m^2 solar radiation, 1 m/s wind speed and a flow rate of 7 CFM/ft^2 (Hollick, J., 2005).

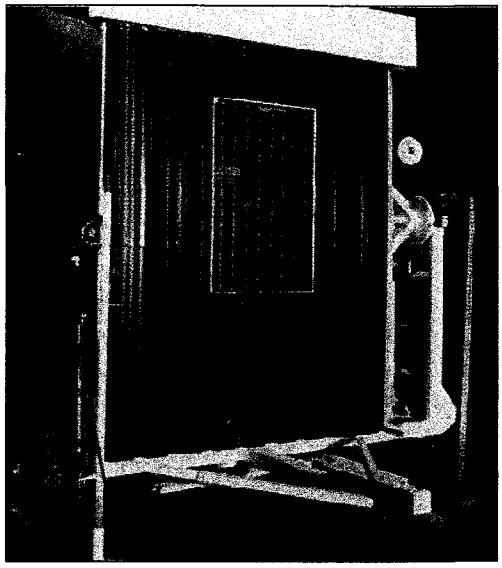

Figure 2.11. The test set-up at CANMET (Hollick, J., 2005).

Table 2-1. Companies producing hybrid PV/T systems.

Air-based PV/T systems		
Company	**Country**	**Products**
Conserval	Canada	SolarWall
Grammer Solar	Germany	TwinSolar
SolarVenti Ltd (formerly Aidt Miljø)	Denmark	Hybrid solar SV line
Secco Sistemi	Italy	Tetto Ibrido Solarizzato
Millenium Electric	Israel	Multi Solar PV/T/A System
PVT Solar	US	Echo™
Liquid-based PV/T systems		
Company	**Country**	**Products**
PVTWINS	The Netherlands	PV-T Collectors
Millenium Electric	Israel	Multi Solar PV/T/A System Energy MUST®
Power-Spar	Canada	Concentrated solar heat for electricity and hot water

Table 2-2. BIPV/T demonstration projects around the world.

Country	Project
Canada	Eco Terra home, Eastman, Québec (Aloutte homes/Concordia)
Canada	Alstonvale Net Zero House, Hudson, Quebec (SEVAG POGHARIAN DESIGN/Concordia
Canada	West Prep School in Toronto
USA	Louisville, Kentucky, PV/T solar House, SunWatt Corporation
USA	Applebee's restaurant (Innovative Design)
Italy	Ispra, ElSA Building, ventilated PV façade
Spain	Library of Mataro, ventilated PV façade
Switzerland	Aerni, Airsorf , ventilated PV façade
Denmark	The yellow House in Aalbor, ventilated PV façade
Denmark	Lundebjerg, Shouvlunde, Copenhagen
Netherlands	City Archives in Rotterdam, hybrid PV roof

2.2 Water-Based Solar Collectors and Liquid PV/T Systems

A solar collector can be considered as a special type of a flat-plate collector, which is a special kind of heat exchanger that transforms solar radiation into heat (Duffie, J.A. & Beckman, W.A., 2006). The typical configuration consists of an absorber plate with back-mounted pipes in which water or another liquid is circulated to remove the energy absorbed by the plate. These collectors can be covered with a layer of glass to minimize convective heat losses to the exterior due to wind and to radiation.

A liquid PV/T collector is basically a solar collector in which the absorber plate has been replaced with a PV module (see Figure 2.12).

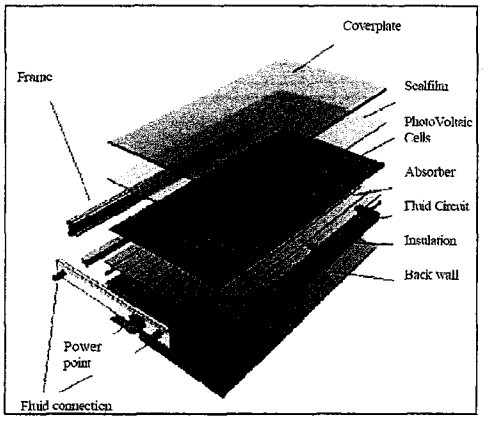

Figure 2.12. Typical closed loop liquid-cooled PV/T system (Bosanac, M. et al., 2003).

The first studies on the detailed performance of flat plate solar collectors go back to the 1940s at the Massachusetts Institute of Technology (Hottel, H.C. & Woertz, B., 1942). It must be noted that the fluid used in the study was water.

Literature on modelling and performance evaluation of PV-thermal water based systems is discussed by Zondag, H.A. (2008b). It must be noted that since these systems work in a closed loop where water or another liquid is circulated in pipes behind the PV, they suffer from the problem of higher stagnation temperatures. Zondag and van Helden (2002) reported stagnation temperatures of around 130°C for a glazed PV-T water collector in outdoor test conditions in the Netherlands. Other problems with liquid fluids are freezing or boiling of the fluid in the pipes that can render the system inoperable. It was also noted that problems with the encapsulation material of the solar cells, EVA, (ethylene vinyl acetate) can exist if the temperature exceeds 130 °C. The study also revealed that the time constant for this type of collector is larger due to its higher thermal mass. When there is water flowing in the pipes the time constant can be as low as 2 minutes; in the case of no flow conditions, the time constant is on the order of 30 minutes.

Numerical work on water-based hybrid PV/T collectors was carried out in the Netherlands (Zondag, H.A. *et al.*, 2002). The work compared one-dimensional, two-dimensional, and three-dimensional numerical models for transient and steady states. It was found that a one-dimensional steady state was sufficiently accurate for annual thermal energy output calculation. However, it is recognized that 2D and 3D models give more information regarding thermal distribution and relevant information needed to improve the collector design.

A publication from researchers at the University of Delaware and the University of Florida examines a water hybrid PV/T system connected to a heat pump with the objective of supplying enough domestic heat for the house (Böer, K.W. & Tamm, G., 2003). The publication also emphasizes that electrical and thermal efficiencies should not be simply added, since the effect of the different entropies of the energies involved must be included. The publication states that because of this, the electrical yield of the system has to be maximized.

2.3 Demonstration Projects

A survey on PV/T products was carried out by Esbensen, a consulting engineering company based in Denmark (Sorensen, H. & Munro, D., 2000). In the survey nine air-based systems were examined for roofs and six systems for façades; one of them being SolarWall, the commercial available product from Conserval Engineering from Canada. This was installed at the West Prep School at Toronto and consisted of 15 m^2 of solar wall and two PV modules of 60 W each. The heated air is used to improve indoor air quality in the classroom.

Another demonstration project was done in Ispra, Italy in the ELSA building. This building has a façade covered by an array of 505 m^2 of amorphous PV with a peak power rating of 21 kWp. The air is being heated as it flows from an existing gap between the PV and insulation, and is later used for ventilation purposes.

The Yellow House in Aalborg, Denmark, has five different groups of PV systems. In Switzerland, in 1991 a company called Atlantis Energy Systems, built a ventilated PV installation with an installed electrical capacity of 62 kW and a thermal output of 115 kW. In the Netherlands there is an installation at the City Archives in Rotterdam. In this installation there are 1840 m^2 of PV modules on the roof. During the summer months the heat recuperated is stored in the ground to provide heating in winter. Conversely, during the cold months, cold air is used to lower the ground's temperature in order to provide cooling during the summer.

The aforementioned EQuilibrium projects (EcoTerra and Alstonvale), as well as the façade are also relevant demonstration projects carried out in Canada.

A summary of institutions working on BIPV/T systems is presented in Table 2-3.

Table 2-3. Main BIPV/T research groups listed by country.

Country	Research group/University	Researchers
The Netherlands	Energy Research Center of the Netherlands (ECN), Eindhoven, Eindhoven University of Technology,	Zondag, De Vries, van Helden, van Zolingen, van Steenhoven
Greece	University of Patras (Physics department)	Tripanagnostopoulos
UK	Cardiff University, University of Wales, University of Strathclyde, London South Bank University, University of Northumbria, Centre for Renewable Energy Systems Technology, Loughborough University	Brinkworth, Clarke, Mei, Infield
Denmark	Esbensén Consulting Engineers	Bosanac, Miroslav, Sorensen
India	(Center for Energy Studies) Indian Institute of Technology, (Department of Mechanical Engineering) University of Roorkee	Jaurker, Tiwari
China	(Department of Thermal Science and Energy Engineering) University of Science and Technology of China, (Division of Building Science and Technology) City University of Hong Kong, The Hong Kong Polytechnic University	Yang, Wang,
Germany	Department of Building Physics, Hochschule fur Technik, Stuttgart, Germany	Eicker
USA	University of Florida, North Carolina State University, National Institute of Standard and Technology	Davis, Dougherty, Fanney, Boer, Gawlik
Canada	Conserval (SolarWall), Concordia University, Waterloo University	Hollick, Collins, Hollands, Athienitis
Australia	(Centre for Sustainable Energy Systems) Australian National University, (National Solar Architecture Research Unit, Faculty of the Built Environment), University of New South Wales, University of Melbourne	Bazilian, Prasad, A. Blakers
European Union	Institute for Environment and Sustainability, Research Centre, Institute for Environment and Sustainability, Italy	Bloem

3. Convective Heat Transfer Coefficients in a Building-Integrated Photovoltaic/Thermal System

3.1 Introduction

Accurate convective heat transfer coefficients (CHTCs) are essential for solving the energy balance equations used for lumped parameter thermal network modelling of Building Integrated Photovoltaic/Thermal systems (Figure 3.1). The CHTC's are necessary to quantify the thermal and electrical energy production of BIPV/T systems, which in turn provide adequate means for sizing associated equipment, such as heat exchangers and electrical inverters. The PV temperatures obtained by solving the energy balance equations for the PV modules are useful in designing the array layout in order to maximize the total energy production by connecting modules with similar temperatures in parallel as much as possible. The heat transfer coefficients are also important for the development of algorithms to control the airflow (Candanedo, J.A. & Athienitis, A.K., 2010) since the higher the airflow, the more is the heat recovered and the lower the PV temperature (with correspondingly higher electrical efficiency). However, in practice there is an optimum outlet air temperature determined by the planned utilization of the heated air and the fan energy consumption.

In this thesis, the BIPV/T system of interest incorporates a variable speed fan that controls air flow in order to produce an air outlet temperature that is suited for the specific desired application. The system's application may include preheating fresh air, acting as a source for a heat pump or as a heating application through a heat exchanger (e.g. air-to-water heat exchanger to heat water).

When modelling BIPV/T systems, researchers and designers have usually relied on heat transfer correlations developed for pipes and channels. This approach is not satisfactory due to the inherent complexity of BIPV/T channels, which include heating asymmetry, high aspect ratios, non-constant heat fluxes, non-uniform wall temperatures, non-developed flow conditions and non-uniform cross sections (due to structural framing).

The focus of this chapter is the determination of the internal convective heat transfer coefficients for a BIPV/T system with outdoor air as the cooling fluid. Two configurations were tested. The first is a smooth channel that has an aspect ratio (width-to-height) of 10. The channel studied in this work is smooth in order to obtain the lower limits of the actual heat transfer coefficients. The second configuration consists of a ribbed BIPV/T channel in order to simulate the installation utilized in the EcoTerra™ EQuilibrium demonstration solar house (Chen, Y. *et al.*, 2007b) designed by Concordia's Solar and Daylighting Laboratory.

Figure 3.1 presents a thermal network schematic of a typical BIPV/T system. For the particular BIPV/T design prototype studied in this paper, an amorphous PV module is attached with an adhesive that comes with the PV Module to a metal roof sheet. The amorphous PV module is formed from different layers. These layers are, from top to bottom: TEFZEL (an encapsulant material), antireflective coating, amorphous silicon, a backing substrate, TEFZEL, adhesive and a stainless steel layer which the adhesive was pasted. R_{Tefzel} and R_{mix} represent the thermal resistances of the PV module encapsulant (R_{Tefzel}), and of the backing substrate and the adhesive combined with the metal roof sheet where it is mounted. The convective heat transfer coefficients for the top and bottom surfaces are represented by h_{ct} and h_{cb} and are linked to the bulk air temperature (T_b) node respectively. T_{plate} and T_{ins} represent the temperatures of the plate and the insulation used to

compute the radiative and convective heat transfer coefficients. R_{ins} is the thermal resistance of the insulation.

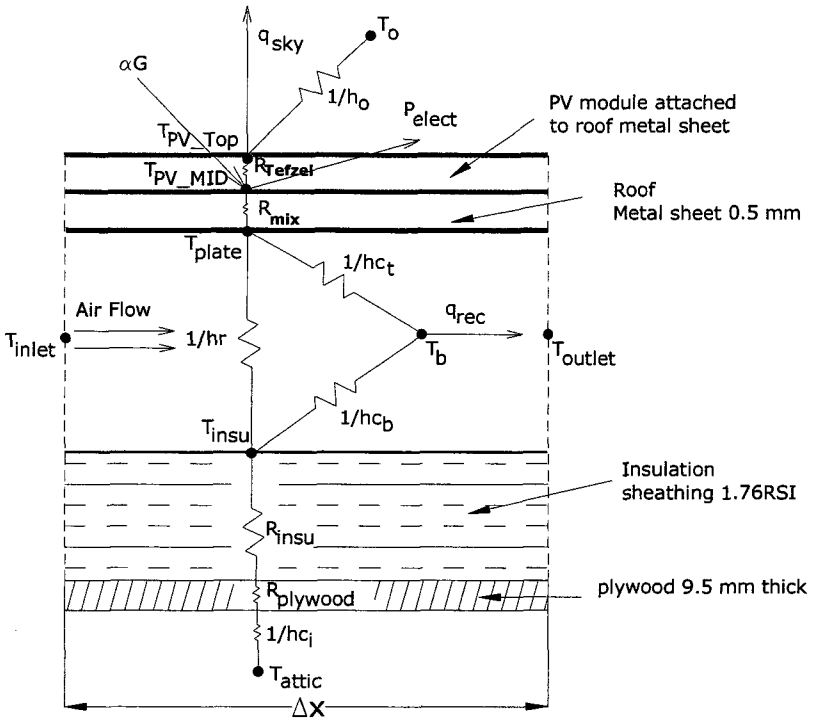

Figure 3.1. BIPV/T thermal network model showing the interior convective heat transfer coefficients h_{ct} and h_{cb} (Candanedo, L.M. et al., 2010) (the configuration shown corresponds to an experimental prototype studied in this thesis).

3.3 Convective Heat Transfer Coefficients

Several studies report that typical correlations used to evaluate the heat transfer coefficient underestimate their actual values (Eicker, U. *et al.*, 1999; Bazilian, M.D. & Prasad, D., 2002; Bloem, J.J., 2004; Charron, R. & Athienitis, A.K., 2006b). A brief discussion of available representative related literature for BIPV/T applications and solar air heaters in which air is drawn through the system with a fan is presented below. A discussion on mixed convection effects is also presented. Some of the main correlations from the literature are

summarized in Table 3-1. Work on pure natural convection heat transfer in open-ended rooftop and façade photovoltaic installations is not the focus of this work and is not reviewed. One may refer to the following publications for information on passive cooling of PV modules: (Brinkworth, B.J. *et al.*, 2000; Brinkworth, B.J. & Sandberg, M., 2005; Cipriano, J. *et al.*, 2008; Mittelman, G. *et al.*, 2009)

3.3.1 Correlations employed in BIPV/T models

Eicker *et al.* (1999) developed a model for a BIPV/T façade system and compared it to experimental data. It was reported that the model data could not fit the experimental results by using simple heat transfer correlations (e.g. parallel plate) to represent the heat transfer in the gap formed between the PV module and the colder room-side glass. The reported heat transfer coefficients for the hot PV side with an average air velocity of 0.3 m/s and a gap of 14 cm were between 4 to 5 W/m^2K. For the colder glass side, the convective heat coefficient was about 3 W/m^2K. The Reynolds and Nusselt numbers were not reported; using the information provided, the estimated Reynolds number is around 4800 and the estimated Nusselt number are between 42 to 52 for the hot PV side and 31 for the colder glass side. Bazilian *et al.* (2001) developed a numerical model for a photovoltaic heat recovery system. The model compared three different correlations: one for turbulent flow with uniform heat flux, another one developed for smooth solar air collectors by Malik and Buelow (1998), and the modified Petukhov equation or Gnielinski correlation (Kakac, S. *et al.*, 1987; Duffie, J.A. & Beckman, W.A., 2006). Bazilian and Prasad (2002) presented another numerical model for a ventilated PV-roof façade for the case of natural convection.

The authors point out that the model seemed to underestimate the outlet air temperature and overestimate the PV module temperature.

For solar air heaters, Eicker (2003) recommends the use of the Petukhov equation for turbulent flow (Re>3100) and the Tan and Charters equation for fully developed turbulent flow (1970) (Re>9500). For laminar flow, Eicker recommends Nusselt number correlations by Altfeld (1985) and by Shah and London (1978). For vertical ventilated photovoltaic façades Eicker states that the free convection regime must be taken into account even when the flow is fan-driven. Then, it is recommended that the Nusselt number should be calculated as a weighed value of the laminar and turbulent portions i.e. $\mathrm{Nu} = \sqrt{\mathrm{Nu_{lam}}^2 + \mathrm{Nu_{turb}}^2}$.

Bloem (2004) developed a numerical model for a PV façade in the simulation program TRNSYS and points out that the interior convective heat transfer coefficients were underestimated in the model when compared with measurements. There is no indication which Nusselt number correlation was employed for the validation.

Charron and Athienitis (2006b) used the Gnielinski correlation modified with the Hausen entrance factor (Gnielinski, V., 1983) to estimate the heat transfer in a BIPV/T double façade. The authors argued that the convective coefficient correlations possibly resulted in an underestimation of the actual heat transfer coefficients by up to 50%. Another important conclusion is that the recommended limits for the ratio of Gr/Re^2 have to be revised to determine if the flow is driven by natural, mixed, or forced convection. Chen *et al.* (2007a) modeled a BIPV/T roof system with a correlation for turbulent flow (Kreith, F. & Bohn, M.B., 2001). Candanedo *et al.* (2007) employed the Gnielinski correlation for turbulent flow

and another correlation for laminar developing heat transfer (Lienhard, J.H.I. & Lienhard, J.H.V., 2008).

3.3.2 Correlations employed in air hybrid photovoltaic/thermal (PV/T) collector models

Sopian *et al.* (1996) employed a Nusselt number correlation for fully developed turbulent flow (Duffie, J.A. & Beckman, W.A., 2006) for asymmetric heating to model a hybrid photovoltaic/thermal (PV/T – i.e. modular - not BIPV/T) heater. Garg and Adhikari (1997) employed the Tan and Charters correlation in their numerical model. Hegazy (2000a) used a Nusselt number correlation that contains an exponential correction to account for the diminishing convective heat transfer away from the entrance (Altfeld, K. *et al.*, 1988).

Ong, K.S. (1995b) employed different Nusselt number correlations depending on the fluid flow regime. He employed the Heaton correlation for laminar flow, the Hausen correlation for transitional flow, and the Tan and Charters and the Petukhov correlations for fully turbulent flow. The difference between predicted and experimental air temperature predictions was around 5 °C (Ong, K.S., 1995a; Ong, K.S., 1995b).

Ito *et al.* (2006) used the Mercer correlation for laminar convection (Duffie, J.A. & Beckman, W.A., 2006). For forced convection he employed a modified version of the Kays and Crawford correlation which considers the developing flow conditions (Duffie, J.A. & Beckman, W.A., 2006).

3.3.3 Context of the heat transfer correlations

The previously mentioned correlations are generally valid as long as the conditions for which they were developed are met. A brief description of how the correlations were obtained through experiments is presented below. It identifies under which conditions the correlations would represent the convective heat transfer in a BIPV/T cavity.

Dittus and Boelter (1930; 1985) developed their correlation for tubes by averaging the results of different researchers. Incropera and DeWitt (Incropera, F.P. & De Witt, D.P., 2002) recommend the use of the Dittus-Boelter correlation for Re>10,000 and length to D_h ratios (L/D_h) > 10. In contrast, McAdams (1954) recommends the Dittus-Boelter correlation but in a more restrictive manner for the range 10,000<Re<120,000 and for ratios of L/D_h of 60 or more. McAdams (1954) also recommends the equation for "moderate temperature differences" without giving detail on what can be considered moderate temperature differences.

A correlation that has not been used in BIPV/T systems nor in solar air collectors is the Martinelli equation (Martinelli, R.C., 1947). This equation is recommended in Kakac and Yener (1995) for turbulent flow in pipes and for parallel plates. The original paper contains typos in some of the equations. The corrected equations can be found in (McAdams, W.H., 1954) and a list of the assumptions is given. One of the main benefits of the Martinelli equation is that it can explain the heat transfer behavior for different Prandtl numbers. It considers the use of the bulk air temperature to determine the heat transfer coefficient and the friction factor.

Tan and Charters (1969) studied the effect of the entrance length using a duct with 103 diameters of heated length. The Reynolds numbers ranged from 9500 to 22000. In the

report, there is no indication that the channel was tilted. The work was further expanded to present a Nusselt number for developed flows (Tan, H.M. & Charters, W.W.S., 1970). The experimental data showed lower heat transfer rates compared to the Dittus-Boelter correlation. Results agree with those obtained by Sparrow for an asymmetrically heated channel (Sparrow, E.M. *et al.*, 1966). In Sparrow's investigation, the duct had two sections, an initial unheated section with a length of 40 D_h followed by the heated section with length equal to 140 D_h (in Sparrow's investigation the orientation of the duct was horizontal). A description of the setup can be found in (Novotny, J.L. *et al.*, 1964).

Cheng and Hong (Cheng, K.C. & Hong, S.W., 1972) performed a numerical study with inclined tubes at low Reynolds numbers ($5<Re<20$). For the tilted tube, strong buoyancy effects on heat transfer were found at Rayleigh numbers above 100.

Experimental results by Malik and Buelow (1973) were obtained using ducts of length 162 D_h. Although not explicitly stated, it appears that the duct was horizontal. Two ducts were analyzed, one with a flat cover and one with a corrugated cover.

3.3.4 Limitations of the correlations that have been used in BIPV/T modelling

Most of the correlations were developed for high Reynolds numbers (above 10,000), and employed long heated lengths to establish fully developed conditions. Also, most of the studies have been carried out in horizontal channels and pipes where buoyancy effects might not be as significant. Most of them investigated symmetrical heating while in a BIPV/T system it is asymmetric. In a typical roof BIPV/T system, such as the one in EcoTerra™

EQuilibrium demonstration solar house (Chen, Y. *et al.*, 2007b), the length of the system is about 5.8m. It has an L/D_h ratio of about 70 and is installed at a 30° tilt angle.

3.3.5 Mixed convection studies

The maps by Metais and Eckert (1964) for the regimes of free, forced and mixed convection for horizontal and vertical pipes can be employed to determine when mixed convection heat transfer must be taken into account. Previously, Metais (1963) developed a correlation to determine the Nusselt number at mixed regime for a horizontal tube. The equation was obtained using fluids with Prandtl number in the range $2.43<Pr<1200$. The correlation has a margin of error of 20%. The same equation is listed by (Metais, B. & Eckert, E.R.G., 1964) who state that the figures are useful for preliminary assessment and that they "...may have to be adjusted when more results become available." For this reason the figures should not be used as a final determination of the actual convection regime.

Petukhov (1976) presented equations to establish Grashof numbers for forced convection, for vertical, and for horizontal pipes when buoyancy effects will affect the heat transfer by about 1% relative to its value. When these limits are surpassed, the actual Nusselt numbers will be at least 1% higher than the values predicted by the forced convection correlation for circular pipes. The equations are functions of Reynolds and Prandtl numbers as follows:

For vertical pipes:

$$Gr_q = \frac{1.3 \cdot 10^{-4} Re^{2.75} Pr\left[Re^{1/8} + 2.4\left(Pr^{2/3} - 1\right)\right]}{\log(Re) + 1.15\log(5Pr + 1) + 0.5Pr - 1.8} \qquad 3.1$$

For horizontal pipes:

$$Gr_q = 3 \cdot 10^{-5} Re^{2.75} Pr^{0.5} \left[1 + 2.4\left(Pr^{2/3} - 1\right) Re^{-1/8}\right] \qquad 3.2$$

where,

$$Gr_q = \frac{g\beta q_w D^4}{\upsilon^2 k} \qquad 3.3$$

Gnielinski (1983) states that there are two main factors that influence the heat transfer coefficient for air, nitrogen, and helium: a) variable physical properties and b) natural convection. Variable physical properties for gases do not increase the heat transfer more than 10%. However, the effect of free convection may increase the heat transfer to three to four times the estimated heat transfer due to pure forced convection alone.

Jackson *et al.* (1958) studied combined free and forced convection in a vertical tube where the tube wall temperature was maintained constant. A Nusselt number correlation was developed. Brown and Gauvin (1965) studied combined free and forced convection in aided flow in a vertical pipe (aided or assisted flow occurs when air flows upward in a heated pipe and downward in a cooled pipe). Brown and Gauvin's results show a decrease in Nusselt numbers for assisted laminar flow compared to experimental data presented by Hallman (Hallman, T.M., 1961) and Brown (1960). However, for turbulent flow, the heat transfer was augmented compared to the equation presented by Hausen (1959) for assisted flow.

Mori *et al.* (1966) studied heat transfer in a horizontal pipe using air as the heat transfer fluid; the pipe was uniformly heated. Their results show that the experimental Nusselt numbers were higher than the value 48/11 which corresponds to Poiseuille flow. The constant value 48/11 (4.36) is for pipes with uniform surface heat flux and laminar fully

developed conditions and is independent of Re, Pr and axial location (Incropera, F.P. & De Witt, D.P., 2002).

McComas and Eckert (1966) carried out experiments in a horizontal circular tube with air as the fluid. The tested Reynolds number was in the laminar region (100 to 900) and the Grashof number ranged from 0.13 to 1000. It was found that for the Gr = 1000 and Re = 220 the experimental Nu was around 1.8 times the value of 4.36 (48/11) at x/D_h=45.

Axcell and Hall (1978) carried out experiments for downward flow of air in a vertical pipe for Reynolds numbers between 20,000 to 130,000. For a Reynolds number of 18,800, the measured Nusselt number was 164 - more than 2.7 times higher than the Nusselt number predicted with the Petukhov and Kirillov equation and 3.1 times higher than the Nusselt number given by the Dittus-Boelter correlation. Axcell and Hall (1978) also compared their experimental results against a correlation developed by Fewster and Jackson (1976) for turbulent buoyancy-assisted flows; their results were still 20 to 25% higher than what the corrected correlation was predicting.

A study on laminar mixed convection heat transfer for water flow through horizontal parallel plates with asymmetric heating was done by Osborne and Incropera (1985). As expected, it was found that the asymmetric heat flux caused higher Nusselt numbers at the bottom insulated surface than at the top surface.

Maughan and Incropera (1987) carried out numerical and experimental studies on mixed convection heat transfer for airflow in horizontal and inclined channels. The studied channel was heated from below and the Re was in the range of 125 to 500. The Nusselt number increased with the influence of higher Grashof numbers.

A comprehensive review of mixed convection in vertical tubes is presented by Jackson *et al.* (1989). They report that for laminar mixed convection regimes in assisted flow convection in vertical tubes, the heat transfer is almost always enhanced. However, for some values of $\overline{Gr_b}/Re^{2.7}$ in the turbulent flow mixed convection regime for pipes, the results show that there is a heat transfer drop. For the case of downward buoyancy opposed flow, the heat transfer is always enhanced. The same type of behavior is reported in a paper by Aicher and Martin (1997) on mixed turbulent convection in vertical tubes.

Sudo *et al.* (1990) carried out experiments in a vertical duct and explored the effect of aspect ratio on heat transfer. Results were reported based on dimensional parameters. When $Gr_x/Re_x^{21/8}Pr^{1/2}$ is between 10^{-4} and 10^{-2}, in both aiding and opposing flow, the heat transfer is on average higher than those predicted by correlations. Presented in their paper is the ratio of the measured Nusselt number to the Nusselt number predicted by the Dittus-Boelter. Correlations are also presented based on aiding and opposing flows. In Sudo *et al.*'s investigation, most of the time, heat transfer enhancement was found for buoyancy assisted and opposed flows.

Smyth and Salman (1991) carried out experiments on combined free and forced convection heat transfer in a rectangular duct for the laminar region. For Gr_q in the order 10^7, the Nusselt number was found to be in the range of 14 to 19.

Zhang and Dutta (1998) studied mixed buoyancy-assisted convection with asymmetric heating conditions in a vertical, square channel. The employed fluid was water. It was found that the Nusselt number was higher than predicted with the Gnielinski equation. The Nusselt numbers were also higher when compared to the Nusselt number ratio predicted by the Cotton and Jackson equation (1989). The authors presented a new formula in Dutta *et*

al. (1998) to correlate Gr/Re with the ratio of the actual Nusselt number to the Nusselt number predicted by the Dittus-Boelter correlation.

Busedra and Soliman (2000) studied laminar mixed convection in an inclined semicircular duct for both assisted and opposed conditions. The experiment was carried out for 3 Reynolds numbers (500, 1000 and 1500). The employed fluid was water. For the tilt angle inclination of 20° from the horizontal (this was the maximum angle tested), the fully developed Nusselt number was found to increase with $Gr_{q,r}$ number (based on heat flux and radius) and was less dependent on Re number.

Chong *et al.*(2008) studied the effect of the inclination angle for an inclined rectangular duct with a heated plate in the middle of the channel. The studied Reynolds numbers were in the range of 420 to 2630, while the Gr was in the range of 6.8×10^3 to 4.1×10^4. The tested angles were -90°, -60°,-30°, 0°, 30°, 60° and 90°. The negative sign is used to indicate opposed flow conditions. The authors report that the maximum heat transfer occurred at 30° tilt angle and that for Reynolds numbers above 1800, the influence of the tilt angle on the Nusselt number seemed to diminish.

3.3.6 Friction factor correlations

Many of the heat transfer correlations employed in the literature have been developed as a function of a friction factor. ASHRAE (2005) recommends the use of the friction factor equation developed by Churchill (1977). The advantage of the equation is that it is valid for all ranges of Reynolds numbers (laminar, transitional and turbulent).

The equation is:

$$f = 8\left[\left(\frac{8}{Re_{D_h}}\right)^{12} + \frac{1}{(A+B)^{1.5}}\right]^{1/12} \qquad 3.4$$

where

$$A = \left[2.457\ln\left(\frac{1}{\left(\frac{7}{Re_{D_h}}\right)^{0.9} + \left(0.27\frac{\varepsilon}{D_h}\right)}\right)\right]^{16} \qquad 3.5$$

$$B = \left[\frac{37530}{Re}\right]^{16} \qquad 3.6$$

Table 3-1. Nusselt number correlations for flow in a cavity or duct

Author / Reference	Correlation/ Comments		Flow & Heating conditions
Dittus-Boelter (1930; McAdams, W.H., 1954; 1985; Winterton, R.H.S., 1998)	$Nu = 0.023Re^{0.8}\mathrm{Pr}^{0.4}$	3.7	Average Nu for forced convection and symmetrical heating
	Recommended for fully developed turbulent (hydrodynamically and thermally) flow in smooth pipes for Re≥10,000 and L/D≥10 0.7<Pr<160 (Incropera, F.P. & De Witt, D.P., 2002) 10,000>Re>120,000 , L/D>60 and moderate ΔT(McAdams, W.H., 1954)		
Gnielinski correlation (Incropera, F.P. & De Witt, D.P., 2002)	$Nu = \frac{(Re-1000)Pr\frac{f}{8}}{1+12.7\sqrt{\frac{f}{8}}(Pr^{\frac{2}{3}}-1)}$	3.8	Average Nu for forced convection and symmetrical heating
	Smooth tubes, For 3000<Re<5×10⁶ 0.5<Pr<2000		
Modified Petukhov equation for short channel lengths and	$Nu = \frac{(Re-1000)Pr\frac{f}{8}}{1+12.7\sqrt{\frac{f}{8}}(Pr^{\frac{2}{3}}-1)}\left(1+\left(\frac{D_h}{L}\right)^{2/3}\right)$	3.9	Average Nu for forced convection and symmetrical heating

(Eicker, U., 2003) pipes	Where, $f = (0.79\ln(Re) - 1.64)^{-2}$ and Re≥3,000		
Tan and Charters (Eicker, U., 2003) for air (Pr ≈ 0.71)	$Nu = 0.0158Re^{0.8} + (0.00181Re + 2.92)e^{(-0.03795L_c/D_h)}$	3.10	Average *Nu* for forced convection and asymmetrical heating
	for a horizontal duct, Re>9500		
Martinelli (McAdams, W.H., 1954) Note: Original Nu correlation presented in (Martinelli, R.C., 1947) but had typographical errors and was corrected in (McAdams, W.H., 1954).	$Nu = \dfrac{Re \cdot Pr \cdot \sqrt{f/2}}{\left(\frac{t_w - t_b}{t_w - t_c}\right) \cdot 5 \cdot \left(Pr + ln(1 + 5Pr) + 0.5N_{DR}ln\left(\frac{Re}{60}\sqrt{\frac{f}{2}}\right)\right)}$	3.11	Average *Nu* for forced convection and symmetrical heating
	where T_w is the temperature of the wall, T_b the bulk air temperature, and T_c temperature at the center of the pipe. N_{DR} is a diffusivity ratio that depends on Re and Peclet number. N_{DR} is plotted against Re and Pr in (Martinelli, R.C., 1947), for air Pr=0.71 and 1000<Re<10000, 0.7<N_{DR}<0.98. t_w-t_b = Δtmean, t_w-t_c = Δtmax For air $(t_w-t_b)/(t_w-t_c)$ 0.78 to 0.84 for 2000<Re< 10000		
Malik and Bluelow (Bazilian, M. *et al.*, 2001)	$Nu = \dfrac{0.0192Re^{\frac{3}{4}}Pr}{1 + 1.22Re^{-\frac{1}{8}}(Pr - 2)}$	3.12	Average *Nu* for forced convection and asymmetrical heating
	Recommended for 10000<Re<40000 and L/D_h >162		
Mercer correlation (Duffie, J.A. & Beckman, W.A., 2006)	$Nu = 4.9 + \dfrac{0.0606\left(\frac{RePrD_h}{L}\right)^{1.2}}{1 + 0.0909\left(RePr\frac{D_h}{L}\right)^{0.7}Pr^{0.17}}$	3.13	Average *Nu* for forced laminar convection and asymmetric heating
	Laminar flow Re<2300		

3.4 Experimental Setup

The experimental setup used in this research consists of a near full-scale BIPV/T system and a similar system without PV panels (just metal roof) connected to an outdoor test facility fully instrumented for air collector testing. The BIPV/T system is a small scale version of the roof BIPV/T system in the EcoTerra™ EQuilibrium demonstration near net-zero energy solar house (see Figure 3.2) (Chen, Y. *et al.*, 2007b).

Clear days with low wind conditions were selected for the experiments so as to reduce the variability due to wind effects and passing clouds.

Figure 3.2. Photograph of the BIPV/T roof in the EcoTerra™ House. The amorphous PV modules are attached to a metal roof skin on vertical and horizontal wood framing that also creates the flow channel. (The roof has a length of 5.8 m in the flow direction shown by the arrows).

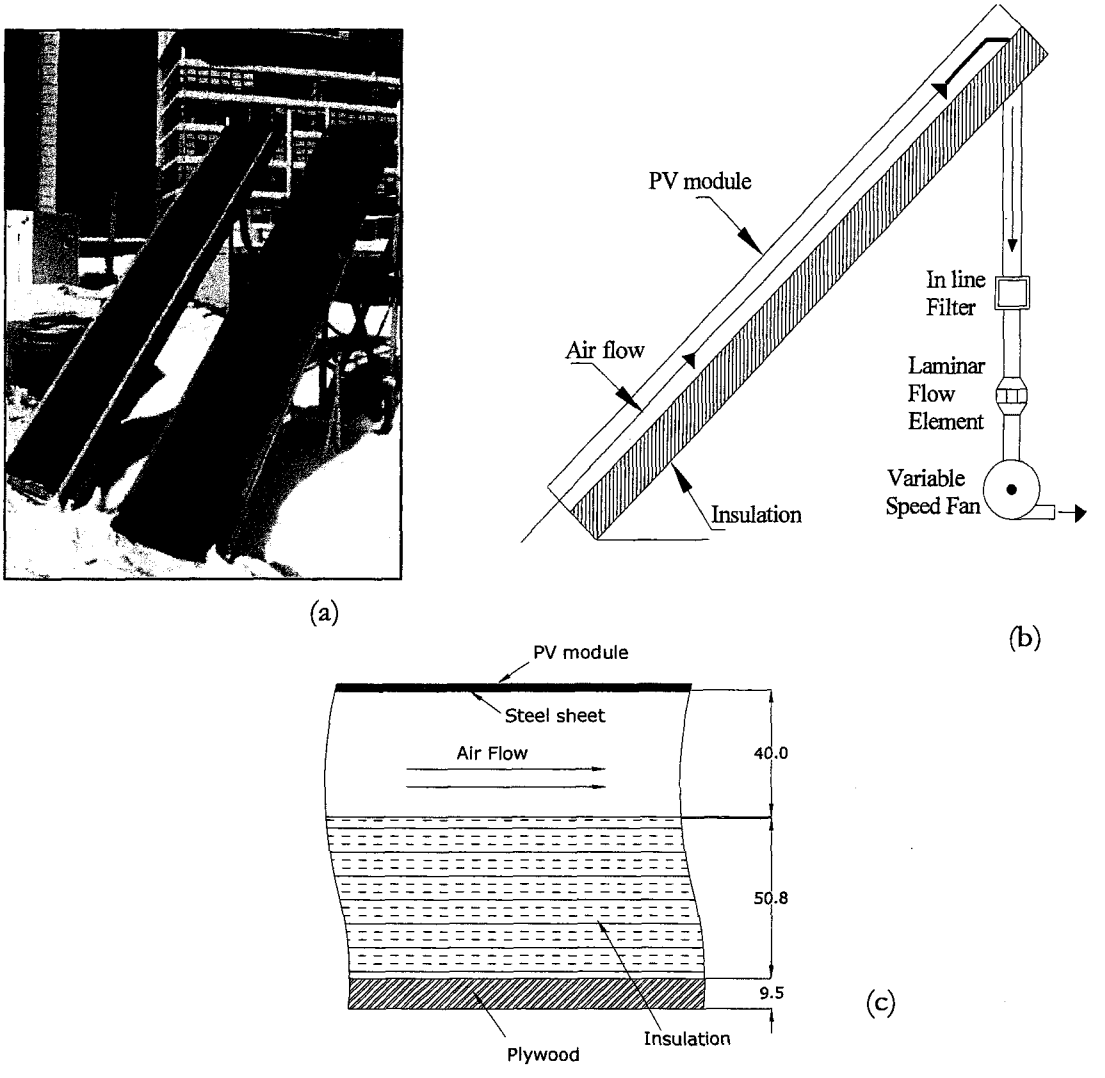

Figure 3.3. (a) Experimental BIPV/T setup replicating 1 strip of the BIPV/T system of the EcoTerra house with and without amorphous PV modules attached; (b) schematic of the setup; (c) cross section details of BIPV/T.

The solar air collector, (without the PV module) was employed to determine how heat generation is affected by attaching PV panels (Candanedo, L.M. *et al.*, 2010).

The BIPV/T system included an amorphous PV module with an electrical efficiency of 6.1% at standard test conditions. This module was attached by built-in adhesive to a steel metal roof sheet with a thickness of 0.5 mm. The cross-sectional area of the channel, A_c was 0.01549 m^2. The hydraulic diameter D_h is given by $4A_c/U$, where U is the wetted perimeter (D_h= 0.073 m). The length of the channel was 2.84 m. The thermocouples were special limit T-type with a 0.3°C maximum error. The tilt angle employed in the majority of the experiments was 45°, followed by several tests at a tilt angle of 30° to determine whether natural convection had any significant effects in this slope range. The channel considered was smooth with no framing. The bottom of the channel consisted of 2 inches of polysterene insulation (1.76 Km^2/W, R-10) and 9.5 mm (3/8 in) thick plywood board (see Figure 3.3).

Since the major thermal gradients exist along the direction of the flow, 40 thermocouples were placed along the middle of the channel from the inlet to the outlet. Infrared photos of the metal channel showed insignificant thermal variation along its width. The same type of behavior was reported by Ong (1995a). The following temperatures were measured: average inlet and outlet air temperature, the temperature of the interior side of the metal plate and the surface temperature of the insulation.

The data was recorded at 1 minute intervals through a data acquisition system. The PV module was connected to a charge controller with a maximum power point tracker. The wind speed and ambient air temperature were recorded by a weather station. The anemometer was a 3-cup type. The wind speed and the ambient air temperature sensors were placed about 10 m above ground.

The total convective heat transfer to the air for each of the control volumes in the BIPV/T cavity was calculated as follows:

$$Qin_{cv} = \dot{m}c_p(T_{outlet} - T_{inlet}) \qquad 3.14$$

T_{outlet} is the average temperature of the air at the outlet and T_{inlet} is the average air temperature at the inlet, which may be higher than T_o due to local heating from the ground. The specific heat c_p is given by the equation:

$$c_p = c_{pa} + W \cdot c_{pv} \qquad 3.15$$

where W is the air moisture content, c_{pa} is the specific heat of dry air and has the value of 1.0 kJ/(kga-K) and c_{pv} is the specific heat of water vapor and has the value of 1.86 kJ/(kgv-K). The moisture content of the air has been calculated using the relative humidity (RH) and the dry bulb temperature. The saturation pressure has been calculated based on correlations provided by ASHRAE (2005). The mass flow rate was measured with a laminar flow element (LFE). The LFE comes with a calibration curve in order to determine the actual volumetric flow rate. This curve gives the flow rate as a function of the pressure drop across the LFE.

It was found that taking 40 measurements per minute gave a reading that was sufficiently representative for the flow rate calculations. The LFE was calibrated by the manufacturer for a range of 0 to 0.05 m^3/s (0 to 105 CFM). The pressure drop at the maximum flow rate was about 2000 Pa (8 in of water). For this LFE, the largest error was 0.25 CFM compared to its calibration standard. The fan can provide a flow rate of up to 0.023 m^3/s (47.5 CFM) with a maximum average velocity of 1.45 m/s through the channel. The pressure transducer used for the LFE can measure pressures from 0 to 2500 Pa (10 inches of water) with 0.25% full scale accuracy.

Because of relatively high longitudinal thermal gradients for the metal plate and the insulation along the direction of the flow, the channel was divided into six control volumes. The radiation exchange for a control volume between the interior surface of the metal plate and the insulation surface is given by

$$Qrad_{cv} = \frac{F_{plate,insu} \cdot A_{cv} \cdot \sigma \cdot \left(\overline{T^4{}_{plate}} - \overline{T^4{}_{insu}}\right)}{\frac{1}{\varepsilon_1} + \frac{1}{\varepsilon_2} - 1} \qquad 3.16$$

where ε_1 and ε_2 are the longwave emissivities of the surfaces. The emissivities were measured using a calibrated hemispherical emissometer. The measured emissivity of the steel plate was 0.80 while the corresponding value for the insulation board was 0.20. $F_{plate,insu}$ is the view factor between the two cavity surfaces (Incropera, F.P. & De Witt, D.P., 2002).

3.4.1 Transient response

For approximately constant solar radiation and exterior wind speed, the BIPV/T system usually reached steady state after 8-9 minutes, as shown in Figure 3.4.

With numerical analysis, Kakac (1968) studied the effect of step changes in the boundaries of a channel; the transient response for Re≈9370 needed approximately 0.07 seconds to reach steady state for the studied configuration. This analysis however does not consider the thermal capacitance and resistance of the materials.

A practical way of analyzing the time response of the system is to consider it as a simple RC thermal circuit. The time required to reach 63% of steady state change is the product RC (time constant), where R is the thermal resistance and C the total thermal capacitance. After

five time constants, steady state is approximately attained. The combined thermal capacitance of the module and the metal roofing steel sheet is 7838 J/m^2K; their combined thermal resistance is $0.011 m^2K/W$. The time constant, (RC), is 86.2 seconds. The approximate time to reach steady state (about five time constants) is 7.2 minutes. This value is significantly close to the measured value stated above (8-9 minutes).

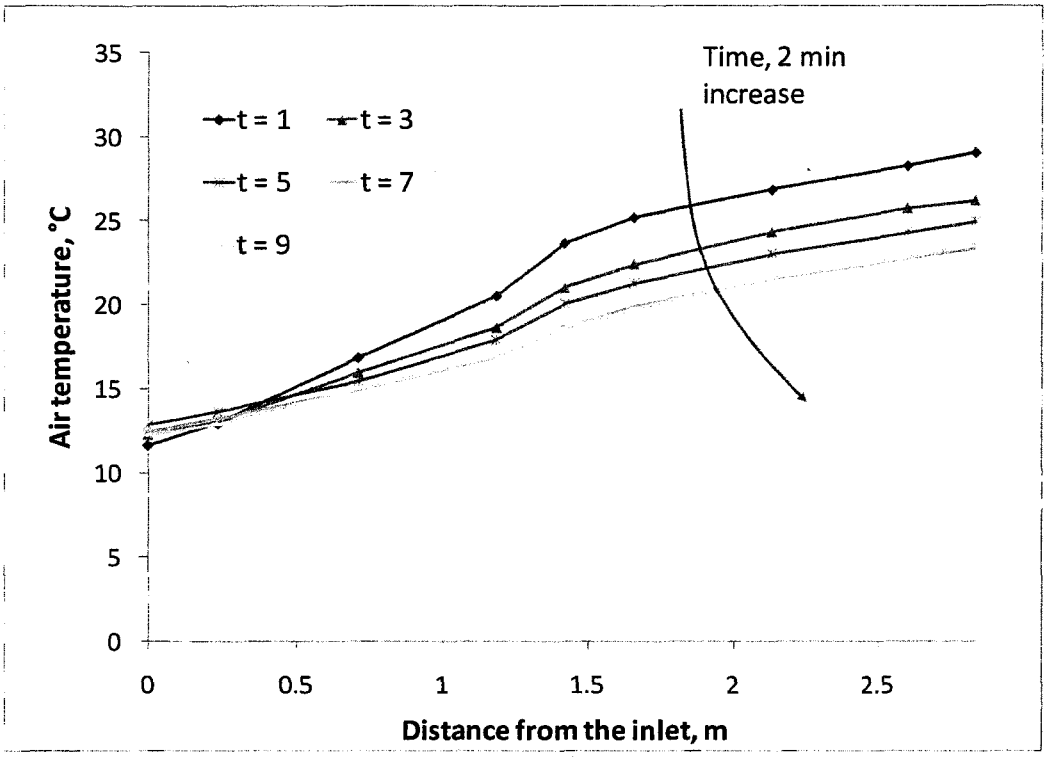

Figure 3.4. Transient response of the bulk air temperature for constant volumetric flow rate $0.021 m^3/s$ and incident total solar radiation 815 W/m^2 (the arrow shows increasing time).

The bulk air temperature rise in the channel follows an exponential trend. Using Mathcad (Parametric Technology Corporation, 2007), an exponential correlation was fitted to the experimental data, which was based on an optimized version of the Levenberg-Marquardt. The equation has the following form

$$T_b(x) = A\left(1 - e^{-\frac{x}{B}}\right) + C \qquad 3.17$$

where A, B, and C are fitted parameters. The correlation coefficients (R^2) of the regressions shown in Figure 3.5 are high ($R^2 \approx 0.99$).

It was noted that the temperature increase had a distinctive bent around x/D_h =19. This can be due to the fact that less thermocouples were employed to determine the air temperature before and after the middle section (x/D_h=16 and x/D_h = 22). It is expected, however, that the exponential fitting of the curve would lower the uncertainty in the determination of the bulk air temperature.

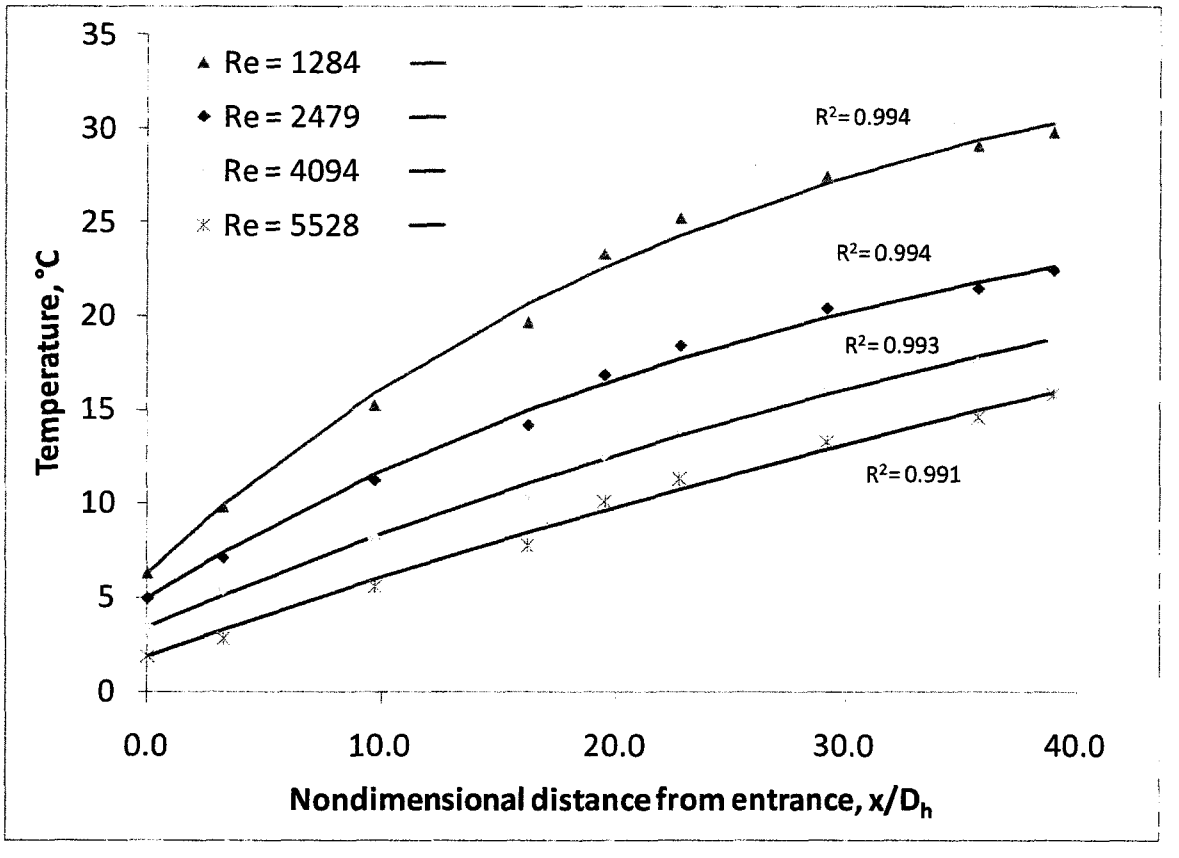

Figure 3.5. Bulk air temperature for different Reynolds numbers compared with exponential correlation fits (points show experimental measurements and solid lines the exponential fit).

3.4.2 Computation of convective heat transfer coefficients

Average internal instantaneous CHTC values were obtained by using the local control volume averaged temperatures of the plate and the insulation (T_{plate} and T_{insu}) each minute. Since the air temperature distribution is known from the corresponding exponential fit for each of the tested flow rates, local coefficients can be calculated for each control volume. The convective heat transfer coefficient for the corresponding control volume for the top plate was computed as

$$hc_{t,cv} = \frac{Qin_{cv} - Qrad_{cv}}{A_{cv}\left(\overline{T_{plate_{cv}}} - \overline{T}_{b_{cv}}\right)} \qquad 3.18$$

where Q_{incv} was determined with equation (20) and Qr_{adcv} was computed with equation (3.16).

For the bottom surface,

$$hc_{b,cv} = \frac{Qrad_{cv}}{A_{cv}\left(\overline{T}_{insu,cv} - \left(\overline{T}_{b,cv}\right)\right)} \qquad 3.19$$

In this analysis, the bottom heat loss can be considered negligible due to the comparatively high thermal resistance value of the insulation. This approach of employing two heat transfer coefficient is not new. Two Nusselt numbers -one for each of the control boundaries- have been used for parallel plates and channels by (Hatton, A.P. & Quarmby, A., 1963; Sparrow, E.M. *et al.*, 1966; Osborne, D.G. & Incropera, F.P., 1985) and for asymmetric heating in concentric circular tubes (Kays, W. *et al.*, 2005).

The average Nusselt numbers are, in turn, given by

$$Nu_{top} = \frac{\overline{hc_t} D_h}{k_{air}} \qquad 3.20$$

for the top channel surface and by

$$Nu_{bot} = \frac{\overline{hc_b} D_h}{k_{air}} \qquad 3.21$$

for the bottom surface.

3.5 Results and Discussion

3.5.1 Local effects

The local Nusselt numbers are plotted in Figure 3.6. As can be seen, when the flow is turbulent, it reaches fully developed conditions in shorter lengths. The behavior is opposite for the laminar flow conditions. It is important to determine when the fully developed heat transfer condition is reached in order to decide whether a local or an average heat transfer coefficients is appropriate.

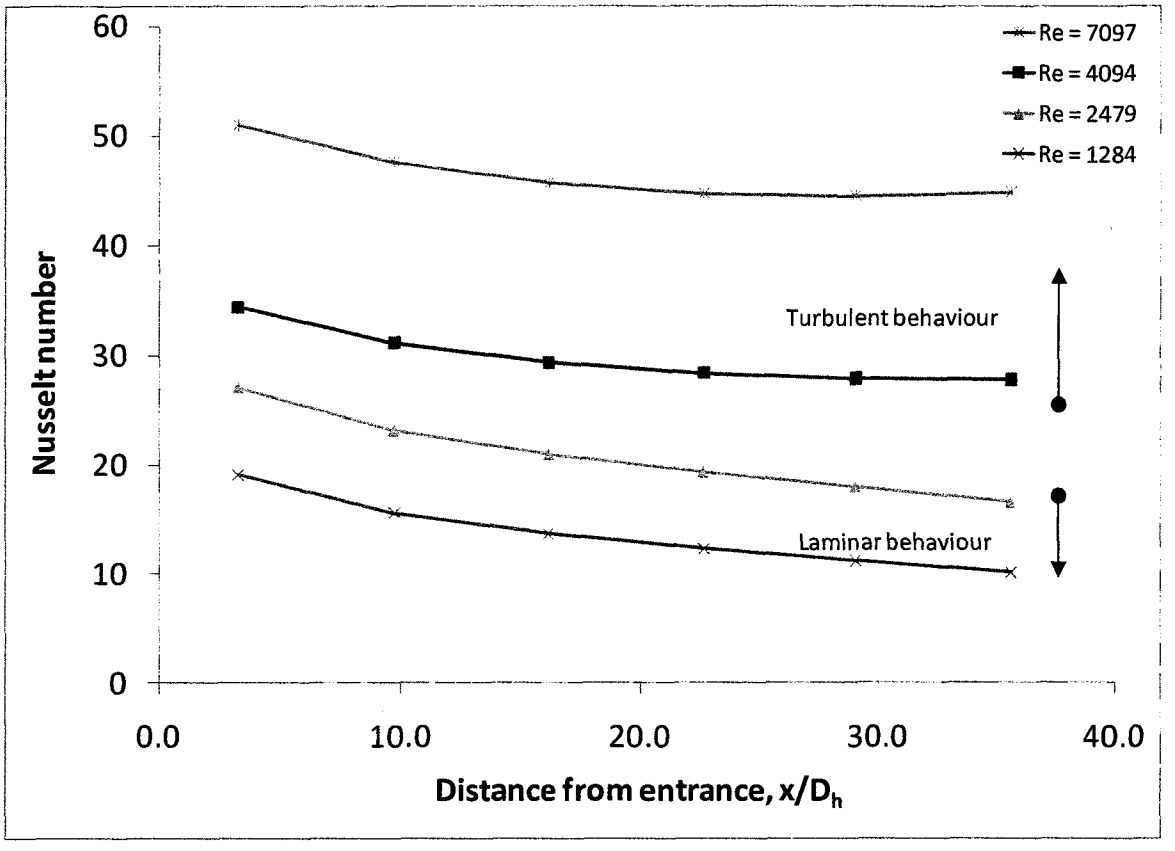

Figure 3.6. Local Nusselt number for the top surface versus non-dimensional distance from the entrance.

Many researchers have studied Nusselt number development length solutions for laminar and turbulent flow. To obtain the fully developed solution for the laminar flow (Re≤2300) Kays (Kays, W. *et al.*, 2005) recommends using the entry length solution for the circular tube relationship

$$\frac{x}{D_h} \approx 0.05RePr \qquad 3.22$$

while Hallman (Hallman, T.M., 1961) employs the relationship

$$\frac{x}{D_h} > 0.0425RePr \qquad 3.23$$

For the turbulent region, White (White, F.M., 2003) states that the development length is shorter and that it can be estimated with

$$\frac{x}{D_h} \approx 4.4Re^{1/6} \qquad 3.24$$

The experimental results agree with the previous correlations to determine the development length. For instance, based on equation 3.23 at Re ≈ 1284, the developed flow conditions are reached when $x/D_h \geq 38.7$. Comparing this result to Figure 3.6 where for $x/D_h = 29$ to $x/D_h = 36$ the change in Nusselt number is about 9.6%, indicating that the flow is clearly not being fully developed yet. However, in the turbulent region, for Re ≈ 4094 the developed flow conditions are reached when $x/D_h \geq 17.6$ based on equation 3.24. The experimental data suggest that for an increase of x/D_h from 16.2 to x/D_h=22.6, the Nusselt number decrease is only 3%.

3.5.2 Average Nusselt numbers

In Figure 3.7 and Figure 3.8, the average Nusselt number coefficients for the top and the bottom surfaces were calculated from the local distributions and graphed as a function of the Reynolds number. Since this is an outdoor experiment with an uncontrolled inlet air temperature, Nusselt number data for other Rayleigh numbers cannot be studied directly. Because of that, a correlation for the average Nusselt number as a function of the Reynolds number has been obtained. As shown later, this is an acceptable approximation for air-based open loop BIPV/T systems It was found by means of an optimized version of the Levenberg-Marquardt method for minimization (Parametric Technology Corporation, 2007).

The following correlations provide acceptable estimates of Nu at the top and bottom BIPV/T channel surface.

For the top surface, for $250 \leq Re \leq 7500$,

$$Nu_{top} = 0.052Re^{0.78}Pr^{0.4} \tag{3.25}$$

and for the bottom surface, for $800 \leq Re \leq 7100$,

$$Nu_{bottom} = 1.017Re^{0.471}Pr^{0.4} \tag{3.26}$$

The correlations, along with the uncertainty in the data, are plotted in Figure 3.7 and Figure 3.8. Appendix B summarizes how the uncertainties were calculated. As can be seen, the Nusselt numbers for the bottom surface are higher than the ones for the top surface. Sparrow *et al.* (1966) found the same behavior in the experiments where the heated wall had a lower Nusselt number than the unheated one. In the present case, because the bottom surface is insulated, the heat gain by longwave radiation from the top heated surface is approximately equal to the heat transfer to the air by convection, thus resulting in a small temperature difference between the bottom surface and the air.

The uncertainties in the Nusselt numbers for the top surface are very small. In general, they range between 4.8% to a maximum of 7% for $1760<Re<7500$. The highest uncertainties occur at the lowest Reynolds numbers. For example, the uncertainty is 66% at Re = 256 and 13% for Re = 802. The same behavior has been reported by Novotny *et al.* (1964). The uncertainties for the Re numbers are between 3.3 to 8% for $1100<Re<7500$. At low flow rates the uncertainties are higher, e.g. for Re = 250 the uncertainty is 31% and for Re = 800 it is 10%.

The experimental results show significantly more uncertainty regarding the heat transfer coefficients of the bottom surface; however, their effect on outlet air temperature calculation is far less important than that of the heat transfer coefficients of the heated top surface. The high uncertainties are due to the fact that the air bulk temperature and the surface temperature are very close -small error in the temperature measurement can cause high errors in the heat transfer coefficient-. Barrow (Barrow, H., 1962) obtained similar scattered results in the data because of high uncertainty in the Nusselt number.

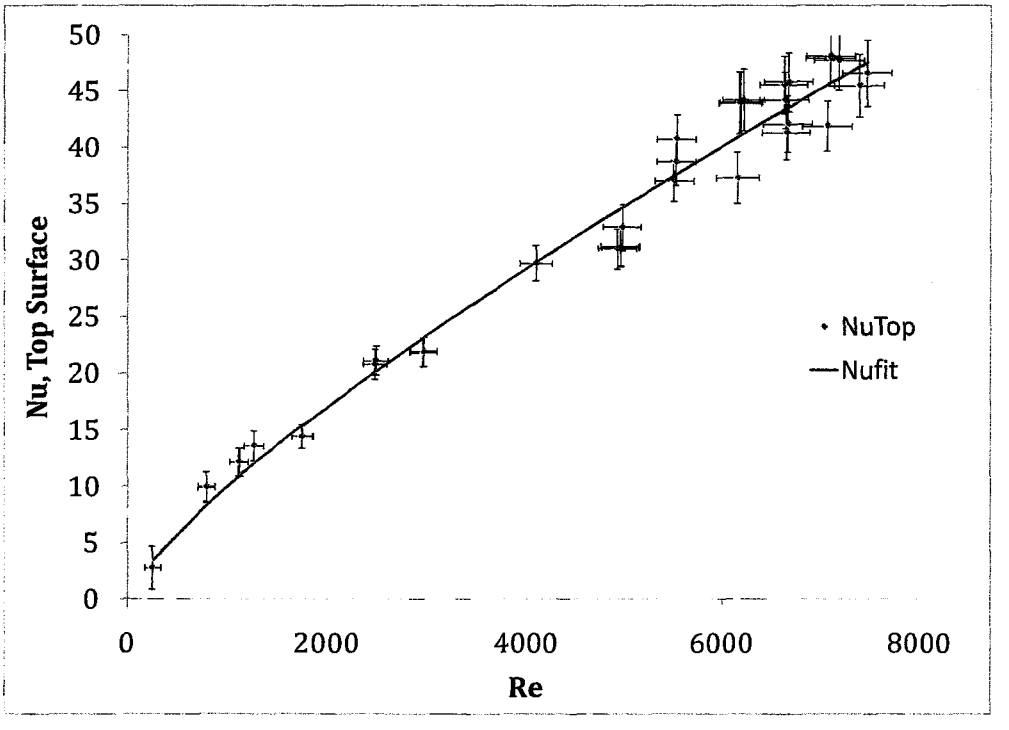

Figure 3.7. Nusselt numbers for the top surface versus Reynolds number. The data is compared with the correlation given by equation 3.25. The uncertainties of each of the data points are shown by the vertical line segments.

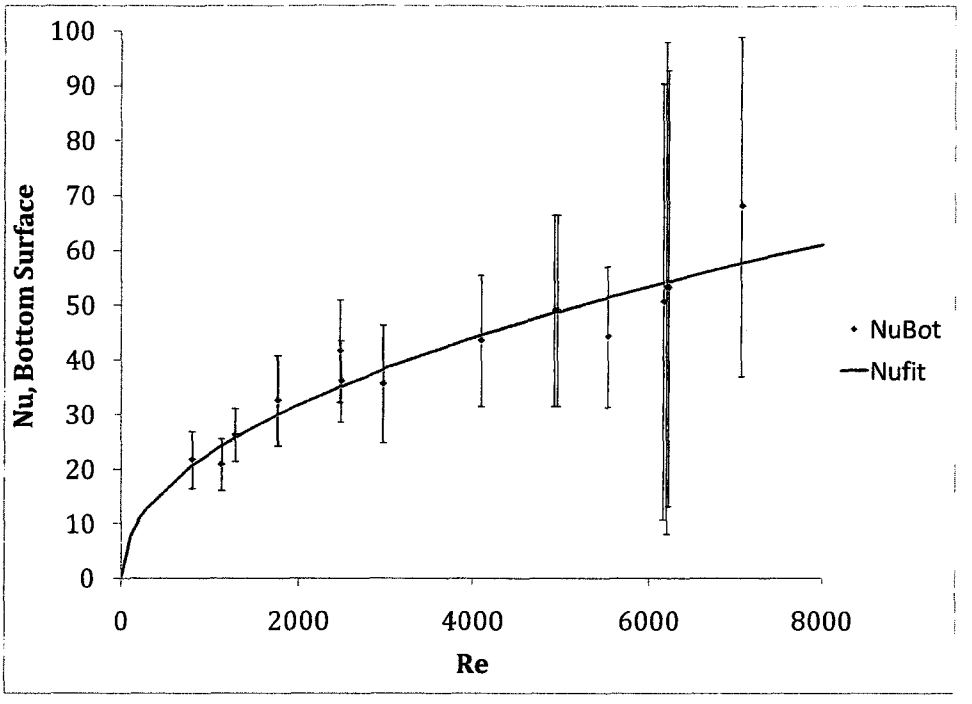

Figure 3.8. Nusselt numbers for the bottom surface versus Reynolds number. The data is compared with the correlation equation 3.26. The uncertainties of each of the data points are shown by the vertical bars.

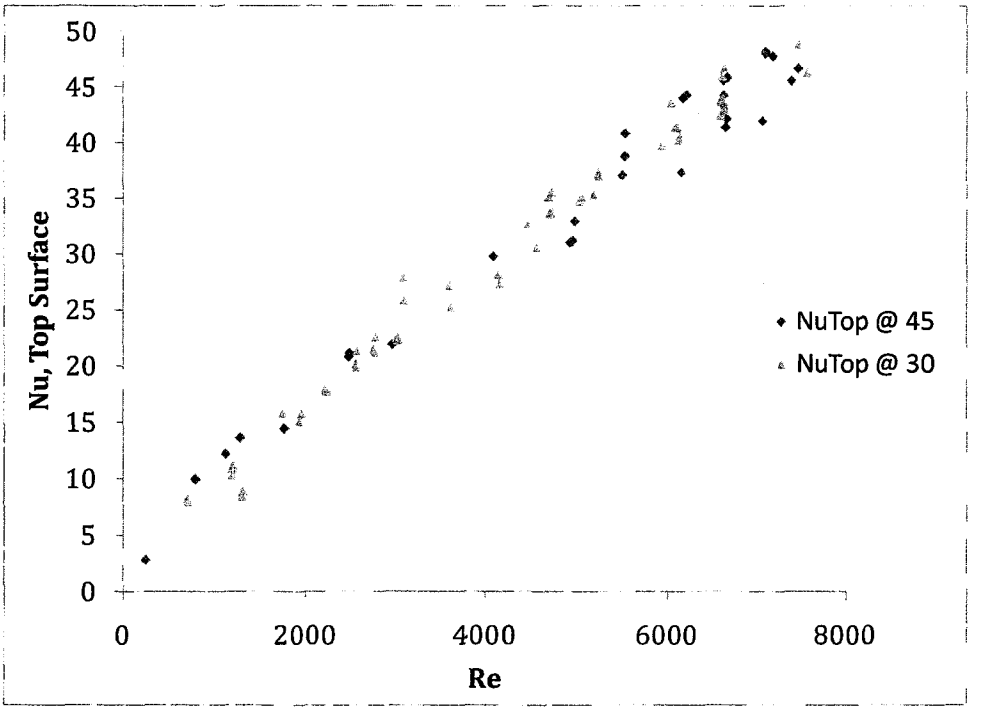

Figure 3.9. Nusselt numbers for the top surface versus Reynolds number comparison for 45° and 30° tilt angles.

The experiment was performed for tilt angles of 30° and 45° since this range represents most Canadian sloped roof housing (see Figure 3.9). The results show no significant difference between the Nusselt numbers for the two tilt angles that were studied, except for low Reynolds numbers (up to about 1600) where stronger buoyancy effects (due to the steeper angle) were evident. Nevertheless, for the correlations developed, this effect was not considered significant enough to be represented for modelling and design purposes, because the flow rates corresponding to Re < 1600 are too low for most practical applications (resulting in low thermal efficiency).

3.5.3 Comparison of the new correlation with previous results

The Nusselt numbers for the top surface (eq. 3.25) are compared with a few of the most typical correlations in Figure 3.10. The Martinelli and Gnielinski correlations were evaluated with the friction coefficient proposed by Churchill (1977).

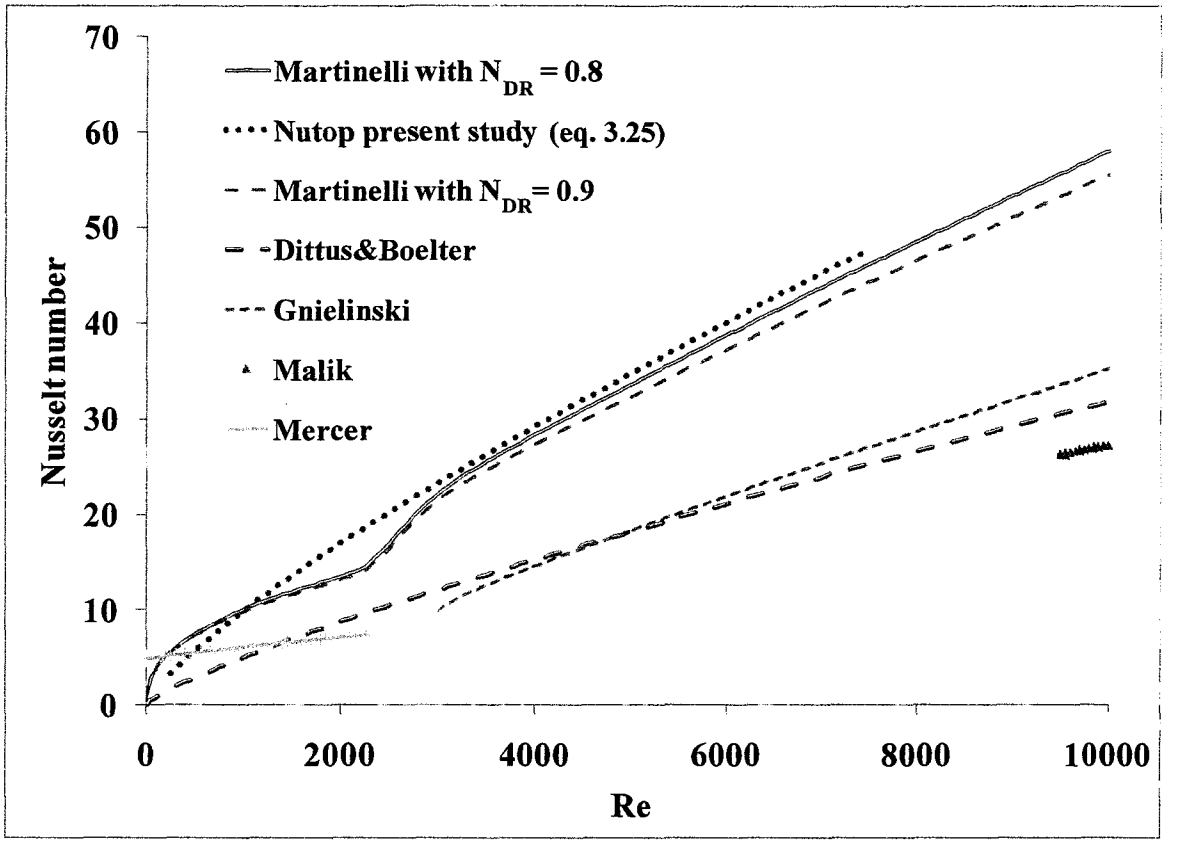

Figure 3.10. Comparison of the top channel surface Nusselt number correlation (eq. 3.25) with Dittus-Boelter, Gnielinski, Martinelli, Malik and Mercer correlations.

Although the Dittus-Boelter correlation is recommended for Re> 10,000, it has been plotted to indicate the possible low limit of the heat transfer. As can be seen from Figure 3.10, the Dittus-Boelter and Gnielinski correlations predict very similar values. Martinelli's correlation includes a correction for the ratio of temperature difference of the wall, the bulk air temperature and the temperature at the center of the duct. The ratio $(T_w-T_b)/(T_w-T_c)$ was computed from the experimental data and ranges from 0.9 to 0.96. Martinelli's correlation predicts the measured Nusselt number for the top surface very close to the current correlation. The experiment, in general, shows higher values of Nusselt numbers in the low

Reynolds number range compared to the Mercer correlation and this is mainly due to the fact that fully developed conditions are not attained.

3.5.4 Local Nusselt numbers for the top surface

The Nusselt number distributions for the development length, x, have been calculated for the top surface for the whole length of the BIPV/T system ($39D_h$). They are expressed by the following formulas.

For laminar region, $250 \leq Re \leq 2400$

$$Nu_{top}(x) = 0.039Re^{0.78}Pr^{0.4}e^{-\frac{x}{20 \cdot D_h}} + 0.034Re^{0.78}Pr^{0.4} \qquad 3.27$$

For turbulent region, $2400 < Re \leq 7100$

$$Nu_{top}(x) = 0.012Re^{0.78}Pr^{0.4}e^{-\frac{x}{9.09 \cdot D_h}} + 0.049Re^{0.78}Pr^{0.4} \qquad 3.28$$

Both correlations represent the convective heat transfer distribution up to the maximum length of the analyzed BIPV/T system. The last term in the Nusselt number distribution for the turbulent region ($0.049Re^{0.78}Pr^{0.4}$) represents the fully developed value. For the laminar region, the last term represents the Nusselt number value at the maximum length of the BIPV/T system. It is expected that for larger lengths, the Nusselt number will tend to keep decreasing.

3.5.5 Grashof and Rayleigh numbers

Petukhov (Petukhov, B.S., 1976) pointed out that when Grashof numbers surpass a certain upper limit, actual Nusselt numbers will be at least 1% higher than the value predicted by forced convection correlations for circular pipes. This "maximum" Grashof number is a function of the Reynolds number (Figure 3.11), and is different for vertical and

horizontal pipes. As can be seen in Figure 3.11, the Grashof numbers measured in the BIPV/T channel exceed, by several orders of magnitude, the Petukhov's upper limit curves given by equations 3.1 and 3.2. This indicates that forced convection correlations commonly used for circular pipes will be inadequate for the cases discussed in this paper, in which natural convection effects will clearly play an important role.

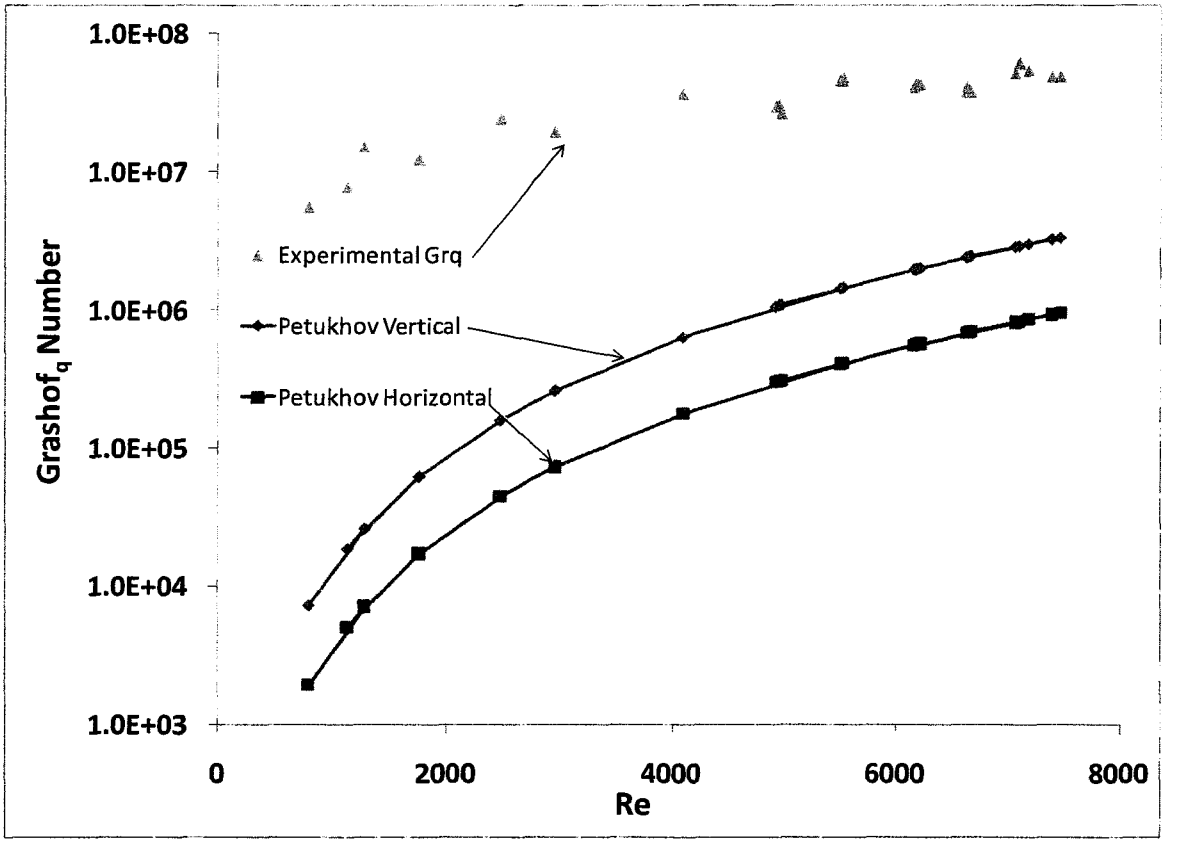

Figure 3.11. Comparison of Equations 3.1 and 3.2 with the experimental data (Pr=0.71). All the experimental points are above the limits established by the equations.

The product RaD_h/L was computed from the experimental data and plotted in Figure 3.12a. As can be seen, most of the experimental data falls in the mixed convection regime

for both laminar and turbulent flow regimes as compared to the map by Metais and Eckert (1964) (Figure 3.12b) for vertical tubes. The Ra numbers are in the range of 1×10^5 to 9×10^5.

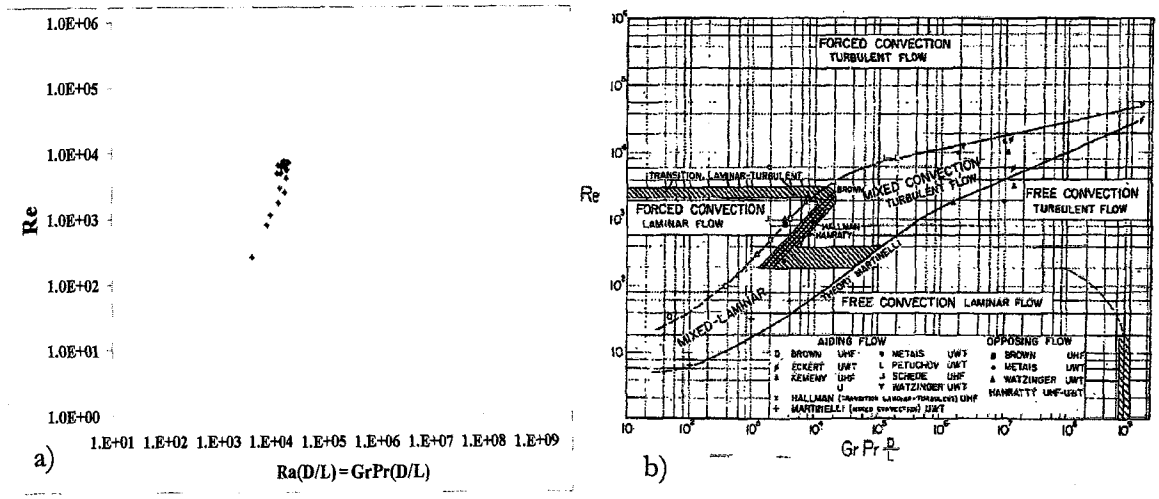

Figure 3.12. a) Experimental Re and Ra(D_h/L) data. b) Metais and Eckert (1964) map for vertical tubes.

The experimental Nusselt data are also in agreement with the results obtained by Sudo *et al.* (Sudo, Y. *et al.*, 1990) for a vertical heated rectangular channel, for which the Nusselt number is 1.7 to 2.4 times the value predicted by the Dittus-Boelter correlation.

3.5.6 Nusselt numbers for the laminar convection regime (Re<2300)

Incropera and De Witt (2002) and Kays *et al.* (2005) have mentioned that a common practice is to correlate mixed convection heat transfer with an expression of the form

$$Nu^n = Nu_F{}^n \pm Nu_N{}^n \qquad 3.29$$

where Nu_F corresponds to correlations for forced convection and Nu_N for natural convection correlations. The + sign is recommended for assisting and transverse flows.

It was found that for the laminar regime the effective Nusselt number could be represented as the simple addition of the forced convection and the natural convection effects (n = 1). For the forced convection, the Dittus-Boelter equation 3.7 is employed. For the natural convection, a correlation developed by Azevedo and Sparrow using water in an inclined channel is used (equation 3.30). Equation 3.30 is quoted by Incropera and De Witt (2002).

$$Nu_N = 0.645\left[Ra\frac{D_h}{L}\right]^{1/4} \qquad 3.30$$

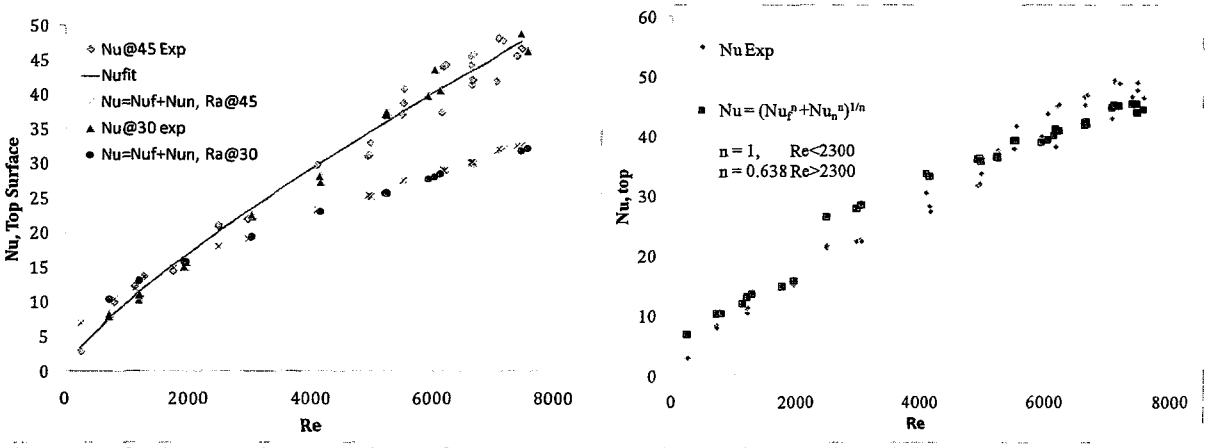

Figure 3.13. a) Experimental data of measured Nusselt number to the addition of the Dittus-Boelter and natural convection components for 30° and 45° tilt angle (n=1 in equation 3.29). b) Experimental data comparison of Nusselt numbers to equation 3.29 (for n = 1 for Re< 2300 and n = 0.638 for Re>2300).

As can be seen in Figure 3.13a, the Nusselt number predicted as the simple addition of the two components works relatively well for the laminar region Re<2300. However, it seems to slightly overestimate the Nusselt number. If the uncertainties in the measurement are taken into account, the difference is negligible. For the turbulent convection regime,

another exponent –n- should be found for the forced convection and the natural convection.

A curve-fitting technique was used to determine the n exponent that will give the least square error using equation 3.29. This value of n was found to be 0.638. Figure 3.13b compares the results for the two regimes. For 2300<Re<4500, the n = 0.638 fitting over predicts the Nusselt number values. For higher Re numbers, the effect of the natural convection tends to diminish.

3.5.7 Comparison with Wu, Xu and Jackson correlation

Wu *et al.* (2002) developed a correlation where the ratio of effective Nusselt number to the Nusselt number for forced convection is given by a function of the Grashof (based on heat flux), Re and Pr numbers. The equation was developed for a vertical annular passage. In this configuration, there was a heated core and a thermally insulated outer casing. The employed fluid was water. The experimental results were represented with the following equation:

$$\frac{\mathrm{Nu}}{\mathrm{Nu_{F,Wu}}} = \left[1 + 1.25 \times 10^5 \left(\frac{\mathrm{Gr_q}}{\mathrm{Re^{3.425}Pr^{0.8}}}\right)\left(\frac{\mathrm{Nu}}{\mathrm{Nu_{F,Wu}}}\right)^{-2}\right]^{0.46} \qquad 3.31$$

where $\mathrm{Nu_{F,Wu}}$ is an equation for forced convection developed by Wu *et al.* (2002). $\mathrm{Nu_{F,Wu}}$ predicts values that are about 6% higher than those predicted by the Dittus-Boelter equation.

$$\mathrm{Nu_{F,Wu}} = 0.042\mathrm{Re}^{0.74}\mathrm{Pr}^{0.4} \qquad 3.32$$

The Wu *et al.* equation is valid for 6,000<Re<20,000. Equation 3.32 was developed for opposed flow conditions.

One of the strengths of equation 3.31 is that it correlates the influences in Grashof, Re and Pr numbers. The experimentally calculated values of Gr_q in the BIPV/T system are in the range of 5.56×10^6 to 6.13×10^7. Equation 3.31 is plotted together with the experimental data for the BIPV/T system for Re>6000 (see Figure 3.14). A least-square optimization technique was employed to find the constant that multiplies the ratio of Grashof to Re and Pr numbers.

$$\frac{Nu}{Nu_{F,Wu}} = \left[1 + 1.9 \times 10^6 \left(\frac{Gr_q}{Re^{3.425}Pr^{0.8}}\right)\left(\frac{Nu}{Nu_{f,Wu}}\right)^{-2}\right]^{0.46} \qquad 3.33$$

is valid for the BIPV/T system for 6000>Re>7500. Equation 3.33 is plotted in Figure 3.14, as well. It must be kept in mind that the equation must be validated for different combinations of Grashof and Re numbers.

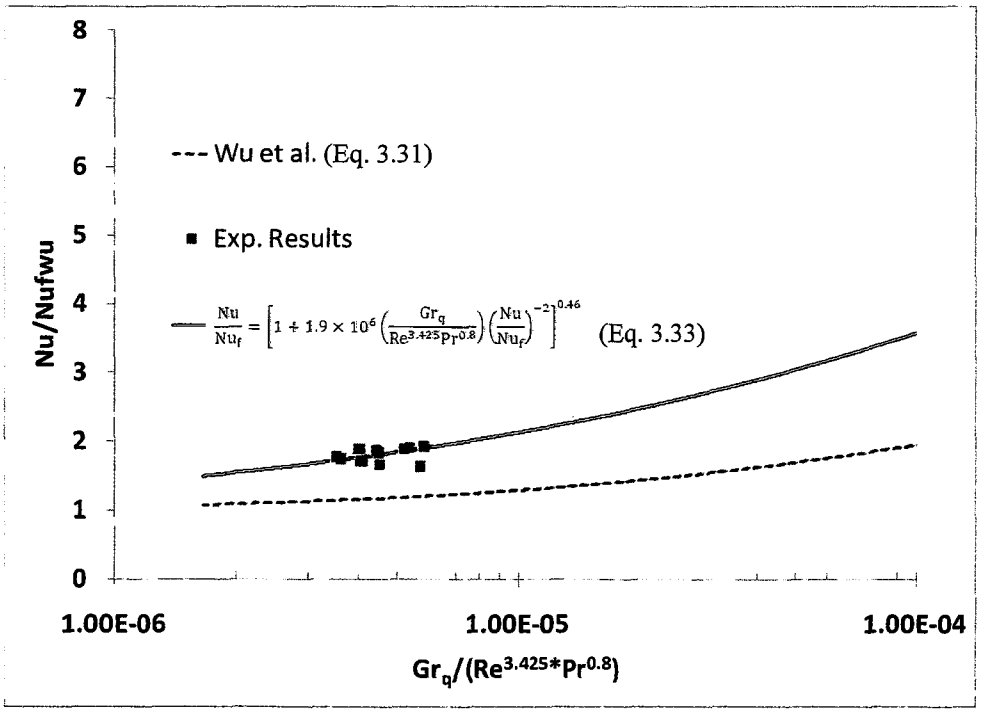

Figure 3.14. Experimental data comparison to Equations 3.31 and 3.33.

3.6 Framing Effects on Nusselt Number

PV modules are usually installed on the roof by means of custom made metallic or wood support framing, such as the one found in the BIPV/T system of the Northern Light Canadian Solar Decathlon 2005 house (Pasini, M. & Athienitis, A.K., 2006) (see Figure 3.15a). These structural framing members enhance the heat transfer by increasing turbulence and they change the local distribution of the convective heat transfer coefficients.

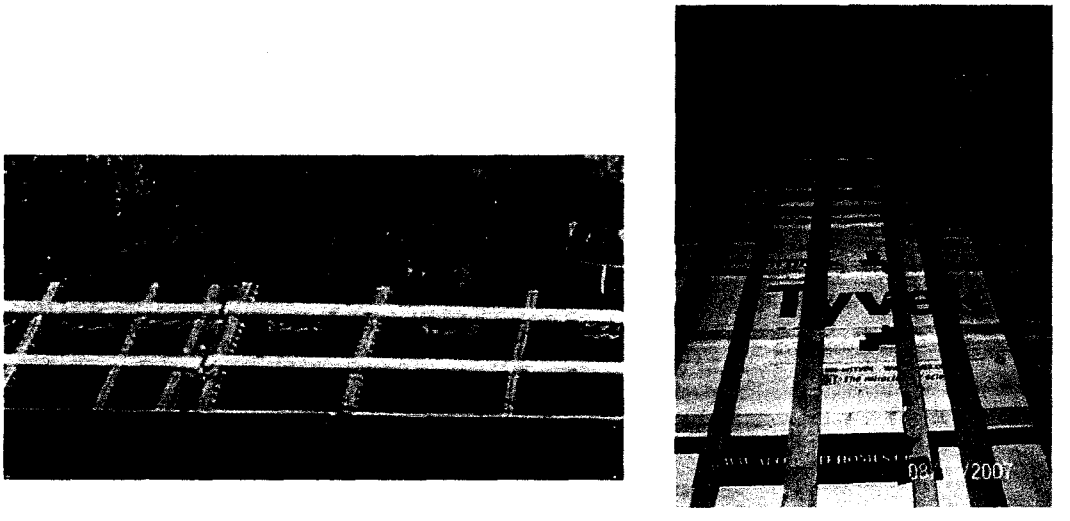

Figure 3.15. a) Photo of the wood framing structure employed to support the PV modules in the BIPV/T system of Northern Light Canadian Solar Decathlon 2005 house (Pasini, M. & Athienitis, A.K., 2006) b) Photo of the wood framing elements employed to support the PV modules in the BIPV/T system of the EcoTerra demonstration house (Chen, Y. et al., 2007a).

In order to replicate the conditions in Figure 3.15b, wood framing elements were inserted at the bottom of the BIPV/T experimental setup. Four rectangular pieces of wood were spaced equally starting at the leading edge of the channel, at distances of 0.508 m (see Figure 3.16).

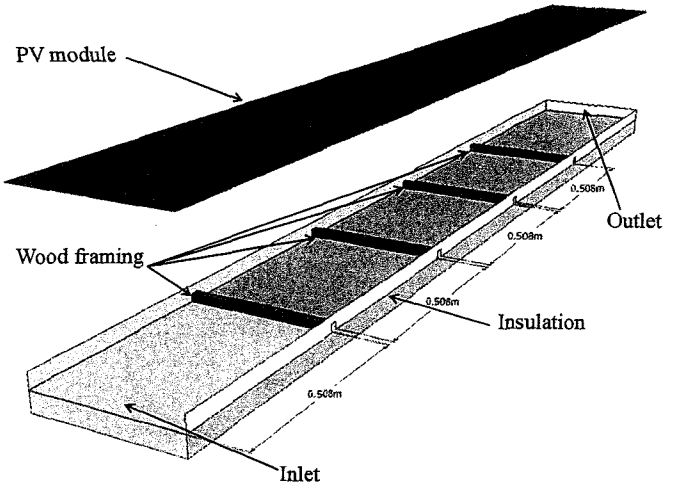

Figure 3.16. Sketch of the wood framing effect test in the BIPV/T channel.

The top and bottom Nusselt numbers were computed as described in the previous section.

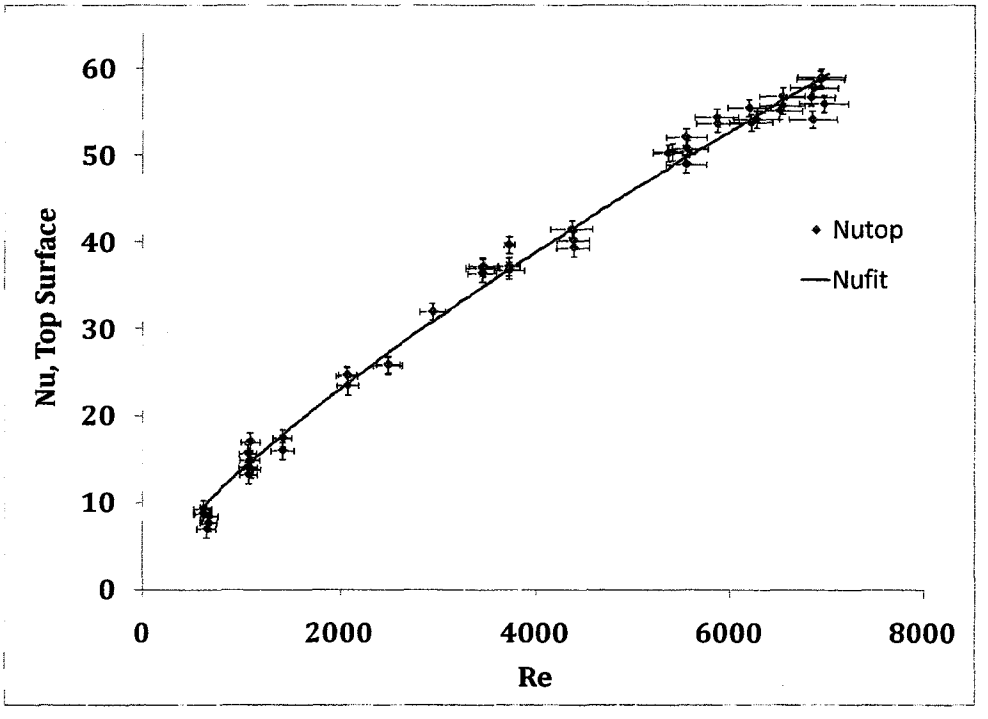

Figure 3.17. Nusselt numbers for the top surface versus Reynolds number. The data is compared with the correlation given by equation 3.34 . The uncertainties of each of the data points are shown by the vertical and horizontal line segments.

For the top surface, for $620 \leq Re \leq 7000$

$$Nu_{top} = 0.085Re^{0.755}Pr^{0.4} \quad 3.34$$

For the bottom surface, for $620 \leq Re \leq 7000$

$$Nu_{bottom} = 4.772Re^{0.498}Pr^{0.4} \quad 3.35$$

Equation 3.34 yields Nusselt numbers that are on average about 30% higher than those obtained with equation 3.25. Equation 3.34 gives on average Nusselt 2.6 times higher than the equation given by Dittus-Boelter (Equation 3.7) –although the latter is developed for smooth pipes.

The measured Nusselt numbers for the framing case are compared with similar studies done in rectangular ribbed channels. In order to compare the results, some parameters typically employed in ribbed channels are defined: the pitch of ribs, P (m) and the rib height, e (m) (See Figure 3.18). For the studied BIVP/T system, the ratio of P/e is 25.4 and the ratio of e/D_h is 0.274.

Similar studies on rectangular channels have reported very similar results. Promvonge and Thianpong (2008) measured Nusselt numbers in a rectangular channel with an aspect ratio of 15, P/e is 6.67 and a e/D_h ratio of 0.16. The experiments were done using air in the Re ranging from 4000 to 16,000. On average, the ratio of the measured Nusselt number to the Nusselt number given by Dittus-Boelter correlation was around 2.7. The ratio remained about the same for the whole range of Re numbers. In a similar study, SriHarsha *et al.* (2009) measured Nusselt numbers for a rib configuration with $P/e = 10$ and $e/D_h = 0.25$. The tested Re numbers were 10,000, 15,000 and 30,000. At Re 10,000, the ratio of the Nusselt number to the Nusselt number given by Dittus-Boelter was between 2 and 4.5.

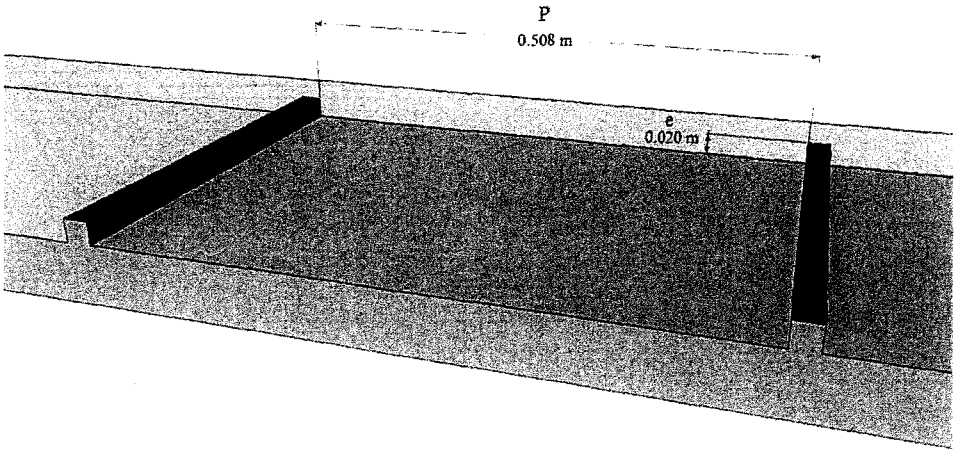

Figure 3.18. Pitch of ribs and rib height in the BIPV/T channel.

The data points, together with the corresponding uncertainty, are plotted in Figure 3.17. Appendix B summarizes how the uncertainties were calculated.

For the top surface, the uncertainties in the Nusselt numbers are small. In general, they range between 6% to a maximum of 7% for 2000<Re<7000. Again, the highest uncertainties occur at the lowest Reynolds numbers. For example, the uncertainty is 20% for Re = 620 and 11% for Re = 1100. The uncertainties for the Re numbers are between 3.6 to 5.3% for 2000<Re<7000. At low flow rates the uncertainties are higher, e.g. for Re = 660 the uncertainty is 15% and for Re = 1080 it is 8.5%.

In the framing case, there is an even smaller temperature differential between the bottom surface and the bulk air. Consequently, the uncertainties in the determination of the bottom coefficient are considerably higher. They are typically in the range of 100% to 700%. Therefore correlation 3.35 is only used to have an idea of the order of magnitude of the bottom heat transfer coefficient. Again, because the bottom surface is adiabatic, the

influence of the convective heat transfer coefficient on the outlet air is not as critical. This is discussed in detail in section 5.10.

3.6.1 Local Nusselt numbers for the top surface

In general, the Nusselt number for the turbulent region (Re>2300), has a tendency to increase slightly with increasing development length. The increase is especially marked at Re = 6930, for which the increase in the Nusselt number from the entrance to the exit of the BIPV/T system is 18.5% (see Figure 3.19). For the laminar region, the Nusselt number decays in an exponential fashion.

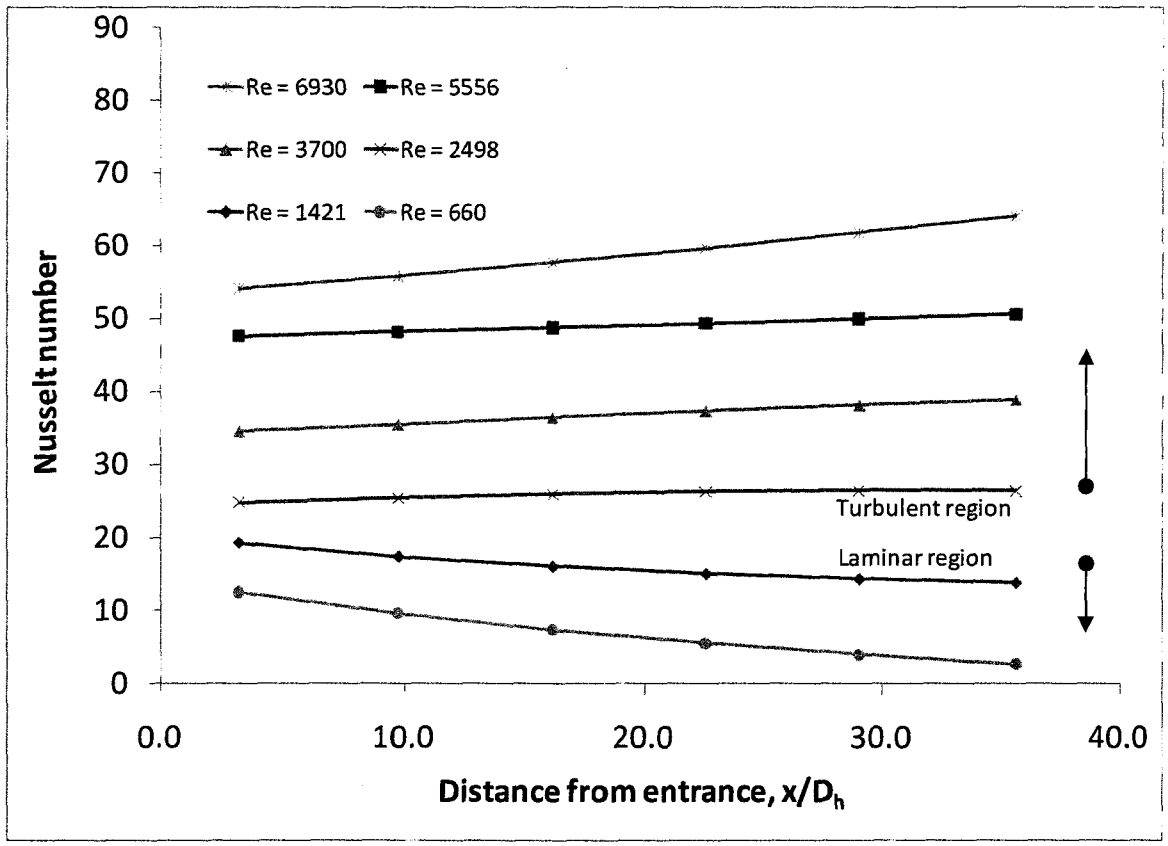

Figure 3.19. Local Nusselt number for the top surface for the framing test versus non dimensional distance from the entrance.

3.7 Pressure Drop in the BIPV/T systems

Figure 3.20 includes pressure drop measurements for the BIPV/T systems for both the smooth and the framing configurations. The regression curves in Figure 3.20 show that the pressure drop, as expected, varies with the square of the flow rate.

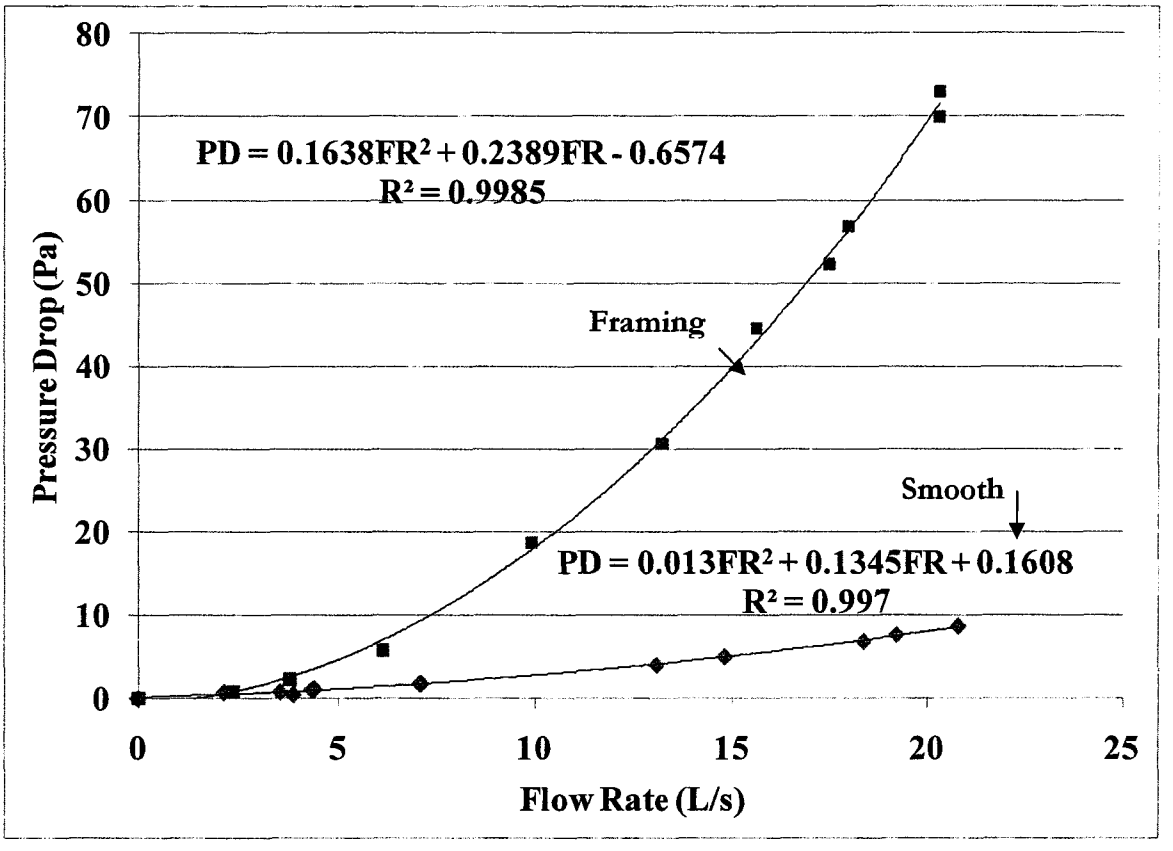

Figure 3.20. Pressure drop as a function of the flow rate in the channel in L/s.

The measured pressure drops for the smooth channel are relatively small; for a flow rate of 19 L/s (40 CFM), the pressure drop is around 7 Pa. Assuming that the combined efficiency of the electric motor and the fan is only 20%, the resulting electric power consumption would be: (0.019 m^3/s)(7 Pa)/0.20 = 0.66 W. For the framing case, the pressure drop at 19 L/s (40 CFM) is around 62 Pa. Assuming a combined efficiency of 20%, the theoretical fan consumption would be: (0.019 m^3/s)(62 Pa)/0.20 = 5.8 W. These result

illustrate the usefulness of air-based BIPV/T systems, as the required power consumption for driving the flow in the channel is small in comparison with the recovered energy (in this case, 68 W of electric power, and hundreds of watts of thermal energy). This information is very useful for design purposes: it suggests that it is advisable to optimize the ducting system and connecting manifold, since the most significant pressure drops will be much larger there than in the BIPV/T channel.

3.7.1 Friction factors

The Darcy friction factor has been calculated at different flow rates in the BIPV/T system for the two configurations (smooth and framing), with the following equation:

$$f = \frac{\Delta P}{\left(\frac{L}{D_h}\right)\frac{\rho V^2}{2}} \qquad 3.36$$

As a comparison, the ratio of the measured friction factors to the friction factor predicted for turbulent flow in a circular smooth pipe using the Blasius relationship is calculated for the turbulent region. The Blasius (White, F.M., 2003; McKeon, B. *et al.*, 2005) relationship is given by:

$$f_B = \frac{0.3164}{Re^{0.25}} \qquad 3.37$$

The friction factor for the laminar region, Re<2300 (ASHRAE, 2009), is calculated using:

$$f_{lam} = \frac{64}{Re} \qquad 3.38$$

The results for the turbulent region are shown in Figure 3.21 and Figure 3.22. As expected, the friction factor diminishes for higher Reynolds numbers for the two configurations, as seen in the Moody diagram (White, F.M., 2003) (see Figure 3.21). The ratio of friction factors for the framing in the BIPV/T system lies in the range of 44 to 52.

This result agrees with the results presented in the work by SriHarsha *et al.* (2009). In SriHarsha *et al.'s* study, the friction factor ratio was in the same range (48-50) for Re ranging from 5,000 to 15,000. The results by (Promvonge, P. & Thianpong, C., 2008) for their ribbed channel are very close to the measurements. They reported friction factors in the range of 1.2 to 1.3 for Reynolds numbers ranging from 4000 to 16000. Their friction factor ratio (f/f_b) is in the range of 30 to 40. For the smooth BIPV/T system case, the ratio is almost constant; in the range 5 to 6 (see Figure 3.21).

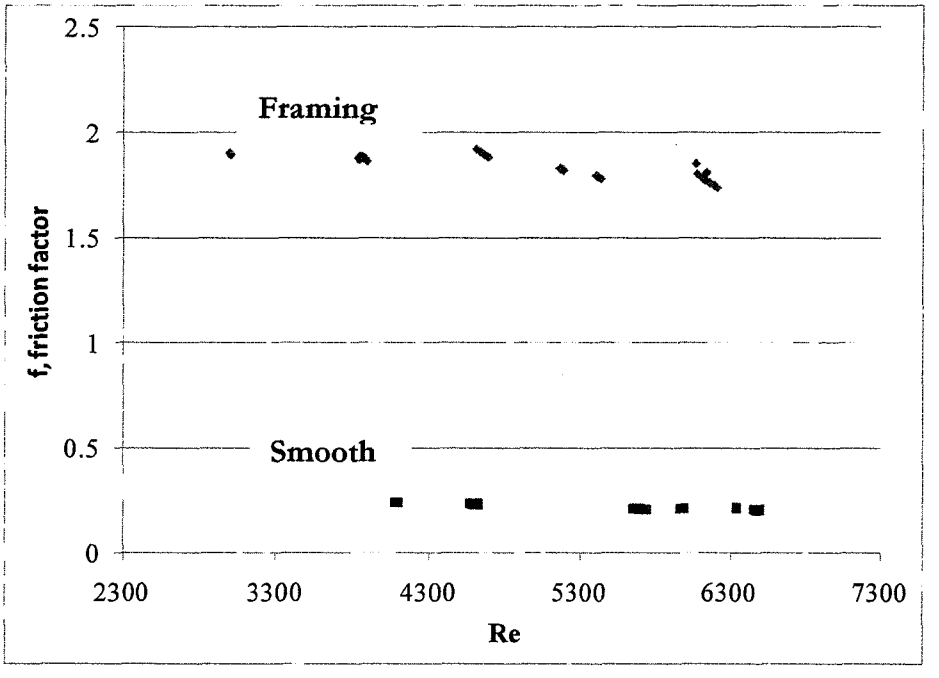

Figure 3.21. Measured friction factors in the two BIPV/T systems as a function of Re number.

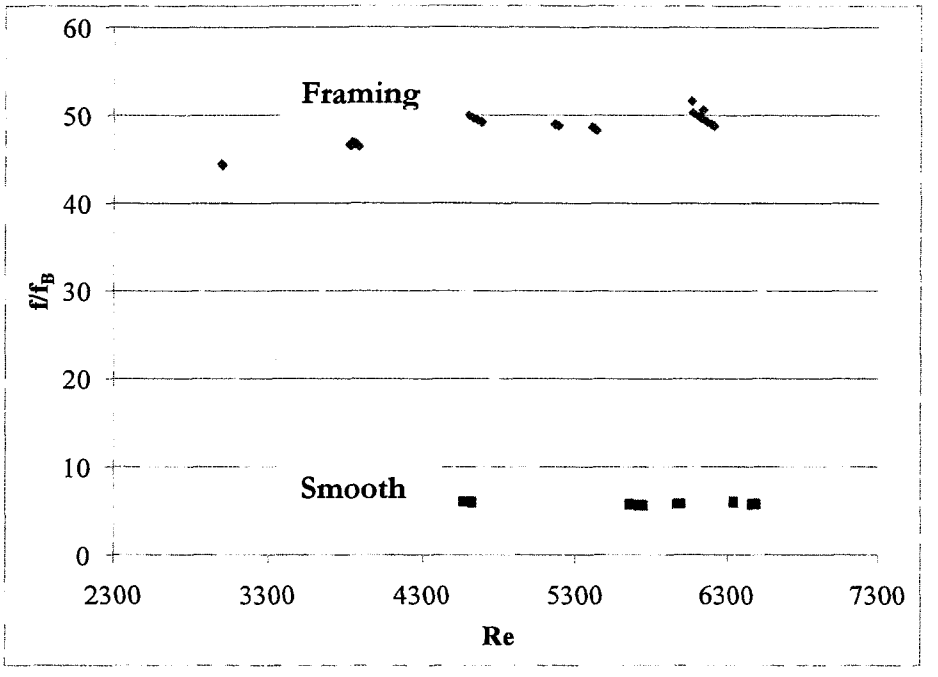

Figure 3.22. Friction factors ratio in the two BIPV/T systems as a function of Re number.

In the laminar region, the results are summarized in Figure 3.23 and Figure 3.24.

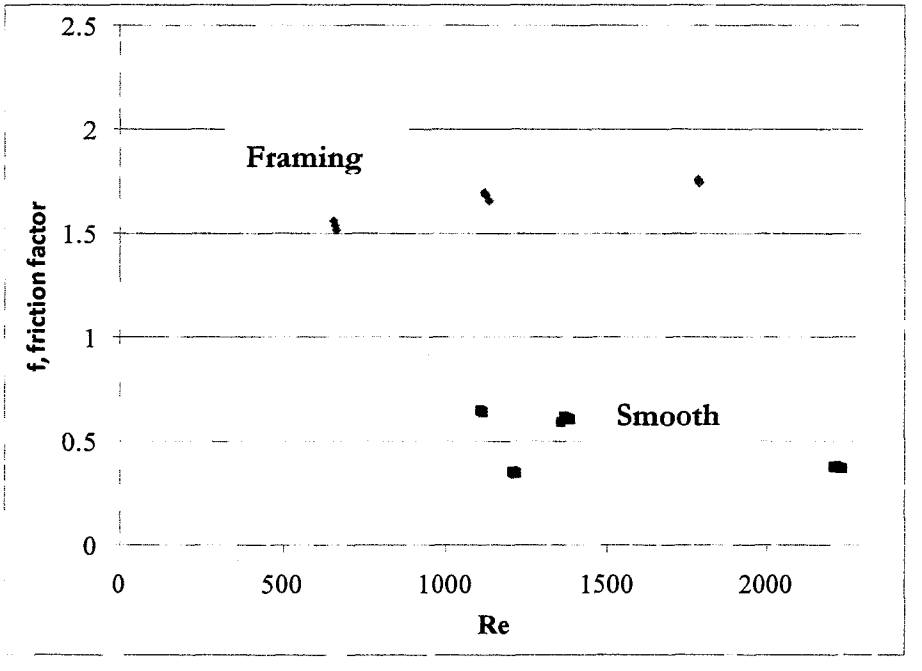

Figure 3.23. Measured friction factors in the two BIPV/T systems in the laminar region.

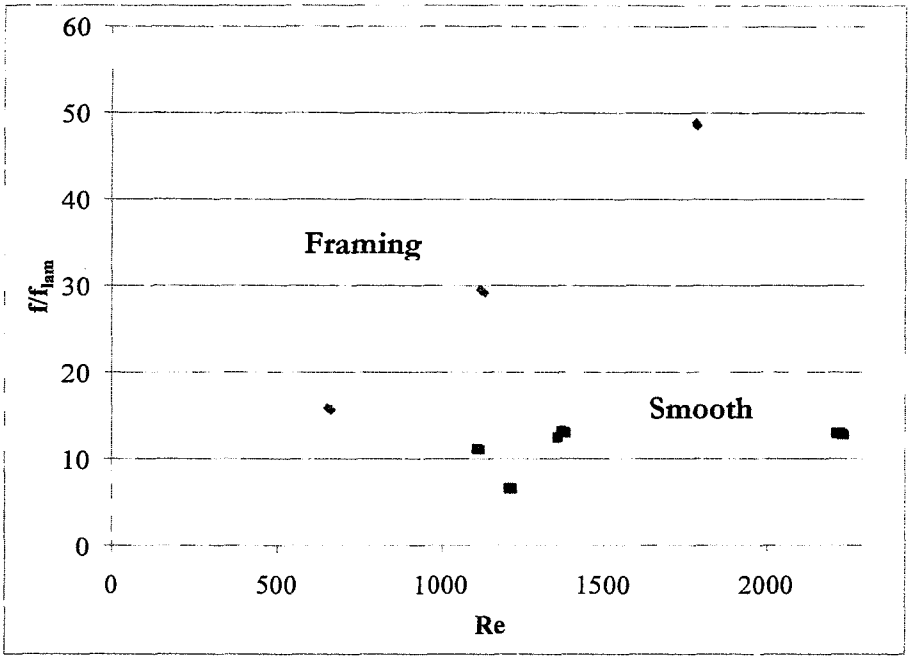

Figure 3.24. Friction factors ratio in the two BIPV/T systems in the laminar region.

For the laminar region, the friction factors for the smooth BIPV/T system also decrease with Re. Meanwhile, for the framing case, the friction factor is slightly larger at higher Re numbers (see Figure 3.23). The ratio of friction factors for the smooth case in the laminar region is in the range of 6 to 13. For the framing case, the ratio of friction factors is in a wider range, from 16 to 49.

4. Comparison of Electrical Models for the Tested Photovoltaic Modules

Electrical models for the PV module used in this research have been implemented and compared with two existing PV models: a five-parameter single-diode model developed by (De Soto, W. *et al.*, 2006) and the photovoltaic array performance model developed by King *et al.* (2004) at Sandia National Laboratories. The five-parameter model developed by De Soto *et al.* is suitable because its parameters can be found with typical data provided by the PV module manufacturer. The *De Soto et al.* model also borrows some of the concepts developed in the Sandia model for the treatment of absorbed solar radiation in the solar cell. The Sandia model uses empirical parameters obtained for different PV modules.

4.1. Single-Diode Model

The single-diode model presented is based on the work by De Soto, W. *et al.* (2006). As seen in chapter 1, solar cells and PV modules can be modeled as a current source in parallel with a diode. A diode is a two-terminal device that allows electrical current to flow in only one direction. The standard model of a solar cell is called a single-diode model (DGS, 2005), and includes a parallel resistance (shunt resistance R_{sh}) to account for leakage losses, and a series resistance (R_S) to account for voltage losses, between the semiconductor and the electrical contacts of the module.

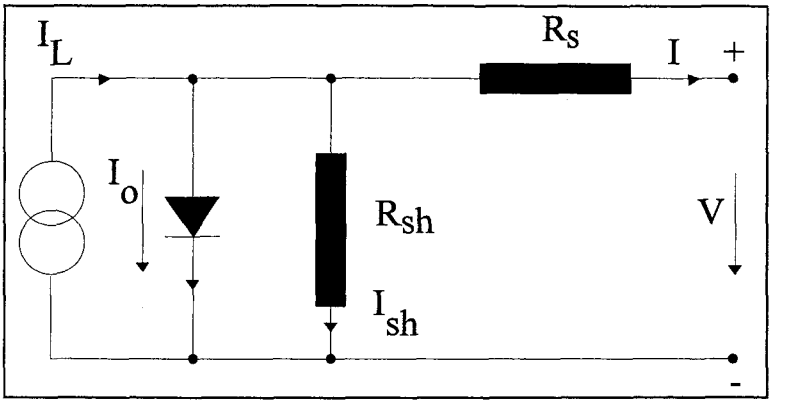

Figure 4.1. Single-diode circuit (De Soto, W. et al., 2006).

In Figure 4.1, V is the solar cell terminal voltage, I_o is the diode reverse saturation current, I_L is the so-called light current or photocurrent (the ideal current produced by the panel), I_{SH} is the parallel resistor current or shunt current, I is the solar cell terminal current, R_{SH} is the parallel or shunt resistance, and R_S is the series resistance.

The characteristic equation of the circuit is given by:

$$I = I_L - I_o - I_{SH} = I_L - I_o\left(e^{\frac{V+I\cdot R_S}{a}} - 1\right) - \frac{V + I\cdot R_S}{R_{SH}} \qquad 4.1$$

where the first term corresponds to the photocurrent, the second term represents the current through the diode, and the third term represents the current through the parallel resistor. The electrical power is the product of $I \cdot V$:

$$P = I \cdot V \qquad 4.2$$

The parameters I_0, a, R_S and R_{SH} in 4.1 depend on the photovoltaic technology employed, as well as on the construction of each cell. The physical parameter a depends on the temperature of the panel (De Soto, W. *et al.*, 2006) and is given by:

$$a = \frac{N_S n_I k T_c}{q} \qquad 4.3$$

where q represents the electron charge, k the Boltzmann's constant, n_I is the ideality factor, N_S is the number of cells in series and T_C is the cell temperature.

To calculate the five parameters of the equations, the reference values can be obtained easily from the manufacturers' data. These conditions are obtained at standard test conditions as previously discussed in the introduction. Three equations come from current-voltage pairs, the short circuit current, the open circuit voltage, and the current and voltage for the maximum power point. Another equation comes from the knowledge that the derivative of V at the maximum power point is zero.

The first equation gives the short circuit current by replacing $I_{sc,ref}$ and $V=0$ into equation 4.1:

$$I_{sc,ref} = I_{L,ref} - I_{o,ref}\left[e^{\frac{I_{SC,ref}R_{S,ref}}{a_{ref}}} - 1\right] - \frac{I_{SC,ref}R_{s,ref}}{R_{sh,ref}} \qquad 4.4$$

The second equation by evaluating equation 4.1 at open circuit voltage, when $I=0$ and $V = V_{oc,ref}$

$$0 = I_{L,ref} - I_{o,ref}\left[e^{\frac{V_{oc,ref}}{a_{ref}}} - 1\right] - \frac{V_{oc,ref}}{R_{sh,ref}} \qquad 4.5$$

The third equation is obtained by evaluating equation 4.1 at the maximum power point conditions:

$$I_{mp,ref} = I_{L,ref} - I_{o,ref}\left[e^{\frac{V_{mp,ref}+I_{mp,ref}R_{S,ref}}{a_{ref}}} - 1\right] - \frac{V_{mp,ref} + I_{mp,ref}R_{S,ref}}{R_{sh,ref}} \qquad 4.6$$

The derivative with respect to V at the maximum power point is zero,

$$\frac{I_{mp,ref}}{V_{mp,ref}} = \frac{\frac{I_{o,ref}}{a_{ref}}\left[e^{\frac{V_{mp,ref}+I_{mp,ref}R_{S,ref}}{a_{ref}}}\right] + \frac{1}{R_{sh,ref}}}{1 + \frac{I_{o,ref}Rs}{a_{ref}} e^{\frac{V_{mp,ref}+I_{mp,ref}R_{S,ref}}{a_{ref}}} + \frac{Rs}{R_{sh,ref}}} \qquad 4.7$$

Another equation can be written by knowing the temperature coefficient of open circuit voltage

$$\mu_{VOC} = \frac{V_{oc} - V_{oc,ref}}{T_C - T_{C,ref}} \qquad 4.8$$

However, the equation requires computing the V_{oc} at a different cell temperature. In De Soto *et al.* (2006) it is stated that the temperature chosen is not critical. Their analysis showed that a temperature difference of between 1 and 10 °C above or below the reference temperature would yield basically the same results.

To obtain *a* at a different cell temperature, the following expression is employed

$$\frac{a}{a_{ref}} = \frac{T_C}{T_{C,ref}} \qquad 4.9$$

The I_o parameter depends on the temperature as well. Messenger and Ventre (2004) provided an expression to obtain I_o at different temperatures.

$$\frac{I_o}{I_{o,ref}} = \left(\frac{T_C}{T_{C,ref}}\right)^3 e^{\left(\frac{1}{k}\left(\frac{Eg_{T_{C,ref}}}{T_{C,ref}} - \frac{Eg_{T_C}}{T_C}\right)\right)} \qquad 4.10$$

In the equation above, *k* is the Boltzmann's constant and *Eg* is the material band gap. For silicon cells at $T_{C,ref}$ it has the value of 1.12eV. For the UNI-SOLAR PVL-68 module, which uses triple junction amorphous cell technology, $Eg_{TC,ref}$ has a value of 1.6 eV. The *Eg* value for a different cell temperature is found using the following expression (De Soto, W. *et al.*, 2006)

$$\frac{Eg}{Eg_{T_{C,ref}}} = 1 - 0.0002677(T - T_{C,ref}) \qquad 4.11$$

The next equation to define is the light current formula. It is usually expressed as a linear function of the absorbed incident solar radiation.

$$I_L = \frac{S}{S_{ref}} \frac{M}{M_{ref}} \left[I_{L,ref} + \alpha_{ISC}(T_C - T_{C,ref}) \right] \qquad 4.12$$

In the equation above S_{ref} and M_{ref} are the absorbed solar radiation and the air mass modifier at the standard reference conditions. The temperature coefficient at the short circuit, α_{ISC}, is a commonly measured and provided parameter in the specification sheets of PV modules. The absorbed solar radiation, S, is a parameter that affects the results significantly and it is analyzed further here. The absorbed solar radiation at reference conditions is $S_{ref} = G_{ref}(\tau\alpha)_b$. The air mass modifier ratio M/M_{ref} is expressed as a summation of empirical parameters that are a function of the air mass. The air mass is the ratio of air that the beam radiation has to traverse at a specific location and time to the amount of air it must traverse if the sun were directly overhead. King *et al.*(1998) uses the following expression for the air mass

$$AM = \frac{1}{\cos(\theta_z) + 0.5057(96.080 - \theta_z)^{-1.634}} \qquad 4.13$$

where θ_z is the zenith angle in degrees.

King *et al.* (2004) uses the following expression for the air modifier,

$$\frac{M}{M_{ref}} = \sum_{0}^{4} a_i (AM)^i \qquad 4.14$$

In the Sandia National Laboratories (2002) online database, there is a list of different PV modules with their empirically determined a_i parameters.

Duffie and Beckman (2006) provide different methods to compute the absorbed solar radiation, S. For the case where there is global (direct + diffuse) measurement of solar radiation I_T on the plane of the module, a reasonable assumption is to assume that the absorbed solar radiation is the following:

$$S = (\tau\alpha)_{av} I_T = 0.96(\tau\alpha)_b I_T \qquad 4.15$$

S_{ref} is defined as $G_{ref}\tau\alpha_n$. Using the results by King *et al.* (1998) Duffie and Beckman (2006) arrive at the equation $K\tau\alpha_b(\theta) = (\tau\alpha)_b/(\tau\alpha)_n$. Then the previous equation can be rewritten in terms of $(\tau\alpha)_n$, as follows:

$$S = 0.96(\tau\alpha)_b I_T = 0.96 K\tau\alpha_b(\theta)(\tau\alpha)_n I_T \qquad 4.16$$

Therefore, the ratio S/S_{ref} can be expressed as

$$\frac{S}{S_{ref}} = \frac{0.96 K\tau\alpha_b(\theta) I_T}{G_{ref}} \qquad 4.17$$

The value of $K\tau\alpha_b(\theta)$ is given by a summation of empirical parameters (b_i) measured at Sandia Laboratories and also available in an online database (King, D.L. *et al.*, 2004). It is defined as

$$K\tau\alpha_b(\theta) = \sum_{i=0}^{5} b_i\, \theta^i \qquad 4.18$$

In order to complete the model, the dependence of R_s and R_{sh} are addressed. De Soto, W. *et al.* (2006) assumes that the R_s is completely independent from temperature. It follows that for a different temperature $R_s = R_{sref}$. For R_{sh}, it is assumed that its value varies with the absorbed solar radiation and can be expressed as

$$\frac{Rsh}{R_{sh,ref}} = \frac{S_{ref}}{S} \qquad 4.19$$

The set of equations is complete to determine the IV curve. The first step is the determination of the reference parameters. For that, equations 4.4, 4.5, 4.6, 4.7, 4.8, 4.9, 4.10, 4.12, and equation 4.5 evaluated at a different temperature must be solved simultaneously. In order to obtain the reference parameters, the terms in equation 4.12, corresponding to the total absorbed radiation and the air modifiers, are set to: $S=S_{ref}$ and $M=M_{ref}$. From the previous definition, it also follows that for reference parameter determination, $R_{sh}=R_{shref}$ from equation 4.19.

It is important to state that the set of equations is highly non-linear, thus it is important to use reasonable initial guesses for each of the parameters to find the solutions. Duffie and Beckman (2006) provide guidelines to set the initial guesses for the solution of the equations.

4.2. Photovoltaic Array Performance Model (Sandia)

The model presented here is based on the research work done by *King et al.* (1997; 1998; 2004). This model is also currently used in the building energy simulation program EnergyPlus (US DOE & Lawrence Berkeley National Laboratory, 2009).

The equations define five points of the IV curve. These include the I_{SC}, V_{OC}, (V_{mp},I_{mp}). The two other intermediate points are the ones for $V = 0.5\ V_{OC}$ and current I_X, and for $V = 0.5(V_{OC}+V_{mp})$ and corresponding current I_{XX}.

The equations are defined below

$$I_{SC} = I_{SC,ref}\frac{M}{M_{ref}}\left[1 + \alpha_{ISC}(T_C - T_{C,ref})\right]\left[\frac{G_b K\tau\alpha_b(\theta) + G_d}{G_{ref}}\right] \qquad 4.20$$

$$I_{mp} = I_{mp,ref}\left[c_o E_e + c_1 {E_e}^2\right]\left[1 + \alpha_{IMP}(T_C - T_{C,ref})\right] \qquad 4.21$$

$$I_X = I_{X,ref}\left[c_4 E_e + c_5 {E_e}^2\right]\left[1 + \left(\frac{\alpha_{ISC} + \alpha_{IMP}}{2}\right)(T_C - T_{C,ref})\right] \qquad 4.22$$

$$I_{XX} = I_{XX,ref}\left[c_6 E_e + c_7 {E_e}^2\right]\left[1 + \alpha_{IMP}\left(T_C - T_{C,ref}\right)\right] \quad 4.23$$

$$V_m = V_{vm,ref} + c_2 N_S \delta(T_C)\ln(E_e) + c_3 N_S[\delta(T_C)\ln(E_e)]^2 + \beta_{Vmp} E_e\left(T_C - T_{C,ref}\right) \quad 4.24$$

$$V_{Oc} = V_{OC,ref} + N_S \delta(T_C)\ln(E_e) + \beta_{VOC} E_e\left(T_C - T_{C,ref}\right) \quad 4.25$$

$$P_{mp} = I_{mp} V_{mp} \quad 4.26$$

$$E_e = \frac{I_{sc}}{I_{sc}\left[1 + \alpha_{ISC}\left(T_C - T_{C,ref}\right)\right]} \quad 4.27$$

$$\delta(T_C) = \frac{n_D k T_C}{q} \quad 4.28$$

In equation 4.20, the term $G_b$corresponds to the beam component of solar irradiance incident on the module, $G_b = E_{dni}cos(\theta)$. G_d is the diffuse component of solar irradiance incident on the module surface. The empirical model parameters c_o *to* c_7, $I_{sc,ref}$, $I_{x,ref}$, $I_{xx,ref}$, $I_{mp,ref}$, $V_{oc,ref}$, $V_{mp,ref}$, a_{ISC}, a_{Imp}, β_{VOC}, β_{Vmp}, N_s, N_D are found in the Sandia Database (Sandia National Laboratories, 2002) for different photovoltaic modules. The system of equations is solved using Mathcad and has also been coded in MATLAB; the codes can be found in Appendix C and D.

4.3 Model Performance Comparison at STC

The two models are compared based on the specification papers for the Uni-Solar PVL-68 module. The specification papers from the manufacturer list the data in Table 4-1.

Table 4-1. Reference parameters at STC conditions for Uni-Solar PVL-68 manufacturer's data

Maximum Power	68 W
V_{mp}	16.5 V
I_{mp}	4.13 A
I_{SC}	5.1 A
V_{oc}	23.1 V
α_{ISC}	5.1×10^{-3} A/K
μ_{VOC}	-0.088 V/K

Table 4-2. Sandia Model Parameters at STC for Uni-Solar PVL-68

Area	1.1225	a_2	-0.0259
Material	3-a-Si	a_3	0.003174
Series Cells	11	a_4	-0.00011
Parallel C-S	1	b_0	1
$I_{sc,ref}$	5.1	b_1	-0.00502
$V_{oc,ref}$	23.1	b_2	0.000584
$I_{mp,ref}$	4.1	b_3	-2.3E-05
$V_{mp,ref}$	16.5	b_4	3.83E-07
aI_{sc}	0.00085	b_5	-2.3E-09
aI_{mp}	0.0012	$d(Tc)$	1
C_0	1.096	fd	1
C_1	-0.096	a	-3.581
β_{Voco}	-0.098	b	-0.113
β_{Vmpo}	-0.052	C_4	1.044
n	3.77	C_5	-0.044
C_2	-1.14162	$I_{x,ref}$	4.72
C_3	-2.89115	$I_{xx,ref}$	2.9
a_0	1.047	C_6	1.13
a_1	0.000821	C_7	-0.13

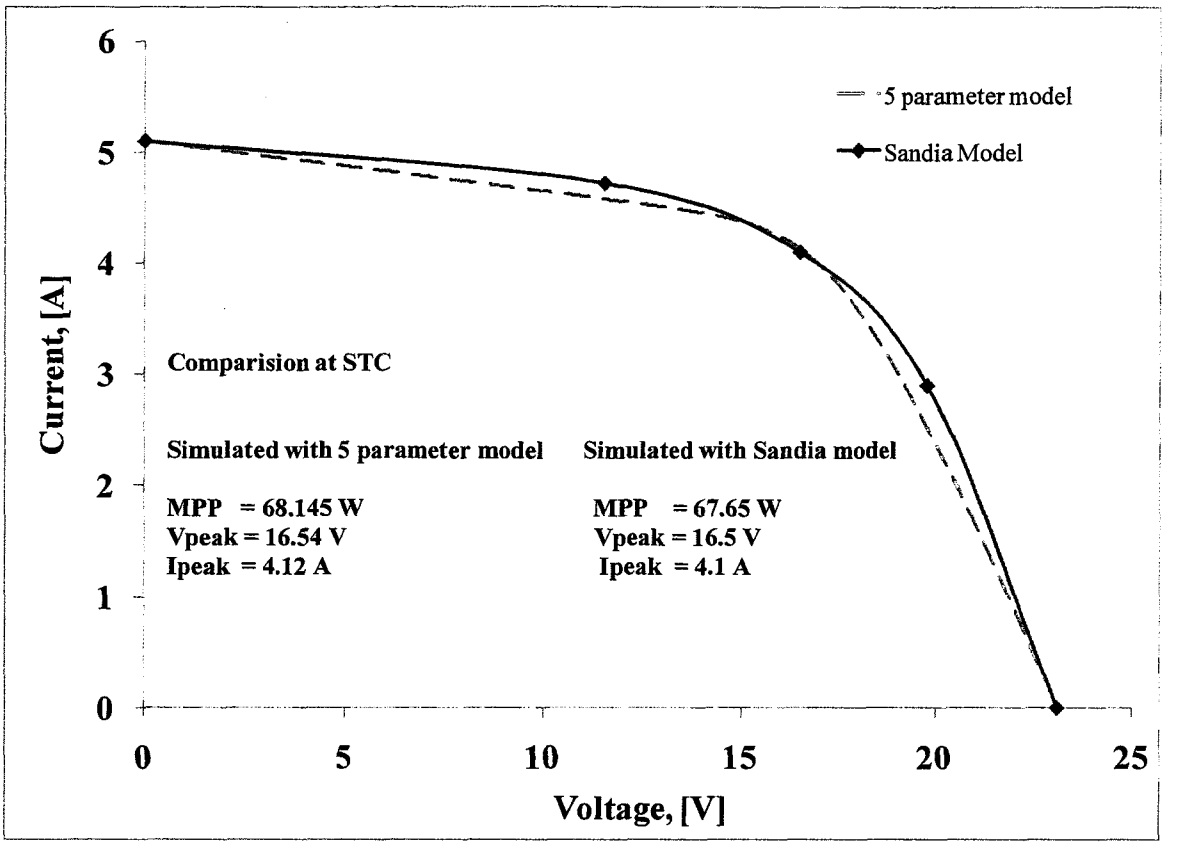

Figure 4.2. Current-Voltage (I-V) curve simulated with the five parameter model and Sandia Model.

As can be seen from Figure 4.2, the two models yield essentially the same results at STC conditions. The small difference found in between the maximum power points for the two models is mainly caused by the discrepancies in the reference parameters from the Sandia model and in the specification sheet of the manufacturer i.e. For Sandia V_{mp}= 16.5 V and I_{mp}=4.1 A, according to the manufacturer V_{mp}=16.5 V and I_{mp}=4.13 A.

4.4 Model Performance Comparison at Different Temperatures

The two models yield very similar results up to about 40°C, when the percent difference based on the Sandia Model is 4.9%. Table 4-3 presents Maximum Power Point comparison at different temperatures.

Table 4-3. Maximum power at different cell temperatures for 1000 W/m^2 radiation obtained with five parameter model and Sandia model for Uni-Solar PV-68.

Cell Temp °C	MP 5 Parameter Model W	MP Sandia Model W	$MP_{5p} - MP_S$ W	$\left(\frac{MP_{5p} - MP_S}{MPs}\right)100$ %
25	68.14	67.65	0.49	0.72
30	66.27	66.98	-0.71	-1.06
35	64.35	66.30	-1.95	-2.94
40	62.38	65.61	-3.23	-4.92
45	60.36	64.91	-4.55	-7.00
50	58.31	64.19	-5.88	-9.16
55	56.21	63.46	-7.25	-11.42
75	47.48	60.41	-12.93	-21.40

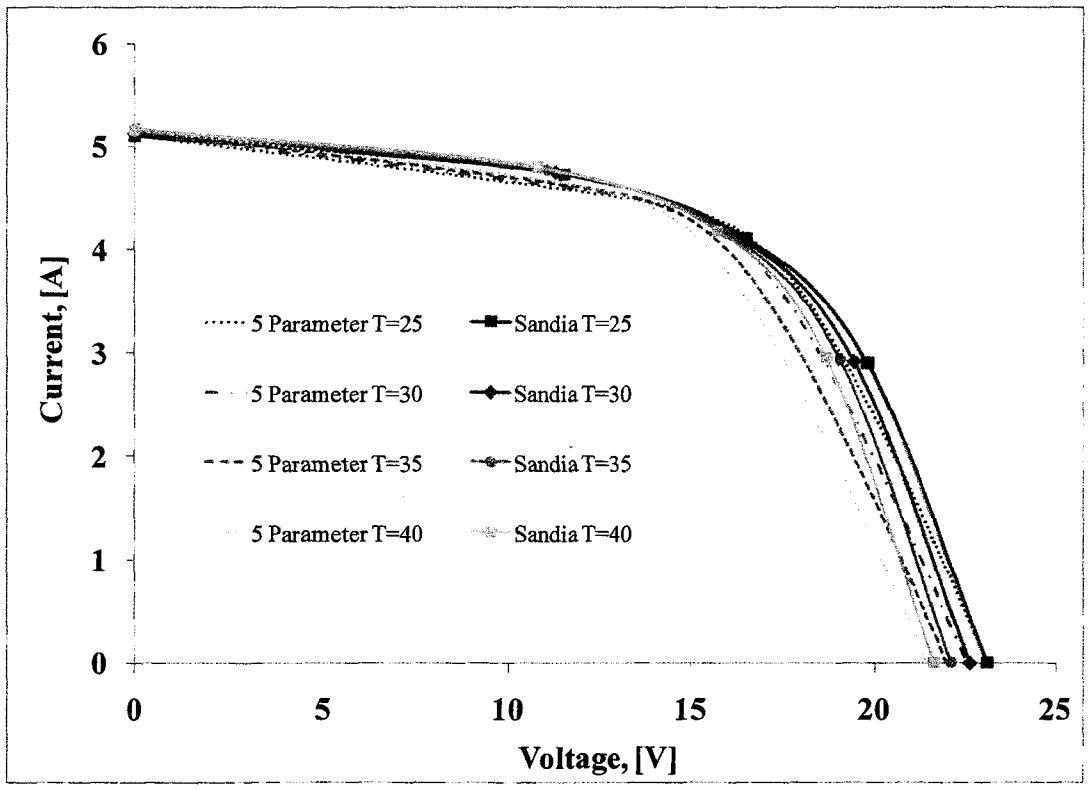

Figure 4.3. Current-Voltage (I-V) curves simulated with the five parameter model and Sandia Model for 1000 W/m^2 radiation and different cell temperatures.

4.5 Model Performance Comparison at Field Conditions

I-V curves for the Uni-Solar PVL-68 module have been experimentally measured at different solar radiation and temperature conditions. A Daystar DS-100C IV tracer was employed for the measurements; it has an accuracy of 0.5% of the measured voltage and current.

The total amount of solar radiation going in to the solar module has been measured with a LI-200 pyranometer sensor. It is a silicon photovoltaic-based sensor that incorporates a cosine corrected head. The maximum error estimated by the manufacturer is 5% of the reading (LI-COR, 2005). However, King and Myers (1997) state that the error could be as large as 10%.

Actual electrical performance of photovoltaic modules (power output) will depend on many factors besides the solar irradiance level, e.g. cell temperature, soiling, solar spectrum and the angle of incidence. The models employed here (five-parameter and Sandia Model) correct for the solar spectral influence due to the air mass and the angle of incidence. The corrections do not account for more random atmospheric factors such as water vapor content, aerosols and turbidity (King, D.L. *et al.*, 1997). Also, these models do not account for stabilization characteristics after solar exposure (degradation).

Amorphous photovoltaic modules have been shown to suffer from power-output degradation. The work by King *et al.* (2000a) showed that triple-junction amorphous modules can suffer power degradation of about 16% of their rated peak power at STC in the first year of continuous use, and up to 20% degradation in a little bit less than 2 years (Figure 4.4). Evidence of thermal annealing effects for these modules was also found. Thermal annealing refers to when PV modules recover some or all of their initial

performance at elevated temperature. The data of King *et al.* (2000a) shows about a 7% improvement due to thermal annealing effects.

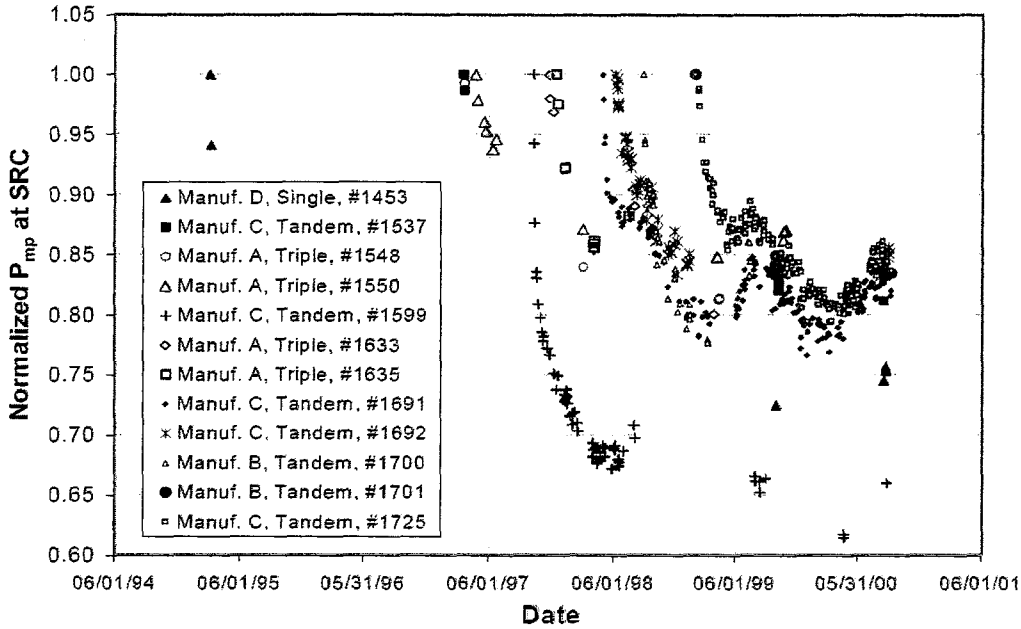

Figure 4.4. Normalized Performance at STC for 13 a-Si modules by (King, D.L. et al., 2000a)

Long-term peak power degradation can be represented by three components –an initial degradation seen in the first year, a seasonal variation and a long-term variation as described by (Delahoy, A.E. *et al.*, 2002) (see Figure 4.5). Although Figure 4.5 does not show many points, the seasonal trend variation, has been shown in (Ruther, R. *et al.*, 2008) for the field factor (See Figure 4.6).

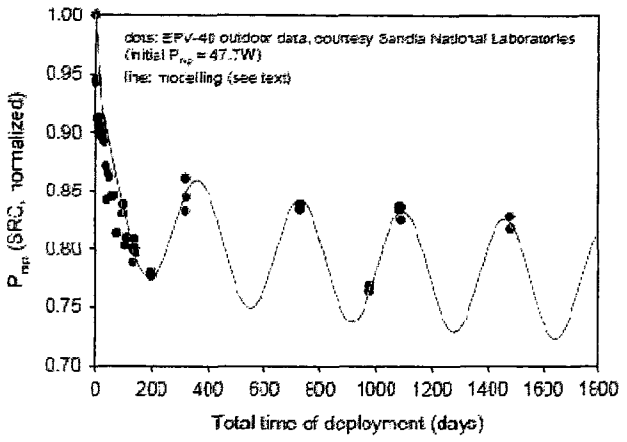

Figure 4.5. Degradation curve for amorphous silicon module by Delahoy, A.E. *et al.* (2002)

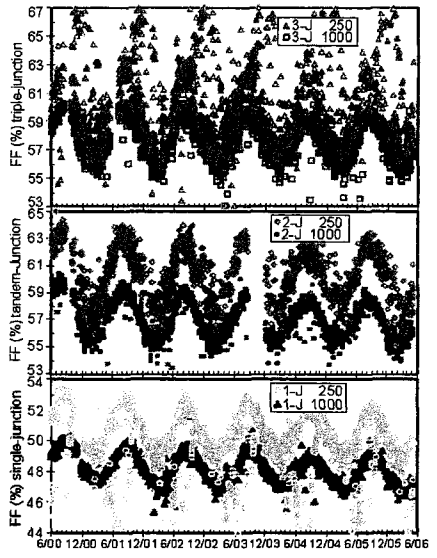

Figure 4.6. Fill factor curve for amorphous silicon modules at 250 and 1000 W/m^2 by Ruther, R. et al. (2008)

I-V curve measurements have been compared using the two numerical models on two different days (November 28th, 2009, and March 5th, 2010, Figure 4.7 and Figure 4.8 respectively). Both measurements were performed at conditions close to solar noon. The main solar parameters are listed in the figures, as well.

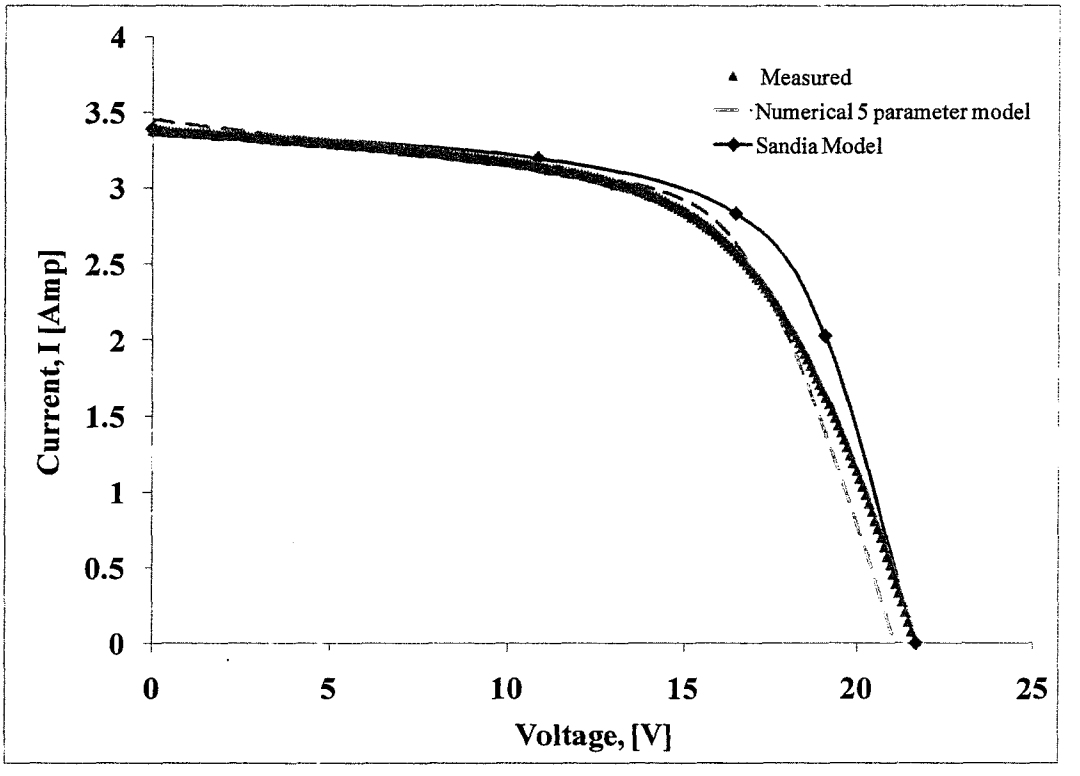

Figure 4.7. Models comparison to I-V measurements for November 28th, 2009.

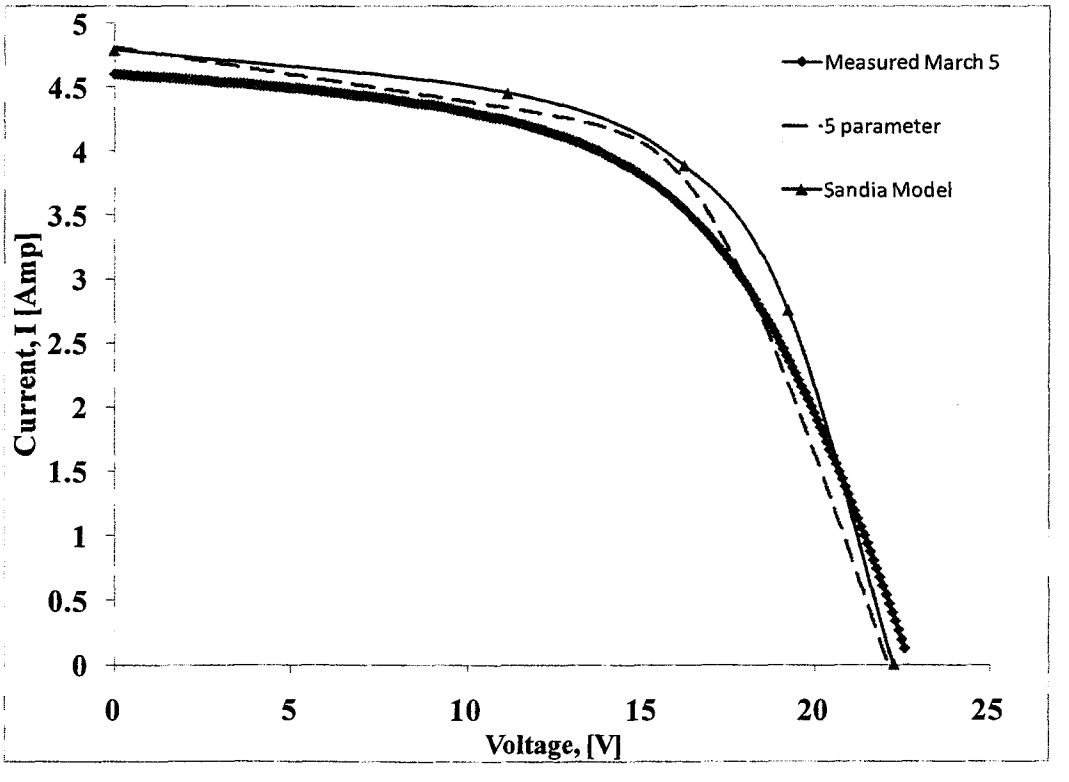

Figure 4.8. Models comparison to I-V measurements for March 5th, 2010.

Table 4-4. Models comparisons for November 28th, 2009 (AST = 12.4hr).

Input Parameters	Measured	Five-parameter model	Sandia Model
I_t =734 W/m^2			
θ_z=67.2°			
θ =37.5°			
T_{back}=40°C			
G_a = 656.75 W/m^2			
MP	43.1 W	44.3 W	46.6 W
V_{peak}	15.8 V	15.7 V	16.5 V
I_{peak}	2.7 A	2.8 A	2.9 A

Table 4-5. Models comparisons for March 5th, 2009 (AST = 11.4hr).

Input Parameters	Measured	Simulated with Five-parameter model	Simulated with Sandia Model
I_t =974 W/m^2			
θ_z=57.5°			
θ =24°			
T_{back}=33°C			
G_a = 933 W/m^2			
MP	57.5 W	61.5 W	62.9 W
V_{peak}	15.7 V	15.7 V	16.2 V
I_{peak}	3.7 A	3.9 A	3.9 A

In both Figure 4.7 and Figure 4.8, the numerical models were compared using the maximum measured temperature in the PV back surface as the temperature input. The input and the measured data are summarized in Table 4-4 and Table 4-5. For November 28th, 2009, the two models' predictions agree more with the measurement than the predictions for March 5th. The five-parameter model over-predicts the maximum electrical power production by 2.3%, while the Sandia model over predicts the maximum power by 8.12%. However, the Sandia model gives a better prediction for the I_{sc} and V_{oc} conditions.

For March 5th, 2010, the five-parameter model over-predicts the maximum power by 7% whereas the Sandia model over-predicts it by 9.4%. The better agreement of the numerical models for November 28th when compared to March 5th, can be explained by the fact that the air mass modifier predicts a lower amount of absorbed solar radiation for November

28th. On November 28th the correction for the air mass is 0.93 whereas for March 5th the correction is 0.99.

In conclusion, the most complete model of the two is the Sandia Array performance model. It was found that the five-parameter single-diode model might not give accurate results when the temperature of the panel is above 40°C. It must be noted that none of the two models offer corrections for PV output degradation and this should be addressed by future models.

5. Transient and Steady State Models for Open-Loop Air-Based BIPV/T Systems

5.1 Introduction

Air-based BIPV/T systems are usually installed in an open-loop configuration (see Figure 5.1), in which outdoor air is used to cool the PV modules by convection (commonly forced convection). The heated air is used to provide thermal energy to one or more functions in the building before being exhausted to the exterior. Open-loop air systems are normally preferred over closed loop air systems as the latter would likely lead to overheating of the PV (reducing its durability and possibly causing delamination) unless fins are built into the PV design. It has been reported by (King, D.L. *et al.*, 2000b) that delamination is more common and more severe in hot and humid climates, sometimes occurring after less than 5 years of exposure. Also, open-loop systems allow for the potential use for fresh air preheating. Since the inlet temperatures are lower than in the case of closed-loop systems, the BIPV/T system normally operates with higher thermal efficiencies, although its air exit temperatures are lower.

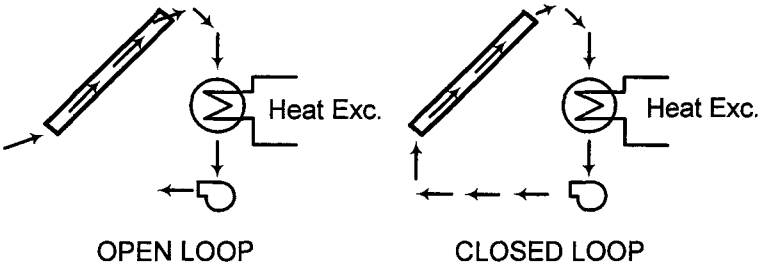

Figure 5.1. Open and closed loop configurations for solar collectors (the heat exchanger may be eliminated in the open loop configuration).

BIPV/T systems contain several features that complicate their study, such as heating asymmetry and a relatively complex geometry. Mathematical models of different levels of complexity, emphasizing different phenomena, have been developed over the years (a brief literature review is presented below). This chapter presents two models bringing together some of the ideas presented in previous works by the authors, and the most relevant findings obtained from measurements at the experimental facilities and demonstration projects of the Canadian Solar Buildings Research Network (Athienitis, 2008). The models could readily be adapted as a design tool for air-based open-loop BIPV/T systems in cold climates. By incorporating meteorological data, this model can be used as a decision-making tool in pre-feasibility studies.

5.2 Existing Numerical Models

As presented in chapter 2, mathematical models for the particular case of forced-convection open-loop BIPV/T systems have been developed by Clarke *et al.* (1997) , Eicker and Fux (2000) , Bazilian *et al.* (2001), Bazilian and Prasad (2002), Eicker (2003) and Bloem (2004). Models for air hybrid photovoltaic/thermal (PV/T) collectors – not necessarily installed as a building component – have been developed by several researchers. Examples include the work of Sopian *et al.* (1996) (thermal model for single and double pass hybrid PV/T air collector); Garg and Adhikari (1997) (hybrid solar air collectors); and Hegazy (2000a) (four configurations of hybrid PV/T systems).

Models of naturally ventilated BIPV systems have also been studied by several researchers. Moshfegh and Sandberg (2001) have carried out CFD simulations of naturally ventilated PV façades with heating on one side to simulate solar radiation. Yang *et al.* (1996)

developed a numerical model for a natural ventilated PV roof and façade system. Brinkworth *et al.* (2000) presented a model for a natural ventilated PV roof installation. A model of a PV/T air façade was developed in TRNSYS and presented by Bosanac *et al.* (2003). Mittelman *et al.* (2009) developed a natural ventilated model where Nusselt numbers are also reported.

At Concordia University, different BIPV/T numerical models have been developed both for research on these systems and as design tools for demonstration projects. These models include the works by Charron (2004), Charron and Athienitis (2006a; 2006b), Athienitis *et al.* (2005), Liao (2005), Liao *et al.* (2007), Pantic (2007), Candanedo *et al.* (2007), Chen *et al.* (2007b) and Candanedo *et al.* (2009).

The aforementioned models, based on energy balances in control volumes, have used different levels of complexity to model the energy interactions between the surfaces. Some of the most relevant differences in approach are presented below:

5.3 Common Modelling Approaches

5.3.1 Steady state vs transient solution.

The vast majority of the models have relied on a steady state approach, neglecting the thermal capacitance effects of the PV module. In contrast, Ito *et al.* (2006) developed a fully-explicit finite difference model for a solar air collector. The authors found that the transient model is useful to account for the effects of rapid changes (e.g., variable cloudiness, wind speed fluctuations), and therefore it can be useful for the development of robust control algorithms for control of flow rate.

5.3.2. Air temperature variation within the control volume.

The simplest approach uses a linear approximation to model the air temperature variation within the CV (Ong, K.S., 1995b). In this case, the average air temperature inside the control volume is the arithmetic mean of the inlet and outlet temperatures. However, most recent investigations use an exponential air temperature variation, which is the exact solution if the temperatures of the surrounding surfaces are assumed to be uniform inside the CV. The average air temperature (used for the energy balances) is calculated as $\mathrm{Tavg} = \int \mathrm{Tdx}/\Delta\mathrm{x}$.

5.3.3. Radiative heat transfer.

Most investigations have used the mean temperature of the surrounding surfaces (T_m) to calculate a linearization factor ($4\sigma T_m^3$), as this facilitates the solution of the equations. The radiatiave heat transfer coefficient, h_r is given then by $4\sigma T_m^3 / \left(\frac{1}{\varepsilon 1} + \frac{1}{\varepsilon 2} - 1\right)$, assuming a view factor of 1 between the plates. The radiation exchange difference by using this coefficient assuming two plates at 350 and 273 K is about 1.5% underestimated from the exact value given by the equation:

$$h_r = \sigma(T2^4 - T1^4) / \left(\frac{1}{\varepsilon 1} + \frac{1}{\varepsilon 2} - 1\right) \qquad 5.1$$

5.3.4. Effect of view factors.

The majority of the models assume, often without stating it explicitly, that the view factor between the two surfaces of interest is close to 1. In reality, this assumption is not always accurate. Charron (2004) took view factor calculations for radiative heat transfer modelling into account.

5.3.5. Convective interior heat transfer correlations.

As explained above, heat transfer in BIPV/T has several particularities due to the asymmetric heating (i.e., heat transfer occurs mainly through one side of the BIPV/T channel) and the more complex geometry. However, most researchers have used Nusselt number correlations developed for pipes and ducts with uniform boundary conditions for a given cross section, such as the classic correlation by Dittus and Boelter (1930), and the Pethukov equation (Bazilian, M. *et al.*, 2001; Eicker, U., 2003). These correlations tend to underestimate convective heat transfer coefficients, because several heat-transfer enhancing factors are not taken into account, such as the presence of the framing structure and surface imperfections (which act as turbulence promoters) and developing flow conditions at the inlet.

5.3.6. Convective and radiative exterior heat transfer coefficients.

The determination of the heat loss to the surroundings has been carried out through many different approaches. The McAdams formula reported by Duffie and Beckman (2006) developed in the 50s, combines radiation and convection into one coefficient. The McAdams formula has often been used (Ong, K.S., 1995b; Ito, S. *et al.*, 2006). This approach is satisfactory for glazed collectors, since the addition of the glass layer significantly increases the insulation, and the effect of the exterior heat transfer coefficients becomes less important. Most researchers separate exterior heat losses in two components: convection to the exterior air and radiation to a representative sky temperature. The convective heat transfer correlations by Test (1981) and Sharples and Charlesworth (1998) were developed for roof-mounted flat-plate collector and are preferable to the McAdams formula, as confirmed by the experimental observations mentioned in this paper. Both correlations have

been used in modelling BIPV/T systems (Chen, Y., 2009). The Model by Berdahl and Martin (1984) presented a simplified calculation for a representative sky temperature, which can be used to calculate radiative heat transfer losses.

5.3.7. Incidence angle adjustments.

Few researchers have accounted for the effect of the variation of the optical properties (transmittance, reflectance, absorptance) of the significant surfaces as a function of the angle of incidence. In contrast, incidence angle adjustments has often been considered in investigations dealing with the electrical performance of PV and BIPV systems (Fanney, A.H. *et al.*, 2003; King, D.L. *et al.*, 2004).

5.3.8. Effect of moisture content.

Moisture has an important effect on the physical characteristics of the fluid, in particular on the effective specific heat of the air, accounting for a 1-4% increase with respect to the specific heat of dry air. This effect is less significant under cold winter conditions.

5.3.9. Inlet air temperature effects.

In BIPV/T systems, the inlet air temperature is sometimes slightly higher than the exterior air temperature. This is especially true in BIPV/T roofs, where the inlet air has been warmed by thermal energy released by the building's façade. However, few works have considered this effect in BIPV/T modelling (Saelens, D. *et al.*, 2004).

5.3.10. Electrical efficiency modelling.

Most BIPV/T investigations account for the effect of the PV modules' temperature on their electrical efficiency with a very simple linear model (Candanedo, J.A. *et al.*, 2007).

5.3.11 Equations solving method.

A common approach has been to linearize all the equations and solve the resulting linear system by matrix inversion. Since the system of equations is relatively robust, it can be solved by the simple method of assuming guess values and iterating until a convergence criterion is met. When the effects of thermal inertia are considered, a transient method, such as the fully explicit finite difference method has been used.

5.3.12 Pressure drop.

The modelling of the pressure drop in the air channel has been largely overlooked in most previous work. It is worth mentioning, however, that the measured pressure drops along BIPV/T roofs and façades is often much smaller than the pressure drop along the ducting system. Pressure drop is evidently a strong function of the geometric configuration of the channel, especially of the framing system used to support the BIPV/T. Since the modules repeat themselves at regular intervals, the air pressure follows a "spatially periodic" variation inside the BIPV/T channel, with an overall linear trend.

5.4 Experimental Facility

The models developed are based on the experimental setup and the inputs to the models are provided from the experimental data obtained in a test channel located at Concordia University, which is shown in Figure 3.3. The BIPV/T channel was built to simulate a section of the roof at the EcoTerra demonstration house (Chen, Y. *et al.*, 2007a). It is shorter in length due to practical construction limitations. The top of the channel consists of an amorphous PV module, with 6% efficiency under standard test conditions, glued to a 0.5 mm (0.02 in.) stainless steel sheet. The bottom of the channel consists of 2 inches of

polysterene insulation R-10 (1.76 Km^2/W) and 3/8 in. thick plywood board (see Figure 3). There is a 1.57 in (0.04 m) gap between the PV module and the board (D). A wooden frame keeps the top and bottom parts together. The channel's length (L) in the flow direction is 112 in. (2.84 m), and its width is 15.23 in. (0.387 m). The channel is oriented with a due-south azimuth angle and a tilt angle (β) of 45°.

The visible reflectance of the PV module surface has been measured with a reflectometer as 4.3% at a normal incidence angle and it would be expected that the solar value would be close to the visible one. The longwave emissivity of the amorphous PV panel has been taken as 0.95 (LESO-PB/EPFL, L. *et al.*, 2000). The measured emissivity of the steel plate is 0.80 while the corresponding value for the insulation board is 0.20. Thermocouples are installed at the interior surface of the PV module and on the insulation (i.e., top and bottom of the channel) at nine different positions along the channel. Other measured variables include the electrical output of the PV module, solar irradiation, wind speed and relative humidity. No thermocouples were installed on top of the PV module, as the resulting shading would have reduced the electrical output.

The air flow rate was controlled in the experiments; it was measured with a laminar flow element, with an accuracy of 0.4% of the full-scale (105 CFM). The maximum achievable flow rate in the channel is 23.6 L/s (50 CFM), corresponding to an average air velocity in the channel of 1.55 m/s (5 ft/s).

The amorphous PV module is constructed from different layers. These are from top to bottom, Tefzel, antireflective coating, amorphous silicon, a backing substrate, Tefzel, adhesive and a stainless steel layer to where it was pasted. The Models used the material properties summarized in Table 5-1.

Table 5-1. Material Parameters.

Layer	Parameter	Value IP (SI)
TEFZEL	Thickness	0.039 in. (1 mm)
TEFZEL	Density	109.2 lbm/ft^3 (1750 kg/m^3)
TEFZEL	Specific Heat	0.251 Btu/lbm°F(1050 J/kg·K)
TEFZEL	Thermal conductivity	0.139 Btu/h·ft°F (0.24W/m·K)
Anti reflective coating	Thickness	1.9×10^{-5} in. (5E^{-4}mm)
Silicon	Thickness	1.9×10^{-5} in. (5E^{-4}mm)
Silicon	Density	145.4 lbm/ft^3 (2330 kg/m^3)
Silicon	Thermal conductivity	85.5 Btu/h·ft°F (148 W/m·K)
Backing substrate (steel)	Thickness	7.87×10^{-3} in. (0.2 mm)
Backing substrate (steel)	Density	493.181 lbm/ft^3 (7900 kg/m^3)
Backing substrate (steel)	Specific Heat	0.114 Btu/lbm°F(477 J/kg·K)
Backing substrate (steel)	Thermal conductivity	8.61 Btu/h·ft°F (14.9 W/m·K)
TEFZEL	Thickness	0.039 in. (1mm)
Adhesive (Ethylene propylene copolymer)	Thickness	0.024 in. (0.6 mm)
Adhesive (Ethylene propylene copolymer)	Density	134.22 lbm/ft^3 (2150 kg/m^3)
Adhesive (Ethylene propylene copolymer)	Specific Heat	0.263 Btu/lbm°F (1100 J/Kg·K)
Adhesive (Ethylene propylene copolymer)	Thermal Conductivity	0.116 Btu/h·ft°F (0.2 W/m·K)
Steel sheet	Thickness	0.02 in. (0.5 mm)

5.5 Proposed Models: Steady State and Transient

Assumptions:

- The temperatures of the surfaces (PV, steel sheet, insulation board) are assumed to be uniform inside the control volume.
- The resistance of the PV module is taken into account in the calculations.
- No temperature variations are considered across the width of the channel (1-D simulation inside the control volume).
- No edge effects are considered.
- Properties of solid materials remain constant and uniform.
- No air leakage or mixing with exterior air after entering the air gap.
- No humidification or dehumidification of the air stream.

Convective heat transfer is higher at the entrance region before fully developed conditions are established. However, since the focus of this study is the final air temperature and the average PV module temperature, a single uniform value was used for the interior convective heat transfer coefficients (h_{ct}, h_{cb}) for a given air speed.

Models Considered

The two models considered here are shown schematically in Figure 5.2. The two models are identical except in one respect: steady state model does not consider the thermal capacitance of the PV panel (making it a steady-state model), while transient model takes into account the thermal inertia (capacitance) of the PV panels. In a dynamic simulation, the solution of the equations of the steady state model is independent of previous conditions. In

contrast, at every time step, the transient model requires the solution of the previous time step with a fully-explicit finite difference scheme. The programming tool MATLAB is used to numerically find the solution of both models.

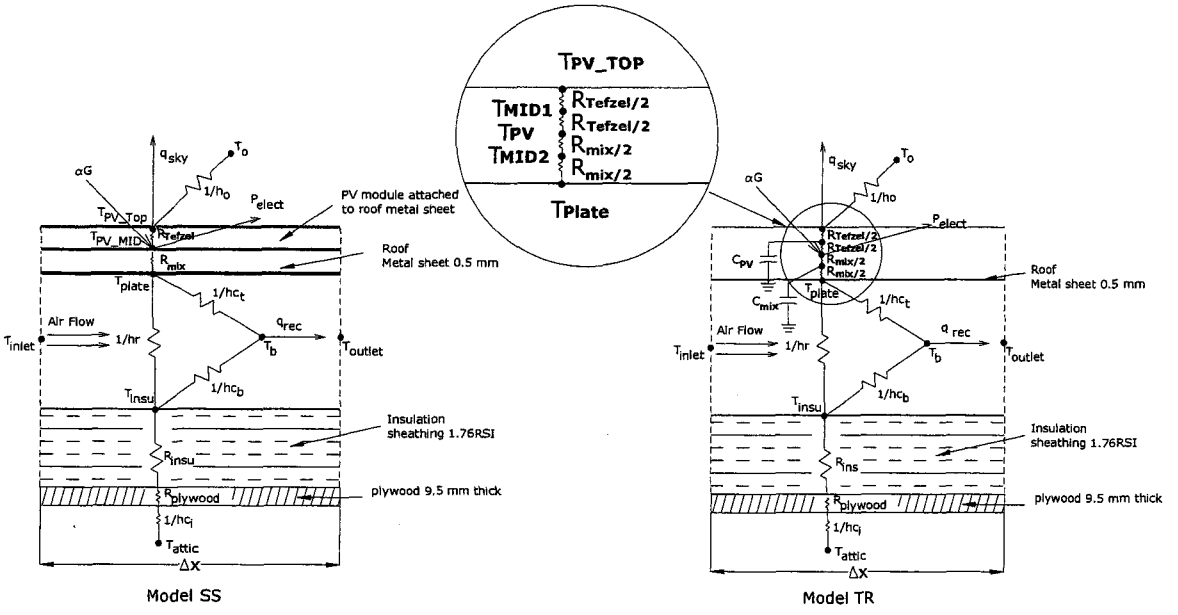

Figure 5.2. Models studied: Model SS (steady state) and Model TR (transient).

5.5.1 Steady state (SS) model

The equations corresponding to a representative control volume in Model SS are shown below. Equations 5.2 through 5.6 respectively correspond to energy balances at the top surface of the PV module, middle of the PV module, bottom surface of the Plate, air node and the surface of the insulation:

$$\frac{T_{PV_{MID}} - T_{PV_{TOP}}}{R_{Tefzel}} - \varepsilon_1 \sigma \left({T_{PV_{TOP}}}^4 - {T_{sky}}^4 \right) - \left(T_{PV_{TOP}} - T_o \right) h_o = 0 \qquad 5.2$$

$$0.96 K \tau \alpha_b (\theta) (\tau \alpha)_n I_T - P_{elect} - \frac{\left(T_{PV_{MID}} - T_{PV_{TOP}} \right)}{R_{Tefzel}} - \frac{\left(T_{PV_{MID}} - T_{Plate} \right)}{R_{MIX}} = 0 \qquad 5.3$$

$$\frac{\left(T_{PV_{MID}} - T_{PV_{TOP}} \right)}{R_{MIX}} - q_{rad} - (T_{Plate} - T_b) h_{ct} = 0 \qquad 5.4$$

$$(T_{Plate} - T_b) h_{ct} + (T_{insu} - T_b) h_{cb} = q_{rec} \qquad 5.5$$

$$q_{rad} - (T_{insu} - T_b) h_{cb} - \frac{(T_{insu} - T_{attic})}{R_{ins} + R_{plywood} + \frac{1}{hc_i}} = 0 \qquad 5.6$$

$$q_{rad} = \sigma F_{plate,insu} \left(\frac{1}{\varepsilon_2} + \frac{1}{\varepsilon_3} - 1 \right)^{-1} \left({T_{Plate}}^4 - {T_{insu}}^4 \right) \qquad 5.7$$

$$\eta_{PV} = \eta_{STC} + \beta_{mp} \left(T_{PV_{MID}} - 25°C \right) \qquad 5.8$$

$$P_{elect} = \eta_{PV} I_T \qquad 5.9$$

$$T_{outlet} = T_{inlet} + \frac{A_{cv} q_{rec}}{\dot{m} c_{p_{air}}} \qquad 5.10$$

$$T_b = \frac{1}{\Delta x} \int_0^{\Delta x} \left(\frac{h_{ct} T_{Plate} + h_{cb} T_{insu}}{h_{ct} + h_{cb}} + (T_{inlet} - \frac{h_{ct} T_{Plate} + h_{cb} T_{insu}}{h_{ct} + h_{cb}}) e^{\frac{-W_{PV}(h_{ct} + h_{cb})}{\dot{m} c_p} x} \right) dx \qquad 5.11$$

In the equation system presented above, there are ten unknowns: $T_{PV_{TOP}}$, $T_{PV_{MID}}$ T_{Plate}, T_b, q_{rad}, η_{PV}, P_{elect}, T_b, T_{outlet} and q_{rec}. The rest of the variables (solar radiation, exterior temperature, mass flow rates, material properties, etc.) are known inputs. However, several additional equations are used:

The view factor $F_{Plate,insu}$ is calculated as a function of geometric parameters (Incropera, F.P. & De Witt, D.P., 2002).

The absorptance α of the exposed PV surface is corrected as a function of the angle of incidence of beam solar radiation, as described by King *et al.* (1997) and in chapter 3 (see equation 4.18). The effect of the angle of incidence is significant during the early morning hours and late afternoon hours. For these models, a correction curve developed specifically for the amorphous PV laminate, calculated according to the procedure described by King *et al.* (1997) and available at the Sandia National Laboratories database (2006), was used. The value of $(\tau\alpha)_n$ has been taken as the difference of 1minus the measured visible reflectance at 90 degrees, (1-0.043) = 0.957.

The sky temperature employed to calculate radiative heat losses to the exterior is obtained with the following correlation (Duffie, J.A. & Beckman, W.A., 2006) :

$$T_{sky} = T_a\left(0.711 + 0.0056T_{dp} + .000073{T_{dp}}^2 + 0.013\cos\left(\frac{\pi \cdot t}{12}\right)\right) \qquad 5.12$$

The specific heat of air (c_p) has been calculated for the conditions of temperature and relative humidity measured at the inlet of the channel.

The exterior convective heat transfer is obtained using different correlations to compare their effects on the results. These are the correlations by Test *et al.* (1981), Sharples and Charlesworth (1998), McAdams (McAdams, W.H., 1954; Duffie, J.A. & Beckman, W.A., 2006) as a function of the wind speed in m/s:

$$h_o = 8.55 + 2.56 \cdot V_{wind} \qquad 5.13$$

$$h_o = 11.9 + 2.2 \cdot V_{wind} \qquad 5.14$$

$$h_o = 5.7 + 3.8 V_{wind} \qquad 5.15$$

The wind speed was measured on site at a height of 10 m above ground in downtown Montreal. The measured wind speed has been adjusted to the average height of the BIPV/T system using the following relationship (Hutcheon, N.B. & Handegord, G.O.P., 1995)

$$V_{wind} = V_g \left(\frac{Z}{Z_g}\right)^{\alpha_w} \qquad 5.16$$

In the previous equation, V_{wind} is the wind speed at the BIPV/T system height, V_g is the measured wind speed at 10 m, Z_g is the height where the wind speed is measured (10 m) and Z the average height of the BIPV/T system. The α_w is the mean speed exponent, and it has been taken as 0.36, which corresponds to the value recommended for a location in a city center (Hutcheon, N.B. & Handegord, G.O.P., 1995).

The interior convective heat transfer coefficients (h_{ct} and h_{cb}) have been calculated using the average Nusselt number correlations developed in chapter 4 (Equations 3.25, 3.26).

The asymmetric heating conditions inside the channel cause h_{cb} to be much larger than h_{ct}, with the consequence that the average air temperature (T_b) is closer to T_{insu} than to T_{Plate}. This result has been confirmed by CFD analysis (see Figure 5.3) and experimental results in the channel.

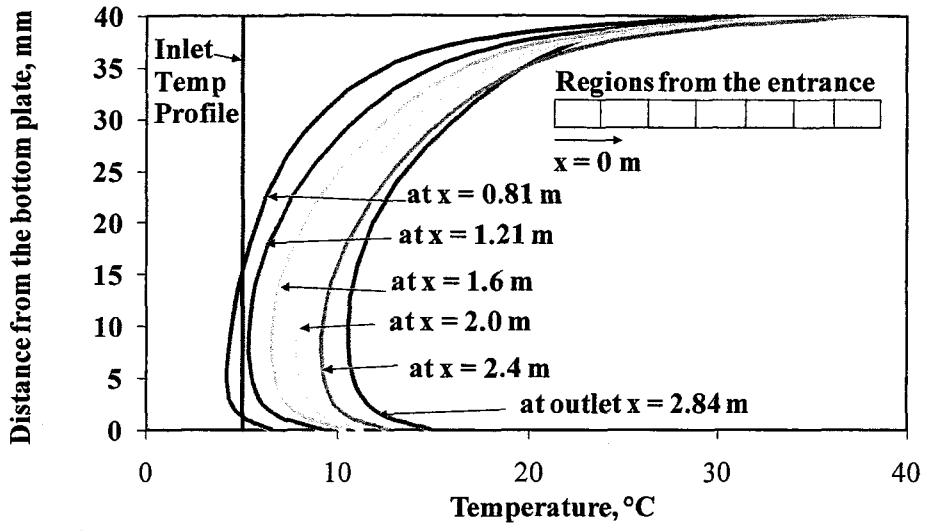

Figure 5.3. Air temperature profiles within the channel as predicted by CFD simulations.

It is evident from Figure 5.3 that the average air temperature is closer to the temperature measured at the bottom of the channel. However, the heat flux through the top of the channel is much larger than the heat transferred from the bottom of the channel to the airstream. As the insulation creates nearly adiabatic conditions, heat loss through the bottom is practically negligible.

5.5.2 Transient (TR) Model

As mentioned above, the transient model includes the thermal capacitance of the PV module. In this case, a fully-explicit scheme has been used (the temperatures for the current time step depend only on the temperatures of the previous time step). Equation 5.19 corresponds to the energy balance in a node associated with a mid-layer of the PV module. This node has a capacitance per unit area of 1800 J/Km^2, obtained from estimates of

material properties. Capacitances are included only in the top part of PV module, since it is exposed to rapidly changing weather conditions including wind and irradiance, whereas the bottom of the channel is insulated. The equations corresponding to the transient model are:

$$\frac{T_{MID1,i+1} - T_{PV_{TOP,i}}}{R_{Tefzel}/2} - \varepsilon_1 \sigma \left({T_{PV_{TOP,i+1}}}^4 - {T_{sky,i+1}}^4 \right) - \left(T_{PV_{TOP,i+1}} - T_{o,i+1} \right) h_o = 0 \quad 5.17$$

$$T_{MID1,i+1} = T_{MID1,i} + \frac{\Delta t}{C_{PV}} \left(\frac{T_{PV_{TOP,i}} - T_{MID1,i}}{R_{Tefzel}/2} + \frac{T_{PV,i} - T_{MID1,i}}{R_{Tefzel}/2} \right) \quad 5.18$$

$$T_{PV,i+1} = \frac{\left(\frac{T_{MID1,i}}{R_{Tefzel}/2} + \frac{T_{MID2,i}}{R_{Mix}/2} + 0.96 K \tau \alpha_b (\theta)_i (\tau\alpha)_n I_{T,i} - P_{elec,i} \right)}{\frac{1}{R_{Tefzel}/2} + \frac{1}{R_{Mix}/2}} \quad 5.19$$

$$T_{MID2,i+1} = T_{MID2,i} + \frac{\Delta t}{C_{PV}} \left(\frac{T_{PV,i} - T_{MID2,i}}{R_{Mix}/2} + \frac{T_{Plate,i} - T_{MID2,i}}{R_{Mix}/2} \right) \quad 5.20$$

$$q_{rec,i+1} = \left(T_{Plate,i} - T_b \right) h_{ct} + \left(T_{insu} - T_b \right) h_{cb} \quad 5.21$$

$$T_{insu,i+1} = \frac{T_{b,i} h_{cb} + \frac{T_{attic,i}}{R_{ins} + R_{plywood} + {}^{1}/_{hci}} + q_{rad,i}}{h_{cb} + \frac{1}{R_{ins} + R_{plywood} + {}^{1}/_{hci}}} \quad 5.22$$

$$q_{rad,i+1} = \sigma F_{plate,insu} \left(\frac{1}{\varepsilon_2} + \frac{1}{\varepsilon_3} - 1 \right)^{-1} \left({T_{Plate,i}}^4 - {T_{insu,i}}^4 \right) \quad 5.23$$

$$\eta_{PV,i+1} = \eta_{STC} + \beta_{mp} \left(T_{PV,i} - 25°C \right) \quad 5.24$$

$$P_{elect,i+1} = \eta_{PV,i} I_{T,i} \quad 5.25$$

$$T_{outlet,i+1} = T_{inlet,i} + \frac{A_{cv} q_{rec,i}}{\dot{m}_i c_{p\_air_i}} \qquad 5.26$$

$$T_{b,i+1} = \frac{1}{\Delta x}\int_0^{\Delta x}\left(\frac{h_{ct}T_{Plate,i} + h_{cb}T_{insu,i}}{h_{ct} + h_{cb}} + (T_{inlet,i} - \frac{h_{ct}T_{Plate,i} + h_{cb}T_{insu,i}}{h_{ct} + h_{cb}})e^{\frac{-W_{PV}(h_{ct}+h_{cb})}{\dot{m}_i c_{p\_air_i}}x}\right)dx \qquad 5.27$$

The magnitudes corresponding to the time step $i + 1$ are written as a function of the magnitudes of the previous time step (i). In equation 5.17, the solution for $T_{PV_{TOP},i+1}$ is found numerically with the MATLAB® function *fzero*, as the rest of the parameters are known as inputs or as the result of the previous time step. The function *fzero* uses a "combination of bisection, secant, and inverse quadratic interpolation methods" (MathWorks, I., 2010). The corrections corresponding to incidence angle, specific heat, view factor and heat transfer coefficients were also applied for the transient model.

In both the steady state and the transient models, the channel can be divided into an arbitrary number of control volumes. The inlet conditions of a control volume correspond to the outlet conditions of the previous control volume.

5.6 Results - Model Performance

The transient and steady state models were applied with input measurements (solar radiation, exterior temperature, wind speed, and channel flow rate) corresponding to February 17th, 2009. During this day, the flow rate in the channel was changed manually several times. Figure 5.4a shows the measured average air speed inside the channel, and the estimated interior heat transfer coefficients according to equations 3.25 and 3.26. The wind speed was measured during this interval as well. The correlations by Test (Equation 5.13)

Sharples and Charlesworth (Equation 5.14) and McAdams (Equation 5.15) were used to estimate the exterior heat transfer coefficient (Figure 5.4b).

In both the steady state and the transient models, four control volumes were used. Results corresponding to the average temperature of the top of the channel (Figure 5.4a) and the outlet temperature of the air (Figure 5.4b) are presented. The time step used for the transient model was 1 second. The output of both models is compared to thermocouple measurements taken at intervals of 1 minute. Exterior air temperature and solar radiation measurements are presented as well. In general, there is a reasonably good agreement between both models and the experimental results. Perhaps the most relevant difference between the models is that the temperature fluctuations predicted by the transient model are much smaller than those predicted by the steady state model. In this respect, the transient model (which includes the capacitive effect) is more accurate than the steady state model. The presence of the capacitance considerably stabilizes the temperatures in the PV module, and dramatically reduces the effect of the varying wind speed (and its associated heat transfer coefficient) and solar radiation changes.

The effect of the exterior convective correlation on the average temperature of the top of the channel can be observed in Figure 5.5. In general, the McAdams correlation over-predicts the temperature of the top of the channel. Test and Sharples' correlations give better estimations to the average PV bottom surface temperature. Although the Sharples correlation give better results, for high wind velocities it seems to overestimate the exterior heat coefficient (h_o) value.

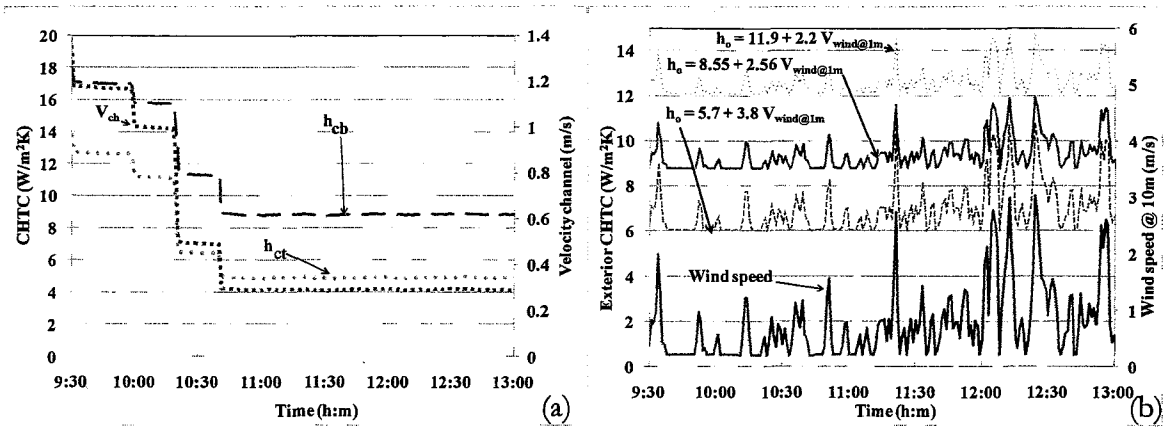

Figure 5.4. (a) Measured average air speed in the channel, and estimated interior heat transfer coefficients; (b) Wind speed and exterior heat transfer coefficient.

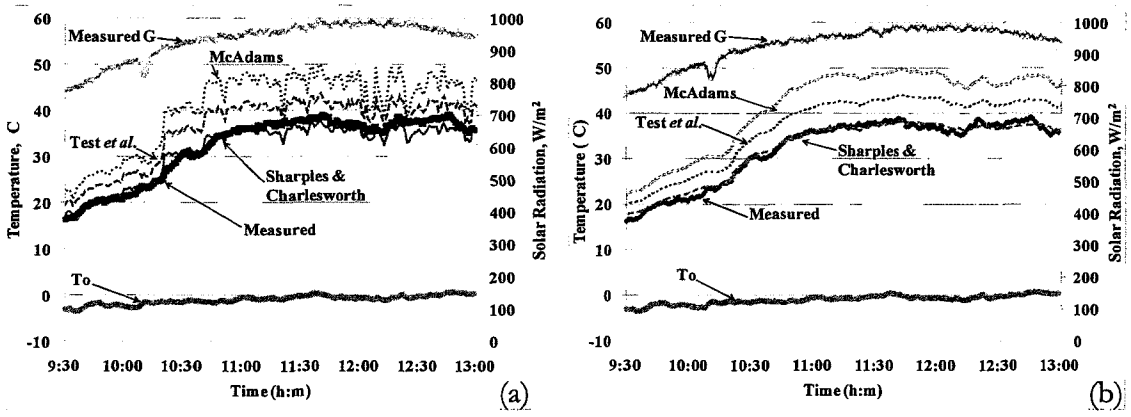

Figure 5.5. (a) Average temperature of the top of the BIPV/T channel (measurements, Model SS), (b) Average temperature of the top of the BIPV/T channel (measurements, Model TR) Solar radiation incident on collector (G) and exterior air temperatures (T_o) are also shown.

The predicted outlet air temperature obtained with Sharples and Charlesworth correlation with the SS and TR models is plotted in Figure 5.6. The agreement with the experimental data was good in general.

The Sharples and Charlesworth correlation seem to yield the best agreement. The transient model with Test correlation practically mirrors the measured curve with an offset of a few degrees, which becomes smaller between 12:00 and 13:00. Interestingly, this is the time when the highest wind speed values were recorded (about 1.5 m/s, versus 0.5 m/s earlier in the day). This result suggests that the test correlation under-predicts h_0 at low wind speeds. This can be attributed to local natural convection effects (not considered in most correlations) that may become the dominant factor at low wind speeds.

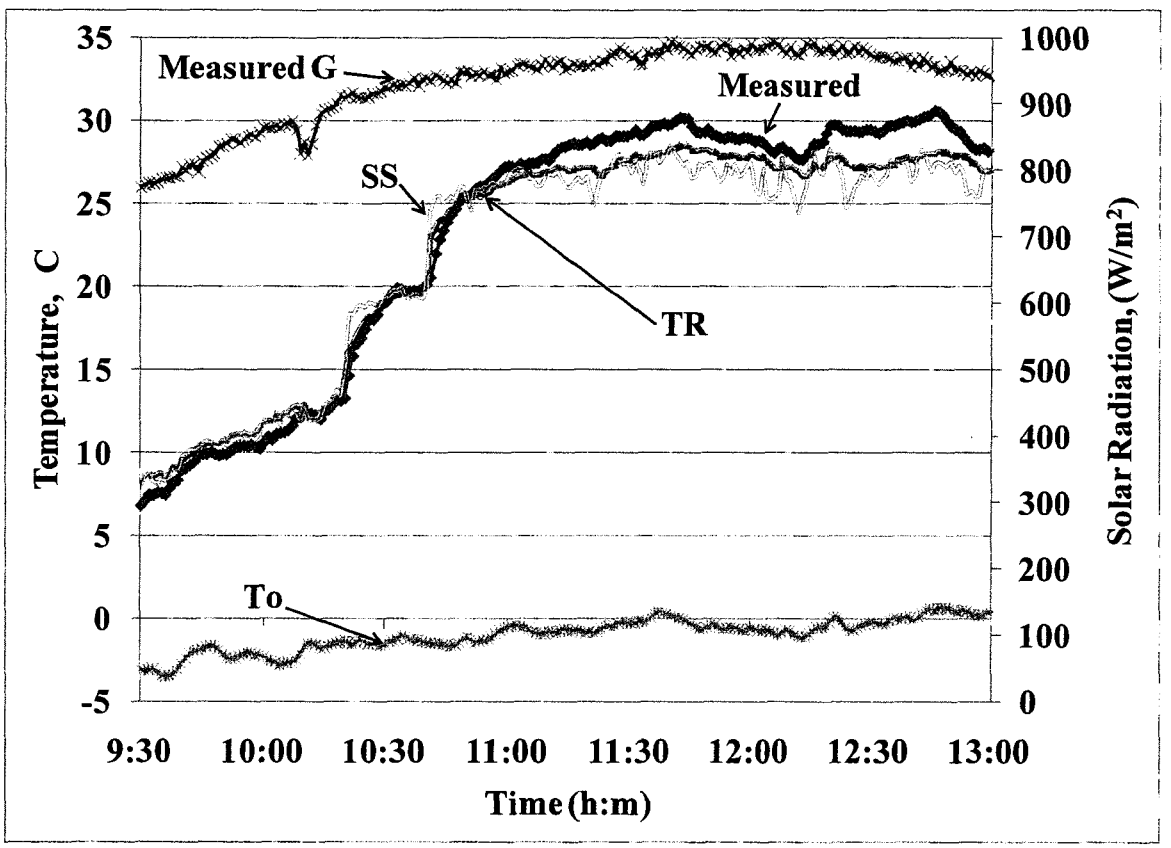

Figure 5.6. Outlet air temperatures (measurements, Model SS and Model TR).

Most researchers have neglected the resistance of the PV module, implicitly assuming that the temperature of the top and bottom faces of the PV are the same. However, recent investigations have included the resistance of the PV module (Ji, J. *et al.*, 2009). Even if the

PV resistance is very small, the heat flux across the PV module represents a difference of a couple of degrees between both sides. For example, if a heat flux of 300 W/m^2 passes through a PV module having a resistance of 0.01 Km^2/W, the temperature difference between both sides is 3 °C. This resistance is not negligible, since there are several layers of material (steel substrate, encapsulation, vinyl, adhesive, etc.).

5.7 Demonstration Project: EcoTerra House

The transient model was applied to data recorded at the EcoTerra™ demonstration house BIPV/T system (Xiang *et al.* 2007). This was a prefabricated modular house, with the BIPV/T system built as one of the modules in the factory. This is the first time such a BIPV/T system is constructed in a factory. Photographs of the BIPV/T module of the house and of the completed house are shown in Figure 5.7 and Figure 5.8. Among the input parameters used in the model are: ambient air temperature, inlet air temperature, insulation R-value, total solar radiation incident on the plane of the PV modules and flow rates. The wind speed was not being recorded for this specific day. The wind speed employed was the one of the neighboring city of Sherbrooke. The results are summarized in Figure 5.9. The length of the roof (flow path) is 5.8 m and the air cavity thickness is 0.038 m.

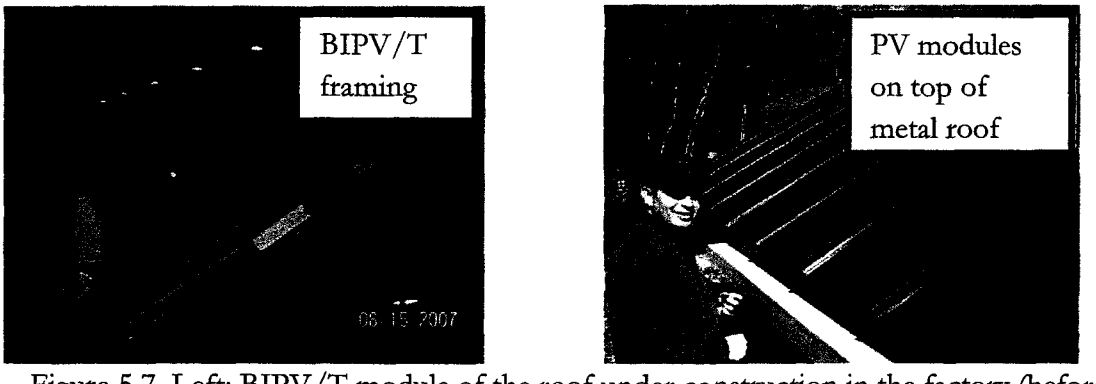

Figure 5.7. Left: BIPV/T module of the roof under construction in the factory (before installing metal layer and PV modules) Right: BIPV/T module completed (with PV modules installed).

Figure 5.8. EcoTerra™ solar house photograph.

Good agreement was observed between the measured data for the PV back surface temperature and the transient simulation result. There was good agreement for the T_b temperature. For the outlet air temperature, the agreement was acceptable but not as good as for T_{PV} and T_b. The temperature difference between 10:40 and 11:20 a.m. is probably due to the thermal capacitance of the wood framing, which is not modeled, and error in the measurement of the flow rate across the BIPV/T roof.

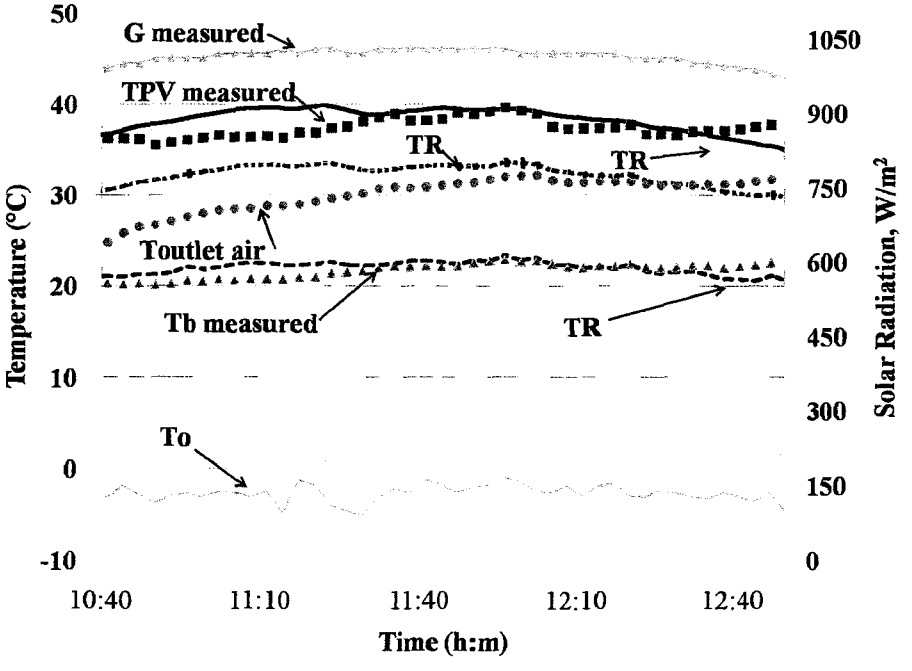

Figure 5.9. Temperature profiles for the EcoTerra house on March 17th, 2008 (measurement and Model TR)

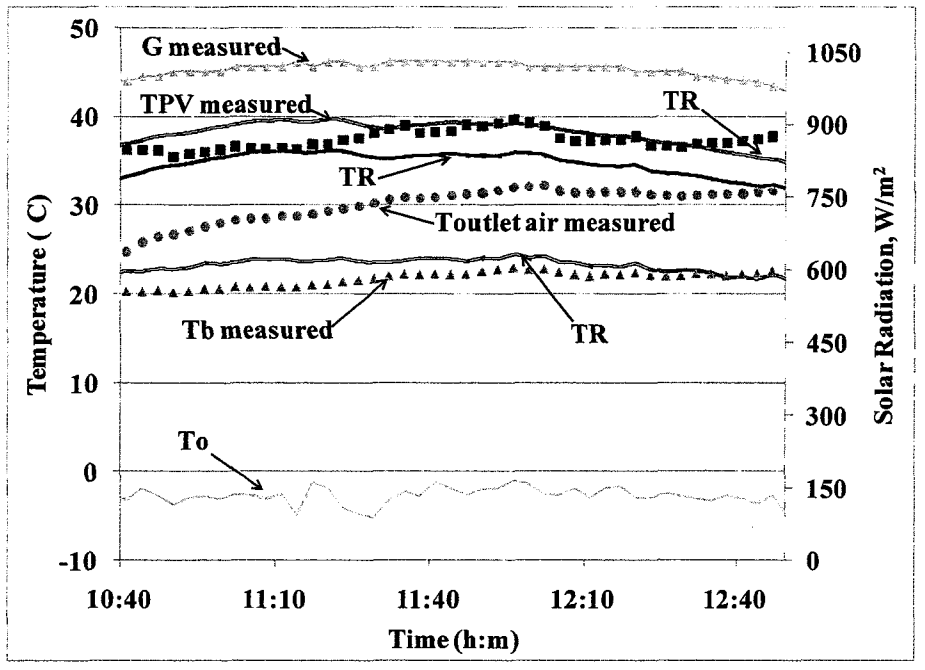

Figure 5.10. Temperature profiles for the EcoTerra house on March 17th, 2008 (measurement and Model TR using framing correlation)

5.8 Heat Removal Factor and Thermal Efficiency

If the BIPV/T channel is treated as a solar collector, a modified form of the Hottel-Whillier-Bliss equation which includes the electricity output can be written as:

$$Q_u = F_R A_c(\alpha G - P_{elect} - U_L(T_i - T_a)) \qquad 5.28$$

In this case, U_L represents the heat loss coefficient (W/m^2) from the air in the BIPV/T channel to the ambient air. Neglecting the heat loss through the bottom of the BIPV/T channel, we can write:

$$U_L = ((h_o + h_r)^{-1} + R_{PV})^{-1} \qquad 5.29$$

Ordinary solar collectors are often designed with a glazing cover and an absorber plate to prevent heat losses, and their U_L value depends mainly on geometric parameters and the materials used, and the influence of convective and radiative coefficients is small. In

contrast, in this BIPV/T channel, U_L undergoes significant changes with the convective and radiative coefficients. The heat removal factor (F_R) can be determined experimentally by solving for it in 5.28.

$$F_R = \frac{Q_U}{A_c(\alpha G - Pelect - U_L(T_i - T_a))} \qquad 5.30$$

By dividing Equation 5.28 by the solar radiation times the area (GA_c), and using the fact that $P_{elect} = \eta_{PV}G$, the following expression for thermal efficiency is obtained:

$$\eta_{Th} = F_R\left(\alpha - \eta_{PV} - U_L\frac{T_i - T_a}{G}\right) \qquad 5.31$$

Figure 5.11a shows the heat removal factor calculated with Equation 5.30 (assuming that the R_{PV} value is 0.01 RSI) for February 17th, 2009, and the thermal efficiency calculated simply as $\eta_{Th} = mc_p\Delta T/GA_c$. As expected, the efficiency is higher when the flow rates inside the channel are higher.

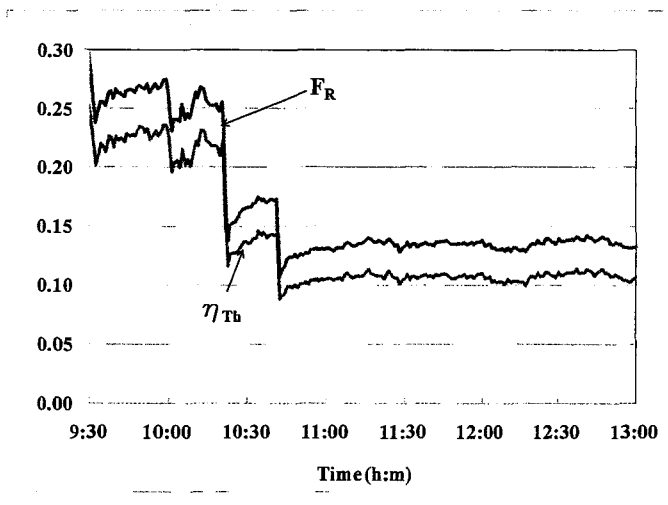

Figure 5.11. Heat removal factor and thermal efficiency of the BIPV/T channel.

As expected, for higher flow rates the efficiency is much higher (e.g. during the time period 9:30 -10:30am in Figure 5.11 due to the higher heat transfer coefficients.

5.9 Numerical Sensitivity Study of Bottom Heat Transfer Coefficient

Nusselt numbers for the bottom channel surface have a higher uncertainty and it is important to assess the impact of this on the BIPV/T performance. However, because the bottom surface is highly insulated and is not subjected to direct solar radiation, the associated uncertainty is not as critical for the quantitative evaluation of the BIPV/T system. In order to study this question, a validated numerical BIPV/T model as described in detail in (Candanedo, L.M. *et al.*, 2010) is employed to assess the sensitivity of the bottom heat transfer coefficient to the outlet temperature. The numerical model solves the system of equations presented in section 5.5.1.

First, the Nusselt number correlations for the smooth case are considered. Some model input parameters are listed below:

- Inlet air temperature = -5°C
- 5 m long BIPV/T system
- Normal incident solar radiation = 1000 W/m^2
- h_o = 10 W/m^2K
- Flow rate = $8.91\times10^{-3} m^3/s$
- Average air velocity = 0.57 m/s
- Re = 3000
- Combined thermal resistance of the insulation and plywood layer = 1.9 Km^2/W

- $D_h = 0.074$ m
- hc_t is 7.89 W/m^2K and hc_b is 13 W/m^2K (from equations (3.25) and (3.26)),
- Exposed area to solar radiation = 1.94m^2
- Longwave emissivity of insulation and metal facing cavity equal to 0.2 and 0.8 respectively.

As a result of employing the parameters above in the numerical model, the final predicted outlet air temperature is 26.92°C. If the value of h_{cb} was set to be 1.5 times more while keeping all the other parameters constant, the final outlet air temperature would be 26.91°C. This represents only a 0.01°C deviation from the first result or less than 1% error. If the hc_b was forced to be 3 times more, the final outlet air temperature would be 26.84°C. The deviation is now only 0.1°C, or less than 1% error in the final computation of outlet air temperature. If the hc_b was forced to be equal to h_{ct}, the final outlet air temperature would be 26.89, being the deviation only 0.03°C from the first result. Therefore, it can be concluded that the bottom Nusselt number uncertainty is not as important for the determination of the BIPV/T system performance.

Finally, the uncertainty in the Nusselt number correlation for the bottom surface for the framing case is studied. The same input model parameters from above are used in the steady state model, but the top and bottom heat transfer coefficients are replaced with:

- hc_t is 9.72 W/m^2K and hc_b is 81.38 W/m^2K (from equations (3.34) and (3.35))

The predicted final outlet air temperature is 28.78°C. If the value of h_{cb} was forced to be 7 times more while keeping all the other parameters constant (maximum estimated uncertainty), the final outlet air temperature would be 28.03°C. This represents only a deviation of 0.72 degrees or less than 2.5% deviation from the first result. If the value of h_{cb}

was forced to be 7 times less, the final outlet air temperature would be 29.11°C. The deviation is only 0.33°C or less than 1.2% deviation from the first result.

Therefore, it can be concluded that the bottom Nusselt number uncertainty is not as important for the determination of the BIPV/T performance.

5.10 Numerical Sensitivity Study of Insulation Level

The steady state model has been used to assess the relative influence of the insulation level to the final outlet air temperature. The objective of the test is not optimization. The model has been tested using the input parameters of section 5.9 and the average Nusselt numbers for the framing BIPV/T case. The results are plotted in a logarithmic fashion for clarity in Figure 5.12 and Figure 5.13.

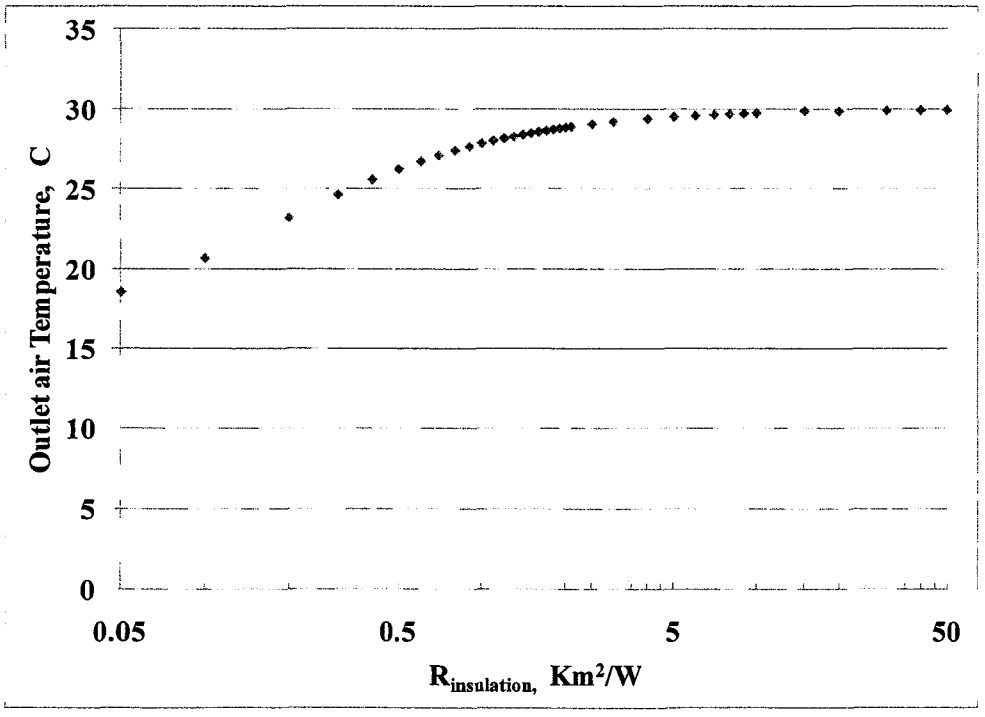

Figure 5.12. The figure shows the effect of increasing the insulation value and its effect to the outlet air temperature.

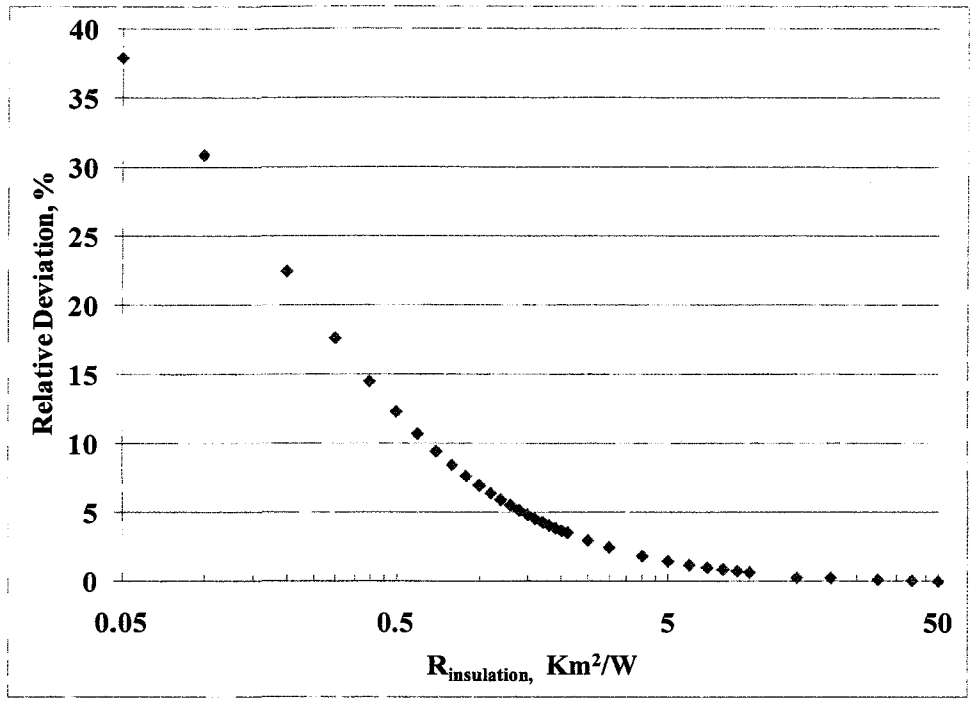

Figure 5.13. The percentage relative deviation from the outlet air temperature at 50 RSI versus the insulation level.

For RSI = 1, the outlet air temperature is 7.0% (2.1 °C deviation) of the value at 50 RSI. For RSI = 2, the outlet air temperature is 3.7% (1.1°C deviation) of the value at 50 RSI. For RSI = 5, the outlet air temperature is 1.5% (0.4°C deviation). Clearly, there are diminishing returns in terms of the outlet air temperature, with the increase of insulation level.

As can be seen in Figure 5.12, the final outlet air temperature shows an exponential trend with the insulation level. The optimum insulation level is a function of costs and design constraints and should be evaluated by the engineer.

6. Conclusion

The objective of this work has been to evaluate and model the performance of a BIPV/T system with outdoor air as the heat transfer fluid. In order to analyze BIPV/T systems, an integrated modelling approach is fundamental for the prediction of the energy fluxes. The typical geometries found in BIPV/T systems, and their particular operating conditions are such that the measurement of the effective heat transfer coefficient was essential for accurate thermal and electrical performance evaluation. In addition, a survey of the literature identified the need for the measurement of convective heat transfer coefficients in order to develop new Nusselt number correlations for BIPV/T systems. Pressure drop and friction factor information were required to assist in the design stage of BIPV/T systems. Pressure drop measurements were taken in BIPV/T systems and friction factors were calculated. Numerical models have been developed and validated against experimental data. The proposed numerical models can be readily integrated into comprehensive building energy simulations tools such as TRNSYS, EnergyPlus and ESP-r.

Experimental measurement of forced convective heat transfer coefficients for open loop BIPV/T systems with outdoor air as the cooling fluid has been carried out in this work. In particular, a roof BIPV/T system was considered because of its significant potential for collecting useful solar heat in addition to the electricity normally generated from building-integrated photovoltaic panels. The BIPV/T system studied had a length/hydraulic diameter ratio of 38 and was tested for 30-45° tilt angles. The measured data shows no significant difference in Nusselt numbers for the 30° and 45° tilt angles (except for low Reynolds number), indicating that buoyancy effects are approximately constant in this range of roof tilt angles that represent the majority of Canadian housing stock.

Because of the heating asymmetry in the BIPV/T system, separate Nusselt number correlations are recommended (for the top and bottom surfaces) at different Reynolds number ranges. However, because the (near adiabatic) bottom surface does not contribute significantly to the amount of heat added to the air, the associated uncertainty in the correlation for this surface is not as important in calculating the heat recovery by the flowing air and its outlet temperature. Forced convection dominates the heat transfer in the cases of practical interest.

This work presented correlations for the average Nusselt number for the top and bottom surfaces in the channel as a function of Reynolds number; the correlations are considered adequate for the design of BIPV/T systems where forced convection dominates. Local heat transfer coefficient distributions are also presented for laminar and turbulent flow conditions. It was found that the Nusselt numbers for the top surface of the BIPV/T channel in the present study are significantly higher than the values predicted by the smooth-pipes forced convection correlations given by Dittus and Boelter, Gnielinski, and Petukhov (Dittus, F.W. & Boelter, L.M.K., 1930; Incropera, F.P. & De Witt, D.P., 2002). Many of the experimental studies were performed for very long and horizontal pipes, and high Reynolds numbers, where buoyancy effects are minimal. The present results also confirm findings by other researchers (Eicker, U. *et al.*, 1999; Bazilian, M.D. & Prasad, D., 2002; Bloem, J.J., 2004; Charron, R. & Athienitis, A.K., 2006b) that the Nusselt numbers were underestimated. The Martinelli equation, although not developed for asymmetric heating, agrees most closely with the presented experimental data. This is due to the fact that the equation accounts for the temperature difference between the wall surface and the bulk air temperature.

Correlations 3.25 and 3.26 developed in this study are recommended for the determination of the average Nusselt number for open loop BIPV/T systems and solar air heaters at tilt angles between 30° and 45°. Correlations 3.27 and 3.28 include the developing length effect for the studied BIPV/T system. The correlations are intended mainly for BIPV/T systems working in an open loop configuration, for which the typical Rayleigh number is in the range of 1×10^5 to 9×10^5. Framing effects on Nusselt numbers were studied and it has been found that wood framing may increase the actual Nusselt numbers by about 30% (relative to correlation 3.25) due to increased turbulence. Correlation 3.34 is recommended to obtain the average Nusselt number for the top surface for the framing BIPV/T case. Correlation 3.34 gives a Nusselt number on average 2.6 times higher than that given by Dittus-Boelter correlation. These results are very close to the results presented by Promvonge and Thianpong (2008) in a rectangular ribbed channel. They found that the ratio of the measured Nusselt number to the Nusselt number given by the Dittus-Boelter correlation was around 2.7.

Friction factors for the smooth configuration and the configuration with wood framing (ribbed) have been presented. It was found that the ratio of the calculated friction factor to the one predicted by the Blasius correlation was in the range 5 to 6 for the smooth case; for the framing case the ratio ranges from 44 to 52. The higher friction factors in the smooth case are explained by the effect of buoyancy that increases the friction factor and by the high aspect ratio of the BIPV/T system. The results for the framing case agree with the results presented in the work by SriHarsha *et al.* (2009), for which the friction factors ratio (f/f_B) are in the range of 48 to 50 for Re values of 5000 to 15000. The results are also very close to the work by Promvonge, P. & Thianpong, C. (2008) where friction factors ratios (f/f_B) are in the range of 30 to 40.

Detailed electrical PV modelling was done using two of the most advanced PV models and their results were compared to field measurements. The first model presented is based on using a single-diode (five-parameter) model developed by De Soto *et al.* (2006). The second model presented is the Sandia array performance model developed by King *et al.* (1997; 1998; 2004). The two models employ corrections for the incidence angle. The De Soto *et al.* (2006) model is built upon the Sandia model in order to determine the amount of energy that is incident on the solar PV cell. Both models also correct for spectral influences due to zenith angle. It was identified that the models do not offer corrections for PV module electrical degradation. Even when the amorphous module was clean, the degradation of the solar cell is evident.

The most complete model of the two is the Sandia performance model. It was found that the five-parameter single-diode model might not give accurate results when the temperature of the cell is above 40°C. In both Figure 4.7 and Figure 4.8 the numerical models were compared using the maximum measured temperature in the back surface of the PV as temperature input. For November 28th, 2009 the two models' predictions agree best with the measurement. The five-parameter model over-predicts the maximum electrical power production by 2.3% while the Sandia model over-predicts the maximum power by 8.12%. However, the Sandia model gives a better prediction for the I_{sc} and V_{oc} conditions.

In this thesis, two models for air-based open-loop BIPV/T systems have been presented. The models included phenomena that have often been neglected, including the effect of the solar incidence angle, the resistance and capacitance of the PV module, view factors between plates and the variation of specific heat with moisture content.

In general, the transient model, which includes thermal capacity effects of the PV, follows experimental measurements better than the steady state model. The transient model indicates a more stable outlet air temperature as well, which reflects the damping effect of the heat capacitance of the materials. However, the transient model is probably not necessary for system design, as it does not significantly improve average accuracy and requires more processing time and more inputs. The transient model is suitable for development of optimal control algorithms of the air flow rate. The models performance could be improved by: (a) using a more accurate correlation for the exterior heat transfer coefficient, and (b) using experimentally measured values for resistance and capacitance.

6.2 Research Contributions

The main contributions of the research presented in this thesis can be summarized as follows:

1. The quantification of convective heat transfer coefficients and development of Nusselt number correlations for two BIPV/T systems -smooth and ribbed configurations- are presented. The Nusselt number local distributions and average values are discussed for the laminar and turbulent flow regimes.
2. The determination of thermal development lengths for laminar and turbulent flow in the smooth BIPV/T systems was studied. For laminar flow, equation 3.23 was found to give a good estimate of the development length for the smooth BIPV/T case. For turbulent flow, thermal developed conditions were reached at shorter lengths and that equation 3.24 was a good estimation for the development length. For the framing BIPV/T case in the laminar region, it was found that the Nusselt number

decayed in a consistent fashion. For the framing BIPV/T case in the turbulent region, the Nusselt number increased from the entrance indicating that the ribbed elements augmented turbulence.

3. Natural convection effects on Nusselt number have been studied, in terms of both Grashof and Rayleigh numbers for the smooth BIPV/T system. It was found that most of the data falls in the mixed convection region established by the Metais and Eckert map (1964). All the experimental data is above the limits of Grashof numbers established by the Petukhov (1976) correlations for vertical and horizontal pipes (correlations 3.1 and 3.2) that established the limit where the deviation from Nusselt number from the forced convection value would be higher than 1%. It was found that in the laminar region (for the smooth case), the effective Nusselt number can be approximated by the addition of the forced and natural convection components. For the turbulent region, the best approximation can be taken by assigning the power n to 0.638.
4. The measurement of friction coefficients and comparison with Blasius friction factor correlation. For the smooth case, the ratio of the measured friction factor to the Blasius friction factor is in the range of 5 to 6. For the framing case, this ratio is in the range of 44 to 52.
5. Electrical PV modelling development using the total impinging radiation and module temperature as inputs, with subsequent validation with measurements was done. It was found that PV module degradation must be taken into account to ensure a more accurate representation of the estimated electrical production.
6. The development of lumped parameter steady state and transient numerical models for BIPV/T systems performance evaluation was done and the modelling results are

validated with experimental data. The transient model has considered thermal capacitive effects in BIPV/T systems for the first time, and is particularly useful for control purposes. It also improves the modelling results by removing effects of quick changes in solar radiation and exterior wind speed.

7. The evaluation and identification of the most adequate available exterior wind coefficient correlations through numerical modelling is an important contribution of the research. It was determined that the correlations by Test (1981) and Sharples and Charlesworth (1998) give the best results compared to the measured data. It was found that the Test (1981) correlation tends to underestimate the exterior wind coefficients h_o at low wind speeds. This suggests that natural convection effects may become important at low wind speeds.
8. Sensitivity studies on the effect of the heat transfer coefficient for the adiabatic bottom surface show that the influence on the final outlet air temperature is less than 1%. Therefore the uncertainty in the bottom coefficient is not important for the determination of the BIPV/T system performance.
9. Sensitivity studies on the effect on final outlet air temperature due to insulation level were performed. Figure 5.12 and Figure 5.13 can be used to obtain a rapid assessment of the insulation level impact on the required final outlet air temperature.

6.3 Design Guidelines and Recommendations

The research presented in this thesis has identified some practical concepts for the optimal design and performance evaluation of BIPV/T systems. These are summarized below:

- For roof BIPV/T installations, the air intake should be placed above the south wall in order to recuperate some of the hot air layer that is heated by the wall surface from the sun. By doing so it is possible to obtain temperatures that are higher than the ambient air.
- Support roof structures for the PV modules should not have any protrusions that could potentially interfere with snow and water shedding. Moreover, the PV modules and their support structure should extend to the end of the roof to prevent any ice dam formation.
- The roof design should consider the possibility of water infiltration and precautions to avoid water damage to the structure are a must.
- The measurement of the outlet air temperature can be difficult due to thermal gradients. Towards the exit, the outlet bulk air temperature is close to the temperature of the insulation surface. The temperature of the insulation at the exit can be monitored for comparison as well.
- When designing a BIPV/T system with flexible amorphous PV modules, materials with low thermal conductivity should be avoided in the selection of a surface on which to mount the PV modules. A high thermal resistance would decrease the recuperated heat.
- PV module construction can be optimized for BIPV/T applications. The backing of the PV silicon layer could consist of a thin layer of a highly conductive material to facilitate the conductive heat transfer. The emissivity of the backing material should be increased to improve radiation heat transfer. Antireflective coatings have been proven to increase electrical and thermal efficiencies in PV/T collectors (Santbergen, R. *et al.*, 2008), and should be considered in BIPV/T designs.

6.4 Recommendations for Future Work

Further research is recommended in the following areas:

- The quantitative evaluation of energy performance assessment and comparison of different BIPV/T systems designs may be carried out considering different parameters such as: photovoltaic modules physical characteristics, climatic conditions, utility rates, construction type (residential/commercial, new /retrofits). This will permit accurate feasibility studies.
- Investigation of Rayleigh number effects on Nusselt number needs to be studied. The Rayleigh number in the collected experimental data was in the order of magnitude of 10^5. An indoor experimental investigation would allow for detailed studies of the Rayleigh number and its influence on Nusselt number. A more adequate Nusselt number correlation should be presented as a function of the combined effects of Reynolds, Rayleight and Prandtl numbers.
- The determination of the optimal operating point for thermal energy collection versus fan power is required for typical applications.
- Research on snow shedding is necessary. The surfaces of PV modules have different roughness levels that can affect how easily snow slides down, and this should be evaluated. The assessment of the tilt angle impact on snow shedding should also be studied.
- The overall thermal and electrical efficiency of the system should be optimized through the careful system installation of the system into the building structure and wiring arrangement.

- Coupling options of BIPV/T systems with heat pumps (or desiccant cooling options) that increase the amount of usable energy that can be supplied into the space or to the storage media need to be investigated.
- The integration of new BIPV/T models into energy simulation programs such as TRNSYS, EnergyPlus or ESP-r may be examined.
- Measurement of exterior wind coefficients and the development of a correlation is needed.
- The design of a BIPV/T manifold should be studied in detail in order to reduce the pressure drop across it.

References

Aicher T & Martin H. (1997). New correlations for mixed turbulent natural and forced convection heat transfer in vertical tubes. *International Journal of Heat Mass Transfer* **40,** 3617-3626.

Altfeld K. (1985). *Exergetische Optimierung flacher solarer Lufterhitzer.* VDI Verlag.

Altfeld K, Leiner W & Fiebig M. (1988). Second Law optimization of flat plate solar air heaters. Part 1: the concept of net exergy flow and the modeling of solar air heaters. *Solar Energy* **41,** 127-132.

Andraos J. (1996). On the propagation of statistical errors for a function of several variables. *Journal of chemical education* **73,** 150-154.

Arulanandam SJ, Hollands KGT & Brundrett E. (1999). A CFD heat transfer analysis of the transpired solar collector under no-wind conditions. *Solar Energy* **67,** 93-100.

ASHRAE. (2005). *ASHRAE Handbook Fundamentals.* Atlanta, GA.

ASHRAE. (2009). *ASHRAE Handbook Fundamentals.* Atlanta, GA.

Athienitis AK, Poissant Y, Collins M & Liao L. (2005). Experimental and numerical results for a building-integrated photovoltaics test facility. *Photovoltaic Specialists Conference, 2005 Conference Record of the Thirty-first IEEE,* 1718-1721.

Athienitis AK & Santamouris M. (2002). *Thermal analysis and design of passive solar buildings.*

Athienitis AK, Tzempelikos A & Poissant Y. (2004). Investigation of the performance of a double skin façade with integrated photovoltaic panels. *Proceedings of Eurosun 2004, ISES, European solar conference, Freiburg, Germany.*

Axcell BP & Hall WB. (1978). Mixed convection to air in a vertical pipe. In *Proce 6th Int Heat Transfer Conference,* pp. 37-42. Toronto, Canada.

Bahaj AS. (2003). Photovoltaic roofing: issues of design and integration into buildings. *Renewable Energy* **28,** 2195-2204.

Barrow H. (1962). An analytical and experimental study of turbulent gas flow between two smooth parallel walls with unequal heat fluxes. *International Journal of heat and mass transfer* **5,** 469-487.

Bazilian M, Groenhout NK & Prasad D. (2001). Simplified numerical modelling and simulation of a photovoltaic heat recovery system. In *17th European photovoltaic solar energy conference*, pp. 2387-2390. Munich, Germany.

Bazilian MD, Kamalanathan H & Prasad DK. (2002). Thermographic analysis of a building integrated photovoltaic system. *Renewable Energy* **26,** 449-461.

Bazilian MD & Prasad D. (2002). Modelling of a photovoltaic heat recovery system and its role in a design decision support tool for building professionals. *Renewable Energy 27*, 57-68.

Berdahl P & Martin M. (1984). Emissivity of clear skies. *Solar Energy* **32,** 663-664.

Bloem JJ. (2004). A TRNSYS type calculation model for double skin photovoltaic façades. *Proc 19th European Photovoltaic Solar Energy Conference and Exhibition, Paris, France, 2004.*

Bloem JJ. (2008). Evaluation of a PV integrated building application in a well controlled outdoor test environment. *Building and Environment* **43,** 205-216.

Böer KW & Tamm G. (2003). Solar conversion under consideration of energy and entropy. *Solar Energy* **74,** 525-528.

Bosanac M, Sorensen B, Katic I, Sorensen H, Nielsen B & Badran J. (2003). Photovoltaic thermal solar collectors and their potential in Denmark, pp. 1-114.

Brinkworth BJ. (2000). Estimation of flow and heat transfer for the design of PV cooling ducts. *Solar Energy* **69,** 413-420.

Brinkworth BJ. (2002). Coupling of Convective and Radiative Heat transfer in PV cooling ducts. *Transactions of the ASME* **124,** 250-255.

Brinkworth BJ. (2006). Optimum depth for PV cooling ducts. *Solar Energy* **80,** 1131-1134.

Brinkworth BJ, Marshall RH & Ibarahim Z. (2000). A validated model of naturally ventilated PV cladding. *Solar Energy* **69,** 67-81.

Brinkworth BJ & Sandberg M. (2005). A validated procedure for determining the buoyancy induced flow in ducts. *Building Service Engineering Research and Technology* **26,** 35-48.

Brown CK & Gauvin WH. (1965). Combined free and forced convection: 1. Heat transfer in aiding flow. *The Canadian journal of Chemical Engineering* **1,** 306-312.

Brown WG. (1960). *VDI-Forschungsh* **26,** 32.

Busedra AA & Soliman HM. (2000). Experimental investigation of laminar mixed convection in an inclined semicircular duct under buoyancy assisted and opposed conditions. *International Journal of Heat and Mass Transfer* **43,** 1103-1111.

Candanedo JA & Athienitis AK. (2010). Investigation of Anticipatory Control Strategies in a Net-Zero Energy Solar House. *ASHRAE Transactions* **116,** 246-259.

Candanedo JA, Pogharian S, Athienitis AK & Fry A. (2007). Design and simulation of a net zero energy healthy home in Montreal. *2nd Canadian Solar Buildings Conference* **1,** 1-8.

Candanedo L, O'Brien W & A.K. A. (2009). Development of an air-based open loop building-integrated photovoltaic/thermal system model. In *Building Simulation 2009*. Glasgow, Scotland.

Candanedo LM, Athienitis AK, Candanedo J, O'Brien W & Chen Y-X. (2010). Transient and steady state models for open-loop air-based BIPV/T systems. *ASHRAE Transactions 2010* **116,** 600-612.

Cengel Y. (1998). *Heat Transfer: A practical approach*. New York.

Charron R. (2004). One- and two-dimensional modelling of ventilated façades with integrated photovoltaics. In *Building, Civil and Environmental Engineering*, pp. 191. Concordia University, Montreal.

Charron R & Athienitis AK. (2006a). Optimization of the performance of double façades with integrated photovoltaic panels and motorized blinds. *Solar Energy* **80,** 482-491.

Charron R & Athienitis AK. (2006b). A two dimensional model of a double façade with integrated photovoltaic panels. *Journal of Solar Energy Engineering, ASME* **128,** 160-167.

Charters WWS. (1971). Some aspects of flow duct design for solar air heater applications. *Solar Energy* **13,** 283-288.

Chen Y. (2009). Modeling and design of a solar house with focus on a ventilated concrete slab coupled with a building integrated photovoltaic/thermal system. In *BCEE*, pp. 163. Concordia University, Montréal.

Chen Y, Athienitis AK, Berneche B & Y. P. (2007a). Design and simulation of a building integrated photovoltaic thermal system and thermal storage for a solar home. In *2nd Canadian Solar Buildings Conference*. Calgary.

Chen Y, Athienitis AK, Galal KE & Poissant Y. (2007b). Design and Simulation for a Solar House with Building Integrated Photovoltaic-Thermal System and Thermal Storage. In *ISES Solar World Congress, Beijing, China*, pp. 327-332.

Cheng KC & Hong SW. (1972). Effect of tube inclination on laminar convection in uniformly heated tubes for flat-plate solar collectors. *Solar Energy* **13,** 363-371.

Chong D, Liu J & Yan J. (2008). Effects of duct inclination angle on thermal entrance region of laminar and transition mixed convection. *International Journal of Heat and Mass Transfer* **51,** 3953-3962.

Churchill SW. (1977). Friction-factor equation spans all fluid flow regimes. *Chemical engineering progress* **44,** 91-92.

Cipriano J, Lodi C, Chemisana D, Houzeaux G & Perpinan O. (2008). Development and characterization of semitransparent double skin PV façades. In *EuroSun 2008*, 1 edn, pp. 8. Lisbon, Portugal.

Clarke JA, Johnstone C, Kelly N & P.A. S. (1997). The simulation of photovoltaic integrated building façades. *Proc, IBPSA 1997*.

Crawford RH, Treloar GJ, Fuller RJ & Bazilian M. (2006). Life Cycle energy analysis of building integrated photovoltaic systems (BiPVs) with heat recovery unit. *Renewable and Sustainable Energy Reviews* **10,** 559-575.

Cross BM. (1994). Development, testing and first installations of an integrated solar roof system. *IEEE First world conference on photovoltaic energy conversion* **1,** 1020-1023.

Davis MW, Dougherty BP & Fanney AH. (2001). Prediction of building integrated photovoltaic cell temperature. *Journal of Solar Energy Engineering, ASME* **123,** 200-210.

Davis MW, Fanney AH & Dougherty BP. (2003). Measured versus predicted performance of building integrated photovoltaics. *Journal of Solar Energy Engineering, ASME* **125,** 21-27.

De Soto W, Klein SA & Beckman WA. (2006). Improvement and validation of a model for photovoltaic array performance. *Solar Energy* **80,** 78-88.

Dehra H. (2004). A numerical and experimental study for generation of electric and thermal power with photovoltaic modules embedded in building façade. In *Department of Building, Civil and Environmental Engineering.* Concordia University, Montreal.

Delahoy AE, Li Y-M, Selvan A, Chen L, Varvar T & Volltrauer H. (2002). Massive parallel processing for low cost a-si production. In *Proceedings of PV in Europe.* Rome.

DGS. (2005). *Planning and installing photovoltaic systems.* James & James.

Dittus FW & Boelter LMK. (1930). Heat transfer in automobile radiators of the tubular type. *University of California Publications* **2,** 443-461.

Dittus FW & Boelter LMK. (1985). Heat transfer in automobile radiators of the tubular type. *International Communications in Heat and Mass Transfer* **12,** 3-22.

Duffie JA & Beckman WA. (2006). *Solar engineering of thermal processes.* John Willey & Sons, Inc., Hoboken.

Dutta S, Zhang X, Khan JA & Bell D. (1998). Adverse and favorable mixed convection heat transfer in a two-side heated square channel. *Experimental Thermal and Fluid Science* **18,** 314-322.

Eicker U. (2003). *Solar technologies for buildings.* West Sussex.

Eicker U & Fux V. (2000). Heating and cooling potential of combined photovoltaic solar air collector façades. *European Photovoltaic Solar Energy Conference , Glasgow, UK, May 2000, pp 1836-1839*

Eicker U, Fux V, Infield D, Mei L & Vollmer K. (1999). Thermal Performance of building integrated ventilated PV façades. In *Proceedings of International Solar Energy Conference, Jerusalem*

Eiffert P & Kiss GJ. (2000). *Building-integrated photovoltaic designs for commercial and institutional structures: a sourcebook for achitects.* Golden, CO.

European Photovoltaic Industry Association. (2010). Global market outlook for photovoltaics until 2014, pp. 28. Brussels, Belgium.

Fanney AH, Dougherty BP & Davis MW. (2003). Short term characterization of Building Integrated Photovoltaic Panels. *Journal of Solar Energy Engineering, ASME* **125,** 13-20.

Fewster J & Jackson JD. (1976). Enhancement of turbulent heat transfer due to buoyancy for downward flow of water in vertical tubes. In *Proc Seminar on Turbulent Buoyant convection.* Beograd.

Fitzpatrick S. (1999). Performance of a building integrated PV thermal system on a bank in North Carolina. In *NC Solar Center*, ed. Conference PoAA, pp. 6. Portland Maine.

FLUENT Inc. (2006). *FLUENT 6.3 User's Guide.* Lebanon.

Gan G & Riffat SB. (2001). Assessing thermal performance of an atrium integrated with photovoltaics. *Building Service Engineering Research and Technology* **22,** 201-218.

Garg HP & Adhikari RS. (1997). Conventional hybrid photovoltaic/thermal (PV/T) air heating collectors: steady-state simulation. *Renewable Energy* **11,** 363-385.

Gawlik K, Christensen C & Kutscher C. (2005). A numerical and experimental investigation of low-conductivity unglazed, transpired solar air heaters. *Journal of Solar Energy Engineering, ASME* **127,** 153-155.

Gawlik K & Kutscher C. (2002). Wind heat loss from corrugated transpired solar collectors. *Journal of Solar Energy Engineering, ASME* **124,** 256-261.

Ge H & Fazio P. (2003). Experimentally establishing local convection film coefficients for a standard metal curtain wall system. In *Proceedings of the 2nd International Building Physics conference.* Leuven, Belgium.

Gnielinski V. (1983). *Forced convection in ducts*, vol. 2. Hemisphere Publishing Corporation, New York.

Gunnewiek LH, Brundreett E & Hollands KGT. (1996). Flow distribution in unglazed transpired plate solar air heaters of large area. *Solar Energy* **58,** 227-237.

Gupta D, Solanki SC & Saini JS. (1993). Heat and fluid flow in rectangular solar air heater ducts having traverse rib roughness on absorber plates. *Solar Energy* **51,** 31-37.

Hallman TM. (1961). Experimental study of combined forced and laminar convection in a vertical tube. . In *TN D-1104*, ed. NASA, pp. 44. Lewis Research Center, Cleveland, Ohio.

Hatton AP & Quarmby A. (1963). The effect of axially varying and unsymmetrical boundary conditions on heat transfer with turbulent flow between parallel plates. *International Journal of Heat and Mass Transfer* **6,** 903-914.

Hausen H. (1959). *Wärmetech* **9,** 75-79.

Hegazy AA. (1996). Optimization of flow channel depth for conventional flat plat solar air heaters. *Renewable Energy* **7,** 15-21.

Hegazy AA. (2000a). Comparative study of the performance of four photovoltaic/thermal solar air collectors. *Energy Conversion & Management* **41,** 861-881.

Hegazy AA. (2000b). Performance of flat plate solar air heaters with optimum channel geometry for constant/variable flow operation. *Energy Conversion & Management* **41,** 401-417.

Hendrie SD. (1982). Photovoltaic/thermal collector development program - final report. . MIT.

Hollands KGT & Shewen EC. (1981). Optimization of flow passage geometry for air heating, plate type solar collectors. *Journal of Solar Energy Engineering, ASME* **103,** 323-330.

Hollick J. (2005). Status of PV thermal in Canada. Toronto.

Hottel HC & Woertz B. (1942). *Transactions of the ASME* **64,** 91-104.

Hutcheon NB & Handegord GOP. (1995). *Building Science for a Cold Climate.*

IEC IEC. (2006). *Photovoltaic devices – Part 1: Measurement of photovoltaic current-voltage characteristics IEC 60904-1.* Geneva, Switzerland.

Incropera FP & De Witt DP. (2002). *Fundamentals of heat and mass transfer.* John Wiley & Sons.

Infield D, Mei L & Eicker U. (2004). Thermal performance estimation for ventilated PV façades. *Solar Energy* **76,** 93-98.

Infield DG, Mei L, Lee WM & Loveday DL. (2003). Thermal aspects of building integrated PV systems. *3rd world conference on Photovoltaic energy conversion.*

Ito S, Kashima M & Miura N. (2006). Flow control and unsteady-state analysis on thermal performance of solar air collectors. *Journal of Solar Energy Engineering, ASME* **128,** 354-359.

Jackson JD, Cotton MA & Axcell BP. (1989). Studies of mixed convection in vertical tubes. *International Journal of Heat and Fluid Flow* **10,** 2-15.

Jackson TW, Harrison WB & Boteler WC. (1958). Combined Free and forced convection in a constant temperature vertical tube. *Transactions ASME* **80,** 739-745.

Jaurker AR, Saini JS & Gandhi BK. (2006). Heat transfer and friction characteristics of rectangular solar air heater duct using rib grooved artificial roughness. *Solar Energy* **80,** 895-907.

Ji J, He H, Chow T, Pei G, He W & Liu K. (2009). Distributed dynamic modeling and experimental study of PV evaporator in a PV/T solar-assisted heat pump. *International Journal of heat and mass transfer* **52,** 1365-1373.

Jones AD & Underwood CP. (2001). A thermal model for photovoltaic systems. *Solar Energy* **70,** 349-359.

Jonsson H & Moshfegh B. (2001). Modeling of the thermal and hydraulic performance of plate fin, strip fin, and pin fin heat sinks-influence of flow bypass. *Components and Packaging Technologies, IEEE Transactions on* **24,** 142-149.

Kakac S. (1968). Transient turbulent flow in ducts. *Wärme- und Stoffübertragung* **1,** 169-176.

Kakac S, Shah RK & Aung W. (1987). *Handbook of single-phase convective heat transfer.*

Kakac S & Yener Y. (1995). *Convective Heat Transfer*, vol. 1. CRC Press, Boca Raton, Florida.

Kays W, Crawford M & Weigand B. (2005). *Convective heat and mass transfer.* McGraw Hill.

King DL, Boyson WE & Kratochvil JA. (2004). Photovoltaic Array Performance Model. Sandia National Laboratories.

King DL & Kratochvil JA. (1997). Temperature Coefficients for PV Modules and Arrays: Measurement Methods, Difficulties, and Results In *26th IEEE Photovoltaic Specialists Conference*, pp. 6. Anaheim, California.

King DL, Kratochvil JA & Boyson WE. (1997). Measuring solar spectral and angle-of-Incidence effects on photovoltaic modules and solar irradiance sensors. In *26th IEEE Photovoltaic Specialists Conference*, pp. 5. Anaheim, California.

King DL, Kratochvil JA & Boyson WE. (2000a). Stabilization and Performance Characteristics of Commercial Amorphous-Silicon PV Modules. In *IEEE Photovoltaic specialists conference*, pp. 1446-1449. USA.

King DL, Kratochvil JA, Boyson WE & Bower WI. (1998). Field experience with a new performance characterization procedure for photovoltaic arrays. In *2nd World Conference and Exhibition on Photovoltaic Solar Energy Conversion* pp. 7. Vienna, Austria.

King DL & Myers DR. (1997). Silicon-photodiode pyranometers: Operational characteristics, historical experiences, and new calibration procedures. In *26 th IEEE Photovoltaic Specialists Conference,*, ed. IEEE, pp. 4. Anaheim, Californai.

King DL, Quintana JA, Kratochvil JA, Ellibee DE & Hansen BR. (2000b). Photovoltaic module performance and durability following long-term exposure. *Progress in photovoltaics* **8,** 241-256.

Kreith F & Bohn MB. (2001). *Principles of Heat Transfer.* Pacific Grove, CA.

LESO-PB/EPFL L, Enecolo AG M & Ernst Schweizer Ag H. (2000). New generation of hybrid solar pv/t collectors, pp. 55. Swiss Federal Office of Energy.

LI-COR. (2005). *LI-COR terrestrial radiation sensors. Instruction Manual.* Lincoln, Nebraska.

Liao L. (2005). Numerical and experimental investigation of building-integrated photovoltaic-thermal systems. In *Building, Civil and Environmental Engineering,* pp. 116. Concordia University, Montreal.

Liao L, Athienitis AK, Candanedo L, Park K-W, Poissant Y & Collins M. (2007). Numerical and Experimental Study of heat transfer in a BIVP-Thermal system. *Journal of Solar Energy Engineering, ASME* **129,** 423-430.

Lienhard JHI & Lienhard JHV. (2008). *A heat transfer textbook.* Phlogiston Press, Cambridge, MA.

Lin GH & Carlson DE. (2000). Photovoltaics in the year 2025. *International Journal of Hydrogen Energy* **25,** 807-811.

Malik MAS & Buelow FH. (1973). Heat transfer characteristics of a solar drier. In *Sun Service Mankind,* ed. UNESCO-Congress. Paris.

Martinelli RC. (1947). Heat transfer to Molten Metals. *Transactions ASME* **69,** 947-959.

MathWorks I. (2010). *MATLAB R2008b User Guide.* Natick, Massachusetts.

Maughan JR & Incropera FP. (1987). Experiments on mixed convection heat transfer for airflow in a horizontal and inclined channel. *International Journal of Heat and Mass Transfer* **30,** 1307-1318.

McAdams WH. (1954). *Heat Transmission.* McGraw-Hill.

McComas ST & Eckert ERG. (1966). Combined free and forced convection in a horizontal tube. *Journal of Heat Transfer Transactions of the ASME* **88,** 147-153.

McKeon B, Zaragola M & Smit A. (2005). A new friction factor relationship for fully developed pipe flow. *J Fluid Mechanics* **538,** 429-443.

McQuiston FC, Parker JD & Spitler JD. (2005). *Heating, Ventilating, and Air Conditioning.*

Mei L, Infield D, Eicker U & Fux V. (2002). Parameter estimation for ventilated photovoltaic façades. *Building Service Engineering Research and Technology* **23,** 81-96.

Mei L, Infield D, Eicker U, Loveday D & Fux V. (2006). Cooling potential of ventilated PV façade and solar air heaters combined with a desiccant cooling machine. *Renewable Energy* **31,** 1265-1278.

Messenger RA & Ventre J. (2004). *Photovoltaic Systems Engineering.* Boca Raton, FL.

Metais B. (1963). Criteria for mixed convection, pp. 49. University of Minnesota, Minneapolis, Minnesota.

Metais B & Eckert ERG. (1964). Forced, mixed and free convection regimes. *Journal of Heat Transfer,* 295-296.

Mittelman G, Alshare A & Davidson JH. (2009). A model and heat transfer correlation for rooftop integrated photovoltaics with a passive air cooling channel. *Solar Energy* **In Press, Corrected Proof.**

Mohamad AA. (1997). High efficiency solar air heater. *Solar Energy* **60,** 71-76.

Mori Y, Futagami K, Tokuda S & Nakamura M. (1966). Forced convective heat transfer in uniformly heated horizontal tubes 1st report--Experimental study on the effect of buoyancy. *International Journal of Heat and Mass Transfer* **9,** 453-463.

Natural Resources Canada. (2009). Residential End-Use Model. Ottawa.

Novotny JL, McComas ST, Sparrow EM & Eckert ERG. (1964). Heat transfer for turbulent flow in rectangular ducts with two heated and two unheated walls. *AIChE journal* **10,** 466-470.

Ong KS. (1995a). Thermal performance of solar air heaters experimental correlation. *Solar Energy* **55,** 209-220.

Ong KS. (1995b). Thermal performance of solar air heaters: Mathematical model and solution procedure. *Solar Energy* **55,** 93-109.

Oosthuizen PH & Naylor D. (1999). *An introduction to convective heat transfer analysis.* McGraw Hill.

Osborne DG & Incropera FP. (1985). Laminar, mixed convection heat transfer for flow between horizontal parallel plates with asymmetric heating. *International Journal of Heat and Mass Transfer* **28,** 207-217.

Pantic S. (2007). Energy analysis of photovoltaic thermal system integrated with roof and HVAC system. In *Building, Civil and Environmental Engineering,* pp. 215. Concordia University, Montreal.

Parametric Technology Corporation. (2007). Mathcad 14. Needham, MA.

Parretta A, Sarno A, Tortora P, Yakubu H, Maddalena P, Zhao J & Wang A. (1999). Angle-dependent reflectance measurements on photovoltaic materials and solar cells. *Optics Communications* **172,** 139-151.

Pasini M & Athienitis AK. (2006). Systems Design of the Canadian Solar Decathlon House. *ASHRAE Transactions* **112, part 2.**

Petukhov BS. (1976). Turbulent flow and heat transfer in pipes under considerable effect of thermogravitational forces. In *Heat transfer and turbulent buoyant convection,* ed. Spalding DB & Afgan N, pp. 701-717. Hemisphere Publishing Corporation, Washington.

Pottler K, Sippel CM, Beck A & Fricke J. (1999). Optimized finned absorber geometries for solar air heating collectors. *Solar Energy* **67,** 35-52.

Prasad D & Snow M. (2005). *Designing with Solar Power: A Source Book for Building Integrated Photovoltaics (BIPV).* Melbourne, Australia.

Promvonge P & Thianpong C. (2008). Thermal performance assessment of turbulent channel flows over different shaped ribs. *International Communications in Heat and Mass Transfer* **35,** 1327-1334.

Romdhane BS. (2007). The air solar collectors: comparative study, introduction of baffles to favor the heat transfer. *Solar Energy* **81,** 139-149.

Ruther R, Montenegro AA, Del Cueto J, Rummel S, Anderberg A, Von Roedern B & Tamizh-Mani G. (2008). Performance test of amorphous silicon modules in Different climates - Year Four: progress in understanding exposure history stabilization effects. In *33rd IEEE photovoltaic specialists conference*, ed. IEEE. San Diego, California.

Saelens D, Roels S & Hens H. (2004). The inlet temperature as a boundary condition for multiple-skin facade modelling. *Energy and Buildings* **36,** 825-835.

Sandia National Laboratories. (2002). Database of photovoltaic module performance parameters.

Sandia National Laboratories. (2006). Database of Photovoltaic Module Performance Parameters.

Santbergen R, Rindt CCM & Van Zolingen RJC. (2008). Improvement of the performance of PVT collectors. In *Proc of the 5th European Thermal-Sciences Conf.* The Netherlands.

Santbergen R & van Zolingen RJC. (2005). Modelling the thermal absorption factor of photovoltaic/thermal combi-panels. In *Heat transfer in components and systems for sustainable energy technologies*, pp. 239-244. Grenoble, France.

Shah RK & London AL. (1978). *Laminar flow forced convection in ducts.* Academic Press, New York.

Sharples S & Charlesworth PS. (1998). Full-scale measurements of wind-induced convective heat transfer from a roof-mounted flat plate solar collector. *Solar Energy* **62,** 69-77.

Smith DR, Biringer KL & Pritchard DA. (1978). Combined photovoltaic thermal collector testing, pp. Pages: 6. United States.

Smyth R & Salman YK. (1991). Combined free and forced convection heat transfer in a rectangular duct. *International Communications in Heat and Mass Transfer* **18,** 669-680.

Sopian K, Yigit KS, Liu HT, Kakac S & Veziroglu TN. (1996). Performance Analysis of photovoltaic thermal air heaters. *Energy Conversion and Management* **37,** 1657-1670.

Sorensen H & Munro D. (2000). Hybrid PV/Thermal collectors. *The 2nd world solar electric buildings conference: Sydney 8th-th march 2000.*

Sparrow EM, Lloyd JR & Hixon CW. (1966). Experiments on Turbulent heat transfer in an asymmetrically heated rectangular duct. *Journal of Heat Transfer Transactions of the ASME* **88,** 170-174.

SriHarsha V, Prabhu SV & Vedula RP. (2009). Influence of rib height on the local heat transfer distribution and pressure drop in a square channel with 90° continuous and 60° V-broken ribs. *Applied Thermal Engineering* **29,** 2444-2459.

Statistics Canada. (2009). Report on Energy Supply-Demand in Canada 1990-2007. Ottawa.

Sudo Y, Kaminaga M & Minazoe K. (1990). Experimental study on the effects of channel gap size on mixed convection heat transfer characteristics in vertical rectangular channels heated from both sides. *Nuclear Engineering and Design* **120,** 135-146.

Tan HM & Charters WWS. (1969). Effect of thermal entrance region on turbulent forced convective heat transfer for an asymmetrically heated rectangular duct with uniform heat flux. *Solar Energy* **12,** 513-516.

Tan HM & Charters WWS. (1970). An experimental investigation of forced convective heat transfer for fully developed turbulent flow in a rectangular duct with asymetric heating. *Solar Energy* **13,** 121-125.

Taylor JR. (1997). *An introduction to error analysis.*

Test FL, Lessmann RC & Johary A. (1981). Heat transfer during wind flow over rectangular bodies in the natural environmental. . *Transactions of the ASME J Heat transfer* **103,** 262-267.

Thakur NS, Saini JS & Solanki SC. (2003). Heat transfer and friction factor correlations for packed bed solar air heater for a low porosity system. *Solar Energy* **74,** 319-329.

Tiwari A, Sodha MS, Chandra A & Joshi JC. (2006). Performance evaluation of photovoltaic thermal solar air collector for composite climate of India. *Solar Energy Material & Solar Cells* **90,** 175-179.

Tonui JK & Tripanagnostopoulos Y. (2007). Improved PV/T solar collectors with heat extraction by forced or natural air circulation. *Renewable Energy* **32,** 623-637.

Tonui JK & Tripanagnostopoulos Y. (2008). Performance improvement of PV/T solar collectors with natural air. *Solar Energy* **82,** 1-12.

Tripanagnostopoulos Y. (2007). Aspects and improvements of hybrid photovoltaic/thermal solar energy systems. *Solar Energy* **81,** 1117–1131.

Tripanagnostopoulos Y, Bazilian M, Zoulia I & Battisti R. (2000a). Hybrid PV/T system with improved air heat extraction modification. *Proceedings of the PV in Europe- from PV technology to energy solutions conference.*

Tripanagnostopoulos Y, Nousia T & Souliotis M. (2000b). Low cost improvements to building integrated air cooled hybrid PV thermal systems. *Proc 16th European PV Solar Energy Conf,* 1874-1877.

Tripanagnostopoulos Y, Nousia T, Souliotis M & Yianoulis P. (2002). Hybrid photovoltaic/thermal solar systems. *Solar Energy* **72,** 217-234.

US DOE & Lawrence Berkeley National Laboratory. (2009). *EnergyPlus Engineering Reference.*

van Helden WGJ, van Zolingen RJC & Zondag HA. (2004). PV thermal systems: PV panels supplying renewable electricity and heat. *Progress in photovoltaics: research and applications* **12,** 415-426.

Vandaele L, Wouters P & Bloem H. (1996). Hybrid Photovoltaic building components: overall performance assessment by testing and simulation.

Varun, Saini RP & Singal SK. (2007). A review on roughness geometry used in solar air heaters. *Solar Energy* **81,** 1340-1350.

Whillier A. (1964). Black painted solar air heaters of conventional design. *Solar Energy* **8,** 31-37.

White FM. (2003). *Fluid Mechanics.* McGraw-Hill.

White FM. (2006). *Viscous Fluid Flow.* McGraw-Hill International Edition.

Winterton RHS. (1998). Where did the Dittus and Boelter equation come from? *International Journal of Heat and Mass Transfer* **41,** 809-810.

Wu T-H, Xu Z & Jackson JD. (2002). Mixed Convection Heat Transfer to Water Flowing Through a Vertical Passage of Annular Cross Section: Part 2. *Chemical Engineering Research and Design* **80,** 246-251.

Yang H, Burnett J & Ji J. (2000). Simple approach to cooling load component calculation through PV walls. *Energy and Buildings* **31,** 285-290.

Yang HX, Marshall RH & Brinkworth BJ. (1996). Validated simulation for thermal regulation of photovoltaic structures. *Photovoltaic Specialists Conference, 1996, Conference Record of the Twenty Fifth IEEE.*

Zhang X & Dutta S. (1998). Heat transfer analysis of buoyancy-assisted mixed convection with asymmetric heating conditions. *International Journal of Heat and Mass Transfer* **41,** 3255-3264.

Zondag HA. (2008a). Flat Plate PV-Thermal collectors and systems: A review. *Renewable and Sustainable Energy Reviews* **12,** 891-959.

Zondag HA. (2008b). Realized PV/T installations experiences and monitoring results. Energy research Centre of the Netherlands (ECB, Eidhoven.

Zondag HA, De Vries DW, van Helden WGJ, van Zolingen RJC & van Steenhoven AA. (2002). The thermal and electrical yield of a PV-Thermal collector. *Solar Energy* **72,** 113-128.

Zondag HA & van Helden WGJ. (2002). Stagnation temperature in PVT collectors *In: PV in Europe.*

Zondag HA & van Helden WGJ. (2003). PV-thermal domestic systems. In *3rd world conference on Photovoltaic energy conversion.* Osaka, Japan.

Appendix A. Solar Geometry and Availability

In order to be able to predict the total incident radiation on a surface, it is necessary to describe the sun's position in the sky. The total incoming solar radiation can be described by three main components: beam solar radiation, diffuse sky solar radiation and diffuse radiation reflected from the ground.

For solar angles calculation, the solar time (a.k.a. apparent solar time) is used. Solar time is the time based on the apparent angular motion of the sun across the sky with solar noon the time when the sun crosses the meridian of the observer (Duffie, J.A. & Beckman, W.A., 2006).

In general, the solar time does not coincide with local clock time. There is a correction to account for the difference between the observer's longitude and the longitude on which the local standard time is based. There is another correction to account for perturbations in the Earth's rate of rotation, referred as the equation of time (E).

$$\text{Solar time} = 4\cdot(L_{st}-L_{loc}) + E + \text{local standard time} \qquad \text{A.1}$$

In the previous equation, L_{st} is the standard meridian for the location and L_{loc} is the longitude of the location in question. In equation A.1, the L_{st} and L_{olc} are expressed in degrees and E is given in minutes. For Montreal, the standard meridian, L_{st}, is 75° and local longitude, L_{loc}, is 73.5°. The standard time must be adjusted when daylight saving time (DST) is being used.

When DST is used in the location, 1 hour must be subtracted from the clock time to find the local standard time, since clock time is adjusted to be one hour ahead. In Canada, daylight saving time usually begins on the second Sunday in March and ends in the first Sunday in November.

The equation of time, E, is given by the following expression as a function of the day of the year, n (Duffie, J.A. & Beckman, W.A., 2006)3

$$E = 229.2\left[0.000075 + 0.001868\cos\left((n-1)\frac{360}{365}\right) - 0.032077\sin\left((n-1)\frac{360}{365}\right)\right.$$
$$\left. - 0.014615\cos\left(2(n-1)\frac{360}{365}\right) - 0.04089\sin\left(2(n-1)\frac{360}{365}\right)\right] \qquad \text{A.2}$$

The preceding equation A.2 is also presented in (ASHRAE, 2009).

Another equation for computing the equation of time is given by (Athienitis, A.K. & Santamouris, M., 2002).

$$E = 9.87\left[\sin(4\pi\cdot(n-81)/364\right] - 7.53\cos\left(2\pi(n-81)364\right) - 1.5\sin\left(2\pi(n-81)364\right) \qquad \text{A.3}$$

A comparison of equations A.2 and A.3 is shown in Figure A.1.

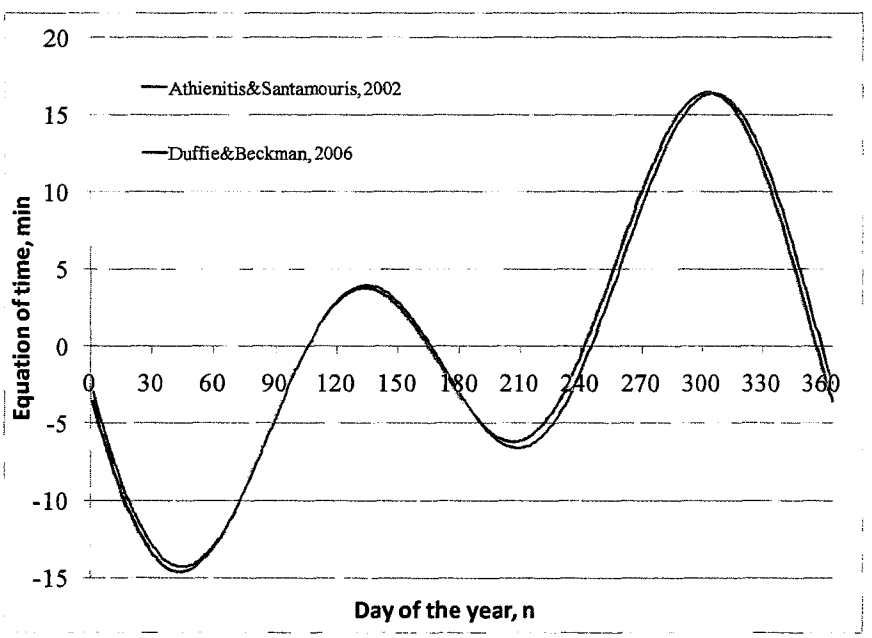

Figure A.1. Equations of time E as function of day of the year.

The maximum difference between the two equations is 1.16 minutes.

The solar geometry angles are represented in Figure A.2.

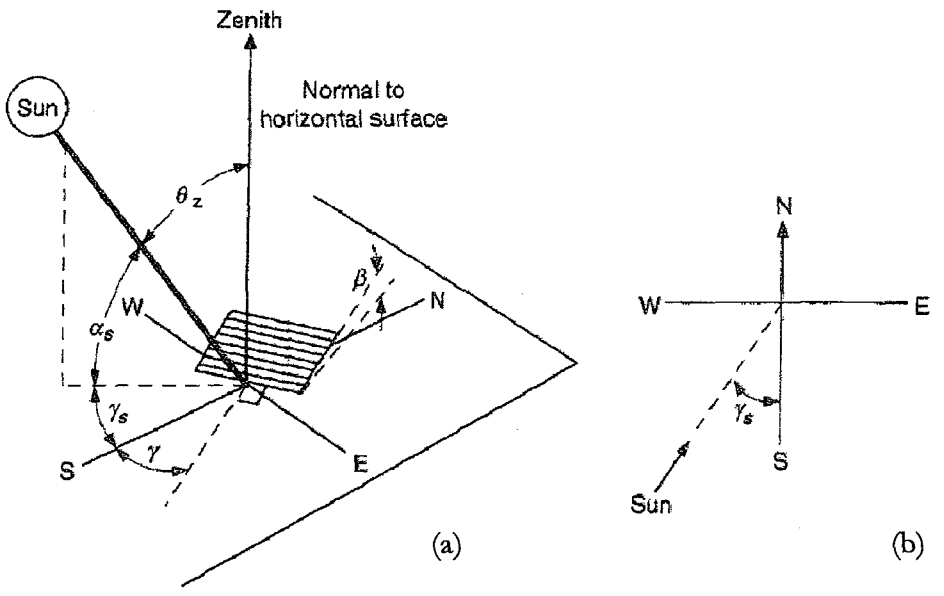

Figure A.2. a) Solar geometry angles for a tilted surface (zenith, slope, surface azimuth, solar b) Plan view showing solar azimuth angle (Duffie, J.A. & Beckman, W.A., 2006).

The position of the sun can be expressed by the following angles:

- La is the latitude of the location. North is positive, $-90° \leq La \leq 90°$.
- δ is the declination, equal to the angular position of the sun at solar noon with respect to the plane of the equator. North is positive $-23.45° \leq \delta \leq 23.45°$.
- β is the slope or tilt angle between the surface and the horizontal. $0° \leq \beta \leq 180°$.
- γ is the surface azimuth angle, equal to the deviation of the projection on a horizontal plane of the normal to the surface from the local meridian. γ is 0° when the projection of the normal to the surface is due south, it is negative when it points towards the east and positive when it points towards the west.
- h is the hour angle (aka ω), which represents the angular displacement of the sun east or west of the local meridian due to the Earth's rotation. The Earth rotates 15° per hour. h is taken as negative in the morning and positive in the afternoon.

- θ is the angle of incidence, which is the angle between the beam radiation on a surface and the normal to that surface.
- θ_z is the zenith angle, which represents the angle between the vertical and the line from a surface to the sun.
- α_s is the solar altitude angle. It is the angle between the horizontal and the line from a surface to the sun. From previous definitions, $\theta_z + \alpha_s = 90°$.
- γ_s is the solar azimuth angle. It represents the angular displacement from south of the projection of beam radiation on the horizontal plane.

The declination angle, δ, is given by the following expression (Duffie, J.A. & Beckman, W.A., 2006).

$$\delta = 23.45\sin(360\cdot(284+n)/365) \qquad \text{A.4}$$

The solar altitude angle can be computed using the following relationship (Athienitis, A.K. & Santamouris, M., 2002)

$$\sin(\alpha_s) = \cos(La)\cos(\delta)\cos(h) + \sin(La)\sin(\delta) \qquad \text{A.5}$$

where the hour angle, h is given by

$$h = (ST - 12hr)\frac{15°}{hr} \qquad \text{A.6}$$

the solar azimuth by

$$\gamma_s = \cos^{-1}[(\sin(\alpha_s)\sin(La) - \sin(\delta))/(\cos(\alpha_s)\cos(La)]\cdot h/|h| \qquad \text{A.7}$$

and the incidence angle by

$$\theta = \cos^{-1}[\cos(\alpha_s)\cos(\gamma_s - \gamma)\sin(\beta) + \sin(\alpha)\cos(\beta)] \qquad \text{A.8}$$

Appendix B. Measurement Uncertainty

The uncertainties associated with the average Nusselt numbers have been calculated with the propagation rules (Andraos, J., 1996; Taylor, J.R., 1997).

Uncertainty in collector area

The exposed collector area was measured with an accuracy of 0.000794 m (1/32in).

The associated error is calculated as

$$\Delta A = 1.1019\sqrt{\left(\frac{0.000794}{2.84728}\right)^2 + \left(\frac{0.000794}{0.387}\right)^2} = 2.282 \times 10^{-3} m^2$$

For the area A_{cv}, the associated error is then

$$\Delta A_{cv} = \frac{1.1019}{6} * \sqrt{\left(\frac{2.282 \times 10^{-3}}{1.1019}\right)^2} = 3.8 \times 10^{-4} m^2$$

Uncertainty in radiative heat transfer rate

First, the errors associated with the radiative heat transfer rate (equation 3.16) are calculated based on the uncertainties in the measurement of the surface emissivities of the insulation and metal plate surfaces, together with the errors in the temperature measurement of the surfaces and the associated error in the control volume area. The uncertainty in each of the measured emissivities is 0.3%. The emissivity factor F_{ε}, and its uncertainty, ΔF_{ε}, is calculated with

$$F_{\varepsilon} \pm \Delta F_{\varepsilon} = \frac{1}{\frac{1}{0.2\pm0.3\%} + \frac{1}{0.82\pm0.3\%} - 1} = \frac{1}{5\pm0.015+1.219\pm3.65\times10^{-3}-1} = \frac{1}{5.2195\pm0.01543} = 0.19158 \pm 0.19158\left(\frac{0.01543}{5.2195}\right)$$

and ΔF_{ε} has a value of 5.6×10^{-4}.

The error associated with equation 3.16, has been calculated by first computing the error in each of the six control volumes associated with the emissivity, the plate temperatures and the area, and finally adding them to compute the total error in the total $\Delta Qrad_{cv}$. i.e.

$$\Delta_{Qradcv(\Delta T)} = \sigma F_{plate,insu} F_{\varepsilon} A_{cv} \sqrt{((4 * 0.3 * (T_{plate} + 273.15)^3)^2 + (4 * 0.3 * (T_{insu} + 273.15)^3)^2}$$

$$\Delta_{Qradcv(\Delta\varepsilon)} = \sigma F_{plate,insu} A_{cv} \sqrt{(T_{plate} + 273.15)^4 - (T_{insu} + 273.15)^4} * 5.6 \times 10^{-4}$$

$$\Delta_{Qradcv(\Delta Acv)} = \sigma F_{plate,insu} F_{\varepsilon} \sqrt{(T_{plate} + 273.15)^4 - (T_{insu} + 273.15)^4} * 3.8 \times 10^{-4}$$

$$\Delta_{Qrad} = \sqrt{\sum_{n=1}^{6} (\Delta_{Qradcv(\Delta T),n})^2 + \sum_{n=1}^{6} (\Delta_{Qradcv(\Delta \varepsilon),n})^2 + \sum_{n=1}^{6} (\Delta_{Qradcv(\Delta Acv),n})^2}$$

The uncertainties calculated are in the range of 1.2% of the total Q_{rad}

Uncertainty in convective heat transfer rate

The uncertainties in the convective heat transfer rate arise from measurement uncertainties in different parameters. There are uncertainties in the mass flow rate due to the pressure transducer and the LFE calibration curve, and to uncertainties in the T_{oulet} and T_{inlet} air temperature measurements.

The highest uncertainty for the flow rate is 0.25 CFM due to the calibration curve fitting according to the manufacturer's data of the LFE. The pressure transducer has an accuracy of 6.25 Pa (0.025 in). Then, the ΔCFM has been calculated as

$$\Delta CFM = \sqrt{\left(1.39297 \times 10^{1} \cdot 0.025\right)^2 + 2\left(\frac{2 \cdot 0.025 \Delta P^2}{\Delta P}\right)^2} + 0.25\text{CFM}$$

The maximum ΔCFM is 0.6357 CFM ($3\times10^{-4}m^3/s$) due to the combined effects of the error of the calibration curve and the uncertainty in the pressure drop measurement. The ΔT is the result of the addition of the uncertainties of T_{outlet} and T_{inlet}. The uncertainty in the thermocouples is 0.3°C, then $\Delta T = \sqrt{0.3^2 + 0.3^2} = 0.424°C$.

The maximum uncertainty in the calculation of c_p of air is 0.01% due to error in the measurement of RH (3%). The estimated error associated to density of air is 0.25% (McQuiston, F.C. *et al.*, 2005). Then, the total uncertainty in ΔQin_{cv} is calculated as:

$$\Delta Qin = \dot{m}c_p (T_{outlet} - T_{inlet}) \sqrt{\left(\frac{\Delta T}{(T_{outlet} - T_{inlet})}\right)^2 + \left(\frac{\Delta CFM \cdot \dot{m}c_p}{\dot{m}c_p}\right)^2 + \left(\frac{\Delta c_p}{c_p}\right)^2 + \left(\frac{\Delta \rho}{\rho}\right)^2}$$

Uncertainty in convective coefficient

To obtain the top heat transfer coefficient uncertainty, it is necessary to calculate the uncertainty of Qin-Qrad. Then

$$\Delta_{(Qin-Qrad)} = \sqrt{\Delta Qin^2 + \Delta Qrad^2}$$

From equation 3.18, it follows that the uncertainty in hc_t must consider the uncertainties in the area measurement and in the temperature differential

$$\Delta hc_t = hc\sqrt{\left(\frac{\Delta_{A\Delta T}}{A\Delta T}\right)^2 + \left(\frac{\Delta_{Qin-Qrad}}{Qin-Qrad}\right)^2}$$

The uncertainties for hc_b have been calculated in a similar fashion.

Uncertainties in Nusselt numbers

From equation 3.20, it follows the uncertainty in Nu_{top} is calculated as

$$\Delta Nu_{top} = Nu_{top}\sqrt{\left(\frac{\Delta k_{air}}{k_{air}}\right)^2 + \left(\frac{\Delta hc_t D_h}{hc_t t D_h}\right)^2}$$

The uncertainty in k_{air} has been calculated with the Sutherland-law thermal conductivity with the constant provided in (White, F.M., 2006). The uncertainty of k_{air} is 2%.

The uncertainties for Nu_{bot} have been calculated in a similar fashion.

Uncertainties in Reynolds Numbers

In order to compute the uncertainties in Re ($\rho V D_h/\mu$), the uncertainties on each of the parameters have been taken into account.

$$\Delta \mathrm{Re} = \mathrm{Re}\sqrt{\left(\frac{\Delta\rho}{\rho}\right)^2 + \left(\frac{\Delta V}{V}\right)^2 + \left(\frac{\Delta D_h}{D_h}\right)^2 + \left(\frac{\Delta\mu}{\mu}\right)^2}$$

The uncertainty in μ has been calculated with the Sutherland-law viscosity with the constants provided in (White, F.M., 2006). The uncertainty of μ is 2%.

Appendix C. Mathcad Single-Diode Model

W. De Soto, S.A. Klein, and W.A. Beckan model implementation in MathCad

The model computers 5 parameters using the manucfacturing data sheet of the PV module

The model has been build using the manufacturers data for the Unisolar PVL-68.

Parameters

$Iscref := 5.1$ $\quad Vocref := 23.1$ $\quad Tc := (273.15 + 25 + 10)$

$Impref := 4.13$ $\quad Vmpref := 16.5$ $\quad Tcref := 273.15 + 25$

$\mu isc := 0.001 \cdot Iscref$ $\quad \mu voc := -.0038 \cdot Vocref$

$\mu isc = 5.1 \times 10^{-3}$ $\quad \mu voc = -0.088$

Guesses

$$aref := \frac{1.5 \cdot 1.381 \cdot 10^{-23} \cdot 298.2 \cdot 11}{1.602 \cdot 10^{-19}} = 0.424$$

$Rshref := 25$

$aref := 0.8$

$a := .85$ $\quad Rsh := 20$

$ILref := 5.1$ $\quad Egref := 1.6$

$IL := 4.1$ $\quad Eg := Egref \cdot [1 - .0002677 \cdot (Tc - Tcref)]$

$Ioref := 1.04 \cdot 10^{-11}$

$Eg = 1.596$

$Voc := 21$

$Rs := 0.541$

$Io := 1 \cdot 10^{-12}$ $\quad Rsref := 0.41$

$ILref = 5.1$

Given

$$Iscref = ILref - Ioref \cdot \left(e^{\frac{Iscref \cdot Rs}{aref}} - 1\right) - \frac{Iscref \cdot Rs}{Rshref}$$

$$ILref = \left[Ioref \cdot \left(e^{\frac{Vocref}{aref}} - 1\right)\right] + \frac{Vocref}{Rshref}$$

$$Impref = ILref - Ioref \cdot \left[e^{\frac{(Vmpref + Impref \cdot Rs)}{aref}} - 1\right] - \frac{Vmpref + Impref \cdot Rs}{Rshref}$$

$$\frac{Impref}{Vmpref} = \frac{\frac{Ioref}{aref} \cdot e^{\frac{(Vmpref + Impref \cdot Rs)}{aref}} + \frac{1}{Rshref}}{1 + \frac{Ioref \cdot Rs}{aref} \cdot e^{\left(\frac{Vmpref + Impref \cdot Rs}{aref}\right)} + \frac{Rs}{Rshref}}$$

$$Io = Ioref \cdot \left(\frac{Tc}{Tcref}\right)^3 \cdot e^{\left[\frac{1.602 \cdot 10^{-22}}{1.381 \cdot 10^{-26}} \cdot \left(\frac{Egref}{Tcref} - \frac{Eg}{Tc}\right)\right]}$$

$$a = \frac{Tc}{Tcref} \cdot aref$$

$$IL = 1[ILref + \mu isc \cdot (Tc - Tcref)]$$

$$0 = IL - Io \cdot \left(e^{\frac{Voc}{a}} - 1\right) - \frac{Voc}{Rsh}$$

$$\mu voc = \frac{Voc - Vocref}{Tc - Tcref}$$

$$Rsh = 1 \cdot Rshref$$

$$\begin{pmatrix} Rshref \\ aref \\ ILref \\ Ioref \\ a \\ Io \\ IL \\ Voc \\ Rs \\ Rsh \end{pmatrix} := Find(Rshref, aref, ILref, Ioref, a, Io, IL, Voc, Rs, Rsh) =$$

	0
0	21.103
1	0.813
2	5.349
3	$1.913 \cdot 10^{-12}$
4	0.84
5	$1.399 \cdot 10^{-11}$
6	5.4
7	22.222
8	1.029
9	21.103

$$\frac{Voc - Vocref}{Tc - Tcref} = -0.088$$

After obtaining reference parameters. Code to obtain the maximum power point.

$IL = 5.4 \qquad a = 0.84 \qquad Io = 1.399 \times 10^{-11}$

$Rs = 1.029 \qquad Rshref = 21.103$

$Imp := 2 \qquad Vmp := 3$

Given

$$\frac{Imp}{Vmp} = \frac{\frac{Ioref}{aref} \cdot e^{\left(\frac{Vmp + Imp \cdot Rs}{aref}\right)} + \frac{1}{Rshref}}{1 + \frac{Rs}{Rshref} + Ioref \cdot \frac{Rs}{aref} \cdot e^{\left(\frac{Vmp + Imp \cdot Rs}{aref}\right)}}$$

$$Imp = ILref - Ioref \cdot \left[e^{\left(\frac{Vmp + Imp \cdot Rs}{aref}\right)} - 1\right] - \left(\frac{Vmp + Imp \cdot Rs}{Rshref}\right)$$

$$\begin{pmatrix} Imp \\ Vmp \end{pmatrix} := Find(Imp, Vmp) = \begin{pmatrix} 4.097 \\ 16.627 \end{pmatrix}$$

$Pmx := Imp \cdot Vmp$

$Pmx = 68.121$

Single Diode Model - Curve Tracing

After obtaining the five model parameters (Ioref, ILref, Rs, Rshref, a), this code is employed to trace the IV curve and compare it to the theoretical max powerpoint equations in (Duffie & Beckman,2006) equations 23.2.13 and 23.2.14.

Parameters

$Ioref = 1.913 \times 10^{-12}$ $\quad ILref = 5.349$ $\quad Rs = 1.029$

$Rshref = 21.103$ $\quad aref = 0.813$

Initial guess for I

$I := 1$

Given

$$I = ILref - Ioref \cdot \left[e^{\left(\frac{Va + I \cdot Rs}{aref}\right)} - 1 \right] - \frac{(Va + I \cdot Rs)}{Rshref}$$

$I(Va) := Find(I)$

$k := 0..2500$

$Varray_k := 0.01k$

$Solution_k := I(Varray_k)$

$Power_k := Solution_k \cdot Varray_k$

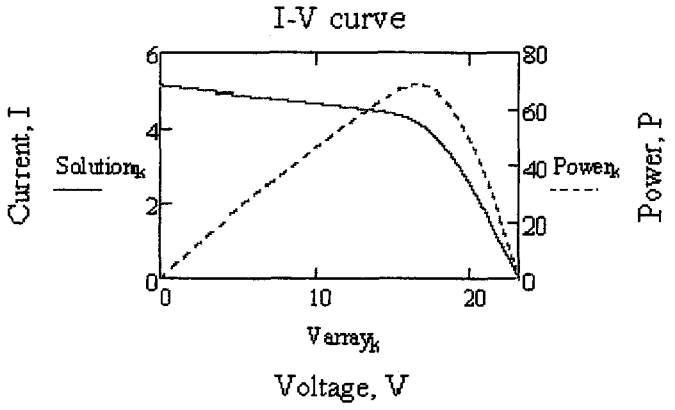

Equations 23.2.13 and equation 23.2.14 are solved simultaneously to obtain a theoretical maximum power point (Duffie&Beckman, 2006)

Initial Guess for Vmp and Imp

$Vmp := 2$

$Imp := 3$ $\qquad Rs = 1.029$

Given

$$\frac{Imp}{Vmp} = \frac{\frac{Ioref}{aref}\cdot e^{\left(\frac{Vmp+Imp\cdot Rs}{aref}\right)} + \frac{1}{Rshref}}{1 + \frac{Rs}{Rshref} + Ioref\cdot\frac{Rs}{aref}\cdot e^{\left(\frac{Vmp+Imp\cdot Rs}{aref}\right)}}$$

$$Imp = ILref - Ioref\cdot\left[e^{\left(\frac{Vmp+Imp\cdot Rs}{aref}\right)} - 1\right] - \left(\frac{Vmp + Imp\cdot Rs}{Rshref}\right)$$

$$\begin{pmatrix} Imp \\ Vmp \end{pmatrix} := Find(Imp, Vmp) = \begin{pmatrix} 4.0969 \\ 16.62746 \end{pmatrix}$$

$Pmx := Imp\cdot Vmp$

$Pmx = 68.121$ $\qquad$ Compare this result to Powerk table.

$(Power_k) =$	$Varray_k =$	$Solution_k =$
0	0	5.1
0.051	0.01	5.1
0.102	0.02	5.099
0.153	0.03	5.099
0.204	0.04	5.098
0.255	0.05	5.098
0.306	0.06	5.097
0.357	0.07	5.097
0.408	0.08	5.096
0.459	0.09	5.096
0.51	0.1	5.095
0.56	0.11	5.095
0.611	0.12	5.095
0.662	0.13	5.094
0.713	0.14	5.094
...	...	...

NextStep

Obtain AST from clock time in the computer and using equation of time and correction for the Longitude of the City

$$ET(n) := \left(9.87 \cdot \sin\left(4 \cdot \pi \cdot \frac{n-81}{364}\right) - 7.53 \cdot \cos\left(2 \cdot \pi \cdot \frac{n-81}{364}\right) - 1.5 \cdot \sin\left(2 \cdot \pi \cdot \frac{n-81}{364}\right)\right) \cdot min$$

$$ET(304+28) = 10.981 \cdot min$$

$$AST := \left[12 + \frac{09}{60} + \frac{42}{60 \cdot 60} + \frac{ET(304+28)}{60min} + \frac{(75-73.5) \cdot 4}{60}\right] hr$$

$$AST = 12.445 \cdot hr$$

$$ET2(n) := 229.2\left[.000075 + 0.001868 \cos\left[(n-1) \cdot \frac{360}{365} deg\right] - .032077 \cdot \sin\left[(n-1) \cdot \frac{360}{365} deg\right] \ldots \right.$$
$$\left. +0 - .014615 \cos\left[2 \cdot \left[(n-1) \cdot \frac{360}{365}\right] deg\right] - .04089 \sin\left[2 \cdot \left[(n-1) \cdot \frac{360}{365}\right] deg\right]\right]$$

$$ET2(304+28) = 11.762$$

$ET2(304+28) = 11.762$ in minutes

$$n := 1, 2 .. 365$$

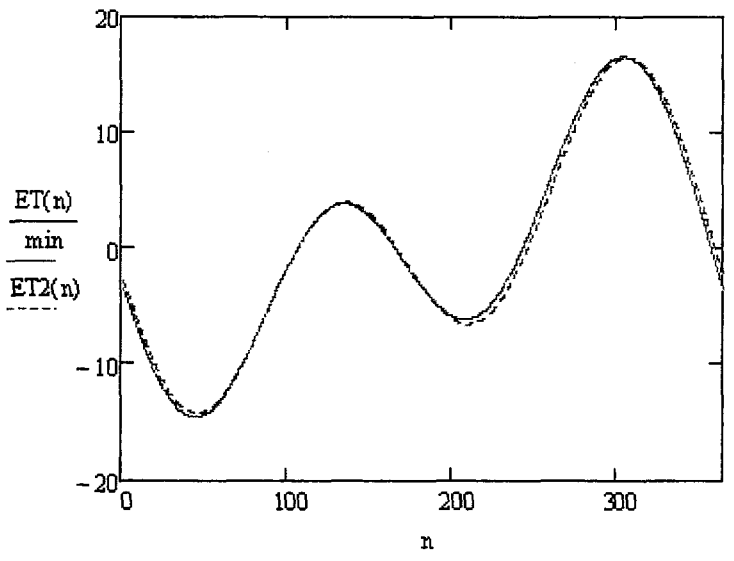

First compute incidence angle

$\beta := 30$ Tilt angle of PV surface (in degrees)

$La := 45.3$ Latitude of Montreal (in degrees)

$surfaceazimuth := 0$ in degrees

Obtain solar posion with aparent solar time

$$h := \left(\frac{AST}{hr} - 12\right)\cdot 15$$

$h = 6.67$ hour angle in degrees $h\cdot\frac{\pi}{180} = 0.116$

$n := 304 + 28$ Day of the year

$$\delta := 23.45\cdot\sin\left[\frac{360}{365}\cdot(284 + n)\cdot\frac{\pi}{180}\right]$$

$\delta = -21.675$

$\delta\cdot\frac{\pi}{180} = -0.378$ in radians $\cos(1) = 0.54$

computing altitude angle

$$\alpha := \operatorname{asin}\left(\cos\left(La\cdot\frac{\pi}{180}\right)\cdot\cos\left(\delta\cdot\frac{\pi}{180}\right)\cdot\cos\left(h\cdot\frac{\pi}{180}\right) + \sin\left(La\cdot\frac{\pi}{180}\right)\cdot\sin\left(\delta\cdot\frac{\pi}{180}\right)\right)$$

$\alpha = 0.397$ in radians

$\alpha\cdot\frac{180}{\pi} = 22.75$ in degrees

$sign(-21) = -1$

$$azim := \operatorname{acos}\left[\frac{\left(\sin(\alpha)\cdot\sin\left(La\cdot\frac{\pi}{180}\right) - \sin\left(\delta\cdot\frac{\pi}{180}\right)\right)}{\left(\cos(\alpha)\cdot\cos\left(La\cdot\frac{\pi}{180}\right)\right)}\right]\cdot sign(h)$$

$azim = 0.117$

$\gamma := azim - surfaceazimuth \cdot \frac{\pi}{180}$ surface solar azimuth in radians

$\gamma = 0.117$

$\gamma \cdot \frac{180}{\pi} = 6.722$ surface solar azimuth in degrees

$$\theta := \frac{180}{\pi} \cdot acos\left(cos(\alpha) \cdot cos(|\gamma|) \cdot sin\left(\beta \cdot \frac{\pi}{180}\right) + sin(\alpha) \cdot cos\left(\beta \cdot \frac{\pi}{180}\right)\right)$$

$\theta = 37.549$ in degrees incidence angle

the incidence angle modifier $K\tau\alpha$ is defined as $\sum_{i=0}^{5} b_i(\theta)^i$ where θ is the incidence angle to the PV module in degreees

```
AIF =
1+(-0.00502)*incidenceangle+0.0005842*incidenceangle^2+(-0
.000023)*incidenceangle^3+3.82E-7*incidenceangle^4+(-2.31E
-9)*incidenceangle^5;
```

bi constants obtained in PV Sandia Database

$$K\tau\alpha(\theta) := 1 + -0.00502 \cdot \theta + .0005842 \cdot \theta^2 + -0.000023 \cdot \theta^3 + 3.826 \cdot 10^{-7} \cdot \theta^4 + -2.31 \cdot 10^{-9} \cdot \theta^5$$

$K\tau\alpha(\theta) = 1.006$

$\theta z := 90 - \alpha \cdot \frac{180}{\pi}$

$\theta z = 67.25$ Zenith angle

$$AM := \frac{1}{\left[cos\left(\theta z \cdot \frac{\pi}{180}\right) + 0.5057 \cdot (96.080 - \theta z)^{-1.634}\right]}$$

Insert zenith angle in degrees in equation for AM (king et al. 1998)

$AM = 2.572$

M_Mref_ratio is defined = $\sum_{i=0}^{4} a_i (AM)^i$

ai constants obtained in PV Sandia Database

$M\_Mref\_ratio := 1.047 + .00082115 \cdot AM - 0.0259 \cdot AM^2 + 0.0031736 \cdot AM^3 + -0.00011026 AM^4$

$M\_Mref\_ratio = 0.927$

$Kto(\theta) = 1.006$

Finally, for performance evaluation, multiply measured radiation times correction factors.

0.96 factor obtained from Duffie&Beckman (when IT is measured)

Gmeasured*0.96*Kth*M_Mref

$Ga = 733.87 \cdot Kto(\theta) \cdot M\_Mref\_ratio \cdot 0.96$

Replace this value in Ga to obtain IV curve

$Ga = 656.754$

NOTE
The IV curve traced will be accurate as long as it is for a sunny clear day. Partial shading of PV modules cells will reduce power production and the model does not account for this.

For operating condition in November 28 2009

$Tcref = 298.15$

$Ga := 656.754$

Insert here radiation corrrected for AMM, KTH and reflectance at normal incidence angle. Then recalculating temperature dependent parameters.

$aref = 0.813$ $\quad Tcnew := 40 + 273.15$

$a := \frac{Tcnew}{Tcref} \cdot aref$ $\quad \mu isc = 5.1 \times 10^{-3}$

$a = 0.853$

$Gref := 1000$

$IL := \frac{Ga}{1000} \cdot [ILref + \mu isc \cdot (Tcnew - Tcref)]$ $\quad Ioref = 1.913 \times 10^{-12}$

$IL = 3.563$

$Egref = 1.6$

$Eg := Egref \cdot [1 - .0002677 \cdot (Tcnew - Tcref)]$

$Eg = 1.594$

$$Io := Ioref \cdot \left(\frac{Tcnew}{Tcref}\right)^3 \cdot e^{\left[\frac{1.602 \cdot 10^{-22}}{1.381 \cdot 10^{-26}} \cdot \left(\frac{Egref}{Tcref} - \frac{Eg}{Tcnew}\right)\right]}$$

$Io = 5.547 \times 10^{-11}$

$Rsh := \frac{Gref}{Ga} \cdot Rshref$

$Rsh = 32.132$

Given

$$\frac{Imp}{Vmp} = \frac{\frac{Io}{a}\cdot e^{\left(\frac{Vmp+Imp\cdot Rs}{a}\right)}+\frac{1}{Rsh}}{1+\frac{Rs}{Rsh}+Io\cdot\frac{Rs}{a}\cdot e^{\left(\frac{Vmp+Imp\cdot Rs}{a}\right)}}$$

$$Imp = IL - Io\cdot\left[e^{\left(\frac{Vmp+Imp\cdot Rs}{a}\right)} - 1\right] - \left(\frac{Vmp + Imp\cdot Rs}{Rsh}\right)$$

$$\begin{pmatrix} Imp \\ Vmp \end{pmatrix} := Find(Imp, Vmp) = \begin{pmatrix} 2.798 \\ 15.827 \end{pmatrix}$$

$Pmx := Imp\cdot Vmp$

$Pmx = 44.278$

Single Diode Model - Curve Tracing

After obtaining the five model parameters (Ioref, ILref, Rs, Rshref, a), this code is employed to trace the IV curve and compare it to the theoretical max powerpoint equations in (Duffie & Beckman,2006) equations 23.2.13 and 23.2.14.

Initial guess for I $\quad I := 1$

Given

$$I = IL - Io\cdot\left[e^{\left(\frac{Va+I\cdot Rs}{a}\right)} - 1\right] - \frac{(Va + I\cdot Rs)}{Rsh}$$

$I(Va) := Find(I)$

$k := 0 .. 2500$

$Varray_k := 0.01k$

$Solution_k := I(Varray_k)$

$Power_k := Solution_k\cdot Varray_k$

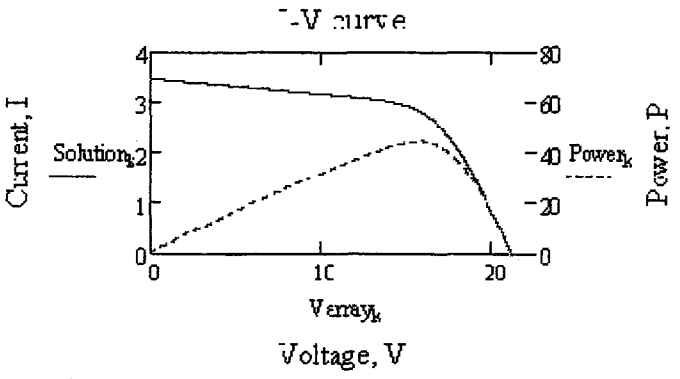

Equations 23.2.13 and equation 23.2.14 are solved simultaneously to obtain a theoretical maximum power point (Duffie&Beckman, 2006)

Initial Guess for Vmp and Imp

$Vmp := 2$

$Imp := 3$ $\qquad Rs = 1.029$

Given

$$\frac{Imp}{Vmp} - \frac{\frac{Io}{a}\cdot e^{\left(\frac{Vmp+Imp\cdot Rs}{a}\right)} + \frac{1}{Rsh}}{1 + \frac{Rs}{Rsh} + Io\cdot\frac{Rs}{a}\cdot e^{\left(\frac{Vmp+Imp\cdot Rs}{a}\right)}}$$

$$Imp = IL - Io\cdot\left[e^{\left(\frac{Vmp+Imp\cdot Rs}{a}\right)} - 1\right] - \left(\frac{Vmp + Imp\cdot Rs}{Rsh}\right)$$

$$\begin{pmatrix} Imp \\ Vmp \end{pmatrix} := \mathrm{Find}(Imp, Vmp) = \begin{pmatrix} 2.79753 \\ 15.82693 \end{pmatrix}$$

$Pmx := Imp\cdot Vmp$

$Pmx = 44.2779$

Compare this result to Powerk table and to experimental measurement

$(Power_k) =$	$Varray_k =$	$Solution_k =$
0	0	3.452
0.035	0.01	3.452
0.059	0.02	3.452
0.104	0.03	3.452
0.138	0.04	3.451
0.173	0.05	3.451
0.207	0.06	3.451
0.242	0.07	3.45
0.276	0.08	3.45
0.31	0.09	3.45
0.345	0.1	3.449
0.379	0.11	3.449
0.414	0.12	3.449
0.448	0.13	3.449
0.433	0.14	3.448
...	...	...

Appendix D. Mathcad PV Performance Sandia Model

Sandia Model. Unisolar PVL-68 parameters. November 28

Parameters

$Iscref := 5.1$

$Vocref := 23.1$

$Impref := 4.1$

$Vmpref := 16.5$

$Tcref := 273.15 + 25$

$\alpha isc := .00085$ $\quad Ns := 11$

$\alpha imp := .0012$ $\quad Nd := 3.77$

$BVoc := -.098$ $\quad k := 1.3806610^{-23}$

$Bvmp := -.052$ $\quad q := 1.6021810^{-19}$

$Ixref := 4.72$

$Ixxref := 2.9$

$c0 := 1.096$

$c1 := -.096$

$c2 := -1.14162$

$c3 := -2.89115$

$c4 := 1.044$

$c5 := -.044$

$c6 := 1.13$

$c7 := -0.13$

Evaluated at these conditions:

$Ga := 656.754$

$Tc := 40 + 273.15$

$Gref := 1000$

Guesses

$Pmp := 65$ $\quad Isc := 4.2$

$Imp := 4$ $\quad Ix := 4$

$Vmp := 20$ $\quad Ixx := 3$

$Ee := 0.9$ $\quad Voc := 20$

Given

$$Isc = Iscref \cdot [1 + \alpha isc \cdot (Tc - Tcref)] \cdot \frac{Ga}{Gref}$$

$$Imp = Impref \cdot \left(c0 \cdot Ee + c1 \cdot Ee^2\right) \cdot [1 + \alpha imp\,(Tc - Tcref)]$$

$$Ix = Ixref \cdot \left(c4 \cdot Ee + c5 \cdot Ee^2\right) \cdot \left[1 + \frac{(\alpha isc + \alpha imp)}{2} \cdot (Tc - Tcref)\right]$$

$$Ixx = Ixxref \cdot \left(c6 \cdot Ee + c7 \cdot Ee^2\right) \cdot [1 + \alpha imp \cdot (Tc - Tcref)]$$

$$Vmp = Vmpref + c2 \cdot Ns \cdot \left(\frac{Nd \cdot k \cdot Tc}{q}\right) \cdot \ln(Ee) + c3 \cdot Ns \cdot \left(\frac{Nd \cdot k \cdot Tc}{q} \cdot \ln(Ee)\right)^2 + Bvmp \cdot Ee \cdot (Tc - Tcref)$$

$$Voc = Vocref + Ns \cdot \frac{Nd \cdot k \cdot Tc}{q} \cdot \ln(Ee) + BVoc \cdot Ee \cdot (Tc - Tcref)$$

$$Pmp = Imp \cdot Vmp$$

$$Ee = \frac{Isc}{Iscref \cdot [1 + \alpha isc \cdot (Tc - Tcref)]}$$

$$\mathrm{Find}(Pmp, Imp, Vmp, Voc, Ixx, Ix, Isc, Ee) = \begin{pmatrix} 46.625 \\ 2.831 \\ 16.467 \\ 21.664 \\ 2.025 \\ 3.195 \\ 3.392 \\ 0.657 \end{pmatrix}$$

Appendix E. MATLAB PV Performance Sandia Model

```
function [x, fval] = Sandia3(Ga,Tc,xo2,options)
% Solves nonlinear equations for power (current and Voltage) at mmp)
% x(1) Isc
% x(2) Imp
% x(3) Ix
% x(4) Ixx
% x(5) Vmp
% x(6) Voc
% x(7) Pmp
% x(8) Ee
Tcref = 25 +273.15; % Operating reference cell temperature

qc = 1.60218E-19; % Elementary charge, (coulomb)
Ns = 11;  % Number of cells in series
k = 1.38066E-23;

Isco = 5.1; % short circuit current (A)
Voco = 23.1; %Open circuit at reference conditions
Impo = 4.1; % max power point current at reference conditions
Vmpo = 16.5; % voltage at max power at reference conditions
aIsc = 0.00085; %Normalized temperature coefficient for Isc(1/degC)
aImp = 0.0012; %Normalized temperature coefficient for Imp (1/degC)
c0 = 1.096; % Empirical coefficients relating Imp to Ee, Co+C1 = 1
(dimensionless)
c1 = -0.096;% Empirical coefficients relating Imp to Ee, Co+C1 = 1
(dimensionless)
BVoco = -0.098; % Temperature coefficient for module open circuit
voltage at reference conditions
mBVoc = 0 ; % coefficient for irradiance dependence of open circuit
voltage temperature coefficient, often zero (V/degC)
BVmpo = -0.052; % Temperature coefficient for module maximum power
voltage at reference conditions
mBVmpo = 0 ; % Coefficient for irradiance dependence of maximum power
voltage temperature coefficient, often zero ((V/degC)
ndiode = 3.77; % empirically determined 'diode factor' for individual
cells
c2 = -1.14162; % Empirical coefficients relating Vmp to Ee (C2
dimensionless, C3 is 1/V)
c3 = -2.89115; % empirical coefficients relating Vmp to Ee (C2
dimensionless, C3 is 1/V)
a0 = 1.047; % Empirical coefficients for f1(AMa) polynomial
a1 = 0.00082115;% Empirical coefficients for f1(AMa) polynomial
a2 = -0.0259;% Empirical coefficients for f1(AMa) polynomial
a3 = 0.0031736;% Empirical coefficients for f1(AMa) polynomial
a4 = -0.00011026; % Empirical coefficients for f1(AMa) polynomial
b0 = 1; %Empirical coefficients for f1(AOI) polynomial
b1 = -0.0052;  %Empirical coefficients for f1(AOI) polynomial
b2 = 0.0005842; %Empirical coefficients for f1(AOI) polynomial
b3 = -.000023; %Empirical coefficients for f1(AOI) polynomial
b4 = 3.826E-7; %Empirical coefficients for f1(AOI) polynomial
b5 = -2.31E-9; %Empirical coefficients for f1(AOI) polynomial
c4 = 1.044; %
c5 = -.044;
Ixo = 4.72;
```

```
Ixxo = 2.9;
c6 = 1.13;
c7 = -0.13;


[x, fval] = fsolve(@(x) nestedfun(x,Ga, Tc),xo2,options);
%nested function that computes the objective function
function f = nestedfun(x,Ga, Tc)

  f(1) = - x(1) + Isco*(1+aIsc*((Tc+273.15)-Tcref))*(Ga/1000)    ;

  f(2) = - x(2) + Impo*(c0*x(8)+c1*(x(8))^2)*(1+aImp*((Tc+273.15)-
Tcref)) ;

  f(3) = -x(3) + Ixo*(c4*x(8)+c5*(x(8))^2)*(1+
((aIsc+aImp)/2)*((Tc+273.15)-Tcref))   ;

  f(4) = - x(4) + Ixxo*(c6*x(8)+c7*(x(8))^2)*(1+ aImp*((Tc+273.15)-
Tcref));

  f(5) = - x(5) + Vmpo + c2*(Ns/qc)*ndiode*k*(Tc+273.15)*log(x(8))+
c3*Ns*(ndiode*k*(Tc+273.15)*log(x(8))/qc)^2 + BVmpo*x(8)*((Tc+273.15)-
Tcref); %

  f(6) = - x(6) +  Voco +  Ns*ndiode*k*(Tc+273.15)/qc*log(x(8))+
BVoco*x(8)*(Tc+273.15-Tcref);

  f(7) = - x(7)+ x(2)*x(5);

  f(8) = - x(8) + x(1)/(Isco*(1+aIsc*(Tc+273.15-Tcref))) ;%


end
end
```

Appendix F. Steady State Model

```
function [xs,fval2] =
BIPVTtransient3_Revisited(To,G,RH,ho,hi,n,l,Tsky,Rin_pA,area,Tin,rho,Tr
oom,e1,e2,e3,efi,hcb,hct,vel,Rtefzel,Rmix)


% constants for saturation pressure
% BIPV/T model using fsolve to solve nonlinearities.

T = 273.15 + To;                    % Operating temperature
T0 = 291.15;                       % Reference temperature for Sutherlands
formula
viscosity0 = 18.27E-6;             % Reference for Sutherlands
                                   % disp(viscosity0)
Cons = 120;                        % Cons sutherlands
viscosity = viscosity0*((T0+Cons)/(T+Cons))*((T/T0)^(3/2));
%Sutherlands formula
%disp(viscosity)                    % air viscosity
%RH = 0.42;

if To >= 0
ab = -5.8002206E3;                 % constants for saturation pressure
bb = 1.3914993;                    % constants for saturation pressure
cb = -4.8640239E-2;                % constants for saturation pressure
db = 4.1764768E-5;                 % constants for saturation pressure
eb = -1.4452093E-8;                % constants for saturation pressure
fb = 6.5459673;                    % constants for saturation pressure
ps = exp( ab/T + bb + cb*T+ db*T^2 + eb*T^3 + fb*log(T)); % saturation
pressure

else
hh = 6.3925247;                  % constants for saturation pressure
l1 = 6.22115701E-7;              % constants for saturation pressure
nn = -9.484024E-13;              % constants for saturation pressure
gg = -5.6745359E3;               % constants for saturation pressure
kk = -9.677843E-3;               % constants for saturation pressure
l2 = 2.0747825E-9;               % constants for saturation pressure
pp = 4.1635019;                  % constants for saturation pressure
ps = exp(gg/T + hh + kk*T + l1*T^2 + l2*T^3+ nn*T^4+ pp*log(T));   %
constants for saturation pressure

end


pv = RH*ps;
%disp('pv')
%disp(pv)
pt = 101325;
Ra = 287.08 ;
Rv = 461.38 ;
pa = pt - pv;
%disp ('pa');
%disp(pa);
densair = pa/(Ra*T);
%disp('air density');
%disp(densair);
```

```
denmois = pv/(Rv*T);
%disp('moisture density');
%disp(denmois);
dentotal = densair + denmois
%disp('total density');
%disp(dentotal)
cpa = 1000;
cpv = 1860;
W = 0.6219 * (pv/pa);
cp = cpa + W*cpv;
%disp('cp')
%disp(cp);

%n = 5; % number of divisions along the channel
%l = 2.884; % length of the channel in meters
xx = linspace(0,l,n+1);
xc = [xx(1,2)/2:(xx(1,3)-xx(1,2)):xx(1,n+1)-(xx(1,2))/2];
DeltaPV = xx(1,2)-xx(1,1);

WidthPV = 0.387; % Channel width
displate = 0.04; % distance between the plates


%ho = 12.5;  % exterior convective heat transfer coefficient
%hi = 12;    % interior of the room heat transfer coefficient

Ro = 1/(ho*(DeltaPV*WidthPV));  %thermal resistance to the exterior

Rroom = 1/(hi*DeltaPV*WidthPV); %thermal resistance to the interior

% hra = 4.7; % radiative heat transfer coefficient to the outside
%
% Rra = 1/hra; % thermal

%vel = 0.57; % air speed in m/s
%area = 0.0152 ; % cross sectional area in m^2
Rflow = 1/(vel*area* dentotal*cp);
%disp('Rflow')
%disp (Rflow)
%To = -2.40 %-1.38;      % Exterior air temperature in C
%Tin = To + 2.2; % Inlet air temperature in C
%disp(Tin)


%Tsky = 253; % Sky temperature in Kelvin


%Troom = 20;

%e1 = 0.77; %emissivity of the interior PV surface
%e2 = 0.20; %emissivity of the insulation
%e3 = 0.84 ; %emissivity of the module to the exterior
```

```
%Rin_pA = 1.4; % Rsi Value of the insulation
Rin = Rin_pA/(DeltaPV*WidthPV);

%hct = 5;
Rpvy = 1/(hct*DeltaPV*WidthPV);

% hcb = 10;  hcb is the air to back surface heat transfer coefficient
 Rins = 1/(hcb*DeltaPV*WidthPV);
%rho = 0.043;

%Ga = (1-rho)*G; % total incident radiation times the absorptivity of
the panel
Ga = G;
rho = rho;
S = Ga*(DeltaPV*WidthPV);
xo = [-77 69 -7 -1.7 19 6.23 0.2 15 4 11 280 4 2 2 2 2 2]';
%efi = .06;

%hcb = [10 10 10 10 10 10 10 10 10 10 10 10 10 10 10 10 10 10 10 10 10
10 10 10 10 10 10 10 10 10 10 10 10 10 10 10 10 10 10 10 10 10 10];
Rins = 1./(hcb*DeltaPV*WidthPV);

 %hct = [8.5 6.4 5.5 5 5 5 5 5 5 5 5 5 5 5 5 5 5 5 5 5 5 5 5 5 5 5 5 5 5
5 5 5 5 5 5 5 5 5 5 5 5 5 5 5 5 5 5 5 5 5 5 5 5];
Rpvy = 1./(hct*DeltaPV*WidthPV);

%Rpvy =

Tpanel = zeros(1,n);  % Pre-alocating the vector of Tpanel
Tob = zeros(1,n);     % Pre-alocating the vector with Tinlet
Tins = zeros(17,n);    % Pre-alocating the vector for the temperature
at the back plate
xs = zeros(17,n);  % pre-alocating the solutions


for i = 1:1:n
  Rey = vel*.073*dentotal/viscosity
    if Rey <2000

    hct = 1.*0.0245/.073*(0.039*(Rey)^0.78*0.71^0.4*exp(-
xc(i)/(20*0.073))+0.034*(Rey)^0.78*0.71^0.4)
    Rpvy = 1./(hct*DeltaPV*WidthPV)

    else
    %hct = 1*0.0245/.073*(0.012*(Rey)^0.78*0.71^0.4*exp(-
xc(i)/(9.09*0.073))+0.049*(Rey)^0.78*0.71^0.4)

    Rpvy = 1./(hct*DeltaPV*WidthPV)
    end
```

```
[x, fval] =
thermal8_Revisited(Rflow,Ro,To,Troom,Rin,Rins,Rroom,Rpvy,e1,e2,e3,S,Del
taPV,WidthPV,efi,Tin,Tsky,displate,Rtefzel,Rmix,rho,xo);


xs(:,i) = x  ;
Tin = xs(13,i)


end;


% tfinal = x(1,13);
% disp('tfinal');
% disp(tfinal);
% nefinal = x(1,14);
% disp('efi final');
% disp(nefinal);
% Totalelectric = nefinal*;
% disp('Total Electric power',
% disp(Totalelectric)
xx(:,1)=[];
xs13= xs(13,:);
% plot (xx, xs(13,:),'o', xc,xs(8,:), 'x', xc, xs(9,:),'g',
xc,xs(7,:),'y')
% A new matrix is defined xs2 in order to use the createfigure fuction
%
% xs2 = [xs(8,:);xs(9,:);xs(7,:)];
% createfigure(xx, xs13, xc, xs2)
```

```
function [x, fval] =
thermal8_Revisited(Rflow,Ro,To,Troom,Rin,Rins,Rroom,Rpvy,e1,e2,e3,S,Del
taPV,WidthPV,efi,Tin,Tsky,displate,Rtefzel,Rmix,rho,xo)
% Solves nonlinear equations in BIPV/T applications
% Variable definitions =
% x(1) q1 heat flux of energy by the incoming air in the channel
% x(2) q2 convective heat flux from the bottom of PV panel to the air
stream
% x(3) q3 convective heat flux from the air to the bottom surface
% x(4) q4 total heat flux crossing the bottom insulation
% x(5) q5 convective heat flux from the top surface to the exterior air
% x(6) q6 radiative heat flux from the top surface to the bottom
% x(7) Temperature of the air at midpoint
% x(8) Temperature of the internal surface of PV module
% x(9) Temperature of the back plate
% x(10) Radiative heat transfer coefficient
% x(11) Mean temperature for radiation computation
% x(12) Thermal Radiation resistance
% x(13) Temperature of the air at the exit of the control volume
% x(14) Final efficiency of the panel
% x(15) q7 Radiative heat flux to the sky
% x(16) Temperature of exterior of the PV module
% x(17) Temperature of the PV module at the mid point between tefzel
and
%Parameters
% To = temperature at the inlet

[x, fval] = fsolve(@(x)
nestedfun(x,Rflow,Ro,To,Troom,Rin,Rins,Rroom,Rpvy,e1,e2,e3,S,DeltaPV,Wi
dthPV,efi,Tin,Tsky,displate,Rtefzel,Rmix,rho),xo);
%nested function that computes the objective function
function f =
nestedfun(x,Rflow,Ro,To,Troom,Rin,Rins,Rroom,Rpvy,e1,e2,e3,S,DeltaPV,Wi
dthPV,efi,Tin,Tsky,displate,Rtefzel,Rmix,rho)
    f(1) = -x(1)-x(2)+x(3);                        %Heat balance in air
node
    f(2) = (1/Rflow)*(Tin-x(13))-x(1);              %Calculation of exit
temperature (Q/(mflow*cp))
    f(3) = (x(9)-Troom)/(Rin+Rroom)-x(4);          %Heat balance at bottom
plate
    f(4) = x(3) + x(6) - x(4);                     %Heat balance at
surface bottom plate (radiative +Convective)
    f(5) = (x(7)-x(9))/(Rins) - x(3);              %Heat balance from the
air to the bottom surface (convective)
    f(6) = (x(16) - To)/Ro  - x(5);                %Convective heat
balance outside
    f(7) = - x(2) - x(6) + (x(17)-x(8))/Rmix;          %heat balance at
bottom surface of PV module
    f(8) = (x(8) - x(7))/Rpvy - x(2);
    f(9) = 1/x(10) -x(12);
    f(10) = (x(8)-x(9))/x(12) - x(6);
    f(11) =
((fij(DeltaPV/displate,WidthPV/displate))*WidthPV*DeltaPV*5.67E-
8*((x(8)+273.15)^4-(x(9)+273.15)^4)/(1/e1+ 1/e2-1))/(x(8)-x(9)) -
x(10); %necessary to add fij(DeltaPV,WidthPV) to account view
factoreffect
    f(12) = ((x(9)+273.15)+(x(8)+273.15))/2 - x(11);
```

```
    f(13) = x(7) - TMA(x(8),x(9),Rpvy,Rins,DeltaPV,WidthPV,Rflow,Tin);
%average air temperature by integration
    f(14) = efi - 0.00014*(x(17)-25) - x(14);
    f(15) = e3*(DeltaPV*WidthPV)*5.67E-8*((x(16)+273.15)^4-(Tsky)^4)-
x(15); % Radiative heat flux to the sky
    f(16) = -  x(5) -x(15)  + (x(17)-x(16))/Rtefzel ;
    f(17) = S*(1-rho) - (x(17)-x(16))/Rtefzel - x(14)*S - (x(17)-
x(8))/(Rmix);
end
end



function y = fij(X,Y)
y = (2/(pi*X*Y))*(log((1+X^2)*(1+Y^2)/(1+X^2+Y^2))^(1/2)
+X*(1+Y^2)^(1/2)*atan((X/((1+Y^2))^(1/2))) ...
     + Y*(1+X^2)^(1/2)*atan(Y/((1+X^2)^(1/2))) - X*atan(X)-Y*atan(Y));
```

Appendix G. Transient Model

```
tic;
clear;
clc;
close all;
DATA = load('C:\Documents and Settings\Luis
Miguel\Desktop\BIPVTmfiles\ecoterramarch172008_2.txt');
sigma = 5.67E-8;
e1 = 0.10;
20;
e2 = 0.80;
e3 = 0.95;
efi = 0.06;
%Acelda = 0.881;
Acelda = 47.4;
%Rpv = 10E-3;
Rsteel = 8.5E-5;
Rtefzel = 4.17E-3;
Rmix = 7.22E-3;
Rinsul = 1.0;
%explicit transient simulation
matrix = size(DATA);
rows = matrix(1,1);
%-----&&&&&& CAPACITANCES&&&&&&&&&&----------------------
Cap_pv = 1837.5; % heat capacitance o the PV module
Cap_b = 30;
CAP_MIX = 6000; %heat capacitance of the mix layers
%-----------------------------------------------------
% ambient air temperature
% initial pv temperature
% input the time for simulation in minutes
% initialize the time vector
Tpv = zeros(1,rows); %preallocating Temperature results
%----DIMENSIONS OF THE CHANNEL----------------
WidthPV = 10.4;
DeltaPV = 5.5;
displate = 0.037;
Le = (4*WidthPV*DeltaPV)/(2*WidthPV+2*DeltaPV);
%-----------------------------------------
Ar = WidthPV*DeltaPV;
%--------INITIAL VALUES-----------------
Tpv(1) = DATA(1,126);
Tma(1) = DATA(1,149);
Tb(1) = DATA(1,152);
qrad(1) = DATA(1,153)/Ar;
Pelect(1) = DATA(1,140)/Acelda;
qsky(1) = DATA(1,127)/Ar;
Toutlet(1) = DATA(1,150);
Tinlet(1) = DATA(1,151);
```

```
qrec(1) = DATA(1,156)/Ar;
Tattic(1) = DATA(1,79);
%-----------------------------------------
Tiempo = DATA(:,1);
for i = 1:rows
To(i) = DATA(i,147);
%ho(i) = 8.55+ 2.56*DATA(i,137); %Correlation by Test
%ho(i) = 13.5+1.50*DATA(i,100);
%ho(i) = 11.4+1.7*DATA(i,137); % Adjusted by Luis
ho(i) = 11.9+2.2*DATA(i,137); % Correlation by Sharpless
%ho(i) = 5.7 + 3.8*DATA(i,100); % McAdams Correlation
% if DATA(i,100) <= 0.22
% ho(i) = incropera(DATA(i,85),DATA(i,111),DATA(i,118)/100,WidthPV,DeltaPV)
*2;
% function h = incropera(Tplate,To, RH,WidthPV,DeltaPV)
% CHURCHIL(Tplate,To, RH,WidthPV,DeltaPV)
% else
% ho(i) = ramacha(DATA(i,85),300,0.024, DATA(i,118)/100, WidthPV,DeltaPV,
DATA(i,100),45)*0.024/Le;
% ramacha(To, q, k, RH, WidthPV,DeltaPV,vel,tilt)
% end
%ho(i) = DATA(i,99); % read from the table
%ho(i) = 14;
%hct(i) = 8.38*DATA(i,139) + 1.7635 ; % hct obtained from experimental formula
hct(i) = 0.024/.074*0.052*(DATA(i,139)*.074*1.2/1.8E-5)^0.78*0.71^0.4;
%hcb(i) = 13.288*exp(1.1734*DATA(i,139)); % hcb obtained from experimental
formula
hcb(i) = 0.024/.074*1.017*(DATA(i,139)*.074*1.2/1.8E-5)^0.471*0.71^0.4;
SR(i) = 0.96*DATA(i,41); %Solar radiation
Tsky(i) = DATA(i,148); %Sky temperature
Tinlet(i) = DATA(i,151); %Initial air temperature
mflow(i) = DATA(i,134); %mass flow rates
cp_air(i) = DATA(i,157); %specific heat of air
Tmanew(i) = DATA(i,149); %mean air emp
Tattic(i) = DATA(1,79); % Tattic
end
%DT = 60; %time interval in seconds
% DT was tested for 60s, 30 s, and 1 s. Numerical Stability must be ensured due to
capacitance.
dT = 1;
%INTERPOLATED VALUES-----------------------------------------------------
Tiempo_int = DATA(1,1):dT:(DATA(rows,1));
Tiempo_int = Tiempo_int';
To = To';
To_int = interp1(Tiempo,To,Tiempo_int,'linear');
ho_int = interp1(Tiempo,ho,Tiempo_int,'linear');
hct_int = interp1(Tiempo,hct,Tiempo_int,'linear');
hcb_int = interp1(Tiempo,hcb,Tiempo_int,'linear');
```

```
SR_int = interp1(Tiempo,SR,Tiempo_int,'linear');
Tsky_int = interp1(Tiempo,Tsky,Tiempo_int,'linear');
Tinlet_int = interp1(Tiempo,Tinlet,Tiempo_int,'linear');
mflow_int = interp1(Tiempo,mflow,Tiempo_int,'linear');
cp_air_int = interp1(Tiempo,cp_air,Tiempo_int,'linear');
Tattic_int = interp1(Tiempo,Tattic,Tiempo_int,'linear');
%Tma_int = interp1(Tiempo,Tmanew,Tiempo_int,'linear');
%-----------------------------------------------------------------------------
n = numel(To_int);
%----CORRECTION TO GET SOLAR TIME------------
for i = 1:n
Tiempo_cor(i) = (AST(76,Tiempo_int(i)/3600,1))*3600;
end
%-----------------------------------------------
%---INITIAL VALUES OF CONSTANTS TO DESCRIBE EXPONENTIAL
RISE---------------
C1(1) = (hct_int(1)*Tpv(1)+hcb_int(1)*Tb(1))/(hct_int(1)+hcb_int(1));
C2(1) = (WidthPV*(hct_int(1)+hcb_int(1)))/(mflow_int(1)*cp_air_int(1));
%-----------------------------------------------------------------------
%----NUMBER OF SECTIONS------------
nsec = 6;
k = 1:nsec; %counter
CAP_PV = Cap_pv;
CAP_B = Cap_b;
SECLENGTH = DeltaPV/nsec;
%-----------------------------------
%---INITIAL VALUES IN SECTIONS------
for k=1:nsec
TPV_TOP(k,1) = Tpv(1);
TMID1(k,1) = Tpv(1)-0.5;
TPV(k,1) = Tpv(1)-.8;
TMID2(k,1) = Tpv(1)-1;
TPV_BOT(k,1) = Tpv(1)-1.2;
TB(k,1) = Tb(1);
TMA_int(k,1) = Tma(1);
QRAD(k,1) = qrad(1)/nsec;
QREC(k,1) = qrec(1)/nsec;
C_ONE(k,1) = C1(1);
C_TWO(k,1) = C2(1);
PELECT(k,1) = Pelect(1)/Ar; %Electrical output per m2
QSKY(k,1) = qsky(1)/nsec;
end
%*****************************************************************************
%********BIG LOOP ***************************************************************
%*****************************************************************************
PROGRESS = 0;
for k = 1:nsec
for i = 1:n-1 % numer of times the equation is solved
```

```
% ENERGY BALANCE EQUATIONS
%-----ENERGY BALANCE IN THE PV MODULE-----------------------
TPV_TOP(k,i+1) = fzero(@(x) EB_TPVELECT2(x,TMID1(k,i),To_int(i),Tsky_int(i),
Rtefzel/2,ho_int(i)),TPV_TOP(k,i));
TMID1(k,i+1) = TMID1(k,i) + (dT/CAP_PV)*( (TPV_TOP(k,i)-TMID1(k,i))/
(Rtefzel/2) + (TPV(k,i)-TMID1(k,i))/(Rtefzel/2));
%TPV(k,i+1) = ((TMID1(k,i))/(Rtefzel/2) + TMID2(k,i)/(Rmix/2) + SR_int(i)*IACor
(48,Tiempo_cor(i)/3600) - PELECT(k,i))/(1/(Rtefzel/2)+1/(Rmix/2));
TPV(k,i+1) = ( (SR_int(i)*IACor(76,Tiempo_cor(i)/3600) - PELECT(k,i))*(Rtefzel/2)*
(Rmix/2) + TMID1(k,i)*(Rmix/2) + TMID2(k,i)*(Rtefzel/2) ) /(Rmix/2 + Rtefzel/2);
TMID2(k,i+1) = TMID2(k,i) + (dT/CAP_MIX)*( (TPV(k,i)-TMID2(k,i))/(Rmix/2) +
(TPV_BOT(k,i)-TMID2(k,i))/(Rmix/2));
TPV_BOT(k,i+1) = fzero(@(x) EB_TPVBOT2(x,TMID2(k,i),TMA_int(k,i),TB(k,i),
Rmix/2,hct_int(i)),TPV_BOT(k,i));
%TPV_BOT,TMID,Tair,Tabs,R1,hair
%-----ABSORBER PLATE------
%TB(k,i+1) = TB(k,i) + (dT/CAP_B)*( (TMA_int(k,i)-TB(k,i))*hcb_int(i) + QRAD(k,
i)); %Absorber Plate
TB(k,i+1) = (TMA_int(k,i)*hcb_int(i) + Tattic_int(i)/Rinsul + QRAD(k,i)) / (hcb_int(i)
+1/Rinsul);
%------------OTHER EQUATIONS-----------------------------------------
C_ONE(k,i+1) = (hct_int(i)*TPV_BOT(k,i)+hcb_int(i)*TB(k,i))/(hct_int(i)+hcb_int
(i));
C_TWO(k,i+1) = (WidthPV*(hct_int(i)+hcb_int(i)))/(mflow_int(i)*cp_air_int(i));
if k <= 1
TMA_int(k,i+1) = (1/SECLENGTH)*quad(@(x) (C_ONE(k,i) + (Tinlet_int(i)-
C_ONE(k,i))*exp(-C_TWO(k,i)*x)),0,SECLENGTH);
else
TMA_int(k,i+1) = (1/SECLENGTH)*quad(@(x) (C_ONE(k,i) + (TOUTLET(k-1,i)-
C_ONE(k,i))*exp(-C_TWO(k,i)*x)),0,SECLENGTH);
end
%Tma_int(i+1) = (Toutlet(i) + Tinlet_int(i))/2;
if k <= 1
TOUTLET(k,i+1) = Tinlet_int(i) + QREC(k,i)*(Ar/nsec)/(mflow_int(i)*cp_air_int
(i));
else
TOUTLET(k,i+1) = TOUTLET(k-1,i) + QREC(k,i)*(Ar/nsec)/(mflow_int(i)
*cp_air_int(i));
end
QREC(k,i+1) = hct_int(i)*(TPV_BOT(k,i)-TMA_int(k,i)) + hcb_int(i)*(TB(k,i)-
TMA_int(k,i));
QRAD(k,i+1) = (fij(SECLENGTH/displate,WidthPV/displate))*sigma*((1/e1+1/e2-
1)^-1)*( (TPV_BOT(k,i)+273.15)^4 - (TB(k,i)+273.15)^4 );
QSKY(k,i+1) = sigma*e3*( (TPV_TOP(k,i)+273.15)^4 - (Tsky_int(i))^4 );
PELECT(k,i+1) = (efi - 0.00014*(TPV(k,i)-25))*SR_int(i)*.8*IACor(76,Tiempo_cor(i)
/3600);
%-----------------------------------------------------------------
PROGRESS = ((k-1)*n+i)/(n*nsec);
```

```
progressbar(PROGRESS);
end
end
%********END OF BIG LOOP*****************
%grid on
%plot(DATA(:,1)/3600,Tpv,'+',DATA(:,1)/3600,DATA(:,85),'o');
%Obtaining PV bottom average%%%
for i=1:n
TOTAL = 0;
for k=1:nsec
TOTAL = TPV_BOT(k,i) + TOTAL;
end
TPV_avg(i) = TOTAL/nsec;
end
%%%%%%%%%%%%%%%%%%%%%%%%%%
%Obtaining  ABSORBER PLATE Average%%%
for i=1:n
TOTAL = 0;
for k=1:nsec
TOTAL = TB(k,i) + TOTAL;
end
TB_avg(i) = TOTAL/nsec;
end
%%%%%%%%%%%%%%%%%%%%%%%%%%
%Obtaining  TPV_TOP Average%%%
for i=1:n
TOTAL = 0;
for k=1:nsec
TOTAL = TPV_TOP(k,i) + TOTAL;
end
TPV_TOP_avg(i) = TOTAL/nsec;
end
%%%%%%%%%%%%%%%%%%%%%%%%%%
%Obtaining TPV Average%%%
for i=1:n
TOTAL = 0;
for k=1:nsec
TOTAL = TPV(k,i) + TOTAL;
end
TPVele_avg(i) = TOTAL/nsec;
end
%%%%%%%%%%%%%%%%%%%%%%%%%%
close all
%--------PV GRADIENT---------------
%plot(Tiempo_int/3600,TPV_TOP(4,:),'*',Tiempo_int/3600,TPV_MID(4,:),'*',
Tiempo_int/3600,TPV_BOT(4,:),'o')
%plot(Tiempo_int/3600,TPV_TOP(4,:),'*',Tiempo_int/3600,TMID1(4,:),'+',
Tiempo_int/3600,TPV_BOT(4,:),'o',Tiempo_int/3600,TPV(4,:),'k',Tiempo_int/3600,
```

```
TMID2(4,:),'b')
%plot(Tiempo_int/3600,TPV_TOP(4,:),'*',Tiempo_int/3600,TMID1(4,:),'d',
Tiempo_int/3600,TPV(4,:),'o',Tiempo_int/3600,TMID2(4,:),'+',Tiempo_int/3600,
TPV_BOT(4,:),'x', Tiempo_int/3600,TB(4,:),'<', DATA(:,1)/3600,DATA(:,116),'>',DATA
(:,1)/3600,DATA(:,85),'o')
%plot(Tiempo_int/3600,TPV_avg,'-',DATA(:,1)/3600,DATA(:,126),'o',Tiempo_int/3600,
TB_avg,'+',DATA(:,1)/3600,DATA(:,152),'d');
%plot(Tiempo_int/3600,TPV_avg,'-',DATA(:,1)/3600,DATA(:,126),'o',Tiempo_int/3600,
TB_avg,'+',DATA(:,1)/3600,DATA(:,152),'d',Tiempo_int/3600,TPV_TOP_avg,'s');
plot(Tiempo_int/3600,TPV_avg,'-',DATA(:,1)/3600,DATA(:,126),'o',Tiempo_int/3600,
TB_avg,'+',DATA(:,1)/3600,DATA(:,152),'d',Tiempo_int/3600,TPV_TOP_avg,'s',
Tiempo_int/3600,TPVele_avg,'x',Tiempo_int/3600,TOUTLET(6,:),'>');
%Temperature ABSORBER PLATE
%plot(DATA(:,1)/3600,DATA(:,116),'*',Tiempo_int/3600,TB_avg,'-');
% X1 = Tiempo_int/3600;
% YMatrix1 = [TPV_TOP(4,:)' TMID1(4,:)' TPV(4,:)' TMID2(4,:)' TPV_BOT(4,:)' TB
(4,:)'];
% X2 = DATA(:,1)/3600;
% YMatrix2 = [DATA(:,116) DATA(:,85)];
%
% createfigure1(X1, YMatrix1, X2, YMatrix2)
toc
```